



# High-resolution time-frequency SAR signal processing for large infrastructure monitoring

Andrei Anghel

## ► To cite this version:

Andrei Anghel. High-resolution time-frequency SAR signal processing for large infrastructure monitoring. Signal and Image processing. Université Grenoble Alpes; Universitatea politehnica (Bucarest), 2015. English. NNT : 2015GREAT107 . tel-01265538

HAL Id: tel-01265538

<https://theses.hal.science/tel-01265538>

Submitted on 1 Feb 2016

**HAL** is a multi-disciplinary open access archive for the deposit and dissemination of scientific research documents, whether they are published or not. The documents may come from teaching and research institutions in France or abroad, or from public or private research centers.

L'archive ouverte pluridisciplinaire **HAL**, est destinée au dépôt et à la diffusion de documents scientifiques de niveau recherche, publiés ou non, émanant des établissements d'enseignement et de recherche français ou étrangers, des laboratoires publics ou privés.



UNIVERSITÉ  
GRENOBLE  
ALPES

## THÈSE

Pour obtenir le grade de

**DOCTEUR DE L'UNIVERSITÉ GRENOBLE ALPES**

**préparée dans le cadre d'une cotutelle entre  
l'Université Grenoble Alpes et l'Université  
Polytechnique de Bucarest**

Spécialité : **Signal, Image, Parole, Télécoms**

Arrêté ministériel : le 6 janvier 2005 - 7 août 2006

Présentée par

**Andrei ANGHEL**

Thèse dirigée par **Cornel IOANA** et **Gabriel VASILE**  
codirigée par **Silviu CIOCHINĂ**

préparée au sein des **Grenoble Image Parole Signal  
Automatique laboratoire (GIPSA-lab)** et **Faculté  
d'Électronique, Télécommunications et Technologies de  
l'Information (ETTI)**  
dans les **Écoles Doctorales EEATS et ETTI**.

**Analyse temps-fréquence et traitement des  
signaux RSO à haute résolution spatiale pour  
la surveillance des grands ouvrages d'art**

Thèse soutenue publiquement le **8 Octobre 2015**,  
devant le jury composé de :

**M. Ljubiša STANKOVIĆ**

Professeur, Université de Monténégro, Président

**M. Hugh GRIFFITHS**

Professeur, UCL, Rapporteur

**M. Laurent POLIDORI**

Professeur, ESGT-CNAM, Rapporteur

**M. Marc LESTURGIE**

Professeur, Centrale-Supélec, Membre

**M. Remus CACOVEANU**

Maître de conférences, Université Polytechnique de Bucarest, Membre

**M. Rémy BOUDON**

Expert Topographie, EDF – DPIH – DTG, Membre invité

**M. Gabriel VASILE**

Chargé de recherche, CNRS, Encadrant

**M. Cornel IOANA**

Maître de conférences, Grenoble-INP, Directeur de thèse

**M. Silviu CIOCHINĂ**

Professeur, Université Polytechnique de Bucarest, Co-Directeur de thèse





# T H E S I S

---

## HIGH-RESOLUTION TIME-FREQUENCY SAR SIGNAL PROCESSING FOR LARGE INFRASTRUCTURE MONITORING

---

Presented and defended by

Andrei ANGHEL

for jointly obtaining the

### DOCTORATE DEGREE

of University of Grenoble

*Doctoral School for Electronics, Power Systems, Automatic Control and Signal Processing  
Specialization: Signal, Image, Speech, Telecommunications*

and the

### PHD DEGREE IN TECHNICAL SCIENCES

of University POLITEHNICA of Bucharest

*Faculty of Electronics, Telecommunications and Information Technology  
Specialization: Electronic Engineering and Telecommunications*

Thesis supervised by Gabriel VASILE

directed by Cornel IOANA and Silviu CIOCHINĂ.

Prepared in the Grenoble Image Parole Signal Automatique laboratory (GIPSA-lab) and at the Faculty of Electronics, Telecommunications and Information Technology.

Defended in Grenoble, on 8th October 2015, in front of the jury:

|                        |                   |  |
|------------------------|-------------------|--|
| <i>President:</i>      | Ljubiša STANKOVIĆ | - Professor, University of Montenegro  |
| <i>Reviewers:</i>      | Hugh GRIFFITHS    | - Professor, University College London |
|                        | Laurent POLIDORI  | - Professor, CNAM, L2G                 |
| <i>Examiners:</i>      | Marc LESTURGIE    | - Professor, Centrale-Supélec          |
|                        | Remus CACOVEANU   | - Associate Professor, UPB             |
| <i>Invited member:</i> | Rémy BOUDON       | - Topography Expert, EDF – DPIH – DTG  |
| <i>Supervisor:</i>     | Gabriel VASILE    | - Research Scientist, CNRS             |
| <i>Director:</i>       | Cornel IOANA      | - Associate Professor, Grenoble INP    |
| <i>Co-Director:</i>    | Silviu CIOCHINĂ   | - Professor, UPB                       |



# Acknowledgements

This thesis is the result of a collaboration between the Grenoble-Image-sPeech-Signal-Automatics Laboratory (GIPSA-lab, Grenoble INP) and the Telecommunications Department of the Faculty of Electronics, Telecommunications and Information Technology, University POLITEHNICA of Bucharest (UPB).

First of all i would like to express my gratitude to my thesis directors Assoc. Prof. Cornel Ioana and Prof. Silviu Ciochină for their guidance, scientific advice and comments provided in the last three years. I would also like to thank Dr. Gabriel Vasile and Assoc. Prof. Remus Cacoveanu for their actual contribution to my work as specialists in the field of radar and signal processing.

I want to thank Prof. Hugh Griffiths and Prof. Laurent Polidori for agreeing to be reviewers of my thesis. I also want to show my gratitude to Prof. Marc Lesturgie for being part of my defense committee. Special thanks to Prof. Ljubiša Stanković for accepting to preside the jury.

I also must acknowledge the engineers from *Électricité de France* who made possible the applicative part of the thesis. Thanks to Mr. Rémy Boudon, Mr. Guy d'Urso, Mr. Alexandre Girard and Mr. Didier Boldo for their advice from a more pragmatic point of view.

Finally, I thank all the members of GIPSA-lab and the Telecommunications Department for the nice atmosphere in both research centers.



# Contents

|   |            |
|---|------------|
| <b>List of Tables</b>   | <b>vii</b> |
| <b>List of Figures</b>  | <b>ix</b>  |
| <b>Abbreviations and acronyms</b>                                   | <b>xv</b>  |
| <b>I Introduction</b>   | <b>1</b>   |
| I.1 Field description . . . . .                                     | 1          |
| I.2 Thesis purpose . . . . .  | 2          |
| I.3 Chapters presentation . . . . .                                 | 3          |
| <b>A METHODOLOGICAL CONTEXT</b>                                     | <b>7</b>   |
| <b>II Time-Frequency and SAR signal processing methods overview</b> | <b>9</b>   |
| II.1 Time-frequency processing of non-stationary signals . . . . .  | 9          |
| II.1.1 Short-Time Fourier Transform . . . . .                       | 10         |
| II.1.2 Measure of Concentration . . . . .                           | 12         |
| II.1.3 High-Order Ambiguity Function . . . . .                      | 12         |
| II.1.4 Time warping and the matched signal transform . . . . .      | 15         |
| II.2 SAR signals processing tools . . . . .                         | 17         |
| II.2.1 SAR signal model . . . . .                                   | 17         |
| II.2.2 Time-domain SAR image formation algorithms . . . . .         | 18         |
| II.2.3 Four-dimensional SAR Tomography Framework . . . . .          | 20         |
| <b>III Range processing of FMCW radar signals</b>                   | <b>23</b>  |

---

# High-Resolution SAR Signal Processing for Infrastructure Monitoring

---

|   |           |
|---|-----------|
| III.1 Nonlinearity problem and state of the art . . . . .                 | 23        |
| III.2 Nonlinear FMCW radar beat signal . . . . .                          | 24        |
| III.3 Discrete signal model and the Cramér-Rao lower bound . . . . .      | 26        |
| III.4 HAF-based nonlinearity correction . . . . .                         | 28        |
| III.5 Range autofocusing nonlinearity correction . . . . .                | 29        |
| III.6 Correction algorithms comparison . . . . .                          | 32        |
| III.7 Conclusions . . . . .   | 36        |
| <br>  |           |
| <b>IV Scattering Centers Monitoring in Refocused SAR images</b>           | <b>37</b> |
| IV.1 Scattering Centers Monitoring Overview . . . . .                     | 37        |
| IV.2 Azimuth Defocusing . . . . .   | 42        |
| IV.3 Back-projection grid focusing . . . . .                              | 45        |
| IV.4 4D Tomography Detection and Tracking of Scattering Centers . . . . . | 46        |
| IV.5 Simulation results . . . . .   | 48        |
| IV.5.1 Radar Geometry to Ground Geometry . . . . .                        | 48        |
| IV.5.2 Refocusing approach vs. Grid interpolation . . . . .               | 48        |
| IV.5.3 Scattering Centers Detection and Tracking Results . . . . .        | 49        |
| IV.5.4 Position test vs. Classical scatterers identification . . . . .    | 61        |
| IV.6 Conclusions . . . . .  | 64        |
| <br>  |           |
| <b>B APPLIED CONTEXT</b>  | <b>65</b> |
| <br>  |           |
| <b>V FMCW radar demonstrator system</b>                                   | <b>67</b> |
| V.1 Short-Range FMCW radar architecture . . . . .                         | 67        |
| V.2 Measurement results . . . . .   | 71        |
| V.2.1 HAF-based correction algorithm testing . . . . .                    | 71        |

## Contents

---

|  |            |
|--|------------|
| V.2.2 Range autofocusing testing . . . . .                                 | 75         |
| V.2.3 Displacement Measurements . . . . .                                  | 78         |
| V.3 Conclusions . . . . .  | 82         |
| <b>VI Combining SAR data with 3D Point Clouds of Large Infrastructures</b> | <b>83</b>  |
| VI.1 Test site and Data description . . . . .                              | 83         |
| VI.1.1 SAR data . . . . .  | 85         |
| VI.1.2 Point Clouds generation . . . . .                                   | 85         |
| VI.1.3 In-situ measurements devices . . . . .                              | 91         |
| VI.2 SAR data and Point Cloud processing . . . . .                         | 93         |
| VI.3 Deformation measurements . . . . .                                    | 101        |
| VI.3.1 Chastel landslide . . . . .   | 101        |
| VI.3.2 Puylaurent dam . . . . .  | 108        |
| VI.4 Conclusions . . . . .   | 113        |
| <b>Overall remarks, contributions and perspectives</b>                     | <b>115</b> |
| <b>Publications</b>  | <b>119</b> |
| <b>Bibliography</b>  | <b>123</b> |
| <i>Abstract (en)</i>   | 133        |
| <i>Résumé (fr)</i>   | 135        |
| <i>Rezumat (ro)</i>  | 137        |
| <i>Résumé étendu (fr)</i>  | 139        |
| I Introduction . . . . .   | 139        |

---

## High-Resolution SAR Signal Processing for Infrastructure Monitoring

---

|   |     |
|---|-----|
| Partie A: Contexte méthodologique . . . . .   | 141 |
| II    Analyse temps-fréquence et traitement des images RSO . . . . .                                    | 141 |
| III   Traitement des signaux radar FMCW en distance . . . . .   | 147 |
| IV    La surveillance des centres de diffusion dans les images RSO recentrées . .                       | 151 |
| Partie B: Contexte appliqué . . . . .   | 156 |
| V     Plateforme radar FMCW . . . . .   | 156 |
| VI    La combinaison entre les données RSO et le maillage 3D décrivant un grand ouvrage d'art . . . . . | 159 |
| Remarques générales, conclusions et perspectives . . . . .  | 166 |

# List of Tables

|      |  |     |
|------|--|-----|
| IV.1 | False Alarm Probability (%) . . . . .  | 52  |
| V.1  | Specifications of the FMCW Radar system . . . . .                                    | 70  |
| V.2  | HAF-based Correction Algorithm, -10 dB Resolution (4 GHz) . . . . .                  | 73  |
| V.3  | Nonlinearity Correction Algorithms, -10dB Resolutions Comparison (3 GHz)             | 76  |
| VI.1 | 2013-2014 High-Resolution TerraSAR-X/TanDEM-X Sliding Spotlight SAR Images . . . . . | 86  |
| VI.2 | Ground Mean Displacement Velocity of the Chastel landslide . . . . .                 | 107 |
| VI.3 | LOS MDV Measurements on the water-dam. . . . .                                       | 110 |



# List of Figures

|       |   |    |
|-------|---|----|
| II.1  | Second order instantaneous moment computation for a quadratic phase signal. . . . .   | 14 |
| II.2  | SAR acquisition geometry for a point having the position vector $\vec{r}_i$ . . . . .   | 18 |
| II.3  | Four-dimensional tomography geometry: (a) 3D view and (b) 2D section parallel to yOz plane. . . . .   | 20 |
| III.1 | Time warping as time resampling: (a) Analog and digital signals in the original time axis, (b) Analog and digital signals in the warped time axis, (c) Resampled digital signal in the warped time axis vs. the analog signal. . . . .  | 27 |
| III.2 | Nonlinearity correction algorithm based on high-order ambiguity functions and time warping. . . . .   | 30 |
| III.3 | Range autofocusing algorithm for a nonlinearity model with 2 parameters. . . . .  | 31 |
| III.4 | Spectrogram (a) and range profile (b) of the initial beat signal. The time-frequency trajectories of the 4 targets are separated, but in the range profile they are completely overlapped. . . . .  | 32 |
| III.5 | Simulated nonlinearity corrected range profiles. Figures (a) and (b) show respectively the range profiles and a zoomed in version (on the target placed at 30 m) when there is one dominant target at 20 m. Figures (c) and (d) show respectively the range profiles and a zoomed in version (on the target placed at 30 m) when all the targets have similar amplitudes. When there is no dominant target, the performance of the autofocusing approach is unaltered, while the HAF-based algorithm doesn't manage to estimate and correct the nonlinearities. . . . . | 33 |
| III.6 | The spectral concentration measure (a) as a function of two variables and (b) its evolution throughout the autofocus optimization. The trajectory described by the two parameters is superimposed in figure (a). The considered scenario is the one when all targets have similar amplitudes. . . . .   | 34 |
| III.7 | Mean absolute error and variance of parameter $p_1$ using both the autofocusing approach and the HAF-based method. The considered simulation scenario is with one dominant target. . . . .  | 35 |

|       |   |    |
|-------|---|----|
| IV.1  | Scattering Centers Detection and Tracking based on SAR Images Refocusing.   | 40 |
| IV.2  | Block diagram of the refocusing algorithm and qualitative representation of the real part of certain intermediate signals in the case of a single scatterer (zero Doppler centroid is assumed for representation simplicity). . . . .   | 41 |
| IV.3  | Layover detection geometry based on zero elevation for on-grid targets. . . . .   | 47 |
| IV.4  | Refocusing Algorithm Simulation: (a) Simulation scenario, (b) Focused SAR image with the Frequency Scaling Algorithm in slant range-azimuth geometry, (c) Refocused image on a grid placed in the horizontal plane containing the scatterers. . . . .   | 49 |
| IV.5  | Comparison between the refocusing approach and 3 interpolation-based methods in terms of phase dispersion (a) and average coherence (b). . . . .  | 50 |
| IV.6  | Envisaged geometric configuration for the detection and tracking simulations.   | 51 |
| IV.7  | Detection probability vs. SNR for one scatterer having a linear motion in LOS. The considered accuracies are 0.5 m, 2.5 m and 5 m and the number of simulated satellite passes are: (a) 5 tracks, (b) 8 tracks, (c) 15 tracks. . . . .  | 53 |
| IV.8  | (a) Dispersion of estimated MDV, (b) Bias of estimated MDV and (c) Displacement dispersion/bias vs. SNR for one scatterer with linear motion in LOS. . . . .  | 54 |
| IV.9  | Estimated elevation-velocity PSD planes for 8 tracks and different SNRs: (a) 5 dB, (b) 15 dB, (c) 25 dB. . . . .  | 55 |
| IV.10 | Estimated elevation-velocity PSD planes for an SNR of 10 dB and different number of satellite passes: (a) 5 tracks, (b) 8 tracks, (c) 15 tracks. . . . .  | 56 |
| IV.11 | Detection probability and MDV for one scatterer having a combination of linear and un-modeled nonlinear motion in LOS. The legend signifies the dispersion of the nonlinear motion. Detection probability for (a) 5 tracks and (b) 8 tracks. MDV (c) dispersion and (d) bias for 8 tracks. . . . .            | 57 |
| IV.12 | Detection probability and MDV for two scatterers (a second target placed in layover with the main one). The legend signifies the amplitude of the second scatterer relative to the main one. Detection probability for (a) 8 tracks and (b) 15 tracks. MDV (c) dispersion and (d) bias for 15 tracks. . . . . | 59 |
| IV.13 | Estimated elevation-velocity PSD planes for 15 tracks, SNR of 20 dB and different amplitudes of the second scatterer relative to the main one: (a) 0 dB, (b) -3 dB, (c) -9 dB, (d) single scatterer . . . . .   | 60 |

## List of Figures

---

|   |    |
|---|----|
| IV.14 Detection probability comparison between Position test, GLRT and PS selection for a single on-grid scatterer with an MDV of 1 mm/time unit, 15 tracks and 2.5 m elevation accuracy. . . . .   | 62 |
| IV.15 Layover rejection comparison between Position test, GLRT and PS selection for a scatterer in layover placed at 50 m in elevation and an SNR of 15 dB. . . . .   | 63 |
| V.1 Block diagram (a) and a picture (b) of the X-band FMCW radar. . . . .   | 68 |
| V.2 Intermediary frequency signal spectrum. The analog filter removes the low-frequency components, improves the signal to noise ratio and acts as anti-aliasing filter. . . . .  | 71 |
| V.3 High-order ambiguity functions of the beat signal for two delay lines. The continuous plots show the functions for a 30 cm air-equivalent length delay line (short path) and the dotted ones for a 240 cm air-equivalent delay line (long path). . . . .  | 72 |
| V.4 Range profiles for two delay lines. The profiles obtained with a linear sweep and HAF-based correction are compared with the profile resulted for a predistorted sweep (shown with dotted line) computed from the measured frequency-voltage calibration curve. There are three cases considered: (a) no correction, (b) short path correction, (c) long path correction. . . . . | 74 |
| V.5 Experimental range profiles for a scene containing two metal bars and one highly reflective metal disc. On the corrected range profile with the HAF-based method the three targets are clearly separated, while in the nonlinear range profile the scatterers cannot be distinguished. . . . .  | 75 |
| V.6 Experimental results obtained with the range autofocusing method. (a) Spectrogram of the initial beat signal. (b) Spectrogram of the corrected beat signal after autofocusing. (c) Spectral concentration measure and the trajectory described by the parameters in the optimization algorithm. (d) Autofocused range profile compared to the initial (nonlinear) one. . . . .    | 76 |
| V.7 Results of the nonlinearity correction applied to a FMCW radar image before azimuth focusing. In the SAR image affected by the VCO's nonlinearity (a) the targets are almost indistinguishable, while in the corrected image (b) the targets are clearly separated. . . . .   | 77 |

---

## High-Resolution SAR Signal Processing for Infrastructure Monitoring

---

|       |   |    |
|-------|---|----|
| V.8   | Simulated displacement error dispersion vs. SNR for targets placed at 2 m and 50 m. The expected measurement error should get below 0.1 mm for SNRs higher than 25 dB. . . . .  | 78 |
| V.9   | Displacement measurements results from: (a) Range profiles and (b) SAR Images. . . . .  | 80 |
| V.10  | Coherence (a) and interferogram (b) of two acquired SAR images computed with a 3x3 boxcar. The coherence is almost 1 and the phase has approximatively constant value in the proximity of the metal targets (marked by the dotted ellipses). . . . .    | 81 |
| VI.1  | Test site in the Lozère region: (a) Google Earth image, (b) Puylaurent water-dam, (c) Chastel landslide. . . . .  | 84 |
| VI.2  | GPS-localized points overlaid by the Google Earth image. . . . .  | 87 |
| VI.3  | Laser scanners positions overlaid on the final point cloud of the Puylaurent dam: (a) lateral view and (b) downstream to upstream view. . . . .   | 88 |
| VI.4  | Laser scanner: (a) placed by forced centering in the position of the total station, (b) in "tilt mount" configuration. . . . .  | 89 |
| VI.5  | Point clouds overlaid on Google Earth images: (a) the Chastel landslide, (b) the Puylaurent dam. . . . .  | 90 |
| VI.6  | In-situ measurement configuration of the Chastel landslide. . . . .   | 91 |
| VI.7  | In-situ measurement points on the Puylaurent dam: (a) overlaid on Google Earth image, (b) detailed diagram (the heights are in IGN 69 system). . .  | 92 |
| VI.8  | Spectrogram of an azimuth defocused line in sliding spotlight acquisition mode. . . . .   | 94 |
| VI.9  | 2D Grid Refocusing. (a) High-Resolution Spotlight TerraSAR-X SAR image of the Puylaurent dam acquired on 11.04.2013. (b) Refocused TerraSAR-X image on the rectangular grid overlaid by the set of GPS measured points on the ridge of the dam. . . . . | 95 |
| VI.10 | TerraSAR-X data, Descending orbit, 24.10.2014: Initial image in slant range-azimuth geometry (a), and zoom in on the Puylaurent water-dam (b) and the Chastel landslide (c). . . . .  | 96 |

## List of Figures

---

|  |     |
|--|-----|
| VI.11 TerraSAR-X data, Descending orbit, 24.10.2014: Refocused image on the water-dam (a) and landslide (b) point clouds (same colorbar) . . . . .   | 97  |
| VI.12 TerraSAR-X data, Ascending orbit, 31.10.2014: Initial image in slant range-azimuth geometry (a), and zoom in on the Puylaurent water-dam (b) and the Chastel landslide (c) . . . . .   | 98  |
| VI.13 TerraSAR-X data, Ascending orbit, 31.10.2014: Refocused image on the water-dam (a) and landslide (b) point clouds (same colorbar) . . . . .  | 99  |
| VI.14 Normalized experimental PSD in the EV plane for a refocused point having one dominant scatterer. The chosen time unit is the satellite's revisit time of 11 days. . . . .  | 100 |
| VI.15 The projection angles intervals for the deformation model of each target. .  | 101 |
| VI.16 Estimated vs. in-situ LOS displacements for the detected scatterers on the Chastel landslide: (a) I1, (b) I4. . . . .  | 103 |
| VI.17 Estimated vs. in-situ LOS displacements for the detected scatterers on the Chastel landslide: (a) I5, (b) I11. . . . .   | 104 |
| VI.18 Estimated vs. in-situ LOS displacements for the detected scatterers on the Chastel landslide: (a) I12, (b) I13. . . . .  | 105 |
| VI.19 Estimated vs. in-situ LOS displacements for the detected scatterers on the Chastel landslide: (a) I15, (b) I17. . . . .  | 106 |
| VI.20 Puylaurent dam's scattering centers and their MDVs on the descending orbit between April-October 2013. On the figure we highlight the angles between the LOS direction and the local unit vectors (tangential, radial, vertical). . . . .                          | 108 |
| VI.21 Puylaurent dam's scattering centers and their MDVs between September-December 2014: (a) Descending orbit, (b) Ascending orbit. On the figures we highlight the angles between the LOS direction and the local unit vectors (tangential, radial, vertical). . . . . | 109 |
| VI.22 Puylaurent dam's displacements time series for corner reflector targets: (a) Descending orbit, between CR1-Ref1 (b) Ascending orbit, between CR3-Ref2.112  | 112 |



# Abbreviations and acronyms

|                |  |
|----------------|--|
| <b>APC</b>     | Antenna Phase Center                                 |
| <b>ASL</b>     | Above Sea Level                                      |
| <b>BPF</b>     | Band-Pass Filter                                     |
| <b>CRLB</b>    | Cramér-Rao lower bound                               |
| <b>D-InSAR</b> | Differential Synthetic Aperture Radar Interferometry |
| <b>DEM</b>     | Digital Elevation Model                              |
| <b>ECEF</b>    | Earth Centered Earth Fixed                           |
| <b>EDF</b>     | Électricité de France                                |
| <b>EV</b>      | Elevation-Velocity                                   |
| <b>FFT</b>     | Fast Fourier Transform                               |
| <b>FM</b>      | Frequency Modulation                                 |
| <b>FMCW</b>    | Frequency Modulated Continuous Wave                  |
| <b>GLRT</b>    | Generalized Likelihood Ratio Test                    |
| <b>GNSS</b>    | Global Navigation Satellite System                   |
| <b>GPS</b>     | Global Positioning System                            |
| <b>HAF</b>     | High-Order Ambiguity Function                        |
| <b>HIM</b>     | High-Order Instantaneous Momentum                    |
| <b>IF</b>      | Intermediary Frequency                               |
| <b>IFL</b>     | Instantaneous Frequency Law                          |
| <b>InSAR</b>   | Synthetic Aperture Radar Interferometry              |
| <b>LIDAR</b>   | Light Detection and Ranging                          |
| <b>LO</b>      | Local Oscillator                                     |
| <b>LOS</b>     | Line Of Sight  |

---

## High-Resolution SAR Signal Processing for Infrastructure Monitoring

---

|               |   |
|---------------|---|
| <b>MAE</b>    | Mean Absolute Error                       |
| <b>MDV</b>    | Mean Displacement Velocity                |
| <b>ML</b>     | Maximum-Likelihood                        |
| <b>MLC</b>    | Multi-Look Complex                        |
| <b>MLE</b>    | Maximum Likelihood Estimation             |
| <b>MST</b>    | Matched Signal Transform                  |
| <b>PDF</b>    | Probability Density Function              |
| <b>PPS</b>    | Polynomial-Phase Signal                   |
| <b>PRF</b>    | Pulse Repetition Frequency                |
| <b>PS</b>     | Permanent Scatterer                       |
| <b>PSD</b>    | Power Spectral Density                    |
| <b>PSI</b>    | Permanent Scatterers Interferometry       |
| <b>PSP</b>    | Principle of Stationary Phase             |
| <b>RF</b>     | Radio-Frequency                           |
| <b>RVP</b>    | Residual Video Phase                      |
| <b>SAR</b>    | Synthetic Aperture Radar                  |
| <b>SCM</b>    | Sample Covariance Matrix                  |
| <b>SLC</b>    | Single-Look Complex                       |
| <b>SNR</b>    | Signal-to-Noise Ratio                     |
| <b>SSC</b>    | Single Look Slant-Range Projected Complex |
| <b>SPECAN</b> | Spectral Analysis azimuth processing      |
| <b>STFT</b>   | Short-Time Fourier Transform              |
| <b>TDX</b>    | TanDEM-X                                  |
| <b>TSX</b>    | TerraSAR-X                                |
| <b>VCO</b>    | Voltage Controlled Oscillator             |
| <b>YIG</b>    | Yttrium Iron Garnet                       |

# CHAPTER I

# Introduction

---

|     |                                 |   |
|-----|---------------------------------|---|
| I.1 | Field description . . . . .     | 1 |
| I.2 | Thesis purpose . . . . .        | 2 |
| I.3 | Chapters presentation . . . . . | 3 |

## I.1 Field description

Microwave remote sensing is a particular type of remote sensing which mainly consists in gaining information about remotely placed objects using electromagnetic waves in the microwave part of the spectrum. An asset of this side of the spectrum is that the electromagnetic waves are not affected by atmospheric scattering and can pass through clouds, dust, haze or rainfall, making the respective sensors largely weather independent. The most used type of remote sensing in the microwave domain is active remote sensing, or radar, which has the particularity that the sensors have their own illumination source, making them able to operate day or night.

A microwave active sensor which has been extensively used and developed for more than 30 years is the synthetic aperture radar (SAR) which has a wide variety of applications in geoscience, climate research, monitoring, mapping or change detection. A SAR image is essentially a two-dimensional backscattering map of a region obtained by moving the sensor over the envisaged scene. The movement direction is termed azimuth direction, whereas the line of sight is denoted slant range. The distance travelled by the sensor creates a "virtual" antenna which provides a high resolution in azimuth, comparable with the one in range.

An essential research topic in the radar remote sensing community is the interpretation and processing of information provided by SAR images. This issues arise because a SAR

image or a reflectivity map in a given bandwidth of the sensor cannot be regarded just like an optic photo. Thus there are several aspects which have to be taken into account, such as the difference in physical meaning of the two axes (slant range and azimuth) of a SAR image, the specific interaction between a target and the electromagnetic waves or the particular acquisition geometry.

## I.2 Thesis purpose

This thesis adds contributions to the interpretation and processing of SAR images using a time-frequency approach and aims to provide our answers to both a theoretical question and a more practical one:

- What can we gain by exploiting the non-stationary time-frequency structure of the radar signals underlying SAR images?
- How can we best monitor with a spaceborne SAR sensor an infrastructure for which a precise digital elevation model is available?

Critical infrastructure monitoring by radar remote sensing has recently become more and more necessary for both economical and security reasons. A remote infrastructure with no incorporated deformation sensors is usually monitored by regular in-situ topographic surveys. However, these surveys cannot be performed very often and complimentary methods are desirable. A feasible way to monitor such a structure is with radar data which can be acquired with ground-based or spaceborne sensors. The information that has to be extracted from remote sensed data consists in deformation estimation of various points of a given structure.

Throughout the thesis, we study separately for ground-based and satellite-based radar signals the time-frequency structure and the techniques that can be employed. More specifically, for ground-based radars we focus on range processing, whereas for spaceborne radars we analyze the azimuth signals from a practical standpoint.

In range, we propose two different methods to mitigate the resolution degradation of wideband frequency modulated continuous wave (FMCW) ground-based radars equipped with oscillators having a nonlinear tuning curve, in the context of infrastructure displacement measurements. This drawback can cause a high degradation of range resolution in ground-based SAR images which implies low signal-to-noise ratio (SNR) and possible target blending. From the point of view of deformation measurements, a lower ratio between the peak level and the noise floor in a range profile will lead to a high phase dispersion which translates in a less accurate displacement estimation. In order to restore the range

## **Chapter I. Introduction**

---

resolution as close as possible to the theoretical value dictated by the system's bandwidth we propose a methodology based on the concept of time warping. In SAR terminology we actually employ a warping of the fast time with the tuning curve in order to mitigate the non-stationary time-frequency content induced by the oscillator's nonlinearity.

In the case of spaceborne data, deformation measurement is commonly performed by differential SAR interferometry (D-InSAR) [1] using SAR products as those provided by the TerraSAR-X, TanDEM-X or COSMO-SkyMed missions [2, 3, 4, 5]. The D-InSAR processing chains for displacements computation usually require particular steps related to the geometry of the envisaged structure in order to separate the topographic phase from the displacement phase in the generated interferograms. The structure's geometry is typically provided by a digital elevation model (DEM). Depending on the processor, the DEM can be introduced in different points of the processing flow. For instance, in some processors the DEM is introduced at the co-registration step [2, 3, 6] in order to increase the registration quality, whereas in others the DEM is used after the interferograms are generated in order to subtract the topographic phase and perform precise orbital phase corrections [7]. However, in either case the SAR focusing kernel does not have as input the DEM and therefore side-look effects such as foreshortening, layovers or shadowing may appear in a focused SAR image in case of structures with significant height variations. Consequently, the position of reliable scattering centers (that can be accurately monitored in time) of a given structure may not be obvious in the original radar geometry in which the SAR product is delivered.

In order to fully integrate the geometry of an infrastructure element, the methodology proposed in this thesis is based on refocusing each SAR image from the initial slant range-azimuth projection to an externally measured 3D point cloud describing the structure under consideration. The refocusing exploits the time-frequency shape of the defocused data in order to accurately compute the impulse response of a scatterer in various imaging modes. Then, the real scattering centers are identified using 4D SAR tomography [8, 9, 10] by testing if the maximum response is placed at zero elevation in a reconstructed elevation-velocity (of deformation) plane.

### **I.3 Chapters presentation**

This thesis is divided in two main parts. The first one presents the theoretical developments in radar signal processing which comprise two research axes: range processing of ground-based FMCW radar signals on one hand, and azimuth-elevation processing of spaceborne SAR images on the other hand. In the second part of the thesis, the focus is on applying the developed methods to ground-based and spaceborne SAR data.

As the beginning of the methodological part of the thesis, Chapter II makes a short review of the time-frequency and SAR signal processing techniques used for theoretical developments in the subsequent chapters. First we present the Short-Time Fourier Transform as the main instrument to look at the time-frequency structure of a signal followed by a glance on the available measures to evaluate the concentration of a time-frequency distribution. Next we introduce two signal processing approaches which act in the time domain, but provide information about the time-frequency structure: the high-order ambiguity function (HAF) in the role of estimator of polynomial phase time-frequency trajectories and the time warping concept presented as part of a matched signal transform. Onwards, we present a synthetic aperture signal model and highlight time-domain focusing principles. Finally we make an overview of the differential SAR tomography framework.

In the third chapter we propose two nonlinearity correction methods for linear frequency modulated continuous wave (FMCW) radars, both based on the concept of time warping. We present the nonlinearity problem caused by the voltage controlled oscillator's nonlinear tuning curve and briefly point out existing solutions. Afterwards we introduce the considered nonlinear signal model adapted to a tuning curve described by an a priori known model which depends only on a few unknown parameters. The core of the chapter presents the main contributions in the field of FMCW SAR signals range processing consisting in the development of two wideband nonlinearity correction algorithms. The first method is based on the high-order ambiguity function, whereas the second is an autofocus-ing algorithm which exploits the spectral concentration of the warped signal. In the last part of the chapter the two methods are tested and compared through various simulation scenarios.

The fourth chapter commences with an overview on SAR scattering centers detection and tracking in the context of infrastructure monitoring. Onwards, we present the main contribution of the thesis in spaceborne SAR images processing -a SAR signal processing methodology for infrastructure monitoring which exploits a digital elevation model or point cloud of the envisaged structure. The methodology comprises three main steps. First, we introduce an azimuth defocusing of SAR images which gives access to the phase history and is compatible with various imaging modes (stripmap, spotlight and sliding spotlight). Next, we present a back-projection of the defocused signal on the available 3D model followed by a scattering centers detection method based on 4D (range-azimuth-elevation-velocity) tomographic reconstruction. The performances and limitations of the developed processing chain are emphasized through extensive simulation results in the last part of the chapter.

The applied part of the thesis starts with Chapter V, which presents a short-range X-band FMCW radar platform developed for displacement measurements in the context of ground-based infrastructure monitoring. Next we present the experimental tests performed with the radar platform in order to validate the nonlinearity correction algorithms proposed

## **Chapter I. Introduction**

---

in Chapter III. Towards the end of this chapter we highlight the platform's displacement measurements capabilities using range profiles and ground-based SAR images.

In Chapter VI we present in detail the monitoring results obtained by applying the methodology proposed in Chapter IV. In the first part we describe the test sites (Puylauron water-dam and Chastel landslide), the available satellite data (high-resolution sliding spotlight TerraSAR-X/TanDEM-X images), the measurement campaigns performed to generate the 3D point clouds (GPS localization, topographic measurements and laser scans) and the in-situ measurement methods (regular topographic surveys and embedded measuring systems). Next we focus on the key points and limitations which appear in real data processing with an emphasis on both the azimuth signal's time-frequency structure determined by the sliding spotlight acquisition mode and the deviations from a linear deformation model. Finally, the computed displacements of the two structures are presented and compared with in-situ data.



## Part A

### METHODOLOGICAL CONTEXT



## CHAPTER II

# Time-Frequency and SAR signal processing methods overview

---

|   |           |
|---|-----------|
| <b>II.1 Time-frequency processing of non-stationary signals . . . . .</b> | <b>9</b>  |
| II.1.1 Short-Time Fourier Transform . . . . .                             | 10        |
| II.1.2 Measure of Concentration . . . . .                                 | 12        |
| II.1.3 High-Order Ambiguity Function . . . . .                            | 12        |
| II.1.4 Time warping and the matched signal transform . . . . .            | 15        |
| <b>II.2 SAR signals processing tools . . . . .</b>                        | <b>17</b> |
| II.2.1 SAR signal model . . . . .   | 17        |
| II.2.2 Time-domain SAR image formation algorithms . . . . .               | 18        |
| II.2.3 Four-dimensional SAR Tomography Framework . . . . .                | 20        |

*This chapter provides a brief review of the specific methods of Time-Frequency and SAR signal processing used throughout the following developments. The merger of certain parts of these methods represents the basis of the theoretical contributions presented in the thesis.*

## II.1 Time-frequency processing of non-stationary signals

In many signal processing applications the analyzed signals are non-stationary in the sense that the frequency changes over time and are comprised of multiple components each having its particular instantaneous frequency law (IFL). Most of the times the phase function of an analytic non-stationary component can be described by a parametric model. If

there is no a priori information of the signal's nature, a widely employed model is the polynomial phase signal (PPS) model based on the Weierstrass approximation theorem. Typical parameters estimation methods for PPSs with multiple components are based on the high-order ambiguity function (HAF) [11, 12, 13, 14] or on nonlinear least squares approaches [15]. These algorithms have to deal with specific problems of multi-component signals: the interaction between the components that may lead to cross-terms and the inability to successively demodulate and separate a certain component in the presence of others.

When the time-frequency shape of the components forming the signal is known, the parameters estimation can be accomplished using a matched signal transform (MST) [16, 17] or equivalently a Fourier transform of a warped version of the signal. This transform localizes signals with a certain nonlinear characteristic basis function at their frequency modulation (FM) rate in the same manner as the Fourier transform localizes sinusoids at their frequencies. Moreover, such a transform avoids the cross-terms problem because it includes an amplitude modulation with the basis function's IFL which makes the components orthonormal [18]. Various classical transforms are actually MSTs such as the Mellin transform [19, 20], the k-th power transform [18] or the exponential transform [21].

In the following we highlight the tools used throughout the thesis for the processing of non-stationary signals: the Short-Time Fourier Transform, some measures of time-frequency distributions, the high-order ambiguity function and the time warping concept embedded in the matched signal transform.

### II.1.1 Short-Time Fourier Transform

Real-world non-stationary signals are usually time-localized and in this case the Fourier transform does not provide information about the frequency content at certain time instants, only an overview of the spectral composition on the whole analyzed period. This happens because the base on which a signal is decomposed in a Fourier transform has a theoretically infinite support which is not compatible with time-localized signals. A straightforward solution to this problem is to perform a spectral analysis only on short intervals of the signal, method which is called the Short-Time Fourier Transform (STFT).

For a signal  $x(t)$  the mathematic expression of the STFT is [22, 23]:

$$F_x(t, f) = \int_{-\infty}^{\infty} x(\tau)h^*(\tau - t) \exp(-j2\pi f\tau) d\tau, \quad (\text{II.1})$$

where  $h^*(\tau - t)$  is a windowing function centered in  $t$ . So in order to obtain the spectral representation around  $t$  the window  $h^*(t)$  is time shifted with  $t$  and a Fourier transform is

## Chapter II. Time-Frequency and SAR signal processing methods overview

---

performed on the resulting windowed signal. The function  $F_x(t, f)$  can also be viewed as the coefficient of the decomposition of signal  $x(t)$  on a base signal defined as:

$$h_{t,f}(\tau) = h(\tau - t) \exp(j2\pi f\tau), \quad (\text{II.2})$$

where  $h(t)$  is interpreted as a mother base function which is translated in time and frequency to obtain all possible base functions.

If the window  $h(t)$  has unitary energy (the admissibility condition), the signal  $x(t)$  is expressed as a linear combination of elementary atoms  $h_{t,f}(\tau)$  multiplied by the coefficient  $F_x(t, f)$ :

$$\begin{aligned} x(\tau) &= \int_{-\infty}^{\infty} dt \int_{-\infty}^{\infty} F_x(t, f) h_{t,f}(\tau) df \\ &= \int_{-\infty}^{\infty} dt \int_{-\infty}^{\infty} F_x(t, f) h(\tau - t) \exp(j2\pi f\tau) df. \end{aligned} \quad (\text{II.3})$$

The simplest pick for the window  $h(t)$  is the rectangular window on a given analysis duration, but a wiser choice is a window which assures a good localization in time-frequency (e.g., Hamming, Hanning or Gaussian windows) as well as a proper smoothness (rapid decrease, multiple times differentiable).

The squared magnitude of the Short Time Fourier Transform is associated with the energy distribution of the signal in the time-frequency plane and is usually called a Spectrogram:

$$S_x(t, f) = |F_x(t, f)|^2 = \left| \int_{-\infty}^{\infty} x(\tau) h^*(\tau - t) \exp(-j2\pi f\tau) d\tau \right|^2. \quad (\text{II.4})$$

The spectrogram can also be expressed using Parseval's theorem (or unitarity property of the Fourier transform):

$$\int_{-\infty}^{\infty} x_1(t) x_2^*(t) dt = \int_{-\infty}^{\infty} X_1(f) X_2^*(f) df, \quad (\text{II.5})$$

which yields

$$S_x(t, f) = \left| \int_{-\infty}^{\infty} X(\nu) H^*(\nu - f) \exp(j2\pi\nu t) d\nu \right|^2. \quad (\text{II.6})$$

In this case the Fourier transform  $H(\nu)$  of window  $h$  is employed as a sliding window which spans the entire spectrum. This standpoint resembles to a processing based on uniform continuous bank filter analysis with constant bandwidth.

The STFT has certain limitations especially when the analyzed signal is perfectly localized in time or in frequency. For instance, in case of a signal which is perfectly localized in time  $x(t) = \delta(t - t_0)$ , the spectrogram is actually the squared magnitude of the window

placed around the moment  $t_0$ , i.e.,  $S_x(t, f) = |h(t_0 - t)|^2$  and the representation is more adapted to the signal when the window is as short as possible. Contrariwise, for a signal perfectly localized in frequency  $x(t) = \exp(j2\pi ft)$  the spectrogram  $S_x(t, f) = |H(f_0 - f)|^2$  is the squared magnitude of the window's Fourier transform around frequency  $f_0$ . In this situation, the representation is more adapted to the signal when the window's spectrum is as narrow as possible. Therefore, the temporal and spectral lengths of the window condition the sharpness of the representation (good resolution in time or good resolution in frequency). Due to Heisenberg's uncertainty principle (the resolutions product  $\Delta t \Delta f$  is lower bounded) is impossible to simultaneously obtain a very good resolution in both domains. So, in the STFT case, the time-frequency analysis is performed by decomposing the signal on atoms which pave the time-frequency plane with constant time resolution  $\delta t$  and constant frequency resolution  $\delta f$ . The window which provides the best compromise between the two resolutions is the Gaussian window.

### II.1.2 Measure of Concentration

A criterion for evaluating the quality of a time-frequency representation is the concentration. A better concentration in the time-frequency plane means that the signal's energy is focused in a smaller region and consequently any detection or estimation performed in the time-frequency plane is expected to be more reliable [22]. Several concentration measures have been proposed in literature which are based on distribution norms [24, 25, 26] or have been derived from a classical definition of a time-limited signal's duration [27]. Each of these concentration measures can be applied only over frequency to obtain a measure of the spectral concentration.

### II.1.3 High-Order Ambiguity Function

In order to define the High-Order Ambiguity Function, the starting point is the high-order instantaneous momentum (HIM), which can be expressed for a signal  $s(t)$  as [12]:

$$\text{HIM}_k[s(t); \tau] = \prod_{i=0}^{k-1} [s^{(*i)}(t - i\tau)]^{\binom{k-1}{i}}, \quad (\text{II.7})$$

where  $k$  is the HIM order,  $\tau$  is the lag and  $s^{(*i)}$  is an operator defined as:

$$s^{(*i)}(t) = \begin{cases} s(t) & \text{if } i \text{ is even,} \\ s^*(t) & \text{if } i \text{ is odd,} \end{cases} \quad (\text{II.8})$$

## Chapter II. Time-Frequency and SAR signal processing methods overview

---

where  $i$  is the number of conjugate operator "\*" applications. The high-order ambiguity function (HAF) of order  $k$  is defined as the Fourier transform of the corresponding HIM:

$$\text{HAF}_k[s; f_k, \tau] = \int_{-\infty}^{\infty} \text{HIM}_k[s(t); \tau] \exp(-j2\pi f_k t) dt. \quad (\text{II.9})$$

If we assume a PPS model for the analyzed signal, i.e.,

$$s_{\text{PPS}}(t) = A \exp \left[ j2\pi \sum_{m=0}^k a_m t^m \right], \quad (\text{II.10})$$

the essential property of the HIM is that, the  $k$ -th order HIM is reduced to an harmonic with amplitude  $A^{2^{k-1}}$ , frequency  $\tilde{f}_k$  and phase  $\tilde{\Phi}_k$ :

$$\text{HIM}_k[s_{\text{PPS}}(t); \tau] = A^{2^{k-1}} \exp \left[ j \left( 2\pi \tilde{f}_k t + \tilde{\Phi}_k \right) \right], \quad (\text{II.11})$$

where

$$\tilde{f}_k = k! \tau^{k-1} a_k \quad (\text{II.12})$$

and

$$\tilde{\Phi}_k = 2\pi \left[ (k-1)! \tau^{k-1} a_{k-1} - 0.5k!(k-1) \tau^k a_k \right]. \quad (\text{II.13})$$

So the HAF of this HIM should have a spectral peak at the frequency  $\tilde{f}_k$ . The estimated value of coefficient  $a_k$  is:

$$\tilde{a}_k = \frac{1}{k! \tau^{k-1}} \arg \max_{f_k} |\text{HAF}_k[s_{\text{PPS}}; f_k, \tau]|. \quad (\text{II.14})$$

Based on this result, an algorithm that estimates sequentially the coefficients  $a_k$  was proposed in [11]. Starting with the highest order coefficient, at each step, the spectral peak is determined, and an estimate  $\hat{a}_k$  of  $a_k$  is computed from (II.12). With this value, the phase term of the higher order is removed:

$$s_{\text{PPS}}^{(k-1)}(t) = s_{\text{PPS}}^{(k)}(t) \exp(-j2\pi \hat{a}_k t^k) \quad (\text{II.15})$$

and the procedure repeats iteratively. A classical problem of this nonlinear method is the propagation of the approximation error from one higher order to the lower ones. If a higher order is necessary a warped-based polynomial order reduction as described in [14] could be employed.

In the following, the iterative algorithm is briefly illustrated on a second order PPS:

$$s^{(2)}(t) = \exp[j2\pi(a_0 + a_1 t + a_2 t^2)]. \quad (\text{II.16})$$

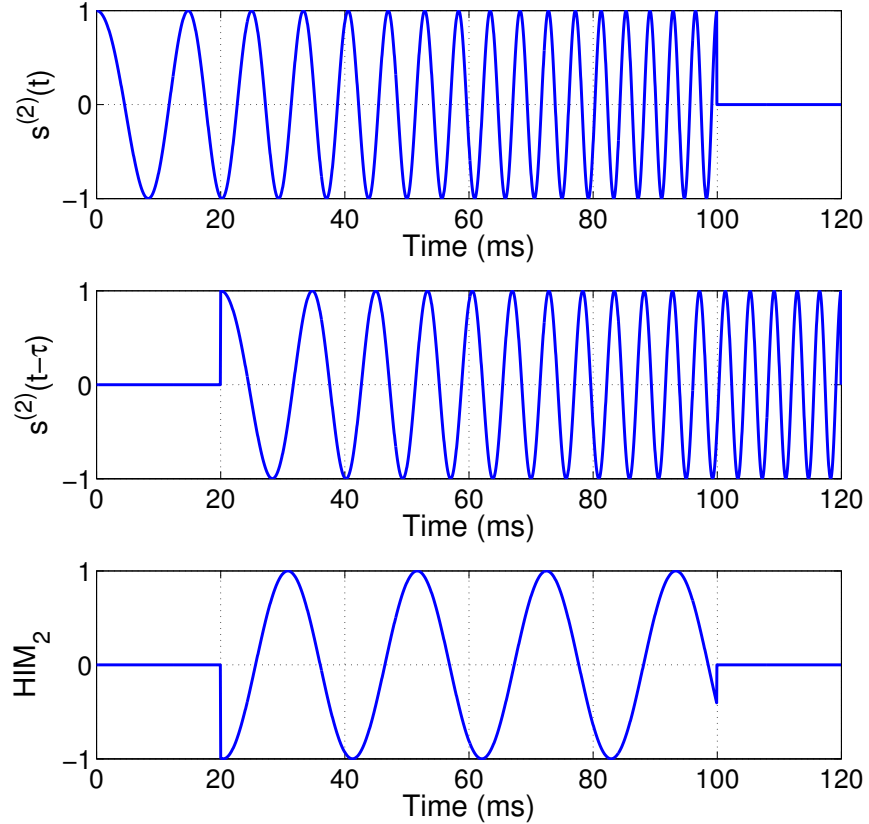


Figure II.1: Second order instantaneous moment computation for a quadratic phase signal.

The HIM of  $s^{(2)}(t)$  is:

$$\text{HIM}_2[s^{(2)}(t); \tau] = \exp \left[ j \left( \tilde{\phi}_2 + 4\pi a_2 \tau t \right) \right]. \quad (\text{II.17})$$

The HIM's computation is graphically illustrated in Fig. II.1 for a signal duration of 100 ms and a lag of 20 ms. Using this HIM, coefficient  $a_2$  is estimated and the quadratic phase term is compensated:

$$s^{(1)}(t) = s^{(2)}(t) \exp(-j2\pi\tilde{a}_2 t^2) = \exp[j2\pi(a_0 + a_1 t)], \quad (\text{II.18})$$

Applying the Fourier transform on  $s^{(1)}(t)$  the coefficients  $a_1$  and  $a_0$  are easily computed as the frequency and respectively the phase of the peak response.

In the previously exposed procedure, the estimation is based on knowing the lag  $\tau$ . This is typically chosen such that it ensures the best resolution for the polynomial coefficient. It can be shown [13] that for a signal duration  $T$  and lag  $\tau$  the resolution of the  $k$ -th order coefficient is written as:

$$\delta a_k = \frac{1}{k! \tau^{k-1}} \frac{1}{T - (k-1)\tau}. \quad (\text{II.19})$$

The minimum of this expression is attained when the lag is

$$\tau_{min} = \frac{T}{k}, \quad (\text{II.20})$$

and the corresponding minimum value is:

$$\delta a_{k,min} = \frac{1}{k!(T/k)^k}. \quad (\text{II.21})$$

Because the minimum resolution depends on the order  $k$ , at each step of the iterative algorithm, the lag  $\tau$  is chosen according to (II.21).

#### II.1.4 Time warping and the matched signal transform

We consider a signal consisting of a sum of non-stationary components each having the same time-frequency shape described by a monotonic one-to-one function of time  $\theta(t)$  (a basis function). We consider that  $\theta(0) = 0$ . Such a signal with  $K$  components can be written as

$$s(t) = \sum_{k=1}^K a_k \exp \{j(\varphi_k + \alpha_k \theta(t))\}, \quad (\text{II.22})$$

where  $a_k$ ,  $\varphi_k$  and  $\alpha_k$  are respectively the amplitude, phase and modulation rate of component  $k$ .

The time-frequency content of these type of signals can be linearized by changing the time and/or frequency axis. This is typically performed using a unitary transformation called an axis transformation [28] or unitary warping operator  $\mathbf{U}$  defined for a finite energy signal  $x(t)$  and a warping law  $w(t)$  as

$$\left\{ \mathbf{U} \left| \frac{dw(t)}{dt} > 0; x(t) \rightarrow \mathbf{U}x(t) = \left| \frac{dw(t)}{dt} \right|^{1/2} x(w(t)) \right. \right\}. \quad (\text{II.23})$$

When operator  $U$  is applied on the signal in II.22 with the warping law

$$w(t) = \theta^{-1}(t) \quad (\text{II.24})$$

the resulting signal is

$$\mathbf{U}s(t) = \left| \frac{d\theta^{-1}(t)}{dt} \right|^{1/2} \sum_{k=1}^K a_k \exp \{j(\varphi_k + \alpha_k t)\}. \quad (\text{II.25})$$

The Fourier transform of (II.25) is expressed as:

$$\mathcal{F}\{\mathbf{U}s(t)\} = \mathcal{F} \left\{ \left| \frac{d\theta^{-1}(t)}{dt} \right|^{1/2} \right\} * \sum_{k=1}^K a_k \exp(j\varphi_k) \delta(\omega - \alpha_k), \quad (\text{II.26})$$

where  $\mathcal{F}$  is the Fourier operator,  $*$  describes the convolution operation and  $\delta$  is Dirac's impulse. Note that this signal is a sum of Dirac impulses in frequency placed at the modulation rates  $\alpha_k$  and convolved with the term  $\mathcal{F} \left\{ \left| \frac{dw(t)}{dt} \right|^{1/2} \right\}$  which determines a certain frequency resolution depending on the basis function. Hence, in order to transform the sum of non-stationary signals in (II.22) in a sum of complex sinusoids, a non-unitary version of the warping operator has to be used:

$$\left\{ \mathbf{W} \left| \frac{dw(t)}{dt} > 0; x(t) \rightarrow \mathbf{W}x(t) = x(w(t)) \right. \right\}. \quad (\text{II.27})$$

Hereinafter, a signal  $x(t)$  warped with operator  $W$  with the warping law  $\theta^{-1}(t)$  is denoted  $x_w(\theta)$ , where the variable  $\theta$  is used for time in order to emphasize that the signal is represented in a new time axis  $\theta = \theta(t)$ . When  $x(t)$  is the signal  $s(t)$  from (II.22), the warped signal in the  $\theta$  time axis is written as:

$$s_w(\theta) = \sum_{k=1}^K a_k \exp \{ j(\varphi_k + \alpha_k \theta) \}, \quad (\text{II.28})$$

and is composed of complex sinusoids.

The Fourier transform of (II.28)

$$S(\alpha) = \mathcal{F} \{ s_w(\theta) \} = \int_{-\infty}^{\infty} s_w(\theta) \exp(-j\alpha\theta) d\theta. \quad (\text{II.29})$$

will give peaks at the modulation rates  $\alpha_k$  of the  $K$  components. The transform in (II.29) can also be computed in terms of the initial time axis  $t$  as

$$\begin{aligned} S(\alpha) &= \int_{-\infty}^{\infty} |\theta'(t)| s(t) \exp[-j\alpha\theta(t)] dt \\ &= \sum_{k=1}^K a_k \exp(j\varphi_k) \delta(\alpha - \alpha_k) \end{aligned} \quad (\text{II.30})$$

Notice that (II.30) is actually a definition of the MST applied for the basis function  $\theta(t)$ . Additionally, it can be shown that the squared magnitude of the MST is a maximum likelihood (ML) estimator for the modulation rate of signals with a certain characteristic function in the same way as the periodogram is an ML estimator for the frequency of sinusoidal signals [17]. This seems natural given that in the warped time axis the spectrum is actually a sum of Dirac impulses (for signals with infinite time support).

In the case of real signals, the support of  $s(t)$  is actually a certain  $[0, T]$  interval and the Dirac impulses from the Fourier transform in the warped time axis are replaced by the transfer function of the weighing window defined on  $[0, \theta(T)]$ . For a rectangular window, the Fourier transform in (II.29) becomes

$$S_T(\alpha) = \sum_{k=1}^K a_k \exp(j\varphi_k) \text{sinc} \left[ \frac{(\alpha - \alpha_k)\theta(T)}{2} \right] \exp \left[ -j \frac{(\alpha - \alpha_k)\theta(T)}{2} \right], \quad (\text{II.31})$$

where  $\text{sinc}(x)$  is the un-normalized sinc function defined as

$$\text{sinc}(x) = \frac{\sin(x)}{x}. \quad (\text{II.32})$$

## II.2 SAR signals processing tools

In the next part we present the SAR signal model, a review of time domain focusing methods and the differential tomography framework. The analysis is concentrated on processing tools which are employed in the following chapters.

### II.2.1 SAR signal model

For the developments from this chapter we consider the raw signal model for synthetic aperture processing described in the following. The geometry under consideration is presented in Fig. II.2. The unit vector  $\vec{u}$  describes the azimuth direction of the sensor. The position of the sensor's antenna phase center (APC) at a certain azimuth (slow) time  $t$  will be written as:

$$\vec{r}_a(t) = \vec{r}_{a,0} + v_0 t \vec{u}, \quad (\text{II.33})$$

where  $\vec{r}_{a,0}$  is the APC position vector at  $t = 0$  and  $v_0$  the sensor's speed in zero-Doppler geometry. For a given target  $i$  having the position vector  $\vec{r}_i$ , the closest approach distance to the synthetic aperture is given by

$$r_{0,i} = \|(\vec{r}_{a,0} - \vec{r}_i) - [(\vec{r}_{a,0} - \vec{r}_i) \cdot \vec{u}] \vec{u}\| \quad (\text{II.34})$$

and the azimuth time at which this distance is attained can be expressed as:

$$t_{\vec{r}_i} = \frac{(\vec{r}_i - \vec{r}_{a,0}) \cdot \vec{u}}{v_0}. \quad (\text{II.35})$$

The distance APC-target  $i$  as a function of azimuth time can be written in terms of the previously defined variables:

$$\begin{aligned} \Delta r_i(t) &= \|\vec{r}_a(t) - \vec{r}_i\| \\ &= \sqrt{r_{0,i}^2 + [v_0(t - t_i)]^2}. \end{aligned} \quad (\text{II.36})$$

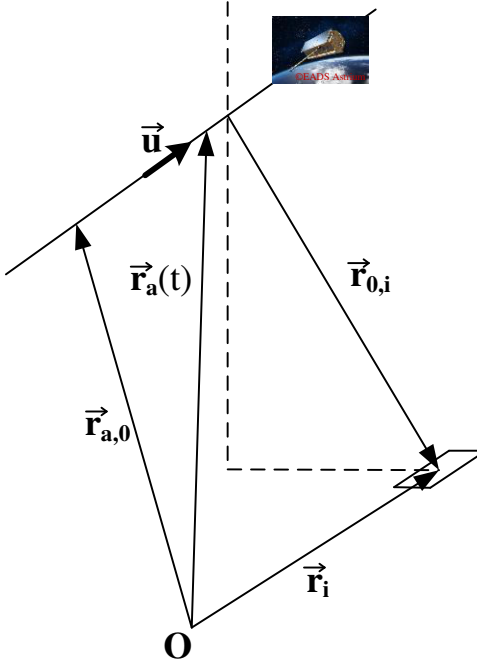


Figure II.2: SAR acquisition geometry for a point having the position vector  $\vec{r}_i$

After demodulation, the response from a set of  $N$  point scatterers located at  $\vec{r}_i$  is a function of two variables (slow time and fast time):

$$s(t, \tau) = \sum_{i=1}^N A_i p_0 \left( \tau - \frac{2\Delta r_i(t)}{c} \right) \exp \left\{ -j \frac{4\pi f_c}{c} \Delta r_i(t) \right\} \text{rect} \left[ \frac{t - t_i}{T_{ap}} \right], \quad (\text{II.37})$$

where  $A_i$  is the complex amplitude of scatterer  $i$ ,  $f_c$  is the central frequency,  $c$  is the speed of light,  $T_{ap}$  is the synthetic aperture duration and  $p_0(\tau)$  is the complex envelope of the transmitted signal as a function of the fast time  $\tau$ . In (II.37), the function  $\text{rect}(t/T_{ap})$  is a gate with length  $T_{ap}$  centered in the origin.

## II.2.2 Time-domain SAR image formation algorithms

A straightforward way to focus a SAR image is by convolving the raw data (in slow time-fast time domain) with a shift-varying filter [29, 30]. A first approach of this method is to perform a correlation in both slow and fast time domains of the raw data with the expected SAR signature for each imaged point. Assuming that we want to compute the response of

## Chapter II. Time-Frequency and SAR signal processing methods overview

---

a point  $k$  situated on a certain grid at the position  $\vec{r}_k$ , its SAR signature will be

$$p_k(t, \tau) = p_0 \left( \tau - \frac{2\|\vec{r}_a(t) - \vec{r}_k\|}{c} \right) \exp \left( -j \frac{4\pi f_c}{c} \|\vec{r}_a(t) - \vec{r}_k\| \right) \text{rect} \left[ \frac{t - t_k}{T_{ap}} \right], \quad (\text{II.38})$$

while the imaging equation can be expressed as a double integral:

$$g_{MF}(\vec{r}_k) = \int_t \int_\tau s(t, \tau) p_k^*(t, \tau) dt d\tau. \quad (\text{II.39})$$

From the implementation standpoint, the two-dimensional integral is actually a double sum over the discrete values of  $(t, \tau)$  on a uniform grid determined by the pulse repetition frequency ( $PRF$ ) in azimuth and the range sampling frequency ( $F_s$ ). If the grid comprises  $M$  pulses in azimuth and for each pulse there are  $N_s$  samples in range, the number of required operations to compute the response is proportional to the product  $M \times N_s$ . In general, in order to generate a SAR image (practically a matrix of points for which the response has to be computed) with the matched filtering algorithm, the computational complexity is proportional to the number of points in the matrix times  $M \times N_s$ , which makes the method impractical in most cases.

A more efficient time domain focusing method is the back-projection technique. This method enhances the computation time by computing separately and in different manners the matched filtered response in slow time and fast time domains, which leads to a separation of the double integral in (II.39). The first step is to perform a convolution in the fast time domain between the raw data and a reversed conjugated version of the transmitted pulse (a matched filtering in range):

$$s_p(t, \tau) = s(t, \tau) * p_0^*(-\tau), \quad (\text{II.40})$$

which leads to a function consisting in a range profile (or range compressed response) for each azimuth time  $t$ :

$$s_{rp}(t, r) = s_p(t, 2r/c). \quad (\text{II.41})$$

The imaging equation will be expressed as a single integral representing the coherent integration of the range compressed responses of a grid point placed at  $\vec{r}_k$  from the entire azimuth aperture:

$$g_{BP}(\vec{r}_k) = \int_t s_p \left( t, \frac{2\Delta r_i(t)}{c} \right) \exp \left[ j \frac{4\pi f_c}{c} \Delta r_i(t) \right] dt. \quad (\text{II.42})$$

Practically, the implementation of (II.42) consists in a discrete-time convolution to obtain  $s_p(t, \tau)$  and a summation over all the pulses. The discrete raw signal can be written as  $s[m, n] = s(m\delta t, n2\delta r/c)$ , where  $\delta t = \frac{1}{PRF}$  is the slow time spacing and  $\delta r$  the range spacing. Similarly, the range focused signal is  $s_{rp}[m, n] = s_{rp}(m\delta t, n\delta r)$ . With this notations,

the azimuth focusing of the range compressed signal is implemented as:

$$g_{BP}(\vec{r}_k) = \sum_m s_{rp}(m\delta t, \|\vec{r}_a(m\delta t) - \vec{r}_k\|) \exp \left[ j \frac{4\pi f_c}{c} \|\vec{r}_a(m\delta t) - \vec{r}_k\| \right]. \quad (\text{II.43})$$

The name back-projection comes from the fact that for each synthetic aperture location (slow time) the range compressed response of a target is traced back in the fast time domain in order to isolate the azimuth response of the envisaged target from other reflections. The value  $s_{rp}(m\delta t, \|\vec{r}_a(m\delta t) - \vec{r}_k\|)$  is not implicitly available because  $s_{rp}(t, \tau)$  is stored on the uniform grid  $s_{rp}[m, n]$  which obviously will not contain exactly the point  $(m\delta t, \|\vec{r}_a(m\delta t) - \vec{r}_k\|)$ . So in order to obtain the required value, a 1D interpolation has to be performed along the fast time axis. No interpolation along the slow time axis is necessary because each discrete value of  $t$  is actually the slow time of a pulse.

### II.2.3 Four-dimensional SAR Tomography Framework

In this subsection we make a review of the four-dimensional SAR imaging model (differential tomography) [9] adapted to SAR images focused on a certain grid using the presented time domain methods. The envisaged geometry is shown in Fig. II.3. We consider  $N$  satel-

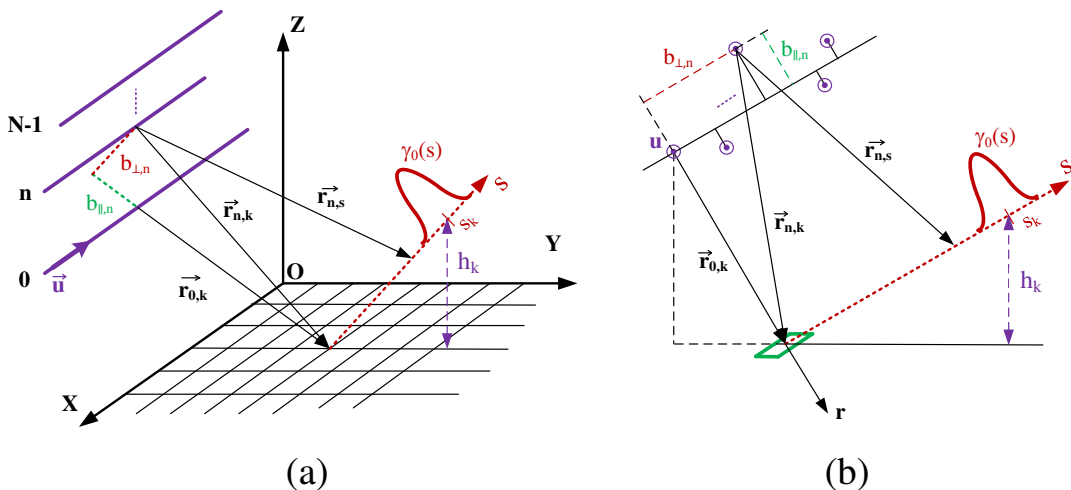


Figure II.3: Four-dimensional tomography geometry: (a) 3D view and (b) 2D section parallel to  $yOz$  plane.

lite tracks corresponding to the time instants  $t_n$  relative to the first track. The orthogonal baseline between a current track  $n$  and the first one is denoted  $b_{\perp,n}$ . The SAR response of a grid point  $k$  for track  $n$  is noted  $g_n(\vec{r}_k)$ . The responses for each track  $g_n(\vec{r}_k)$  are grouped

in a vector with  $N$  components denoted  $\mathbf{g}(\vec{r}_k)$ . Considering the case of the presented time domain methods, the so-called deramping [31] is implicitly performed (geometric phase compensation), and each element of  $\mathbf{g}(\vec{r}_k)$  can be decomposed as [32, 9]:

$$g_n(\vec{r}_k) = \int_{\Delta s} \gamma_0(s) \exp \left[ -j \frac{4\pi f_c}{c} (r_{n,s} - r_{n,k}) \right] \exp \left[ j \frac{4\pi f_c}{c} d(s, t_n) \right] ds, \quad (\text{II.44})$$

where  $\gamma_0(s)$  is the reflectivity profile along elevation having the support  $\Delta s$  and  $d(s, t_n)$  is the deformation in the line of sight of a target placed at the elevation  $s$ . Considering the baselines much smaller than the distances orbit-target, after some calculations and approximations equation (II.44) becomes:

$$\begin{aligned} g_n(\vec{r}_k) &= \int_{\Delta s} \gamma_0(s) \exp \left\{ j \frac{4\pi f_c}{c} \left[ -\frac{s^2}{2r_{0,k}} + s \frac{b_{\perp,n}}{r_{0,k}} + d(s, t_n) \right] \right\} ds \\ &= \int_{\Delta s} \gamma(s) \exp \left\{ j \frac{4\pi f_c}{c} \left[ s \frac{b_{\perp,n}}{r_{0,k}} + d(s, t_n) \right] \right\} ds, \end{aligned} \quad (\text{II.45})$$

where  $\gamma(s) = \gamma_0(s) \exp \left( -j \frac{4\pi f_c}{c} \frac{s^2}{2r_{0,k}} \right)$  is a modified reflectivity profile which incorporates the  $s^2$ -dependent phase term associated to the curvature of the incident wavefront (which corrupts the phase of the final image if it is not mitigated). Onwards, a Fourier expansion is applied to each displacement term  $d(s, t_n)$  and the vector of received and focused data has the following expression:

$$\mathbf{g}(\vec{r}_k) = \int_{\Delta s} \int_{\Delta v} p_\gamma(s, v) \mathbf{a}(s, v) ds dv, \quad (\text{II.46})$$

where  $p_\gamma(s, v) = \gamma(s)p(s, v)$  and  $p(s, v)$  is the elevation-velocity (EV) spectral distribution of the displacement terms,  $\Delta v$  is the velocity support of  $p_\gamma(s, v)$  and  $\mathbf{a}(s, v)$  is the steering vector whose elements are defined as:

$$a_n(s, v) = \exp \left[ j \frac{4\pi f_c}{c} \left( s \frac{b_{\perp,n}}{r_{0,k}} + vt_n \right) \right], \quad (\text{II.47})$$

where  $v$  is the deformation/displacement velocity.

Because the  $(b_{\perp,n}, t_n)$  pairs are sparse and nonuniform, a typical method used for reconstructing the function  $p_\gamma(s, v)$  is the Capon filter [10, 33]:

$$\hat{p}_\gamma(s, v) = \frac{\mathbf{a}^H(s, v) \hat{\mathbf{R}}^{-1} \mathbf{g}(\vec{r}_k)}{\mathbf{a}^H(s, v) \hat{\mathbf{R}}^{-1} \mathbf{a}(s, v)}, \quad (\text{II.48})$$

where  $\hat{\mathbf{R}}$  is a multi-look estimate of the data vector  $\mathbf{g}(\vec{r}_k)$  covariance matrix. The power spectral density (PSD) is then obtained as the power of  $\hat{p}_\gamma(s, v)$ . The elevation and mean displacement velocities of the targets can be extracted as the peaks in the elevation-velocity PSD.



## CHAPTER III

# Range processing of FMCW radar signals

---

|  |    |
|--|----|
| III.1 Nonlinearity problem and state of the art . . . . .            | 23 |
| III.2 Nonlinear FMCW radar beat signal . . . . .                     | 24 |
| III.3 Discrete signal model and the Cramér-Rao lower bound . . . . . | 26 |
| III.4 HAF-based nonlinearity correction . . . . .                    | 28 |
| III.5 Range autofocusing nonlinearity correction . . . . .           | 29 |
| III.6 Correction algorithms comparison . . . . .                     | 32 |
| III.7 Conclusions . . . . .  | 36 |

*This chapter presents the range signal processing algorithms developed for wideband FMCW radars. The contributions are focused on the nonlinearity correction of wideband voltage controlled oscillators performed by exploiting the time-frequency structure of the FMCW radar's beat signal.*

## III.1 Nonlinearity problem and state of the art

The frequency modulated continuous wave (FMCW) radar is an alternative to the pulse radar and is typically used when the envisaged targets' ranges are relatively small (tens or hundreds of meters). In order to measure such distances with a pulse radar the switching time between transmission and reception should be at most tens of nanoseconds. The FMCW radar principle is currently used in applications such as radio-altimeters [34], anti-collision systems [35, 36] or sensors for inhomogeneity identification on transmission lines [37]. The range information from an FMCW radar is encoded in the beat frequency obtained by mixing the received signal with the transmitted waveform. A classical issue of an FMCW radar is the nonlinearity of the transmitted waveform's time-frequency shape

induced by the nonlinear frequency-voltage characteristic of the VCO. This leads to a deteriorated resolution by spreading a target's beat signal in a certain bandwidth during a linear voltage sweep [38]. In the literature there are different approaches for this problem.

A simple correction method is to use a predistorted tuning voltage to obtain a linear frequency modulation [39, 40]. However, this solution has the issue that the pre-distortion is usually done with the static frequency-voltage characteristic (measured by applying certain voltages and reading the resulting frequencies) which may differ from the dynamic one because it does not take into account the driver's response or any change in external conditions (e.g. sweep speed, temperature, supply voltage). Other solutions involve actual hardware modifications like using a feedback delay line [41] or a phased-locked loop circuit [42, 43, 44] to sense and correct the slope error of the generated chirp.

A different way to address the nonlinearity problem is with post-processing methods which are used in most cases for simple, low-cost VCOs. These methods estimate the nonlinearity using either a reference path integrated in the transceiver (eventually a surface acoustic delay line) which acts like a target [45, 46, 47] or a response provided by a real reflector from the scene [48, 49, 50]. The estimation is done either by breaking the beat signal into several sub-bands and computing the frequency peaks [50] or by extracting the phase information from the analytical signal [45, 46].

### III.2 Nonlinear FMCW radar beat signal

For a linear tuning voltage sweep, the transmitted analytical signal of a VCO in the interval  $[0, T]$  can be written as:

$$s_T(t) = \exp \left[ j \left( 2\pi f_0 t + \beta_0 \int_0^t \theta_{\mathbf{p}_0}(x) dx \right) \right], \quad (\text{III.1})$$

where  $f_0$  is the initial frequency,  $\beta_0$  is the chirp rate in the origin and  $\theta_{\mathbf{p}_0}$  is a monotonic one to one function defined on  $[0, T]$  describing the nonlinearity which depends on certain parameters given by the vector  $\mathbf{p}_0 = [p_{0,1}, p_{0,2}, \dots, p_{0,L}]^T$  with  $L$  components. In the following, it is considered that the reflected signal comes from  $K$  different targets. The signal received from these targets can be expressed as a sum of delayed and attenuated versions of the transmitted signal

$$s_R(t) = \sum_{k=1}^K A_k s_T(t - \tau_k), \quad (\text{III.2})$$

where  $\tau_k$  and  $A_k$  are respectively the propagation delay and complex amplitude of the signal received from target  $k$ . By mixing the transmitted and received signals, the beat

signal is written as

$$s(t) = \sum_{k=1}^K A_k s_T(t) s_T^*(t - \tau_k). \quad (\text{III.3})$$

Because the propagation delay  $\tau_k$  is typically a few orders of magnitude smaller than the sweep period, the beat signal can be expressed as

$$s(t) = \sum_{k=1}^K a_k \exp [j(\varphi_k + \alpha_k \theta_{\mathbf{p}_0}(t))], \quad (\text{III.4})$$

where  $a_k$ ,  $\varphi_k = \arg\{A_k\} + 2\pi f_0 \tau_k$  and  $\alpha_k = \beta_0 \tau_k$  are respectively the real amplitude, the phase and the modulation rate of component  $k$ . Note that  $s(t)$  has the same form as the signal in (II.22) and its spectrogram will be composed of a set of non-overlapping time-frequency trajectories having the same shape, but different modulation rates. Hence, if the range profile is computed as the Fourier transform of the multi-component signal in (III.4), the energy of each target would be spread and the resolution deteriorated.

In this context, the correction algorithms developed in the thesis and presented in the following sections aim to estimate the vector of parameters  $\mathbf{p}_0$  and simultaneously transform all the beat signal's components into complex sinusoids using time warping. More precisely, this will be done by warping (III.4) with the non-unitary warping operator described in (II.27) using as warping law the inverse of the estimated nonlinearity function. Moreover, in the context of radar detection, the highly correlated clutter from a nonlinear range profile gets decorrelated in a range profile computed for the new time axis.

The beat signal in a new time axis  $\theta_{\mathbf{p}_0}$  will be written as:

$$s_w(\theta_{\mathbf{p}_0}) = \sum_{k=1}^K a_k \exp \{j(\varphi_k + \alpha_k \theta_{\mathbf{p}_0})\} \quad (\text{III.5})$$

which has the same form as (II.28) except that here the function which gives the non-stationary time-frequency shape depends on the unknown vector  $\mathbf{p}_0$ . Therefore the designed correction methods essentially will differ through the approach used in estimating the nonlinearity coefficients vector  $\mathbf{p}_0$ .

After the corrections, the final result is viewed in the spectrum of the beat signal or the so called range profile when the frequency axis is converted to range axis. In (III.5) the modulation rate  $\alpha_k$  is actually a frequency relative to the warped time axis. The equivalent chirp rate of the corrected beat signal  $\beta_0$  is the ratio between the swept bandwidth  $B$  and the sweep duration in the warped time axis  $\theta(T) - \theta(0) = \theta(T)$ . So the conversion from the frequency axis  $\alpha$  to range is easily done as

$$r = \frac{c}{2B} \frac{\alpha}{2\pi} \theta(T). \quad (\text{III.6})$$

### III.3 Discrete signal model and the Cramér-Rao lower bound

In this section we introduce the digital form of the beat signal, some implementation particularities and the computation of the Cramér-Rao lower bound (CRLB) for the nonlinearity parameters. The discrete form  $s[n]$  of the signal in (III.4) uniformly sampled at  $N$  time instants  $t_0, t_1, \dots, t_{N-1}$  embedded in a white circular Gaussian noise  $w[n]$  with variance  $\sigma^2$  is expressed as

$$x[n] = \sum_{k=1}^K s_k[n] + w[n] \quad (\text{III.7})$$

where

$$s_k[n] = a_k \exp \left\{ j [\varphi_k + \alpha_k \theta_{\mathbf{p}_0}(t_n)] \right\}. \quad (\text{III.8})$$

We introduce the following notations  $\mathbf{a} = [a_1, a_2, \dots, a_K]^T$ ,  $\boldsymbol{\varphi} = [\varphi_1, \varphi_2, \dots, \varphi_K]^T$ ,  $\boldsymbol{\alpha} = [\alpha_1, \alpha_2, \dots, \alpha_K]^T$ ,  $\mathbf{s}_k = [s_k[0], s_k[1], \dots, s_k[N-1]]^T$  and  $\mathbf{w} = [w[0], w[1], \dots, w[N-1]]^T$ . The signal in (III.7) can be rewritten in vectorial forms as

$$\mathbf{x} = \mathbf{s} + \mathbf{w} = \sum_{k=1}^K \mathbf{s}_k + \mathbf{w} \quad (\text{III.9})$$

and the set of unknown parameters is described by the vector  $\boldsymbol{\vartheta} = (\mathbf{p}_0^T, \mathbf{a}^T, \boldsymbol{\varphi}^T, \boldsymbol{\alpha}^T)^T$ . Only the components of  $\mathbf{p}_0$  are nonlinearity model parameters, while the others depend on the actual illuminated scene.

Note that in a warped time axis  $\theta = \theta_{\mathbf{p}_0}$ , the samples of  $x[n]$  are related to the time instants  $\theta_n = \theta_{\mathbf{p}_0}(t_n)$  which leads to a non-uniformly sampled signal. It can be shown that the average sampling interval on the  $\theta$  axis is:

$$\theta_{s,\text{warp}} = \frac{\theta_{\mathbf{p}_0}(T)}{T} T_s, \quad (\text{III.10})$$

where  $T_s$  the initial uniform sampling interval. According to [51], for a nonuniformly sampled signal, the average sampling rate must respect the Nyquist condition. For  $\theta_{\mathbf{p}_0}(T) > T$ , this condition can be fulfilled if the beat signal is oversampled (practically the chirp rate in the origin and the average chirp rate typically have the same order of magnitude, so the oversampling factor shouldn't be too high). If the signal is alias-free, it can be resampled with an interpolation procedure (e.g. with spline functions) in order to obtain a uniformly sampled signal in relation with the  $\theta$  time axis.

Therefore the computation of the Fourier transform of  $x[n]$  in the  $\theta$  time axis can be efficiently implemented by a resampling of the initial signal (to obtain a uniformly sampled

signal) followed by a Fast Fourier Transform (FFT). So a matched signal transform could be performed directly by applying (II.30), but the advantage of the time warping approach is the computation efficiency. Fig. III.1 illustrates the relation between the initial sampled signal, the non-uniformly sampled signal viewed in the  $\theta_{p_0}$  time axis and the final uniformly sampled signal (also in the  $\theta_{p_0}$  time axis) for a polynomial nonlinearity function with two coefficients.

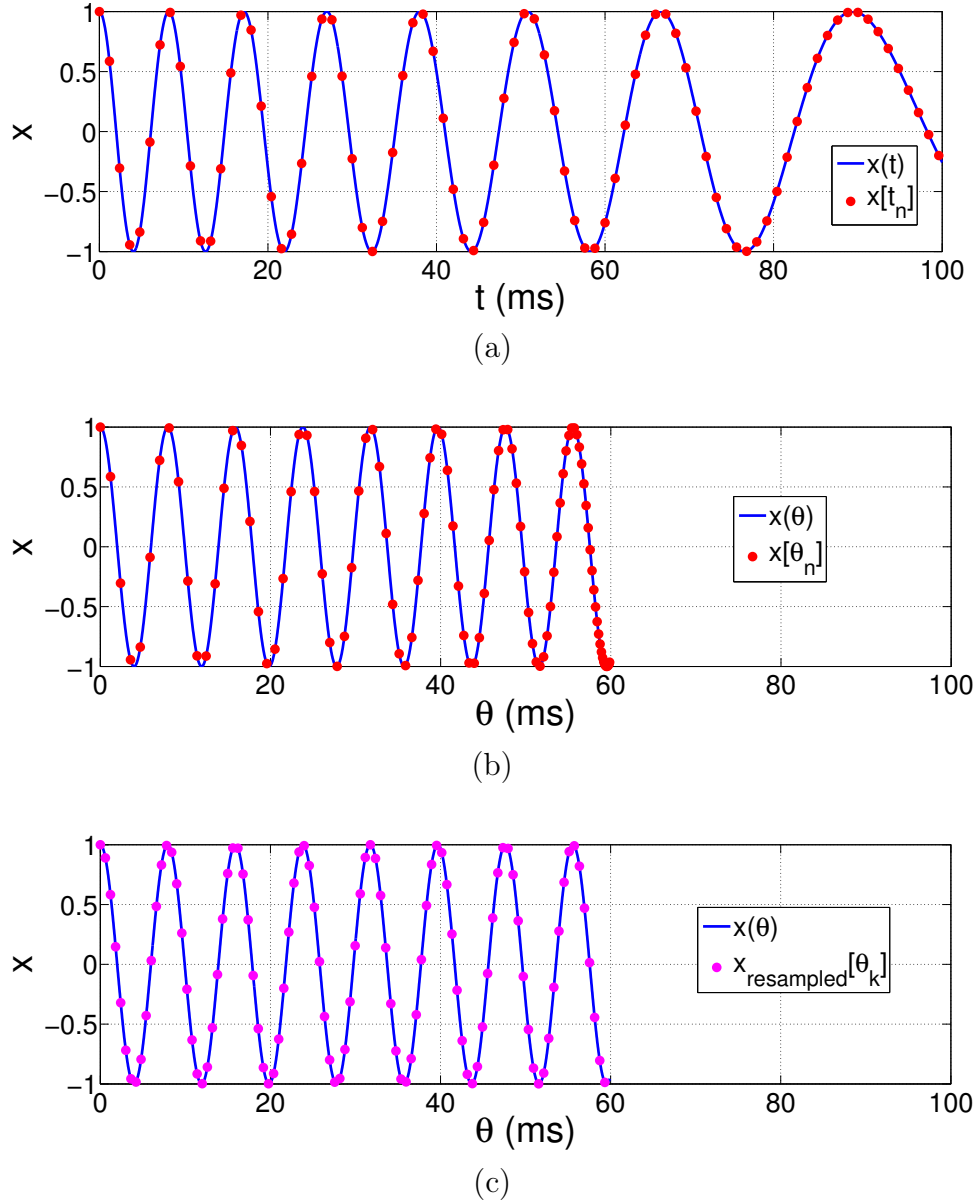


Figure III.1: Time warping as time resampling: (a) Analog and digital signals in the original time axis, (b) Analog and digital signals in the warped time axis, (c) Resampled digital signal in the warped time axis vs. the analog signal.

In order to evaluate the performances of the correction methods as nonlinearity coefficients estimators, the CRLB is computed as follows. From [52] the elements of the Fisher's information matrix are written as

$$I_{ij} = \frac{2}{\sigma^2} \operatorname{Re} \left\{ \frac{\partial \mathbf{s}^H}{\partial \vartheta_i} \frac{\partial \mathbf{s}}{\partial \vartheta_j} \right\}. \quad (\text{III.11})$$

It can be shown that each vector from this expression can take the following four forms depending with respect to which parameter is the derivative taken:

$$\begin{aligned} \frac{\partial \mathbf{s}}{\partial p_{0,l}} &= \{[\mathbf{s}_1 \ \mathbf{s}_2 \ \dots \ \mathbf{s}_K] \boldsymbol{\alpha}\} \circ j \frac{\partial \boldsymbol{\theta}_{p_0}}{\partial p_{0,l}} \\ \frac{\partial \mathbf{s}}{\partial a_k} &= \frac{\mathbf{s}_k}{a_k} \\ \frac{\partial \mathbf{s}}{\partial \phi_k} &= j \mathbf{s}_k \\ \frac{\partial \mathbf{s}}{\partial \alpha_k} &= j \mathbf{s}_k \circ \boldsymbol{\theta}_{p_0} \end{aligned} \quad (\text{III.12})$$

where

$$\begin{aligned} \boldsymbol{\theta}_{p_0} &= [\theta_{p_0}(t_0), \theta_{p_0}(t_1), \dots, \theta_{p_0}(t_{N-1})]^T \\ \frac{\partial \boldsymbol{\theta}_{p_0}}{\partial p_{0,l}} &= \left[ \frac{\partial \theta_{p_0}}{\partial p_{0,l}}(t_0), \frac{\partial \theta_{p_0}}{\partial p_{0,l}}(t_1), \dots, \frac{\partial \theta_{p_0}}{\partial p_{0,l}}(t_{N-1}) \right]^T \end{aligned}$$

and  $\circ$  denotes the element-wise product. After computing the information matrix  $I$  the Cramér-Rao lower bounds on the variances of the estimates are expressed as  $\operatorname{diag}(I^{-1})$ . Notice that due to the presence of multiple components the bounds will depend on the parameters' values and don't have a straight forward analytic expression, but can be numerically computed. A similar situation was reported in [15] for multi-component PPSs.

### III.4 HAF-based nonlinearity correction

For this method, we assume a polynomial frequency-voltage dependence of the VCO. This means that the nonlinearity function can be expressed as:

$$\theta_{p_0}(t) = t \left[ 1 + \sum_{l=1}^L p_{0,l} t^l \right]. \quad (\text{III.13})$$

With this assumption, the beat signal becomes a multi-component polynomial phase signal:

$$s_{PPS}(t) = \sum_{k=1}^K a_k \exp \left\{ j \left[ \varphi_k + \alpha_k t \left( 1 + \sum_{l=1}^L p_{0,l} t^l \right) \right] \right\}. \quad (\text{III.14})$$

The HAF-based estimation is based on the presence of a reference target response (with amplitude  $A_{ref}$  and propagation delay  $\tau_{ref}$ ) in the beat signal. This particular PPS component can be extracted by bandpass filtering the beat signal around the beat frequency corresponding to  $\tau_{ref}$ . The filtered signal can be written as:

$$s_{PPS,f}(t) = s_{PPS,f}(t, \tau_{ref}) + \sum_{m=1}^M s_{PPS,f}(t, \tau_m). \quad (\text{III.15})$$

where  $M$  is the number of significant PPS components located near the reference response in the filter's pass band which cannot be eliminated. In the estimation, it is considered that the reference target is highly reflective relative to the remaining  $M$  components. In this way, although the filtered signal has other components besides the reference response, the beat signal's nonlinearity coefficients can be estimated using the high-order ambiguity function due to its ability to deal with multiple component PPSs if the highest order phase coefficients of the components are not the same [13, 53]. This happens for the FMCW beat signal because each component is linked to a target with a certain propagation delay.

After applying the HAF iterative algorithm (mentioned in the second chapter) to the reference signal and obtaining an estimate of vector  $\mathbf{p}_0$ , the corrected range profile is obtained by time warping the beat signal with the estimated nonlinearity function  $\hat{\theta}_{\mathbf{p}_0}$ . The HAF-based nonlinearity correction algorithm is summarized in the block diagram from Fig. III.2.

## III.5 Range autofocusing nonlinearity correction

Typically, a concentration measure is used to determine an optimum parameter in a time-frequency representation (e.g. the window length for a spectrogram). However, such a measure can also be used to estimate the unknown parameters of the nonlinearity function  $\theta_{\mathbf{p}_0}(t)$ . The idea is to warp the signal in (III.4) with different test functions obtained for various values assigned to the parameters. When the test function matches the real basis function, the warped signal will essentially be a sum of complex sinusoids and its spectrum will have the highest degree of concentration. Consequently, a concentration measure applied to the warped signal's spectrum  $S_p(\alpha)$  will reach its optimum value when the warping is done with the optimal basis function. So the concentration measure can be viewed as a cost function which has to be minimized with respect to some parameters describing  $\theta_{\mathbf{p}_0}(t)$ . After the optimal parameters are determined, the amplitude, phase and range of each component can be extracted from the range profile obtained from the signal  $s(t)$  warped with the best-matched basis function. Note that this approach does not impose a certain model for the nonlinearity, but the number of parameters has to be relatively small due to computational reasons. The term autofocusing is used in order to emphasize

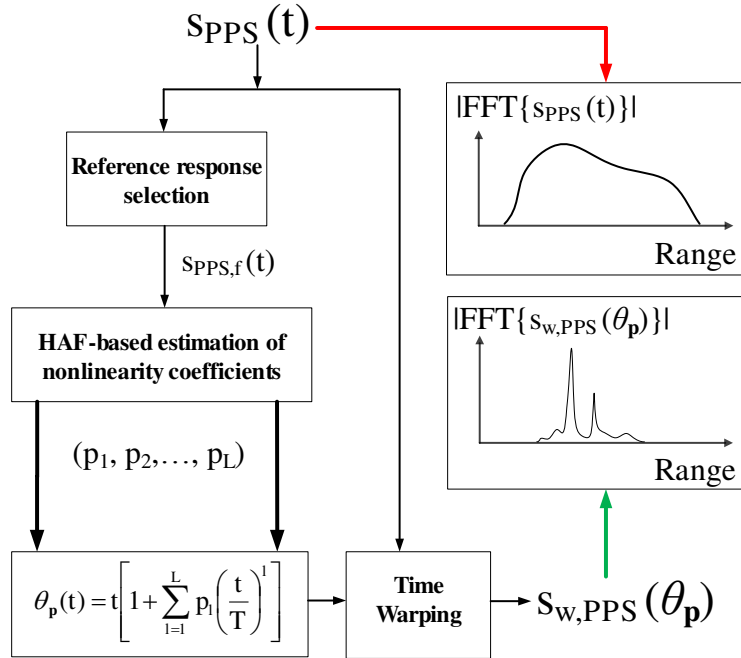


Figure III.2: Nonlinearity correction algorithm based on high-order ambiguity functions and time warping.

that the algorithm needs only the targets in the scene, disregarding their number and does not require any additional path in the transceiver.

We have chosen for the proposed estimation method the spectral concentration measure from [27] because in the optimization process it searches for a compromise such that all components are well concentrated and does not favor peaky components over others. For the beat signal's spectrum (the range profile) this measure is defined as

$$M[S_p(\alpha)] = \frac{\left( \int_{\alpha_{min}}^{\alpha_{max}} |S_p(\alpha)| d\alpha \right)^2}{\int_{\alpha_{min}}^{\alpha_{max}} |S_p(\alpha)|^2 d\alpha}, \quad (\text{III.16})$$

where  $[\alpha_{min}, \alpha_{max}]$  is the support of the warped signal's spectrum for the envisaged scene.

A diagram of the proposed algorithm in the case when the model has two parameters  $p_1$  and  $p_2$  is shown in Fig. III.3. The method requires a grid search which can get computationally demanding for a dense grid. Hence we propose finding the optimal parameters  $p_{1,opt}$  and  $p_{2,opt}$  using the Nelder-Mead optimization algorithm [54, 55] for the cost function  $M(p_1, p_2)$ . The starting point for the algorithm can be obtained with a search on a coarse

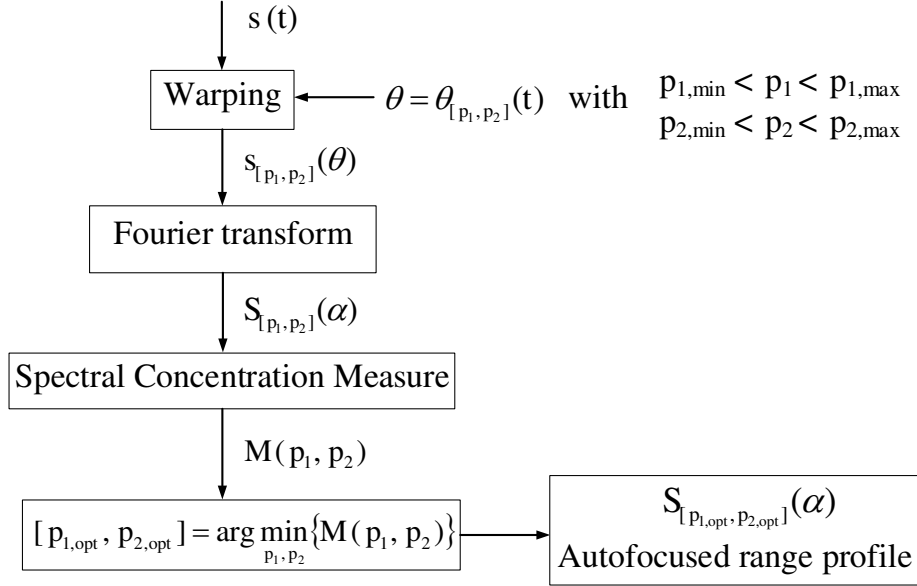


Figure III.3: Range autofocusing algorithm for a nonlinearity model with 2 parameters.

grid which does not increase significantly the computation time. Notice that because  $s(t)$  is an analytical signal derived from a real signal, the instantaneous frequency law of each component and the chirp rate  $\beta_0$  are positive. This means that the time derivative of the nonlinearity function has to be positive:

$$\theta'_p(t) \geq 0. \quad (\text{III.17})$$

Consequently, a constrained version of the Nelder-Mead algorithm [56] is employed in the optimization process.

An essential remark is that the range autofocusing approach, regarded as a parameters estimation algorithm, can be viewed as a generalization of some chirp rate estimation methods based on various transforms: the fan-chirp transform [57, 58], the adaptive harmonic fractional Fourier transform [59] or the multiangle centered discrete fractional Fourier transform [60]. More specifically, in comparison with the previously mentioned works, in the proposed algorithm the base modulation function  $\theta_{p_0}(t)$  can be any kind of monotonic one-to-one function depending on certain parameters (not only a second order polynomial depending on the chirp rate).

### III.6 Correction algorithms comparison

The range profiles of an FMCW radar using an X-band VCO with 20% linearity (defined as the ratio between the maximum frequency deviation of the characteristic from linear and the total sweep bandwidth [61, 62]) were simulated. The chirp bandwidth was 4 GHz, the sweep period  $T = 100$  ms and the sampling frequency 100 kHz. The simulated scene contained 4 scatterers with different amplitudes placed respectively at 20 m, 25 m, 30 m and 35 m from the radar. On the resulting beat signal we applied the two correction methods proposed. The nonlinearity was modeled as a third-degree polynomial expression since the slope of the frequency-voltage characteristic for some radio frequency VCOs may be reasonably approximated by a quadratic curve [61]. This model is compatible with both methods. The nonlinearity function is defined as:

$$\theta_{[p_{0,1}, p_{0,2}]}(t) = t \left[ 1 + p_{0,1} \frac{t}{T} + p_{0,2} \left( \frac{t}{T} \right)^2 \right]. \quad (\text{III.18})$$

The values of  $p_{0,1}$  and  $p_{0,2}$  are -0.09 and -0.25, respectively. For the HAF-based method we have considered as reference target the scatterer placed at 20 m. We analyzed two cases for the amplitude of the reference target -first it was at least 10 dB higher than the amplitude of any other scatterer, and in the second case it was comparable with the others. The spectrogram and range profile of the resulting beat signal when all the targets have similar amplitudes are shown in Fig. III.4.

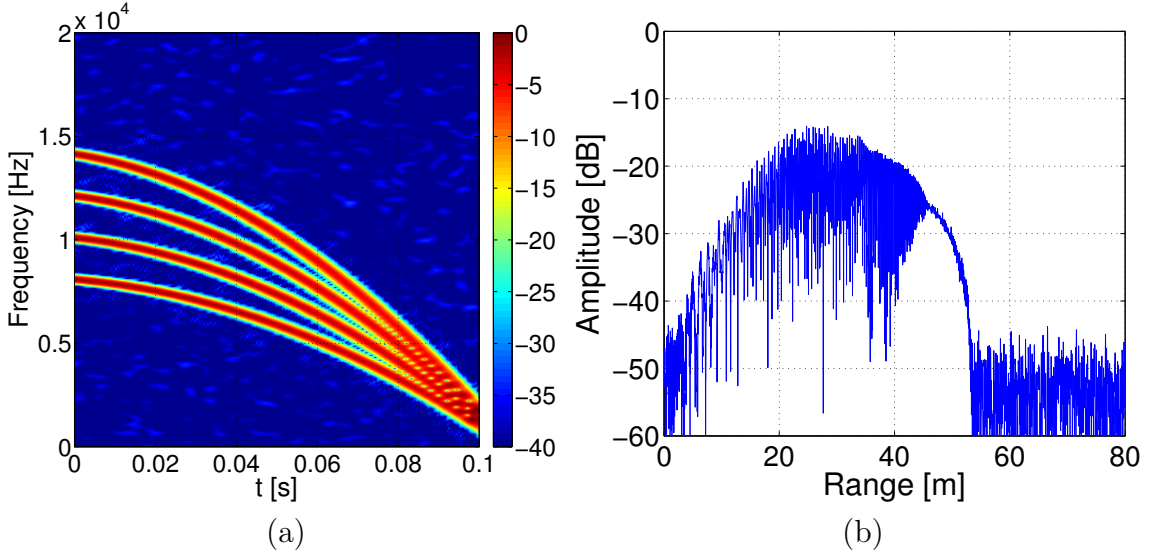


Figure III.4: Spectrogram (a) and range profile (b) of the initial beat signal. The time-frequency trajectories of the 4 targets are separated, but in the range profile they are completely overlapped.

Notice that although in the time-frequency plane the targets' responses are separated, in the frequency domain (in the range profile) they overlap and the scatterers cannot be distinguished. The corrected range profiles for the two possible amplitudes of the reference target are shown in Fig. III.5. Fig. III.5a and III.5c show the range profiles containing the 4 targets for the two possible amplitudes, while Fig. III.5b and III.5d are respectively a zoomed in version of Fig. III.5a and III.5c on the target placed at 30 m.

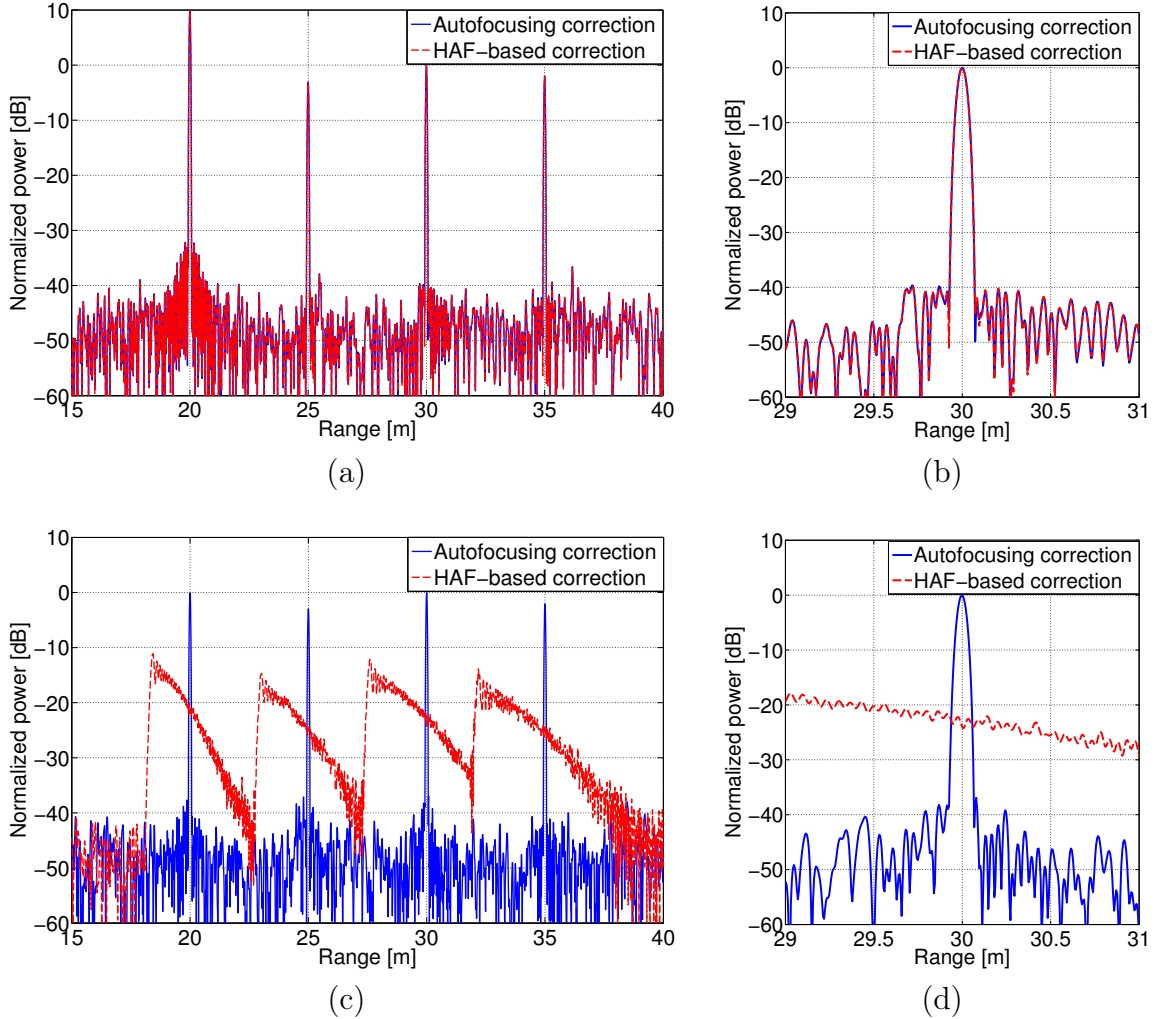


Figure III.5: Simulated nonlinearity corrected range profiles. Figures (a) and (b) show respectively the range profiles and a zoomed in version (on the target placed at 30 m) when there is one dominant target at 20 m. Figures (c) and (d) show respectively the range profiles and a zoomed in version (on the target placed at 30 m) when all the targets have similar amplitudes. When there is no dominant target, the performance of the autofocusing approach is unaltered, while the HAF-based algorithm doesn't manage to estimate and correct the nonlinearities.

When the reference target has a higher reflectivity than other targets, both algorithms perform similarly (the -10 dB resolution is around the theoretical limit and the SNR is increased with around 20 dB). However, when there is no dominant target the performance of the autofocusing approach is unaltered while the HAF-based algorithm does not work. This happens because in the autofocusing approach the spectral concentration measure takes into account all the scatterers in the scene and does not need a reference one.

Fig. III.6 shows the spectral concentration (as a function of two parameters) among with its evolution in the optimization process of the autofocus using as starting point (0,0) in the case when all 4 targets have similar amplitudes. The homogenous area in the lower left side of Fig. III.6a is the region where the constraint in (III.17) is not satisfied.

To assess the performances of the proposed methods as estimators of the nonlinearity parameters, some Monte Carlo simulations were performed considering 1000 realizations for each SNR value. Additionally, the CRLB was numerically computed. The considered test scenario for the simulations was the one with a single dominant target because only in this case the HAF-based method works and its performances can be also evaluated. The mean absolute error (MAE) and variance of  $p_1$  versus SNR are presented in Fig. III.7. Notice that these plots cannot show the general behaviour of the algorithm (they are valid only for the considered nonlinearity function) and if the model is changed, the plots should be re-evaluated in a similar manner.

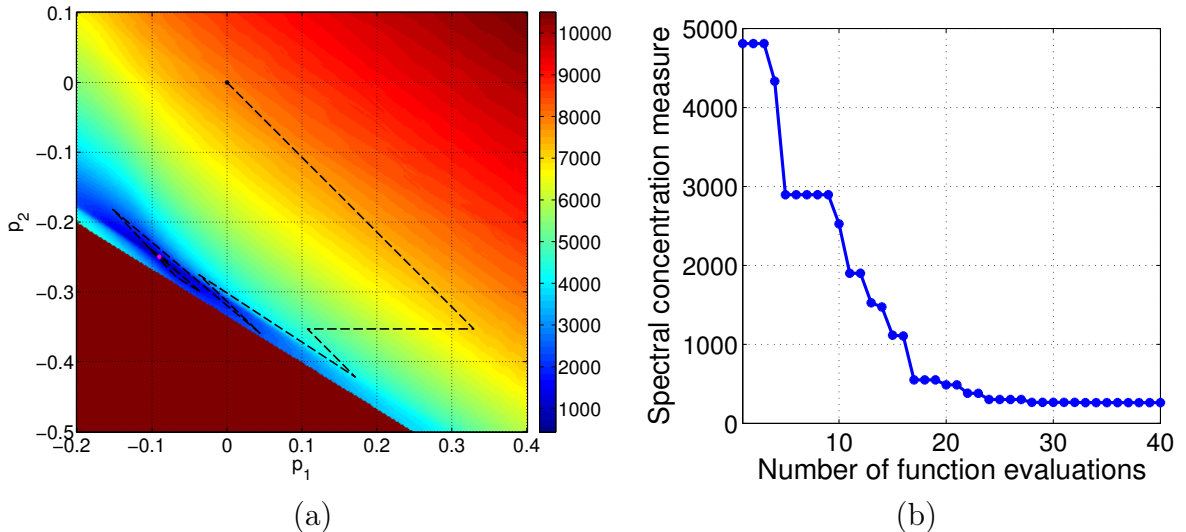


Figure III.6: The spectral concentration measure (a) as a function of two variables and (b) its evolution throughout the autofocus optimization. The trajectory described by the two parameters is superimposed in figure (a). The considered scenario is the one when all targets have similar amplitudes.

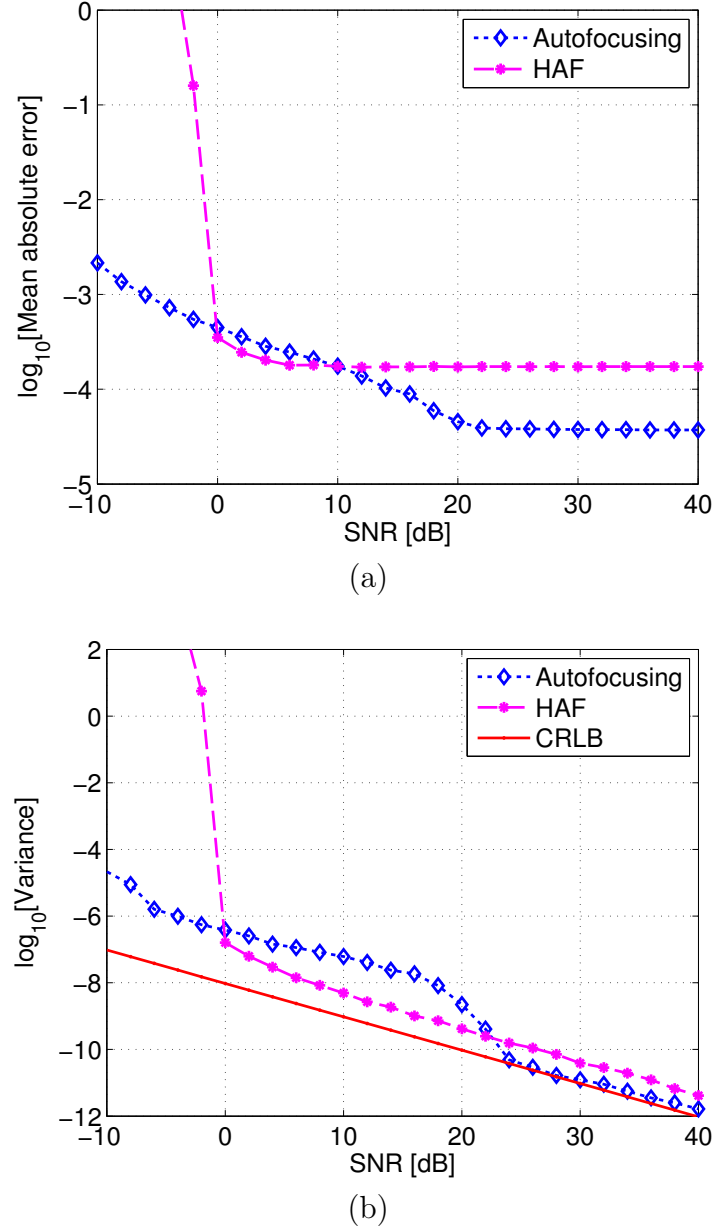


Figure III.7: Mean absolute error and variance of parameter  $p_1$  using both the autofocusing approach and the HAF-based method. The considered simulation scenario is with one dominant target.

From the obtained plots results that in terms of performances as estimator for the considered nonlinearity model, the autofocusing approach has a few advantages compared to the HAF-based method -the variance is closer to the CRLB for high SNR, the MAE is lower for most SNR values and the algorithm works in negative SNR. On the other side, the HAF-based method performs better in terms of variance for moderate SNRs.

### III.7 Conclusions

In this chapter we have proposed two range nonlinearity correction methods for wideband FMCW radars which exploit the specific time-frequency structure of the beat signal using a time warping approach.

The HAF-based method estimates the nonlinearity parameters on the beat signal corresponding to a delay line or a highly reflective target, while the range autofocusing algorithm warps in turn the beat signal according to different modulation functions (obtained for various parameters settings) and selects as the best-matched function the one that delivers the highest spectral concentration of the warped signal.

The autofocusing approach has the main advantage that it does not need an isolated reference target to estimate the nonlinearities and it works in the presence of multiple highly-reflective targets. However, the number of model parameters is limited from an operational point of view: it is not practical to minimize a cost function of too many variables. The HAF-based method allows a greater number of parameters, but is compatible only with a polynomial model and needs a clearly separated target to accurately estimate the nonlinearities.

As a general remark, the nonlinearity correction algorithms that we propose differ from previous works in two ways. On one hand, a typical nonlinearity estimation method (used for example in Vossiek's work [45]) based on the determination of the instantaneous phase of a precision radar reference path is valid only for a single component response, while both the HAF-based estimation and the range autofocusing can extract the nonlinearity coefficients from a multi-component response. On the other hand, the correction method proposed in [46] by Meta et al. requires a multiplication between the beat frequency signal and the nonlinearity term from the transmitted waveform. This implies an oversampling of the beat signal in order to satisfy the Nyquist condition for the nonlinearity term bandwidth and consequently this method is not well suited for large bandwidth nonlinearities (up to gigahertz). In our work, both the estimation and the correction of the nonlinearity are made using only the beat frequency signal, so the bandwidth of the nonlinear term from the transmitted signal does not impose the sampling rate.

## CHAPTER IV

# Scattering Centers Monitoring in Refocused SAR images

---

|  |           |
|--|-----------|
| <b>IV.1 Scattering Centers Monitoring Overview . . . . .</b>                     | <b>37</b> |
| <b>IV.2 Azimuth Defocusing . . . . .</b>   | <b>42</b> |
| <b>IV.3 Back-projection grid focusing . . . . .</b>                              | <b>45</b> |
| <b>IV.4 4D Tomography Detection and Tracking of Scattering Centers . . . . .</b> | <b>46</b> |
| <b>IV.5 Simulation results . . . . .</b>   | <b>48</b> |
| IV.5.1 Radar Geometry to Ground Geometry . . . . .                               | 48        |
| IV.5.2 Refocusing approach vs. Grid interpolation . . . . .                      | 48        |
| IV.5.3 Scattering Centers Detection and Tracking Results . . . . .               | 49        |
| IV.5.4 Position test vs. Classical scatterers identification . . . . .           | 61        |
| <b>IV.6 Conclusions . . . . .</b>  | <b>64</b> |

*In this chapter we present the developed scattering centers monitoring procedure based on refocusing a set of spaceborne SAR images on a provided grid (or point cloud) of a structure and identifying the reliable scattering regions by means of four dimensional tomography.*

## IV.1 Scattering Centers Monitoring Overview

In infrastructure monitoring, it can be often necessary to track the slow displacements of certain points of a given structure (building, water dam, landslide, etc.). This can be done using current spaceborne civil sensors, such as TerraSAR-X and TanDEM-X provided their short wavelength of 3.1 cm, the short revisit time of 11 days and especially the 1 m resolution in spotlight mode [2, 3, 63]. Still, given a certain infrastructure element, from

one acquisition geometry only one side of the structure can be observed. Due to typical side-look effects (layover ambiguities, multi-path scattering effects or shadowing) it is not always clear from what points does the main response return, where is their scattering center positioned, which of them are visible from the respective orbit and consequently which of them can be accurately monitored. If the coordinates of a number of points from the structure are known with at least centimeter accuracy (measured with GPS or LIDAR techniques) their response (if there is any) could be determined if the raw data were focused on a 3-dimensional grid containing precisely these points. However, in most cases in the delivered products the SAR images are already focused on a slant range-azimuth grid which is not related to any specific scatterer.

Since the availability and processing of spaceborne raw SAR data is not very convenient, in this chapter we propose a scattering centers monitoring method based on refocusing [64, 65] the SAR data on a given grid containing the points of a structure that needs to be monitored. The technique used to identify the real scatterers from the given grid (which provide the main response and are not faded by layover) in a stack of refocused images is developed in the context of differential tomography [8, 9, 10]. This is obtained by exploiting the fact that each refocused scattering center will be at zero elevation in the local elevation-velocity (EV) plane. So the actual detection consists in an elevation position testing relative to a certain grid.

An advantage of the refocusing approach on a specific grid is that no shifting or resampling (as part of the coregistration process) are needed because the samples get automatically aligned by refocusing each image on the same grid. Moreover, when computing the SAR impulse responses of the provided 3D geographic model by refocusing the azimuth defocused data, the phase shifts corresponding to the acquisition geometry and to the variable Doppler centroid in the focused image (specific for sliding spotlight mode) are both taken into account. Hence, an implicit coregistration of the images is obtained and the interferometric phase can be computed as the phase difference of corresponding points.

Notice that the proposed approach uses a provided DEM in a completely different manner than typical geometrical registration approaches working in the slant range domain. Furthermore, in comparison with the classical coregistered interferograms, a highly reflective scatterer with known coordinates that needs to be tracked (a mounted corner reflector for instance) cannot have an inconvenient off-grid position for processing in the SAR image (e.g. to be at the edge of 4 neighboring pixels): it will always be placed in the center of the resolution cell on the new grid and its relative displacements will be accurately measured. The off-grid reflectors problem was also addressed in [66] where an algorithm for finding the reflectivity center is proposed. However, in the case of refocusing on a given grid, the purpose is to test if the scattering center is at the specified position (known with centimeter accuracy).

## Chapter IV. Scattering Centers Monitoring in Refocused SAR images

---

The proposed detection method based on elevation position testing could also be employed by converting the grid points from their original coordinates (e.g. Earth Centered Earth Fixed (ECEF) or latitude/longitude/altitude format) to the slant range-azimuth coordinates of a master image and interpolating the complex amplitude using the nearby pixels. However, compared to the refocusing approach, this interpolation-based method requires that all the images are first coregistered. This is even more relevant in the case of sliding spotlight images where any interpolation required for coregistration has to be performed with a modulated kernel in order to follow the Doppler drift in azimuth [2]. From a different point of view, the refocusing procedure can also be seen as an equivalent interpolation kernel (considering that all operations involved are linear) whose parameters will be always adapted to the specific imaging mode. Besides, because the refocusing is applied to a small area of the initial SAR image the increased computational complexity should not be a significant drawback.

In the proposed scattering centers identification procedure the detection problem is posed in a different manner from classical approaches used in SAR tomography which are based on standard detection theory [9, 67, 68, 69]. Classically, the detection is done by comparing the normalized tomographic reconstructed peak to a certain threshold. In this case, the elevation dispersion inherently enters in the detection scheme by affecting the peak value. In the detection scheme proposed in this work the expected elevation is already known (zero for on-grid targets) and the detection actually consists in a position test of the overall maximum in the elevation-velocity plane. Consequently, the elevation dispersion translates in the tolerated accuracy of the scattering center's position relative to the provided grid.

Onwards, the scattering centers monitoring procedure is presented in two stages: the refocusing of the acquired SAR images on the provided grid, followed by the scattering centers detection and displacements computation. A general diagram of the scattering centers detection and tracking procedure is displayed in Fig. IV.1. The refocusing algorithm consists in an azimuth defocusing of the initial SAR images followed by a focusing on the given grid, using a modified back-projection algorithm. The block diagram of the refocusing algorithm is shown in Fig. IV.2 and all the operations are described according to the flow on the processing chain. After the image is refocused, the scattering centers are detected and tracked using the differential tomography framework.

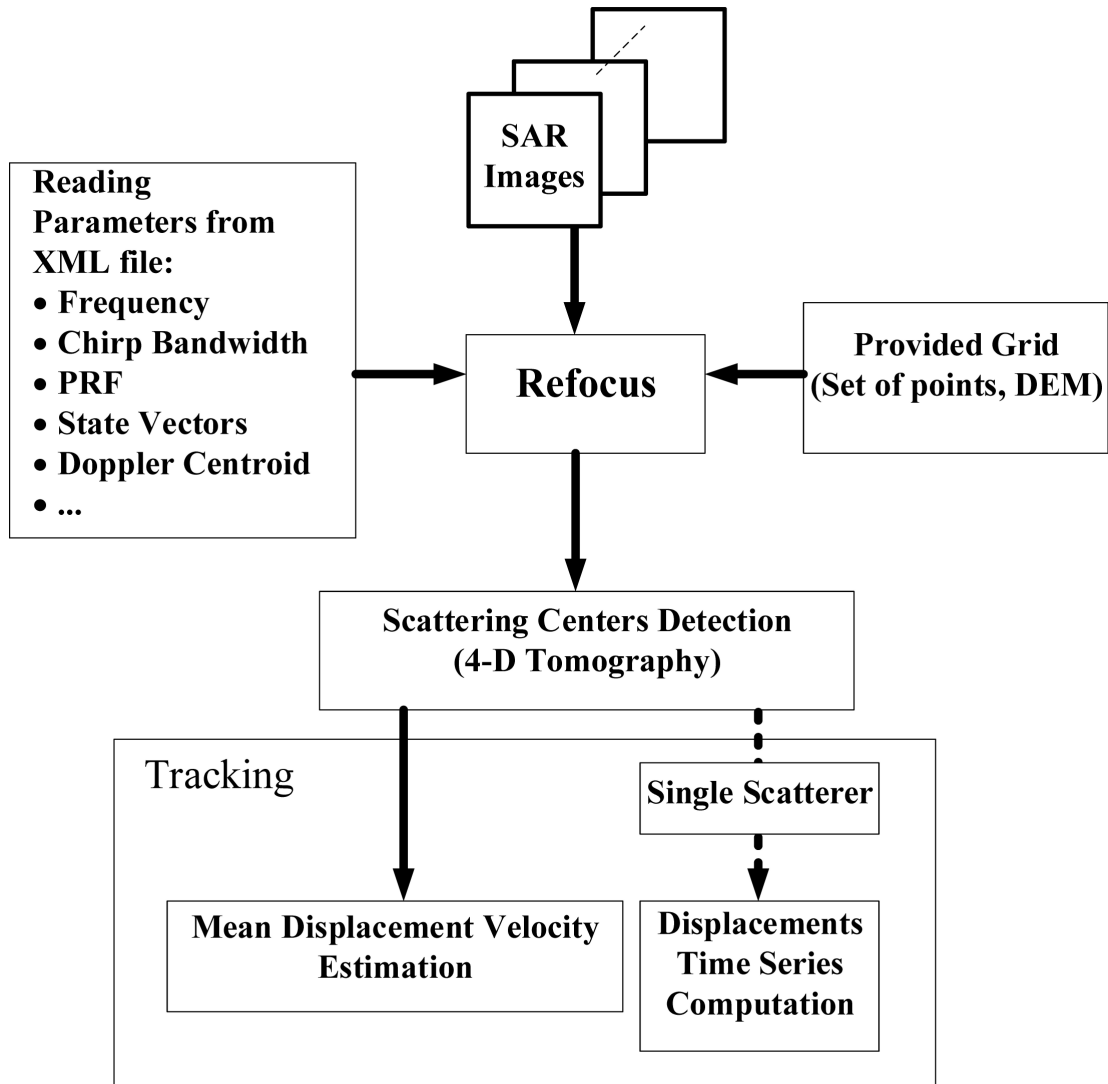


Figure IV.1: Scattering Centers Detection and Tracking based on SAR Images Refocusing.

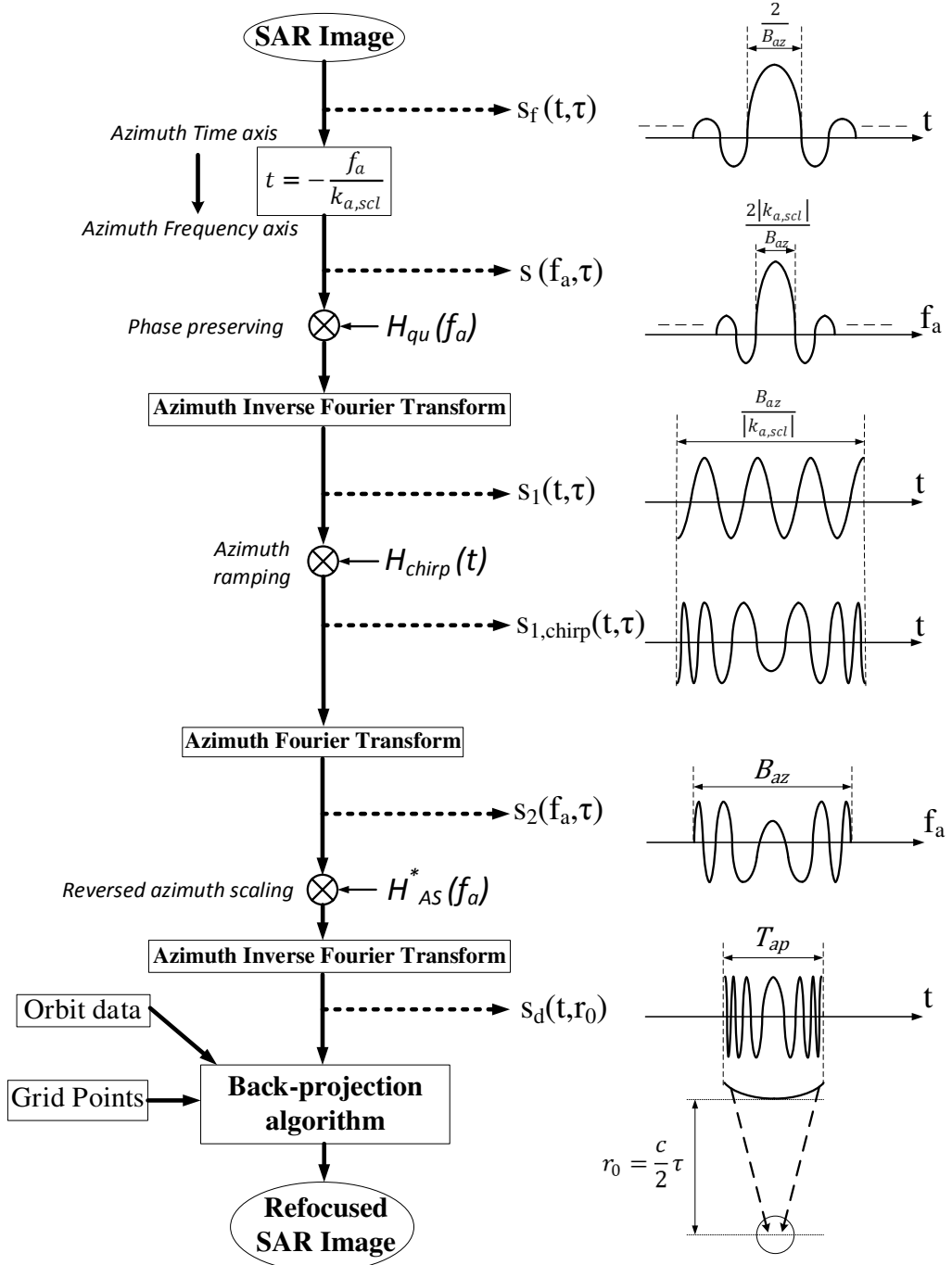


Figure IV.2: Block diagram of the refocusing algorithm and qualitative representation of the real part of certain intermediate signals in the case of a single scatterer (zero Doppler centroid is assumed for representation simplicity).

## IV.2 Azimuth Defocusing

The defocusing procedure is actually based on a reversed version of the Spectral Analysis (SPECAN) processing used for azimuth focusing [70, 71]. This approach is possible because the azimuth scaling consists only in Fourier transforms and complex multiplications which are reversible. The first operation consists in selecting from the initial image the slant range-azimuth region containing the target. Since the range compression is not modified during the processing, the selected region is cropped in range in order to reduce the computation time.

In the case of spotlight SAR images the azimuth sampling frequency is larger than the raw data PRF in order to cover the complete spotlight bandwidth. In the defocusing procedure the sampling frequency is the one of the SAR image, so the subaperture approach used for real-time focusing [72] does not need to be employed. Therefore the subaperture recombination from the focusing algorithm in [71] can be skipped (it was necessary only to keep the PRF at the value from the raw data acquisition just until the final azimuth Fourier transform). An advantage of processing the entire aperture is that the average Doppler centroid will have a very small value which minimizes the azimuth time shifts caused by the azimuth scaling.

The focused two-dimensional signal for  $N$  scatterers (equal to the number of pixels of the cropped SAR image) can be written as:

$$s_f(t, \tau) = \sum_{i=1}^N A_i \exp(-j2\pi f_c \tau) \text{sinc}[\pi B_r(\tau - \tau_i)] \times \text{sinc}[\pi B_{az}(t - t_i)] \exp(j2\pi f_{DC}(t_i)(t - t_i)), \quad (\text{IV.1})$$

where  $t$  is the azimuth (slow) time axis,  $\tau$  is the slant range (fast) time axis,  $B_{az}$  is the target azimuth bandwidth,  $B_r$  is the range chirp bandwidth,  $A_i$ ,  $t_i$ ,  $\tau_i$  represent respectively the complex amplitude, the zero Doppler azimuth time and the slant range delay at closest approach for the scatterer  $i$  and  $f_{DC}(t_i)$  is the Doppler centroid corresponding to a target at the zero Doppler azimuth time  $t_i$ . For simplicity, rectangular windows for both range and azimuth data are assumed, hence the sinc functions in (IV.1). Notice that this analytic expression takes into account that in sliding spotlight mode the spectrum of each target in the focused image is centered around the Doppler centroid corresponding to target's azimuth position [73, 74]. Generally, the Doppler centroid can be written as a linear function of the zero Doppler azimuth time:

$$f_{DC}(t) = f_{DC,0} + \alpha t, \quad (\text{IV.2})$$

where  $f_{DC,0}$  is the Doppler centroid at  $t = 0$  and  $\alpha$  is the Doppler drift rate in the focused scene caused by the beam sweeping in spotlight acquisition modes.

In the SPECAN processing [75] each zero Doppler azimuth time from the focused image is actually linked to an azimuth frequency  $f_a$  by the scaling Doppler rate  $k_{a,scl}$ :

$$t = -\frac{f_a}{k_{a,scl}} \quad (\text{IV.3})$$

and the image can be regarded as a function of azimuth frequency and fast time:

$$\begin{aligned} s(f_a, \tau) &= s_f \left( -\frac{f_a}{k_{a,scl}}, \tau \right) = \sum_{i=1}^N A_i \exp(-j2\pi f_c \tau) \\ &\times \text{sinc} [\pi B_r(\tau - \tau_i)] \text{sinc} \left[ \pi \frac{B_{az}}{k_{a,scl}} (f_a + k_{a,scl} t_i) \right] \\ &\times \exp \left( -j2\pi \frac{f_{DC}(t_i)}{k_{a,scl}} (f_a + k_{a,scl} t_i) \right). \end{aligned} \quad (\text{IV.4})$$

The first multiplication in the processing is made for phase preserving given the subsequent processing steps and is described by a quadratic phase term:

$$H_{qu}(f_a) = \exp \left( j\pi \frac{f_a^2}{k_{a,scl}} \right). \quad (\text{IV.5})$$

Next an azimuth inverse Fourier transform is applied and leads to a two-dimensional signal in the azimuth-fast time domain (computed analytically in a similar fashion as in [76] for the residual video phase removal):

$$\begin{aligned} s_1(t, \tau) &= C_1 \sum_{i=1}^N A_i \exp(-j2\pi f_c \tau) \text{sinc} [\pi B_r(\tau - \tau_i)] \\ &\times \text{rect} \left[ \frac{k_{a,scl}}{B_{az}} \left( t - t_i - \frac{f_{DC}(t_i)}{k_{a,scl}} \right) \right] \\ &\times \exp(j\pi k_{a,scl} (-2t_i t + t_i^2)). \end{aligned} \quad (\text{IV.6})$$

By chirping  $s_1(t, \tau)$  with the function

$$H_{chirp}(t) = \exp(j\pi k_{a,scl} t^2) \quad (\text{IV.7})$$

the resulting signal becomes a sum of chirp functions in azimuth having the zero frequency points at the closest approach azimuth times of each target:

$$\begin{aligned} s_{1,chirp}(t, \tau) &= C_1 \sum_{i=1}^N A_i \exp(-j2\pi f_c \tau) \text{sinc} [\pi B_r(\tau - \tau_i)] \\ &\times \text{rect} \left[ \frac{k_{a,scl}}{B_{az}} \left( t - t_i - \frac{f_{DC}(t_i)}{k_{a,scl}} \right) \right] \exp[j\pi k_{a,scl} (t - t_i)^2]. \end{aligned} \quad (\text{IV.8})$$

In the next step an azimuth Fourier transform is applied to the signal in (IV.8) using the principle of stationary phase (PSP) [76, 77]. The PSP can be employed because the signal is a sum of chirp functions each of which bringing one stationary point in the computation of the Fourier integral for every azimuth frequency. The result is written as:

$$s_2(f_a, \tau) = C_2 \sum_{i=1}^N A_i \exp(-j2\pi f_c \tau) \text{sinc} [\pi B_r(\tau - \tau_i)] \\ \times \text{rect} \left[ \frac{f_a - f_{DC}(t_i)}{B_{az}} \right] \exp \left( -j\pi \frac{f_a^2}{k_{a,scl}} \right) \exp(-j2\pi f_a t_i). \quad (\text{IV.9})$$

The signal in (IV.9) is multiplied with a complex conjugated version of the azimuth scaling function [71] expressed as

$$H_{AS}^*(f_a, \tau) = \exp \left( j\pi \frac{f_a^2}{k_{a,scl}} \right) \\ \times \exp \left[ -j2\pi f_c \tau \left( \sqrt{1 - \left( \frac{f_a \lambda}{2v_0} \right)^2} - 1 \right) \right], \quad (\text{IV.10})$$

where  $\lambda$  is the wavelength at central frequency and  $v_0$  is the zero Doppler azimuth velocity. This operation converts the chirp's quadratic phase to the original range dependent (through the fast time  $\tau$ ) hyperbolic phase history. The signal takes the form:

$$s_{2,hyp}(f_a, \tau) = C_2 \sum_{i=1}^N A_i \exp(-j2\pi f_c \tau) \text{sinc} [\pi B_r(\tau - \tau_i)] \\ \times \text{rect} \left[ \frac{f_a - f_{DC}(t_i)}{B_{az}} \right] \exp(-j2\pi f_a t_i) \\ \times \exp \left[ -j2\pi f_c \tau \left( \sqrt{1 - \left( \frac{f_a \lambda}{2v_0} \right)^2} - 1 \right) \right]. \quad (\text{IV.11})$$

The last step is an azimuth inverse Fourier transform computed for each term of the sum in (IV.11) using the Fourier transform pair in [78]. After this transform the azimuth defocused two-dimensional signal has the form:

$$s_d(t, r_0) = C \sum_{i=1}^N A_i \text{sinc} \left[ \frac{2\pi B_r}{c} (r_0 - r_{0,i}) \right] \\ \times \text{rect} \left[ \frac{t - \left( t_i - \frac{T_{ap}}{B_{az}} f_{DC}(t_i) \right)}{T_{ap}} \right] \\ \times \exp \left( -j \frac{4\pi}{\lambda} \sqrt{r_0^2 + [v_0(t - t_i)]^2} \right), \quad (\text{IV.12})$$

where  $T_{ap}$  is the equivalent synthetic aperture (illumination) time [2]. In (IV.12) each fast time  $\tau$  was written as  $2r_0/c$ , where  $r_0$  is the corresponding closest approach distance.

Given the support of the rectangular window in (IV.12) and that for a SAR image with azimuth extent  $t_{scene}$  the closest approach azimuth times can vary between  $-t_{scene}/2$  and  $t_{scene}/2$  the minimum necessary azimuth support is:

$$T_{az,min} = t_{scene} \left( 1 - \alpha \frac{T_{ap}}{B_{az}} \right) + T_{ap}. \quad (\text{IV.13})$$

Hence the number of points in azimuth should respect the condition:

$$N_{az} \geq F_s T_{az,min}, \quad (\text{IV.14})$$

where  $F_s$  is the azimuth sampling frequency (the equivalent PRF). The necessary number of azimuth points can eventually be chosen as the next power of 2 which fulfills (IV.14) and is obtained by zero padding the initial data. Having  $N_{az}$  and taking into account (IV.3), the scaling Doppler rate is given by:

$$k_{a,scl} = -\frac{F_s^2}{N_{az}}. \quad (\text{IV.15})$$

### IV.3 Back-projection grid focusing

Notice that the signal in (IV.12) has the natural hyperbolic phase history for each target and is not affected by range migration. The discrete azimuth defocused signal can be written as  $s_d[m, n] = s_d(m\delta t, n\delta r)$ . Seen as a matrix,  $s_d[m, n]$  has on each column the phase history for a certain closest approach slant range and each line contains a range profile.

The grid focusing procedure starts by extracting the annotated orbit data [79]. For an azimuth resolution larger than 1 m the straight line trajectory approximation of the orbit is satisfactory (the curved orbit correction is needed only for staring spotlight mode [80]). Hence, the envisaged geometry is the same as the one presented in Chapter II (Fig. II.2). The unit vector  $\vec{u}$  of the azimuth direction is computed as the normalized velocity vector of the satellite at the azimuth time of the image center. The position of the satellite's APC  $\vec{r}_a(t)$  and the closest approach distance  $r_{0,k}$  of a target having the position vector  $\vec{r}_k$  are given by equations (II.33) and (II.34).

The response of the target positioned at  $\vec{r}_k$  is computed using a time-domain back-projection algorithm [81, 29, 82, 30] adapted for data with no range cell migration having the phase history of a point target on a single column of the matrix  $s_d[m, n]$ . Hence, the

target response is computed as

$$g(\vec{r}_k) = \sum_{m=M_-}^{M_+} s_d(m\delta t, r_{0,k}) \exp\left(j \frac{4\pi f_c}{c} \|\vec{r}_a(m\delta t) - \vec{r}_k\|\right), \quad (\text{IV.16})$$

where  $M_-$  and  $M_+$  are the limits corresponding to the total illumination duration of the respective target (the equivalent synthetic aperture time  $T_{ap}$ ). The zero Doppler azimuth time has the same expression as in (II.35) and the summation limits are defined as

$$M_\pm = \left[ F_s \left( t_{\vec{r}_k} - \frac{T_{ap}}{B_{az}} f_{DC}(t_{\vec{r}_k}) \pm \frac{T_{ap}}{2} \right) \right]. \quad (\text{IV.17})$$

Notice that  $r_{0,k}$  in (IV.16) is not necessarily on the range grid (is not written as  $n\delta r$ ) and hence the value of  $s_d(m\delta t, r_{0,k})$  is interpolated in the algorithm from the matrix  $s_d[m, n]$ .

The difference between the focusing equation in (IV.16) and the classic back-projection described by equation (II.43) is that the variable distance  $\|\vec{r}_a(m\delta t) - \vec{r}_k\|$  appears only in the phase compensation term (the complex exponential) while the argument of the data matrix is always the closest approach distance  $r_{0,k}$  regardless of the azimuth time. Additionally, the imposed summation limits take into account the extension of each target's IFL in the time-frequency plane and avoid adding clutter samples by acting like a time-frequency filter.

The actual refocusing is implemented by applying (IV.16) to each point from the given set.

## IV.4 4D Tomography Detection and Tracking of Scattering Centers

For two refocused images, the stable scatterers could be detected by classical coherence evaluation on a vicinity of each refocused point. However, in order to determine if the reflecting scattering center is actually at the given point an approach based on a series of acquisitions is needed in order to create an elevation aperture. Hence, the differential tomography framework presented in Chapter II is employed. By changing the geometrical EV configuration for each refocused target, the scatterer's position on the elevation axis is at  $s = 0$  and any other scatterer situated in layover will be at another distance as presented in Fig. IV.3. Therefore the persistent scatterers from the set of targets which have the real scattering center at the given position and are not affected by layover are the ones that have only one significant maximum value of the PSD in the EV plane at zero elevation clearly separated from other eventual local peaks corresponding to layover targets. Moreover, the

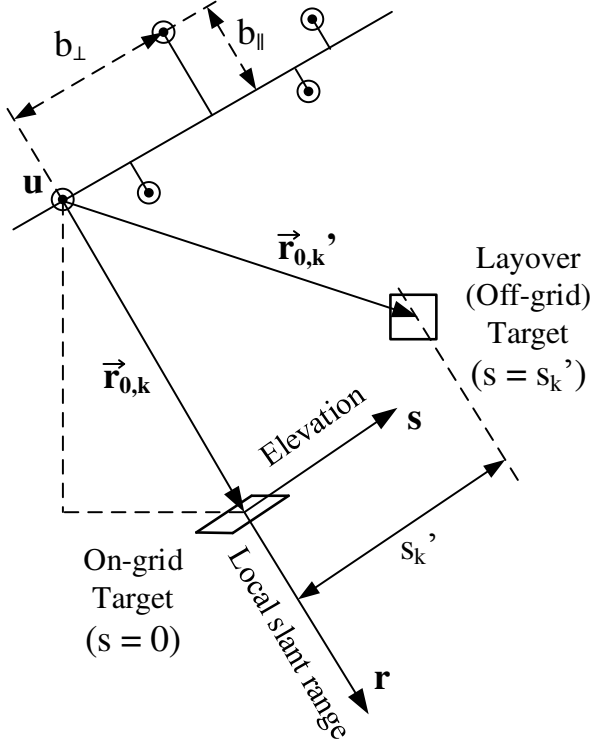


Figure IV.3: Layover detection geometry based on zero elevation for on-grid targets.

dispersion of the elevation estimator can be interpreted as the positioning accuracy of the detected scatterer relative to the provided grid. The mean displacement velocity (MDV)  $\bar{v}_0$  of a detected scatterer is estimated as the location of the peak on the velocity axis at zero elevation.

The displacements time series  $d(t_n)$  of a detected scatterer can be viewed as a sum between the linear displacement and the residual un-modeled motion. Hence, for a single scatterer at zero elevation not influenced by layover targets, the time series is expressed as [9]:

$$d(t_n) = \bar{v}_0 t_n + \frac{\lambda}{4\pi} \arg \left\{ g_n(\vec{r}_k) \exp \left( -j \frac{4\pi \bar{v}_0 t_n}{\lambda} \right) \right\}. \quad (\text{IV.18})$$

This expression is similar to the permanent scatterers interferometry (PSI) case except that here the linear displacement phase term is first subtracted. By computing the time series in this way, only the nonlinear displacement relative to the linear trend has to be below half-wavelength and not the whole displacement.

## IV.5 Simulation results

In this section simulation results are presented in order to test the proposed methodology. Comparisons between the developed algorithm and other SAR images processing methods are performed.

### IV.5.1 Radar Geometry to Ground Geometry

A scene containing 10 point-like scatterers arranged in a rectangular grid as shown in Fig. IV.4a is simulated. The distance between two neighbouring points of the grid is 10 m on Ox and Oy. The flight path is contained in a horizontal plane (parallel to xOy) and oriented at  $45^\circ$  with respect to Ox. The simulation parameters are picked according to the typical values for the TerraSAR-X satellite operating in high-resolution spotlight mode: central frequency 9.65 GHz, total azimuth bandwidth 7 kHz, azimuth sampling frequency 8.5 kHz, equivalent synthetic aperture duration 1.5 s, zero Doppler velocity 7 km/s, mean slant range 750 km, incidence angle  $40^\circ$ . The dechirp-on-receive response of the targets is computed for every pulse in zero Doppler coordinates considering the stop and go approximation. The SAR image is focused using the Frequency Scaling Algorithm [71] with Hamming window weighing in both slant range and azimuth. Fig. IV.4b shows the obtained image in slant range-azimuth geometry. The proposed refocusing algorithm is applied on this image using as new grid an oversampled version of the rectangular grid on which the scatterers are placed having a 20 cm distance between neighbouring points on both axis. The refocused image is presented in Fig. IV.4c. Notice that in the initial image the scatterers are disposed in a parallelogram shape due to the slant range geometry, while in the image refocused on the horizontal grid the correct rectangular shape appears.

### IV.5.2 Refocusing approach vs. Grid interpolation

The proposed position test detection method could also be carried out if the provided 3D model would be converted to slant range-azimuth coordinates and the SAR impulse responses interpolated using nearby pixels. Assuming that the images from the acquired data set are coregistered, the interpolation of the SAR impulse response can be done by various methods.

This subsection presents a few simulation results aimed to compare the performances of the refocusing approach with three usual interpolation methods: spline-based interpolation, truncated sinc and nearest neighbor. The scenario considered for this simulation involves a target placed at random positions on the ground such that in some cases is in the center

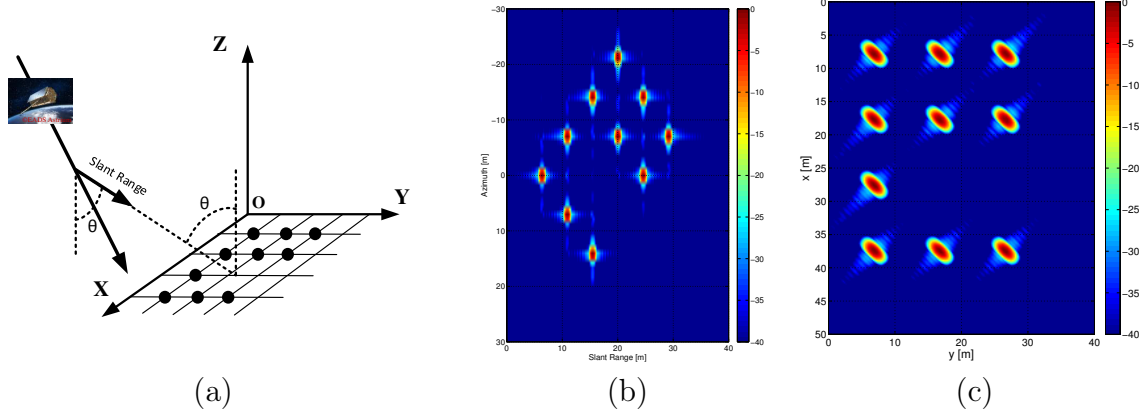


Figure IV.4: Refocusing Algorithm Simulation: (a) Simulation scenario, (b) Focused SAR image with the Frequency Scaling Algorithm in slant range-azimuth geometry, (c) Refocused image on a grid placed in the horizontal plane containing the scatterers.

of a pixel and in others at the edge of 4 neighboring pixels. The refocusing/interpolation grid is a rectangular one centered each time at the target's position. The performances of the methods are compared in terms of phase dispersion and average coherence. 1000 realizations are simulated for different values of the SNR. Fig. IV.5 shows the phase dispersion and average coherence for various signal-to-noise ratios. The refocusing approach provides better results especially for low SNR values, while for high SNRs the methods are comparable. These results are linked to the fact that the refocusing is each time adapted to the specific imaging parameters.

### IV.5.3 Scattering Centers Detection and Tracking Results

This subsection presents the results of a set of simulations which aim to highlight the performances and limitations of the proposed scattering centers monitoring procedure. The impact of different configurations/parameters on the detection and tracking of a scatterer at a certain grid position is studied. The conducted simulations want to emphasize the behaviour of the algorithm especially for a relatively small number of available satellite passes (which can be a practical problem in short-term infrastructure monitoring). Obviously the simulated cases are not exhaustive, but they can give an idea of the expected performances in different scenarios.

The main settings used in the simulations are the same as those presented in subsection IV.5.1, but the simulated scene is the one from Fig. IV.6. Target 1 is a scattering region obtained from the superposition of a few point-like targets which are all displaced in the same manner in every test. Target 0 is used as reference point and all the computed

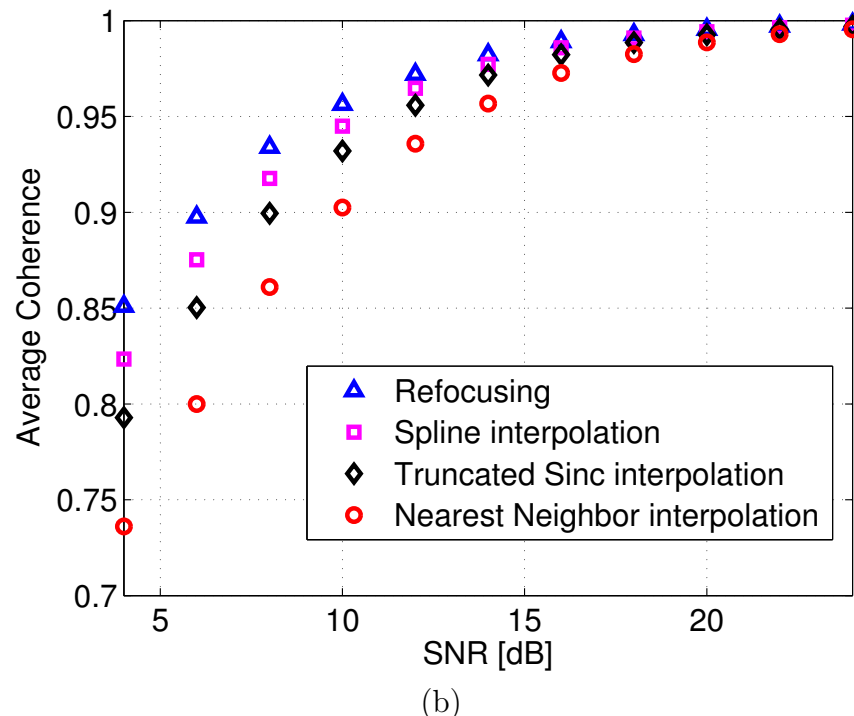
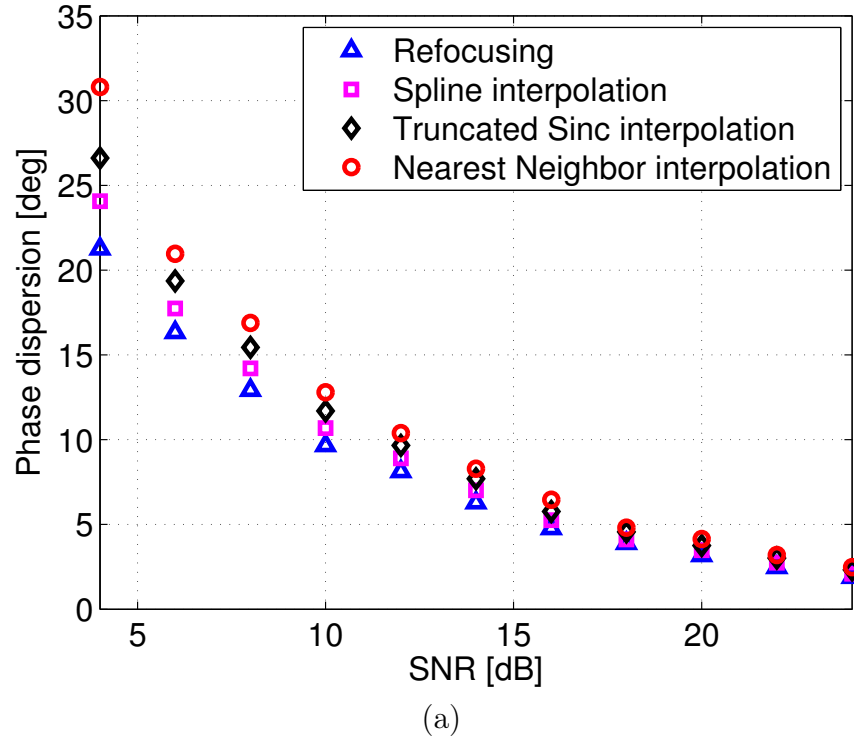


Figure IV.5: Comparison between the refocusing approach and 3 interpolation-based methods in terms of phase dispersion (a) and average coherence (b).

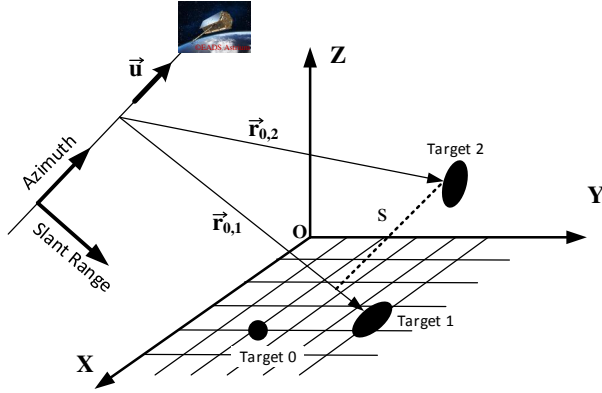


Figure IV.6: Envisaged geometric configuration for the detection and tracking simulations.

displacements are relative to it. Target 2 is positioned such that it is in layover with target 1, but its assigned amplitude is nonzero only for the simulations involving layover scenarios. Several scenes (corresponding to successive satellite tracks) like the one in Fig. IV.6 are simulated by computing the refocused image on a grid in the  $xOy$  plane in an area near target 1. For each track, target 1 is displaced according to the considered test case and the baseline is arbitrarily chosen in keeping with the  $\pm 250$  m orbit tube of the TerraSAR-X satellite. In each simulation are studied the effects of the number of tracks, the SNR and the presence of one or two scatterers in elevation on parameters like detection probability and velocity/displacement bias and dispersion. The noise added to obtain a certain SNR leads to a circular Gaussian complex amplitude fluctuating from one look to another. For each SNR value, 1000 realizations of the process are simulated.

The covariance matrix was estimated using the sample covariance matrix estimator [83]. The number of neighbouring points for the estimation was chosen as a compromise between the degradation in resolution and the condition to have a positive definite estimated matrix (the number of looks used for averaging to be at least equal to the number of tracks [8]). Therefore the number of looks used in each case was the number of tracks plus one.

As described in the previous section, the detection of a scatterer at a given position relies on the presence of the highest peak in the EV plane at zero elevation. From a practical standpoint, this verification means to test on the 2D EV grid if the maximum appears at one of the zero elevation bins. In the presence of noise the maximum can very likely appear in a bin near zero elevation depending on the grid's elevation step. Consequently a tolerance should be added to the detection criterion related to the detection probability. This issue will also impose the minimum necessary elevation step of the EV grid (the maximum value is given by the Nyquist resolution divided by a possible over-sampling factor). Given these matters the detection criterion is reformulated as follows: a given point is a scattering

Table IV.1: False Alarm Probability (%)

| Accuracy \ Number of tracks | 5    | 8    | 15   |
|-----------------------------|------|------|------|
| 0.5 m                       | 0.74 | 0.60 | 0.46 |
| 2.5 m                       | 2.61 | 2.48 | 1.54 |
| 5 m                         | 5.09 | 4.95 | 3.01 |

center if the maximum in the EV plane is placed in the interval  $[-\delta s, +\delta s]$ , where  $\delta s$  is the detection accuracy. Notice that the detection accuracy is a positioning accuracy and is not related to the resolution in elevation. The elevation step of the grid can be picked as high as  $2\delta s$  for computational ease, while the velocity step should be chosen as small as possible for an accurate estimate of the displacement velocity (in the simulations was chosen 0.01 mm / time unit). The notion of detection probability used hereafter is defined as the number of detections of a scattering center in the interval  $[-\delta s, +\delta s]$  divided by the total number of realizations. In a similar manner, the false alarm probability can be viewed as the number of realizations for which the maximum value appears in the interval  $[-\delta s, +\delta s]$  divided by the total number of realizations when the data vector  $\mathbf{g}(\vec{r}_k)$  contains only noise. In the conducted analysis we considered the detection accuracies 0.5 m, 2.5 m and 5 m and the number of tracks was 5, 8 and 15. For each combination we have determined by simulation the resulting false alarm probability which is presented in Table IV.1. Notice that for a given set of acquisitions the tolerated accuracy imposes a fixed level of the false alarm probability. The results of various simulation configurations are presented in the following.

#### IV.5.3.1 One scatterer, linear motion

The first case studied is the one where there is only one scatterer which has a linear motion in line of sight (LOS). The detection probability curves vs. SNR for different accuracies and number of tracks are plotted in Fig. IV.7. Fig. IV.8a shows the dispersion of the estimated MDV and Fig. IV.8b the MDV's bias. Naturally, the detection probability and MDV bias/dispersion enhance as the number of tracks increases. The dispersion and bias of the computed displacements using (IV.18) is presented in Fig. IV.8c. The estimated elevation-velocity PSD planes for various SNRs and number of tracks are presented in Fig. IV.9 and Fig. IV.10, respectively. As expected, the noise floor of the PSD in the estimated EV plane is higher for low SNRs and the main scatterer's lobe diminishes as the number of tracks increases.

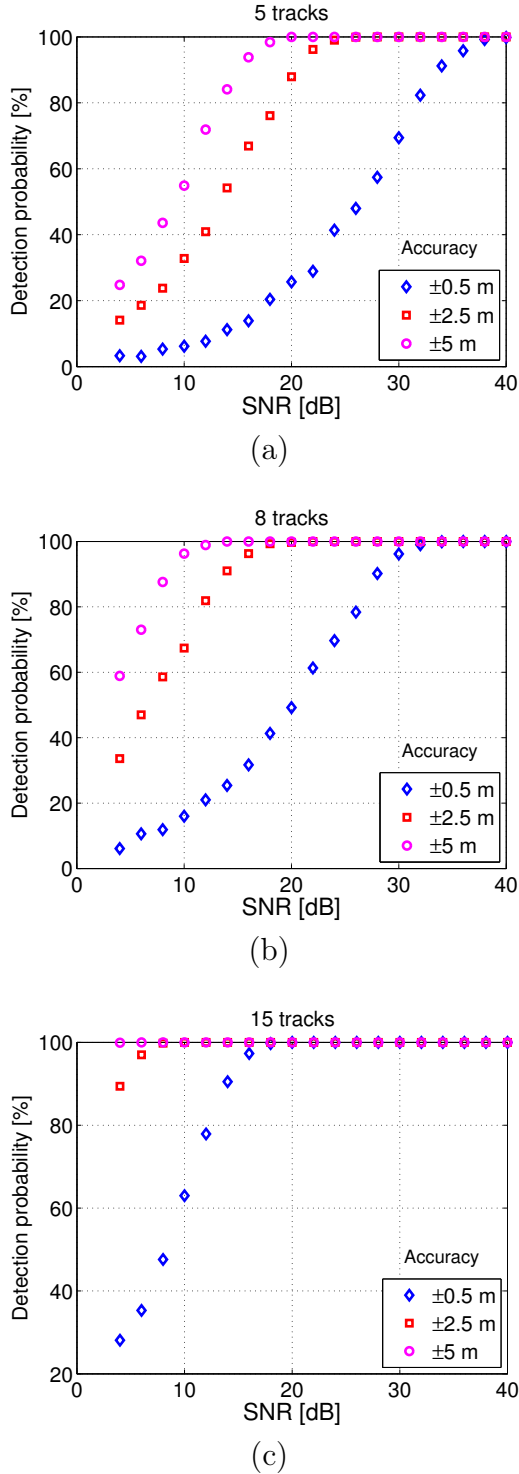


Figure IV.7: Detection probability vs. SNR for one scatterer having a linear motion in LOS. The considered accuracies are 0.5 m, 2.5 m and 5 m and the number of simulated satellite passes are: (a) 5 tracks, (b) 8 tracks, (c) 15 tracks.

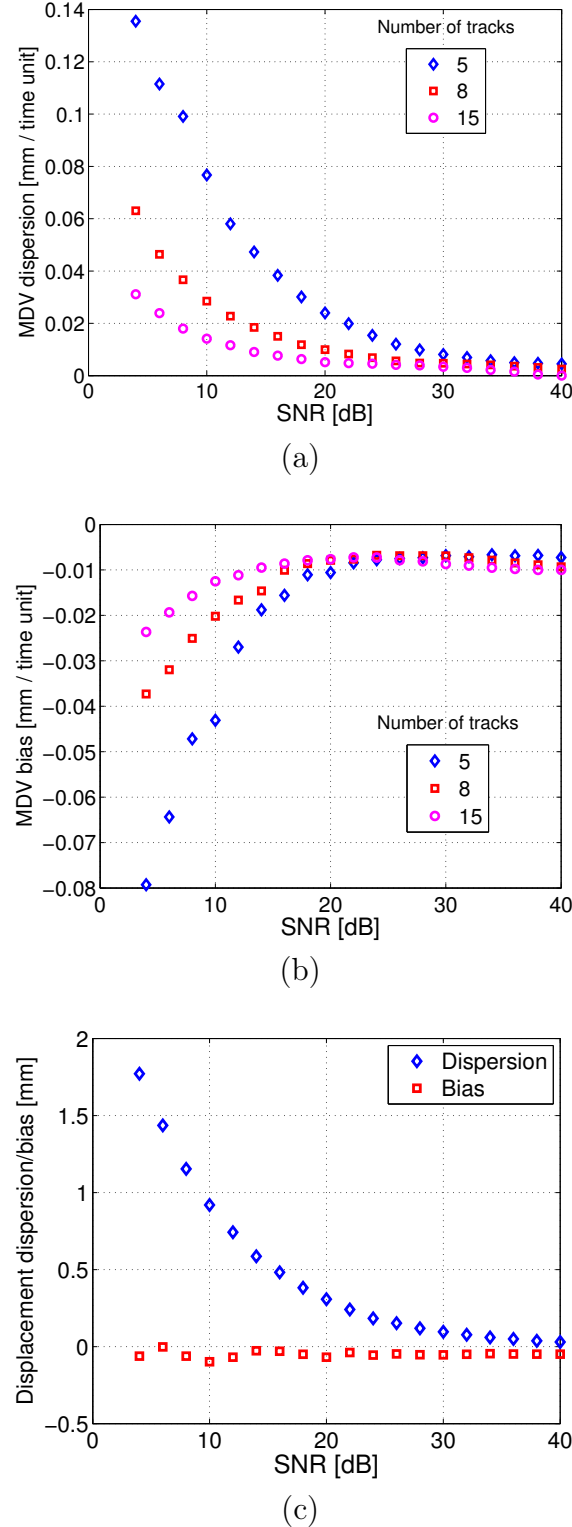


Figure IV.8: (a) Dispersion of estimated MDV, (b) Bias of estimated MDV and (c) Displacement dispersion/bias vs. SNR for one scatterer with linear motion in LOS.

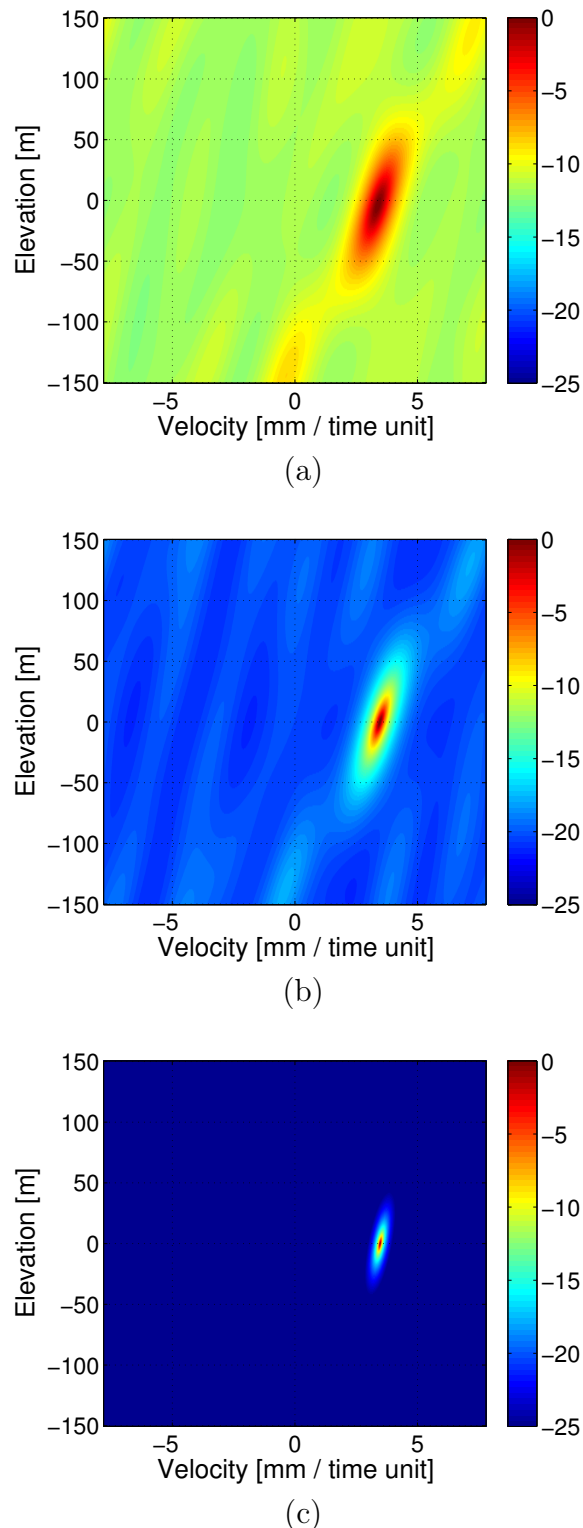


Figure IV.9: Estimated elevation-velocity PSD planes for 8 tracks and different SNRs: (a) 5 dB, (b) 15 dB, (c) 25 dB.

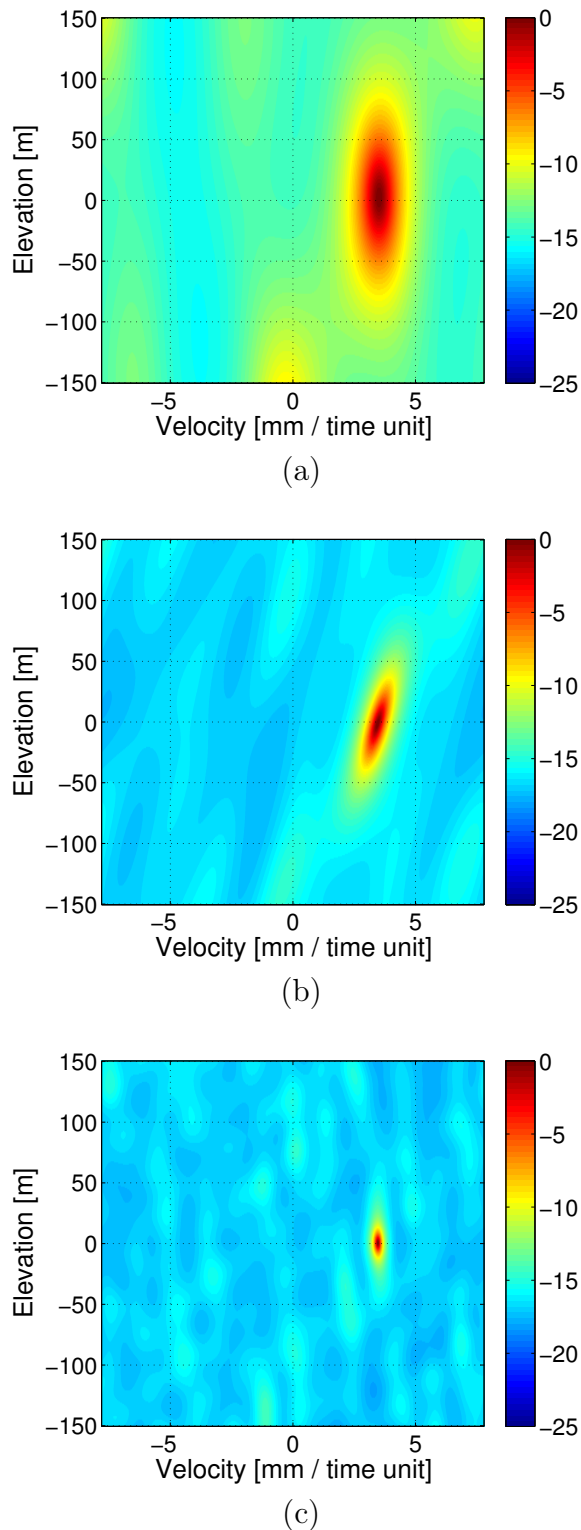


Figure IV.10: Estimated elevation-velocity PSD planes for an SNR of 10 dB and different number of satellite passes: (a) 5 tracks, (b) 8 tracks, (c) 15 tracks.

#### IV.5.3.2 One scatterer, linear trend and un-modeled nonlinear motion

For this part, un-modeled nonlinear motion is added to the scatterer simulated in the previous case. The additional motion consists in randomly generated sets of displacements having different dispersions. In each case, the mean of the nonlinear motion is subtracted in order to maintain the mean velocity of the linear motion.

Fig. IV.11 shows the impact of this change on the detection probability (using  $\pm 2.5$  m accuracy) and MDV bias/dispersion. The curves plotted for 0 mm dispersion correspond to the pure linear motion previously discussed.

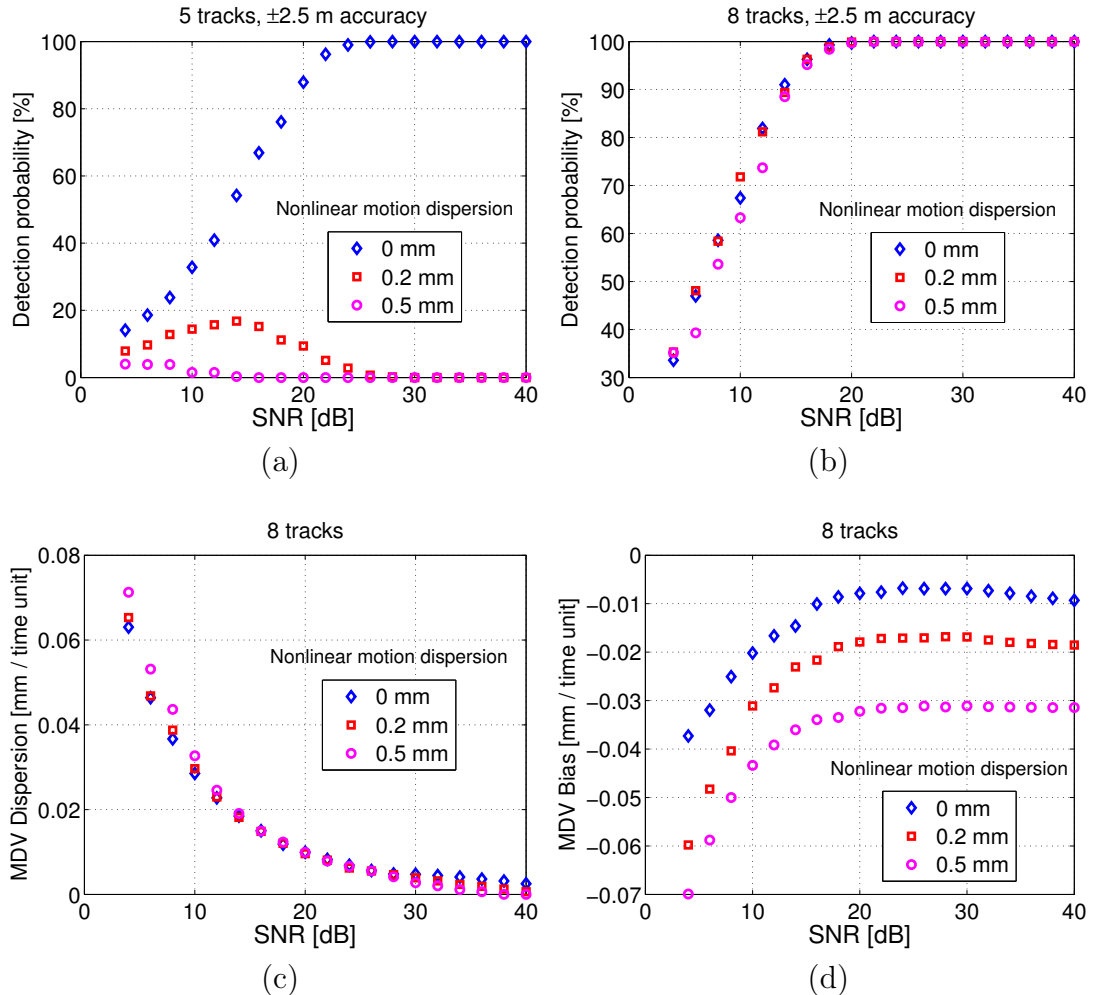


Figure IV.11: Detection probability and MDV for one scatterer having a combination of linear and un-modeled nonlinear motion in LOS. The legend signifies the dispersion of the nonlinear motion. Detection probability for (a) 5 tracks and (b) 8 tracks. MDV (c) dispersion and (d) bias for 8 tracks.

Notice in Fig. IV.11a and Fig. IV.11b that the detection probability is highly diminished by the un-modeled motion for the 5 tracks case, while for 8 satellite passes the effect is negligible. For a higher number of tracks the impact on the detection probability is similar to the 8 tracks situation.

Regarding the MDV dispersion and bias shown in Fig. IV.11c and Fig. IV.11d, besides an additional small bias the effect of the non-linear motion is insignificant provided that the necessary number of tracks for a good detection probability is available.

The dispersion and bias for the displacements time series computed like in the PSI-case are not affected by the nonlinear motion. This happens because for the displacement computation only one track is used relative to the reference one (different from the EV-plane which is estimated using all acquisitions). Hence, the dispersion/bias plots are actually the same as for pure linear motion (Fig. IV.8c).

#### **IV.5.3.3 Two scatterers in layover, linear motion**

In this scenario, as shown in Fig. IV.6, a second scatterer (target 2) is placed in layover with the one of interest (target 1). The effect of the second scatterer on the detection and tracking of the main target is investigated for different amplitudes of target 2 (relative to target 1).

Fig. IV.12 shows the simulation outcome for the two scatterers case. The detection results for a small number of tracks are very sensitive to the presence of the other scatterer and consequently the tracking results are presented only for the 15 passes case.

Fig. IV.13 shows the estimated PSD in the EV planes (at 20 dB SNR) for different relative amplitudes. Notice that the second scatterer fades when its amplitude decreases, but the EV plane noise floor gets quite high in its presence and taking into account the EV planes aspect from the single scatterer cases this happens mainly due to side-lobes interaction between the two scatterers. Therefore a pertinent criterion for the single scatterers identification is to have only one significant peak at zero elevation and any other local maximum to be much lower than it (e.g. a value of 10 dB is appropriate in the simulated cases).

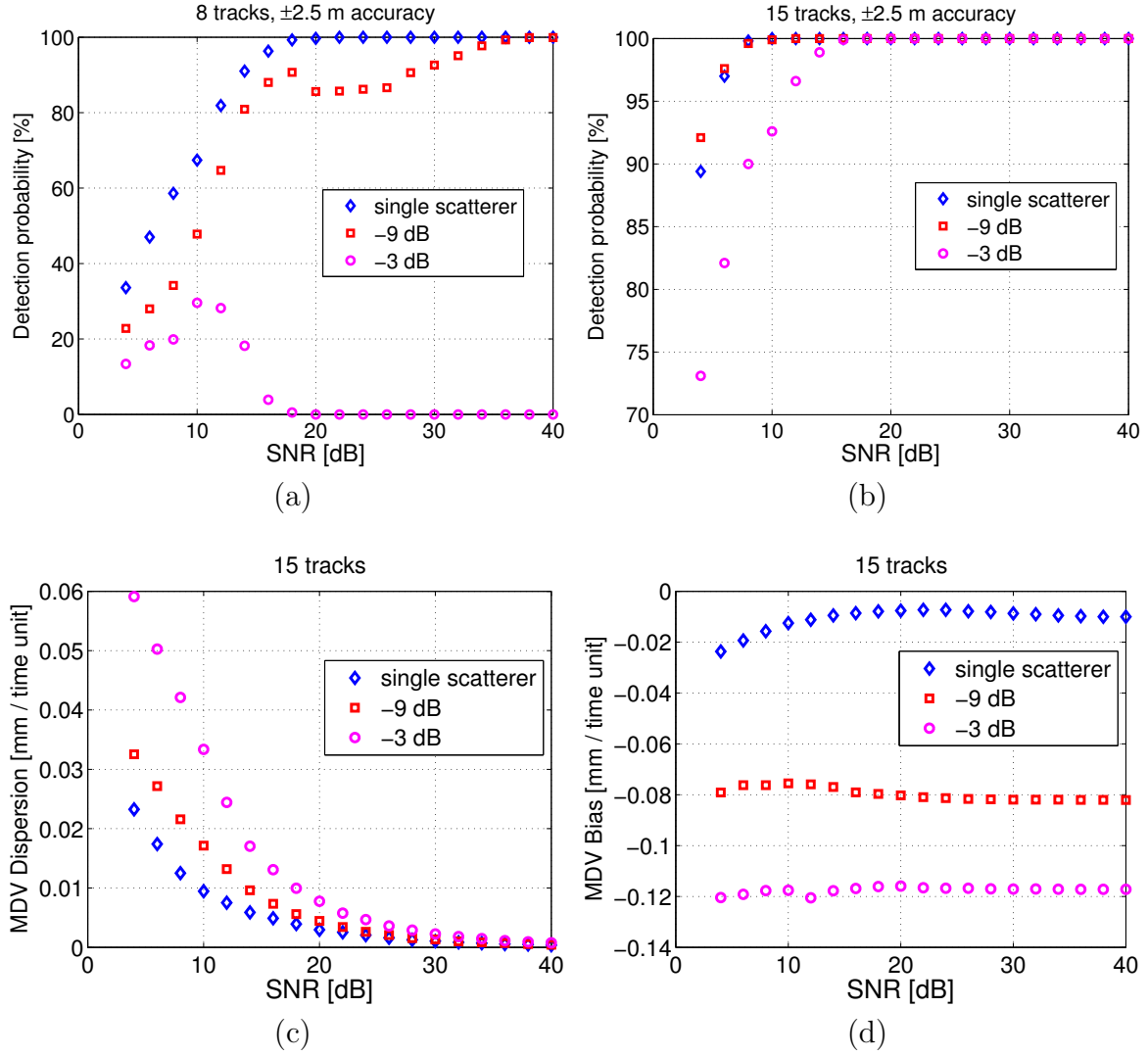


Figure IV.12: Detection probability and MDV for two scatterers (a second target placed in layover with the main one). The legend signifies the amplitude of the second scatterer relative to the main one. Detection probability for (a) 8 tracks and (b) 15 tracks. MDV (c) dispersion and (d) bias for 15 tracks.

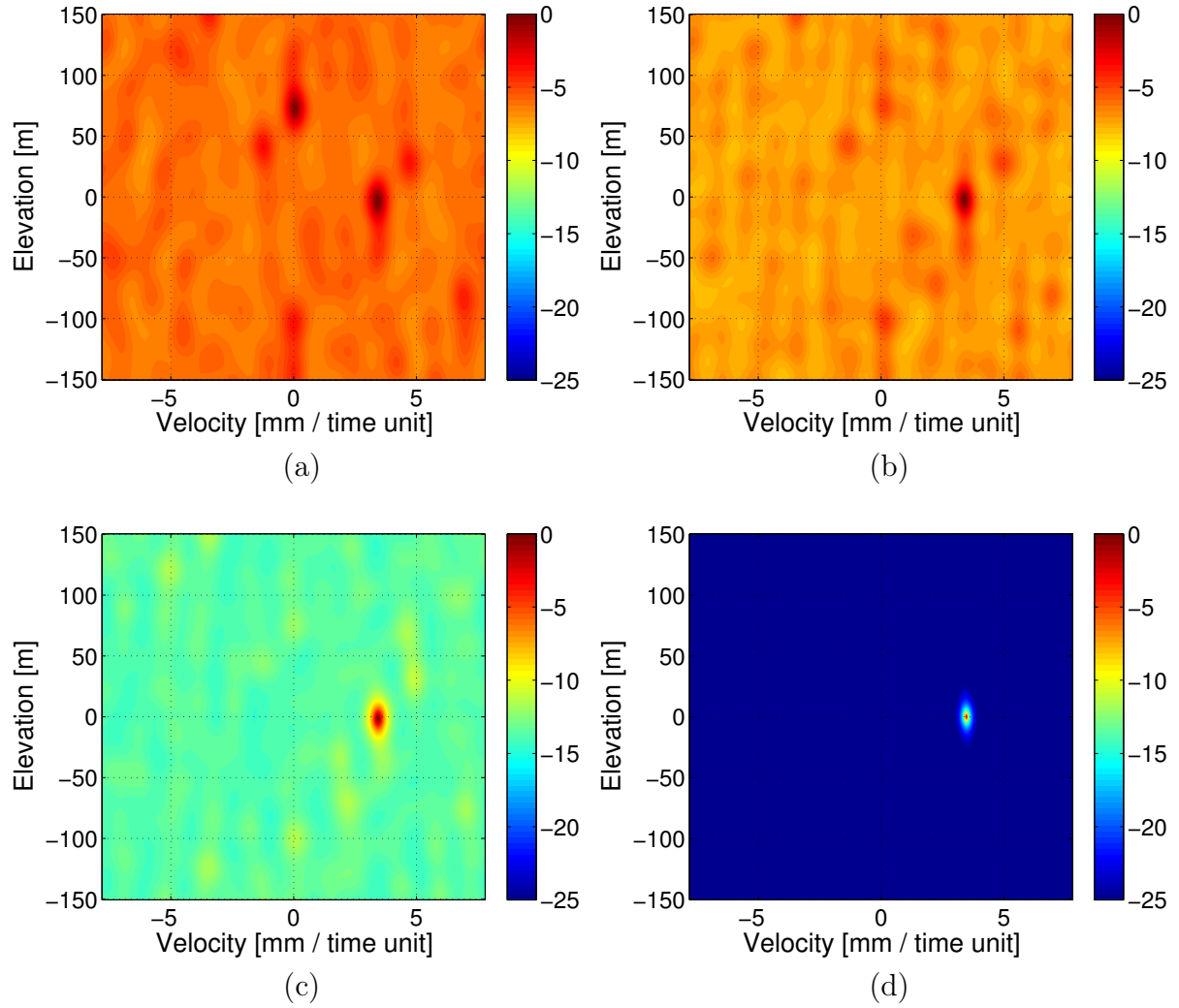


Figure IV.13: Estimated elevation-velocity PSD planes for 15 tracks, SNR of 20 dB and different amplitudes of the second scatterer relative to the main one: (a) 0 dB, (b) -3 dB, (c) -9 dB, (d) single scatterer

### IV.5.4 Position test vs. Classical scatterers identification

In this subsection we compare the proposed position test detection of scattering centers in the given grid with two classical tools used to identify scatterers in stacks of SAR images -the permanent scatterers (PS) selection based on temporal amplitude stability [84] and the generalized likelihood ratio test (GLRT) for single scatterers in multidimensional SAR imaging [67].

The PS selection method is based on comparing the phase standard deviation of a certain pixel in a stack of multi-baseline/multi-temporal SAR images with a certain threshold. The phase deviation is typically estimated from the temporal amplitude stability, usually called dispersion index. The detected scatterers are the ones having the dispersion index below a given value. This approach does not employ spatial multi-looking and is appropriate for detecting single scatterers with deterministic behavior (e.g., point-like scatterers from man-made structures). However, it requires a large time span and dozens of images for good detection results.

The GLRT target detector proposed in [67] performs the detection in the elevation-velocity plane by exploiting both the amplitude and the phase contained in the received signal, which allows it to achieve better detection performances compared to classical PSI techniques (e.g., the single pixel multi-interferogram complex coherence [85]) that match only the phases of the received signal to the corresponding steering vector.

Both the PS selection and the GLRT detector test if a reliable scatterer is present in a given pixel, but are not meant to incorporate in the decision a provided digital elevation model of the imaged scene and to check if the reflection comes or not from a certain point. On one hand, the dispersion index used for PS selection is a ratio between dispersion and mean of a pixel's amplitude and does not use other information. On the other hand, the GLRT decision statistic is able to include external positioning information through the baselines involved in the steering vectors definition (which depend on the chosen ground reference), but the detector tests if the peak in the EV plane is a reliable scattering center, disregarding its position in elevation. Contrariwise to the PS selection and GLRT, the zero elevation position test exploits the externally provided DEM or point cloud and simply checks if the peak is at zero elevation for the refocused stack of images.

In the following, we compare the three methods through Monte Carlo simulations on a similar scenario to the one presented in the previous subsection (Fig. IV.6) for 15 tracks and 2.5 m elevation accuracy. In Fig. IV.14 we plot the detection probabilities for the same false alarm rate (1.54% as given in Table IV.1 for the considered configuration) when the methods are comparable (i.e., in the position of the considered pixel there is one real scatterer).

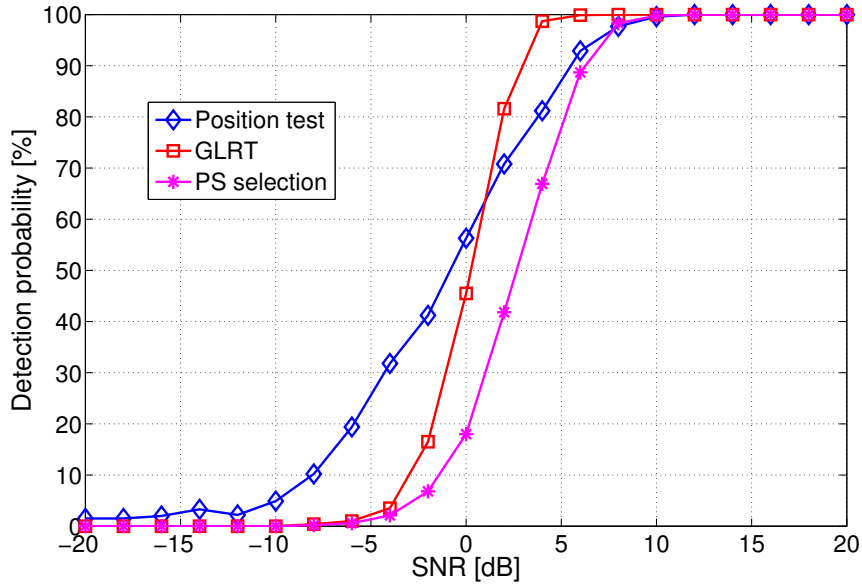


Figure IV.14: Detection probability comparison between Position test, GLRT and PS selection for a single on-grid scatterer with an MDV of 1 mm/time unit, 15 tracks and 2.5 m elevation accuracy.

The position test has a better detection probability at negative SNRs and is situated between the GLRT and the PS selection for small positive SNR values. Above 10 dB all the methods perform in a similar manner in this test case.

The analysis performed in the previous subsection revealed that in the presence of a target in layover, for a reduced number of passes, the detection probability of the position test can dramatically decrease and the estimated deformation velocities of still detected scatterers tend to be biased and dispersed. Consequently, from the perspective of infrastructure monitoring the pixels affected by layover should be rejected because they cannot provide accurate information on the scatter's displacements. In a great measure, the layover rejection naturally happens for the position test because the interaction in the elevation-velocity plane between a target in layover and the one on the grid (graphically shown in IV.13) easily shifts the peak outside the tolerated accuracy around the zero elevation position. To emphasize this aspect we performed a simulation to determine the layover rejection probability (the number of times the detection criterion is not met in the presence of a target in layover) versus the amplitude ratio between the layover target and the on-grid scatterer. We considered 50 m elevation and zero velocity for the target in layover, which is in keeping with the layover configuration that can appear for the real data presented in the applied part of the thesis. The SNR was 15 dB in order to have similar detection probabilities in the absence of layover. The results for the three methods are presented in Fig. IV.15.

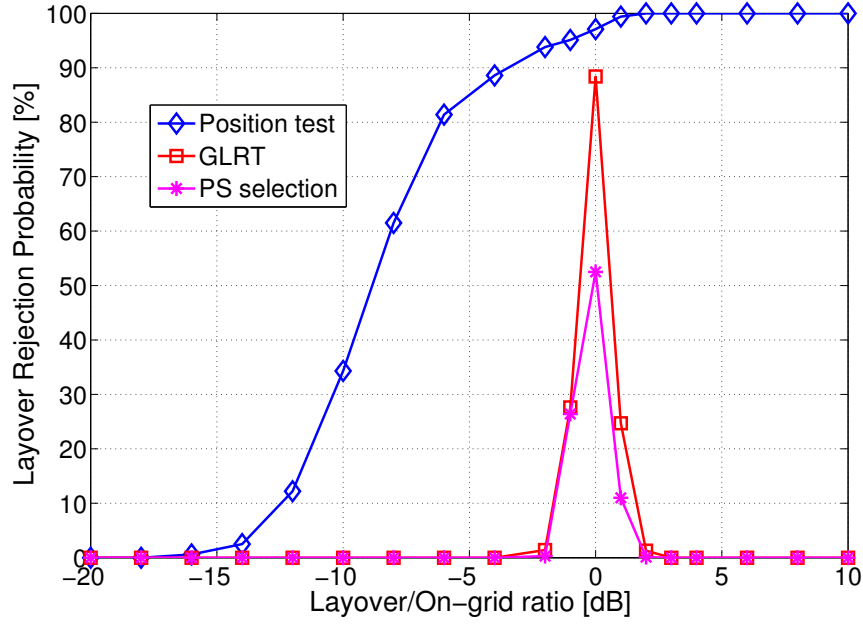


Figure IV.15: Layover rejection comparison between Position test, GLRT and PS selection for a scatterer in layover placed at 50 m in elevation and an SNR of 15 dB.

The position test starts rejecting on-grid scatterers affected by layover from an amplitude ratio of around -15 dB. For positive amplitude ratios the rejection is obvious, since the peak in the EV plane becomes the target in layover. The other methods reject the layover only when the two amplitudes are more or less equal. This behavior seems consistent with the fact that PS selection and GLRT do not take into account the peak's position, and the rejection is due only to the mismatch between the single target model and the signal vector containing two similar responses.

In summary, using the auxiliary information provided by the digital elevation model, the position test can inherently reject layover with quite high probability even for low amplitude ratios. This is an asset in deformation monitoring since these type of scatterers will have a biased MDV and are not reliable.

## IV.6 Conclusions

A 4D tomography based scattering centers detection and tracking procedure for refocused SAR images on a provided grid was presented in this chapter. The performances and limitations of the method were analyzed by simulations for various scenarios. The method is well suited for detecting slowly moving scattering centers from a provided 3D grid, selecting the scatterers unaffected by layover and computing their displacements.

In the following we reiterate a few key points which show that the presented methodology differs from state of the art through several aspects both conceptual and in terms of implementation.

First of all, the usual approach for interferometric processing of SAR images is to identify the pixels which contain the response of stable natural reflectors or permanent scatters [84, 85, 86, 87] and afterwards to link its position to a possible known scatterer on the ground. This linking is done either by knowing a scatter's approximative position (e.g., a corner reflector mounted in a weakly reflecting environment) or by explicit geocoding. In our method, we propose a reversed approach. Having a structure given in a certain way (a regular/irregular grid or a DEM) and refocusing the SAR image on it, we observe which points of the structure provide a response to the satellite flying on a specific orbit. Additionally, from the implementation point of view, by employing the refocusing approach for each acquired image, the coregistration of the SAR images [88, 89] is implicitly performed.

The original version of the back-projection algorithm [82] is used to focus raw data with possible range cell migration, while our modified version is adapted to range compressed-azimuth defocused data where the phase history of a target is on a single column of the data matrix.

In works concerning multiple scatterers monitoring in the same pixel [9, 10, 90, 91, 92] the 4D tomography framework is used to compute the position of different scatterers in elevation relative to a reference surface and the baselines projections are the same for an azimuth line (containing pixels with same slant range). On the other hand, in our approach the differential tomography is employed to test if a given point from a grid is indeed a scatterer. Moreover, the baselines projections change from point to point in order to maintain the zero elevation property of on-grid targets.

For more complex nonlinear movement which spreads the response of a target in the EV plane an on-grid scatterer may not be correctly detected by the proposed method. Still, if the movement follows a particular model, its parameters may be integrated in the framework and estimated in an Elevation-New Parameters space using an approach like the time warp proposed in [93]. However, this is beyond the studied cases.

# Part B

## APPLIED CONTEXT



## CHAPTER V

# FMCW radar demonstrator system

---

|  |           |
|--|-----------|
| <b>V.1 Short-Range FMCW radar architecture . . . . .</b> | <b>67</b> |
| <b>V.2 Measurement results . . . . .</b>                 | <b>71</b> |
| V.2.1 HAF-based correction algorithm testing . . . . .   | 71        |
| V.2.2 Range autofocusing testing . . . . .               | 75        |
| V.2.3 Displacement Measurements . . . . .                | 78        |
| <b>V.3 Conclusions . . . . .</b>                         | <b>82</b> |

*In this chapter is described an FMCW radar experimental platform designed for infrastructure monitoring applications (displacement measurements) and the tests performed to validate the developed correction methods on short-range targets. The demonstrator system's architecture adds a few novel elements to the existing designs in the literature.*

## V.1 Short-Range FMCW radar architecture

Typical FMCW radar implementations have a homodyne architecture transceiver [94, 95] which limits the performances for short-range applications. In the case of targets positioned near the radar, the beat frequency is small and can be situated in the frequency band affected by the classical problems of the homodyne architecture (DC offset, self-mixing and 1/f noise) [96].

The short-range FMCW X-band radar presented in this chapter is based on a heterodyne architecture of the transceiver which eliminates the low frequency self-mixing spectrum [97] and reduces the noise bandwidth. In other works like [98, 99, 100, 101] the heterodyne architecture is used for S-band and X-band FMCW transceivers in order to build a hardware range-gate based on narrow-band communication filters. The range-gate is used either to eliminate from the beat signal some powerful reflections that can reduce

the receiver's dynamic range [98, 99] or just to increase the sensitivity in the range swath of interest [100].

The block diagram and a picture of the FMCW radar are shown in Fig. V.1. The sweep signal is a linear tuning voltage with 100 ms period obtained from the signal generator of an USB oscilloscope. The discrete nature of the command signal leads to a stepped frequency modulation with an unambiguous beat frequency inversely proportional to the step duration [102, 103]. The resolution of the signal generator is 12 bits which for the maximum bandwidth of 4 GHz leads to an unambiguous range of over 100 m (where the behavior is FMCW type). The RF VCO block is a low-cost X-band VCO with 15% linearity which provides the local oscillator (LO) signal. The high nonlinearity of this VCO can be software corrected and is no need of an expensive YIG-based VCO. For a linear tuning voltage, the RF VCO signal in a sweep period  $T$  can be written as:

$$s_{LO}(t) = \cos \left[ 2\pi \left( f_0 t + \frac{1}{2} \beta t^2 \right) + \Phi_{nl}(t) \right], \quad (\text{V.1})$$

where  $\Phi_{nl}(t)$  is the nonlinearity phase term,  $f_0$  is the initial frequency and  $\beta$  is the linear chirp rate. The intermediary frequency (IF) block is a direct digital synthesizer with adjustable frequency (50-250 kHz). The transmitted signal consists of two different signals obtained by mixing the LO signal with the IF signal:

$$\begin{aligned} s_T(t) = & \frac{1}{2} \cos \left[ 2\pi \left( (f_0 + f_{IF})t + \frac{1}{2} \beta t^2 \right) + \Phi_{nl}(t) \right] + \\ & \frac{1}{2} \cos \left[ 2\pi \left( (f_0 - f_{IF})t + \frac{1}{2} \beta t^2 \right) + \Phi_{nl}(t) \right]. \end{aligned} \quad (\text{V.2})$$

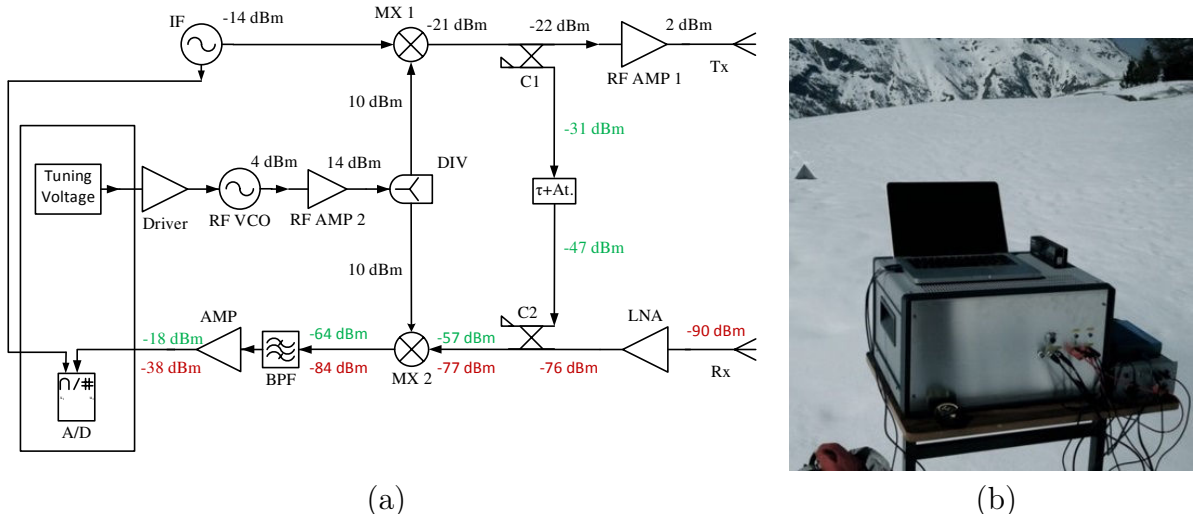


Figure V.1: Block diagram (a) and a picture (b) of the X-band FMCW radar.

## Chapter V. FMCW radar demonstrator system

---

A part of the transmitted signal gets directly to the mixer from the receiver section through the couplers ( $C_1$  and  $C_2$ ) and the delay line. This reference path is used as power level reference and for calibrating the radar with the HAF-based nonlinearity correction algorithm. In the receiver section, the reflected signal that comes from  $K$  different targets is a sum of delayed and attenuated versions of the transmitted signal  $s_T(t)$ :

$$s_R(t) = \sum_{k=1}^K A_k s_T(t - \tau_k), \quad (\text{V.3})$$

where  $\tau_k$  and  $A_k$  are the propagation delay and amplitude corresponding to target  $k$ . The received signal is mixed with the LO and the resulting low frequency signal gets centered around the IF:

$$\begin{aligned} s_{IF}(t) = & \frac{1}{4} \sum_{k=1}^K A_k \left\{ \cos \left[ 2\pi \left( (f_{IF} + \beta \tau_k) t + \right. \right. \right. \\ & \left. \left. \left. (f_0 - f_{IF}) \tau_k - \frac{1}{2} \beta \tau_k^2 \right) + (\Phi_{nl}(t) - \Phi_{nl}(t - \tau_k)) \right] + \right. \\ & \cos \left[ 2\pi \left( (f_{IF} - \beta \tau_k) t - (f_0 + f_{IF}) \tau_k + \frac{1}{2} \beta \tau_k^2 \right) - \right. \\ & \left. \left. \left. (\Phi_{nl}(t) - \Phi_{nl}(t - \tau_k)) \right) \right\}. \end{aligned} \quad (\text{V.4})$$

For short-range applications the delay is very small compared to the sweep period. In consequence the residual video phase (RVP) term [76] can be neglected and the nonlinearity phase term difference can be approximated with the derivative multiplied with the delay. Under these assumptions, the IF signal can be rewritten as:

$$\begin{aligned} s_{IF}(t) \approx & \frac{1}{4} \sum_{k=1}^K A_k \left\{ \cos \left[ 2\pi \left( (f_{IF} + \beta \tau_k) t + \right. \right. \right. \\ & \left. \left. \left. (f_0 - f_{IF}) \tau_k \right) + \tau_k \Phi'_{nl}(t) \right] + \cos \left[ 2\pi \left( (f_{IF} - \beta \tau_k) t - \right. \right. \\ & \left. \left. \left. (f_0 + f_{IF}) \tau_k \right) - \tau_k \Phi'_{nl}(t) \right) \right\}. \end{aligned} \quad (\text{V.5})$$

This signal is filtered, amplified and afterwards sampled with 1 MHz sampling rate. The IF signal spectrum consists of two groups of spectral components placed symmetrically around the intermediary frequency as presented in Fig. V.2. The analog band-pass filter (BPF: 25-500 kHz bandwidth) removes the low-frequency components (resulted from self-mixing and local oscillator leakage in the transmitted signal), improves the signal to noise ratio by reducing the noise bandwidth and acts as anti-aliasing filter. Additional digital filters can be applied to select an imposed range interval before mixing to baseband. The specifications of the wideband FMCW radar system are summarized in Table V.1.

Table V.1: Specifications of the FMCW Radar system

|                               |                     |
|-------------------------------|---------------------|
| Maximum bandwidth             | 8-12 GHz            |
| Sweep period                  | 100 ms              |
| IF frequency                  | 50 - 250 kHz        |
| VCO linearity                 | 15%                 |
| Tuning signal                 | Triangular/Sawtooth |
| Transmitted power             | 2 dBm               |
| Antenna gain                  | 17 dBi              |
| Beamwidth (azimuth/elevation) | 25°/25°             |
| Maximum range                 | 100 m               |

In order to shift the spectrum in baseband, the signal in (V.5) should be digitally multiplied with the sampled IF sinusoidal signal. The resulting beat frequency signal is (neglecting the 0.5 factors resulted from cosine multiplication):

$$s_b(t) = \sum_{k=1}^K A_k \cos \left[ 2\pi (f_0 + \beta t + \Phi'_{nl}(t)) \tau_k \right]. \quad (\text{V.6})$$

If the range profile is computed as the Fourier transform of this beat signal, the nonlinearity terms spread the energy of each target and the resolution gets deteriorated. In order to avoid this shortcoming, the beat signal is processed with the nonlinearity correction algorithms designed in the methodological part. Notice that the same beat signal as the one in (V.6) would be obtained for a homodyne architecture if we neglect the undesired low-frequency components, so the proposed correction methods can be applied to both heterodyne and homodyne architectures.

Note that in contrast to other implementations (like [101]) the proposed architecture has certain differences which start with the main reason for using the intermediary frequency (to avoid the homodyne problems, not to build a range-gate). Using a relatively large sweep period leads to a smaller frequency interval of the expected beat frequencies which implies a reduced noise bandwidth after the weighting window applied in computing the range profile (the equivalent noise bandwidth is around 15 Hz for 100 ms sweep period). Another observation is that both groups of spectral components around the IF are mixed to baseband and cumulated (not only one lateral sideband) which avoids using an image reject filter.

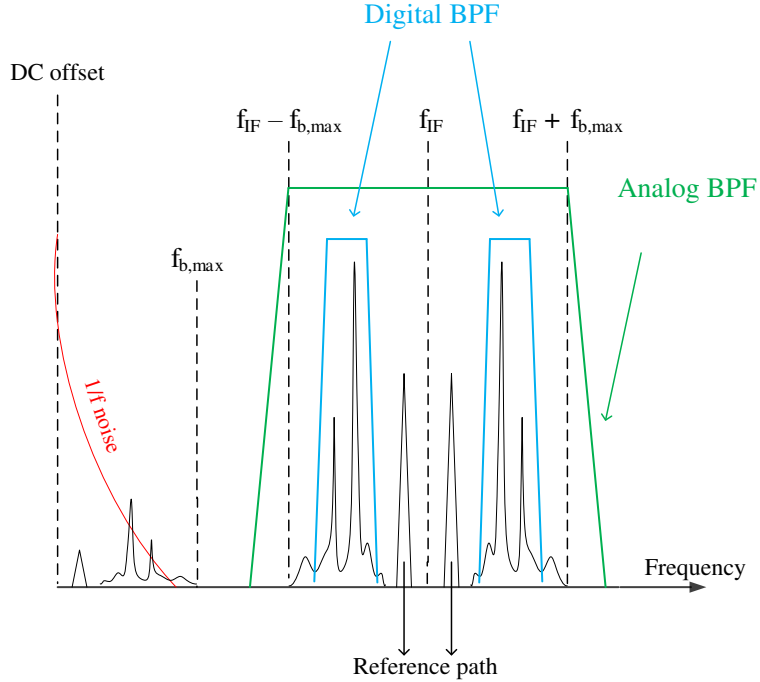


Figure V.2: Intermediary frequency signal spectrum. The analog filter removes the low-frequency components, improves the signal to noise ratio and acts as anti-aliasing filter.

## V.2 Measurement results

This section is divided in two parts: the first part validates the wideband nonlinearity correction algorithms presented in Chapter III on real data, and the second one is concerned with displacement measurements using the interferometric phase derived from range profiles and SAR images.

### V.2.1 HAF-based correction algorithm testing

The HAF-based nonlinearity correction algorithm was first tested using only the transceiver of the implemented radar system and having artificial targets obtained with delay lines and attenuators. The tuning voltage versus frequency calibration curve of the VCO was measured. The range profiles obtained with a predistorted command signal based on the calibration curve were considered as reference. A few data sets were collected under the same external conditions as for the calibration curve measurement. Two delay lines having air-equivalent lengths of 30 cm (short path) and respectively 240 cm (long path) were used as targets. The chirp bandwidth was 4 GHz and the sweep interval 100 ms.

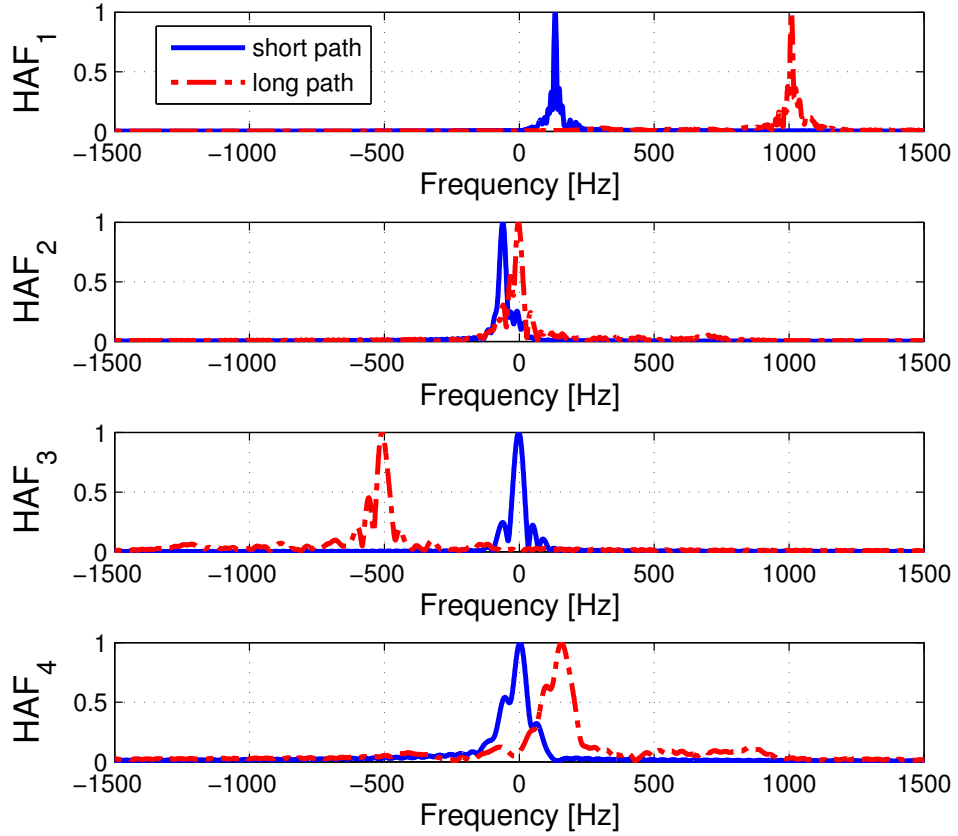


Figure V.3: High-order ambiguity functions of the beat signal for two delay lines. The continuous plots show the functions for a 30 cm air-equivalent length delay line (short path) and the dotted ones for a 240 cm air-equivalent delay line (long path).

The correction was done using both lines in order to analyze the influence of the reference response delay on the algorithm's performance. For a 4th order polynomial approximation, the HAFs plots of the FMCW coefficients in both cases are shown in Fig. V.3. The estimated coefficients were used to generate nonlinearity corrected beat signals by employing the time warping procedure. The range profiles were obtained by applying a Hamming window before the Fourier transform.

Fig. V.4 shows a comparison between the range profiles obtained for the two delay lines in different cases and the range profile obtained for the predistorted sweep (in each comparison the range profiles are normalized such that the short path peak responses have the same level). The range profile for a linear sweep is presented in Fig. V.4a. The energy of both targets is highly spread in frequency and the main lobe for the long path occupies more than 40 resolution cells (expected in view of the high degree of nonlinearity of the VCO). The range profile corrected using the short path coefficients (shown in Fig. V.4b) is similar to the predistorted sweep range profile for the short path response, but the

## Chapter V. FMCW radar demonstrator system

---

energy of the long path is still spread and there are two main lobes for the same target. This effect is linked with the HAFs for the high-order nonlinearity terms (3 and 4) in the short reference path case which are hardly noticeable and cannot be estimated properly. However, the long path calibration range profile from Fig. V.4c is very similar to the one obtained with the predistorted sweep, so the HAF-based method provides good results if the calibration path is long enough to emphasize the nonlinearities (the higher order terms to be highlighted and properly estimated).

A clear advantage of the software correction compared to the predistorted sweep technique is that the nonlinearity parameters can be computed for each sweep and can include various frequency drifts (due to temperature, frequency pushing, etc.).

The results of the range profiles comparison are summarized in Table V.2 where the -10 dB resolutions are computed for both targets. Although the resolution for the long path corrected range profile is better than for the predistorted sweep range profile there are still present some residual nonlinearities (deterministic as well as random) which have small bandwidths and whose effect increases with range. However, they can be further mitigated with methods like those presented in [46, 45, 49].

In order to validate the HAF-based nonlinearity estimation method for a multi-component response, a data set was acquired for a scene containing three main scatterers: one highly reflective metal disc and two vertical metal bars. The range profiles obtained in this case are shown in Fig. V.5. The nonlinearity coefficients are computed on the 1.2-5.2 m range interval taking as reference target the metal disc. While on the initial nonlinear range profile obtained for the linear voltage sweep appears only a large continuous target, on the corrected profile the three targets are clearly highlighted. Notice that the power reflected by the metal disc is more than 10 dB higher in comparison to the other scatterers which is in agreement with the HAF method applicability threshold.

Table V.2: HAF-based Correction Algorithm, -10 dB Resolution (4 GHz)

|                       | Short Path<br>Resolution (cm) | Long Path<br>Resolution (cm) |
|-----------------------|-------------------------------|------------------------------|
| Predistorted sweep    | 8.18                          | 8.47                         |
| Short path correction | 8.23                          | 19.87                        |
| Long path correction  | 8.17                          | 8.45                         |

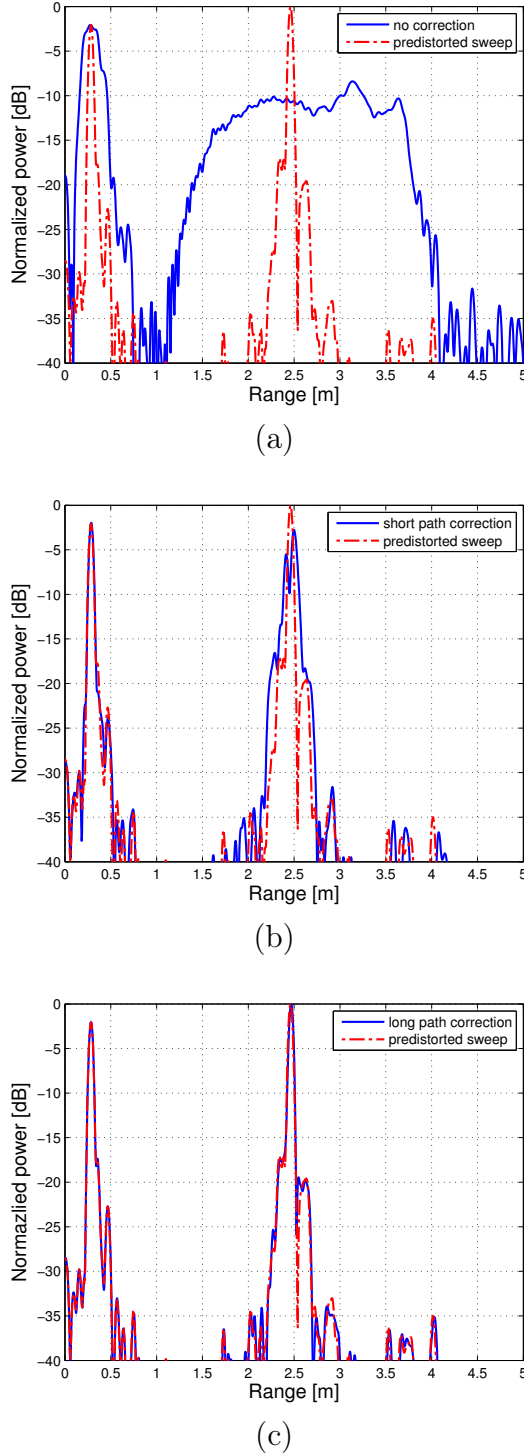


Figure V.4: Range profiles for two delay lines. The profiles obtained with a linear sweep and HAF-based correction are compared with the profile resulted for a predistorted sweep (shown with dotted line) computed from the measured frequency-voltage calibration curve. There are three cases considered: (a) no correction, (b) short path correction, (c) long path correction.

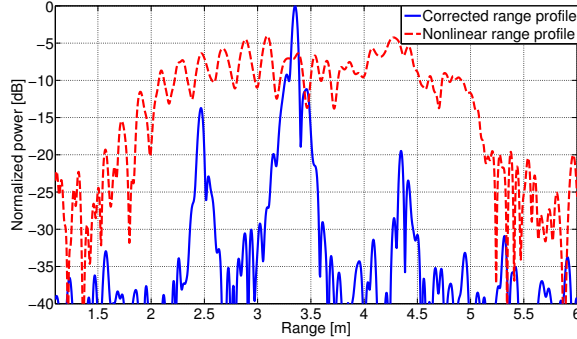


Figure V.5: Experimental range profiles for a scene containing two metal bars and one highly reflective metal disc. On the corrected range profile with the HAF-based method the three targets are clearly separated, while in the nonlinear range profile the scatterers cannot be distinguished.

## V.2.2 Range autofocusing testing

We present the testing of the range autofocusing method for a scene containing two metallic discs (placed at 0.75 m and 3.5 m from the radar). The initial and autofocused spectrograms and range profiles are shown in Fig. V.6. Initially, the targets' energies are spread in frequency, whereas after autofocusing the targets are transformed in clear peaks. The concentration measure and its evolution during the Nelder-Mead optimization algorithm is presented in Fig. V.6c. Note that the autofocusing provides good results even with the amplitude fluctuations during the sweep.

For comparison between the two methods, in Table V.3 we present the -10 dB resolutions at 3 GHz bandwidth and Hamming window obtained with the range autofocusing method for the target at 3.5 m in comparison with the resolutions obtained with the HAF-based correction method when the two targets are in turn used as reference responses. When the correction is applied on a quite different range interval than that of the considered reference target (i.e., using as reference the target placed at 0.75 m and applying the correction for the one placed at 3.5 m), the HAF-based correction is outperformed by the autofocusing approach. This aspect is in keeping with the simulation results from Chapter III.

Fig. V.7 presents the results obtained after applying the range autofocusing for a synthetic aperture image acquired by moving the FMCW radar on a 30 cm rail. The scene in the synthesized image contained some metal bars and one highly-reflective metal disc. The software nonlinearity correction was employed by resampling each line of the initial image before applying the back-projection algorithm [104] to obtain the SAR image. Notice that in the image from Fig. V.7a the targets cannot be distinguished while in the corrected version they are all clearly range focused (Fig. V.7b).

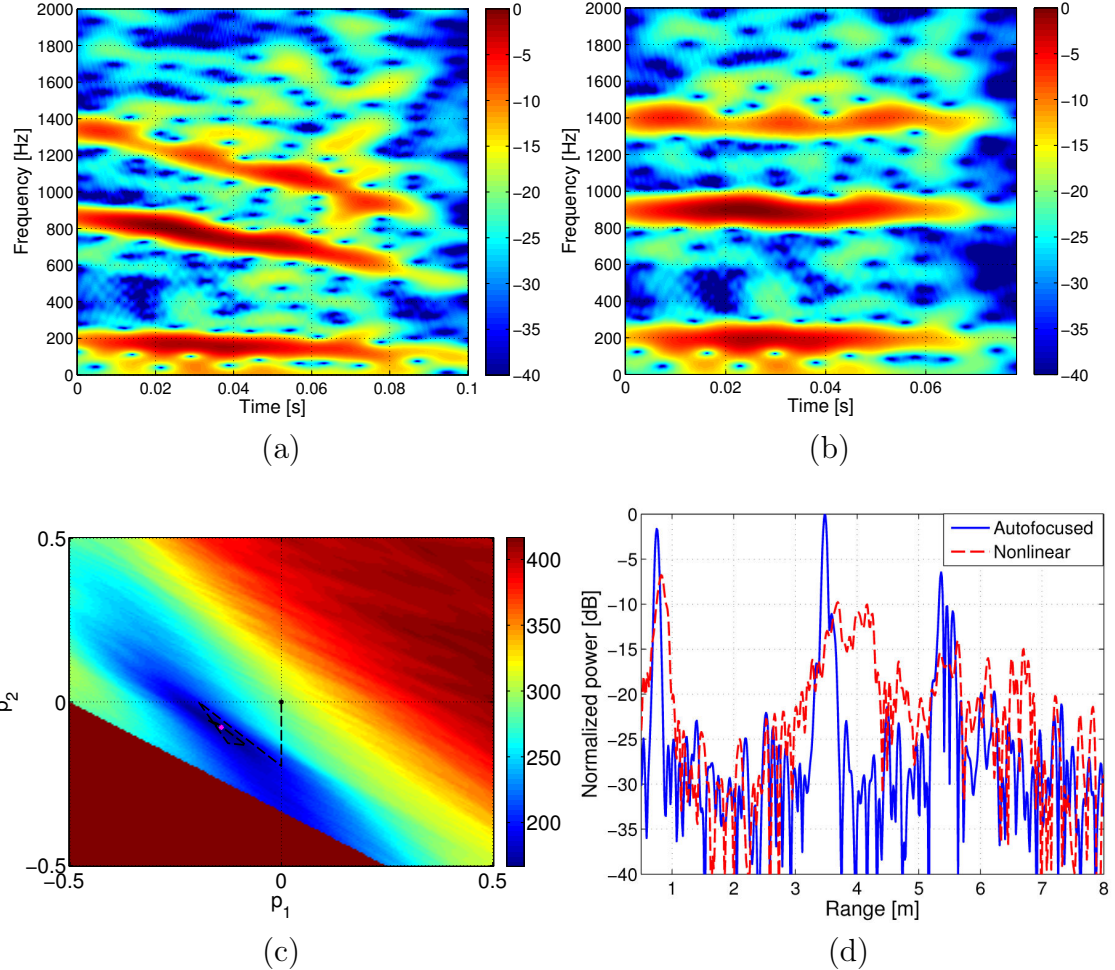


Figure V.6: Experimental results obtained with the range autofocusing method. (a) Spectrogram of the initial beat signal. (b) Spectrogram of the corrected beat signal after autofocusing. (c) Spectral concentration measure and the trajectory described by the parameters in the optimization algorithm. (d) Autofocused range profile compared to the initial (nonlinear) one.

Table V.3: Nonlinearity Correction Algorithms, -10dB Resolutions Comparison (3 GHz)

| Algorithm             | Resolution (cm) |
|-----------------------|-----------------|
| Autofocusing          | 12.43           |
| HAF, 3.5 m reference  | 12.45           |
| HAF, 0.75 m reference | 15.15           |

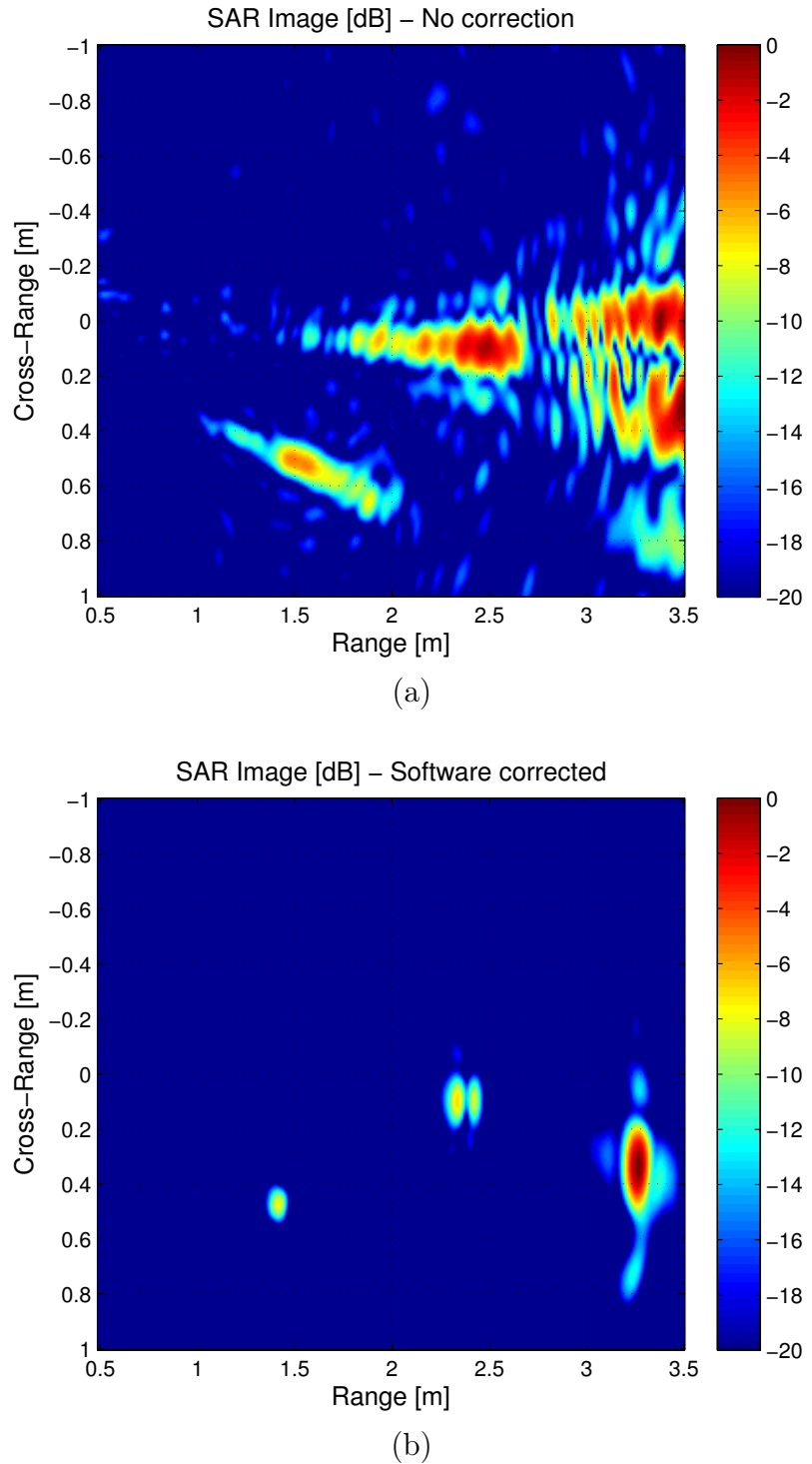


Figure V.7: Results of the nonlinearity correction applied to a FMCW radar image before azimuth focusing. In the SAR image affected by the VCO's nonlinearity (a) the targets are almost indistinguishable, while in the corrected image (b) the targets are clearly separated.

### V.2.3 Displacement Measurements

A set of simulations based on the FMCW platform's parameters was carried out in order to determine the expected theoretical accuracy of the displacement measurements. In each simulation were generated two noisy and nonlinearity corrected range profiles containing one and the same target with a given radar cross section. The target's distance from the radar in the two range profiles differed with 1 mm. The measured displacement was the one obtained from the phase difference of the target's complex amplitudes in the two range profiles. The error was computed as the difference between the 1 mm real value and the measured one. For each simulation, the SNR was computed as the ratio between the target's peak response and the noise floor value (which for a range profile is the noise power computed in the equivalent noise bandwidth of the weighing window used before the Fourier transform). For each SNR value, the error's dispersion was computed over 1000 realizations of the two range profiles. The relationship between the displacement error dispersion and the SNR for targets placed at 2 m and 50 m is plotted in Fig. V.8. Notice that for SNRs greater than 25 dB the displacement measurement error should theoretically stay below 0.1 mm.

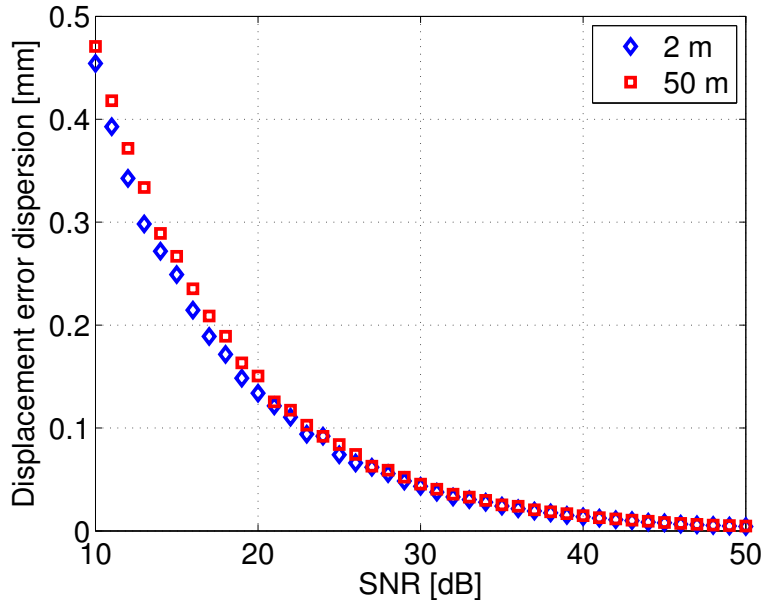


Figure V.8: Simulated displacement error dispersion vs. SNR for targets placed at 2 m and 50 m. The expected measurement error should get below 0.1 mm for SNRs higher than 25 dB.

## Chapter V. FMCW radar demonstrator system

---

The displacement measurements with the FMCW radar were made using both range profiles and synthetic aperture images for the 3 GHz bandwidth. The results are presented in the following.

### V.2.3.1 Range profiles based displacements

Different targets such as metal bars and corner reflectors were placed in front of the radar at various ranges (1-6 m). The displacement measurements were conducted as follows. One target was placed at a certain distance from the radar and the range profile was computed after cumulating the received signal over 10 sweep periods. Afterwards, the target was displaced with a few millimeters using a caliper based device (with 0.02 mm accuracy) bonded to the target and another range profile was obtained. Due to the very small displacement in range, the target will most likely be in the same range bin in both measurements, but the phase from that bin differs proportionally with the displacement. If the range bin is not the same and the displacement is unambiguous (e.g., is lower than half the wavelength corresponding to the central frequency), the displacement is still obtained as a phase difference, but between the phases of the corresponding range bins from the two acquired range profiles. Anyway, the displacement is evaluated using the interferometric phase  $\phi$  of the FMCW complex range profile:

$$\delta r = \frac{c}{4\pi f_c} \phi, \quad (\text{V.7})$$

where  $\delta r$  is the displacement. The measured displacements and their corresponding absolute errors in a few measurements are summarized in Fig. V.9a. The displacements errors are below 0.1 mm which is in keeping with the SNR of over 30 dB (as resulted from the range profiles).

### V.2.3.2 SAR Images based displacements

The measurement procedure for the SAR images based displacements was similar to the one described in the previous part, but the experimental setup was the one used to obtain the nonlinearity corrected SAR image from Fig. V.7b. In turn, one of the targets was moved on different directions between image acquisitions and the displacement was projected on the local line of sight (LOS) direction. Due to the short range the projection angle was different from one target to another.

The complex correlation coefficient  $c = \rho \exp(j\phi)$  was computed for each pair of SAR

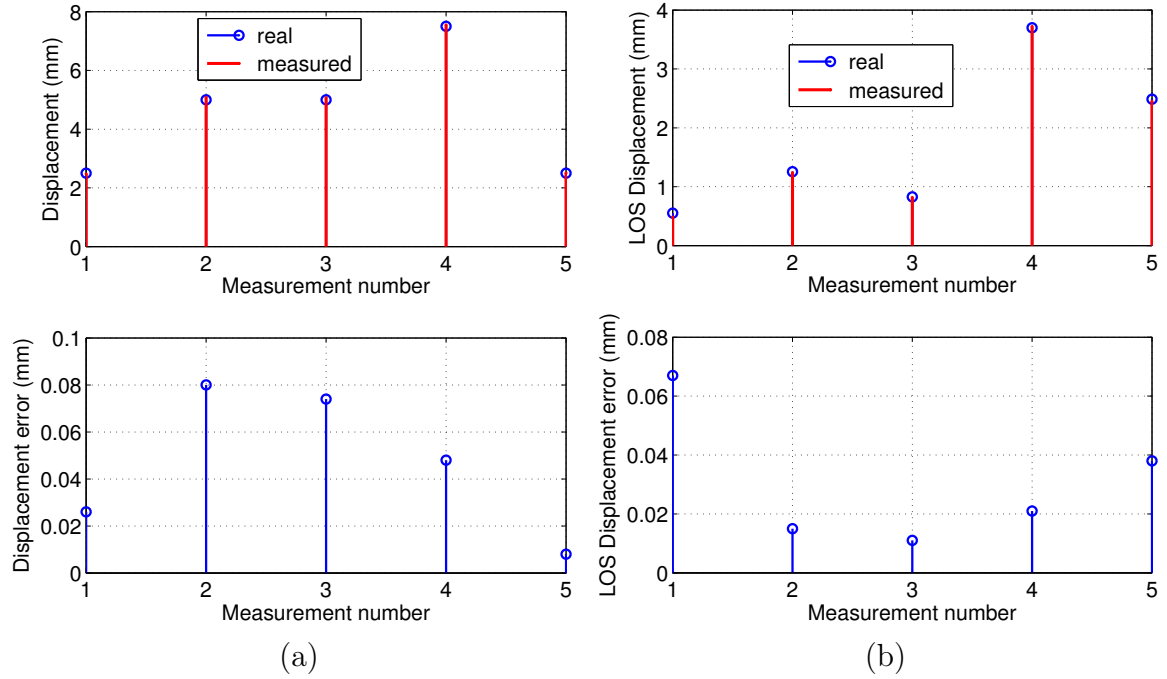


Figure V.9: Displacement measurements results from: (a) Range profiles and (b) SAR Images.

images as [105]:

$$c = \frac{\sum_{i=1}^L z_{1i} z_{2i}^*}{\sqrt{\sum_{i=1}^L |z_{1i}|^2} \sqrt{\sum_{i=1}^L |z_{2i}|^2}}, \quad (\text{V.8})$$

where  $L$  is the number of samples used for spatial averaging and  $z_{1i}, z_{2i}$  are the complex numbers (pixels) corresponding to sample  $i$ . The magnitude  $\rho$  of the correlation coefficient is the interferometric coherence and describes the phase stability within the estimation neighborhood [86]. The LOS displacements between two SAR images were computed from the phase of the correlation coefficient (the interferometric phase) using (V.7). The coherence and interferogram computed for two SAR images with a 3x3 pixels boxcar are shown in Fig. V.10. Notice that in the proximity of the metal targets the coherence is around unity and the phase has approximatively constant value. This is linked to the fact that for the considered experimental setup, there are actually a few scatterers in a resolution cell located in the vicinity of the metal targets which leads to a less perceptible clutter. Fig. V.9b shows a few measured LOS displacements and the corresponding absolute errors.

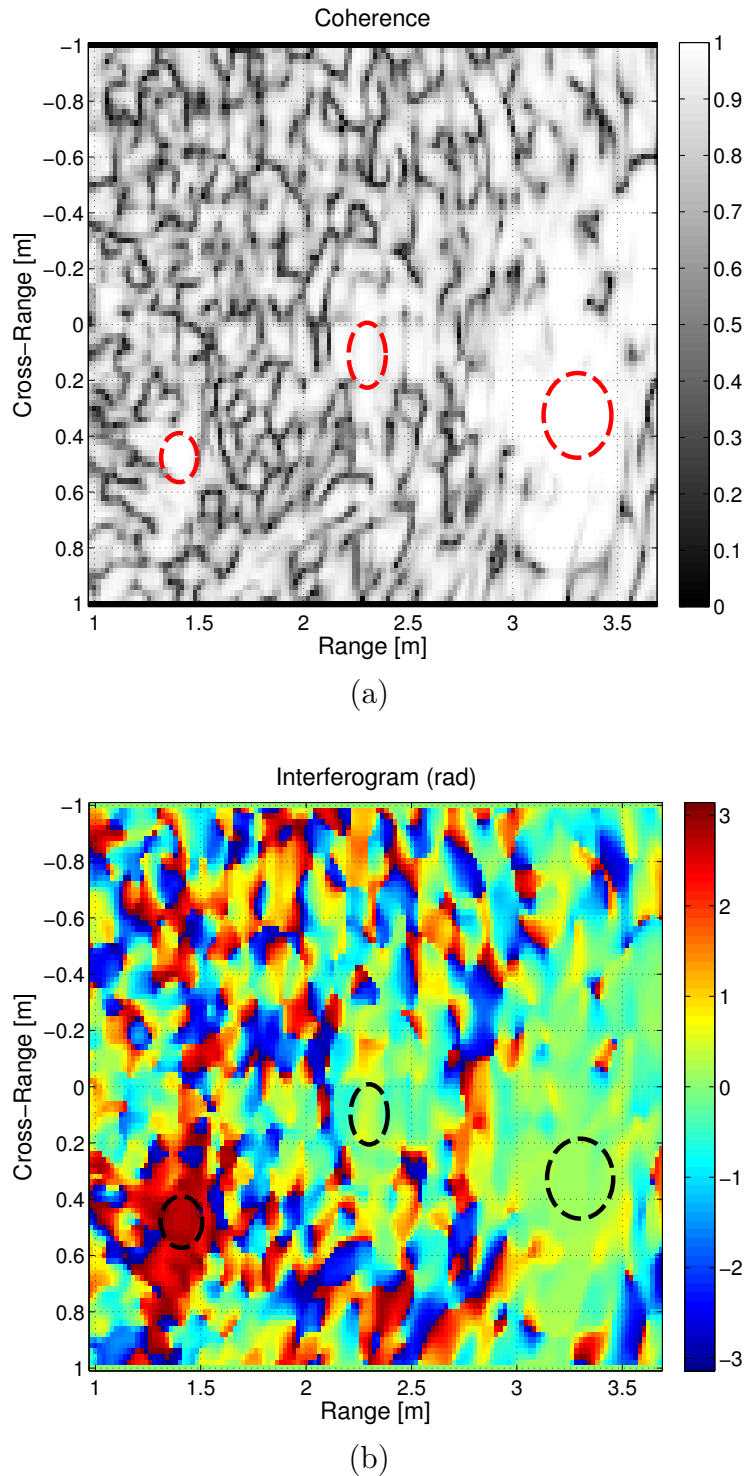


Figure V.10: Coherence (a) and interferogram (b) of two acquired SAR images computed with a 3x3 boxcar. The coherence is almost 1 and the phase has approximatively constant value in the proximity of the metal targets (marked by the dotted ellipses).

### V.3 Conclusions

In this chapter was presented an X-band FMCW radar used for displacements measurement of short-range targets. The radar's transceiver is based on an intermediary frequency architecture in order to avoid the specific homodyne problems and enhance the system's sensitivity.

The system was used to validate the wideband nonlinearity correction methods presented in the first part of the thesis. The improvements due to the nonlinearity correction are clearly highlighted in the range profiles and the SAR images obtained with the FMCW radar system.

The radar's measurement capabilities were validated on the data sets acquired for various targets. The displacements errors were submillimetric for metallic targets placed at a few meters from the radar. In the future this radar platform will be used for infrastructure monitoring applications.

## CHAPTER VI

# Combining SAR data with 3D Point Clouds of Large Infrastructures

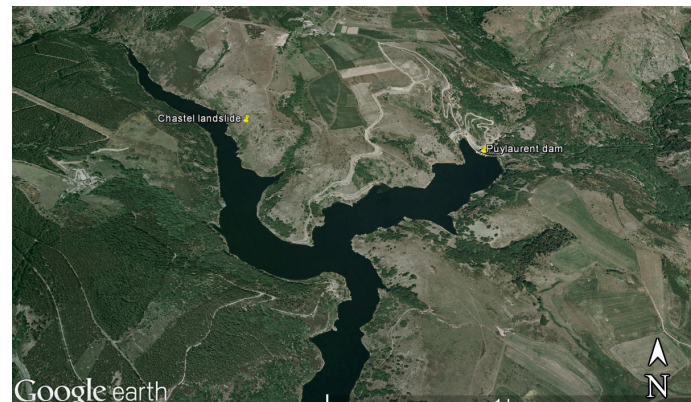
---

|   |            |
|---|------------|
| <b>VI.1 Test site and Data description . . . . .</b>      | <b>83</b>  |
| VI.1.1 SAR data . . . . .                                 | 85         |
| VI.1.2 Point Clouds generation . . . . .                  | 85         |
| VI.1.3 In-situ measurements devices . . . . .             | 91         |
| <b>VI.2 SAR data and Point Cloud processing . . . . .</b> | <b>93</b>  |
| <b>VI.3 Deformation measurements . . . . .</b>            | <b>101</b> |
| VI.3.1 Chastel landslide . . . . .                        | 101        |
| VI.3.2 Puylaurent dam . . . . .                           | 108        |
| <b>VI.4 Conclusions . . . . .</b>                         | <b>113</b> |

*In this chapter, we present the main results obtained in a set of measurement campaigns carried out between 2013-2014 at two test sites in France: the Puylaurent water-dam and the Chastel landslide. The purpose of the campaigns was to validate on real data the proposed infrastructure monitoring method based on combining SAR data with externally measured 3D point clouds describing the respective structure.*

## VI.1 Test site and Data description

The test site is located in France, in the Lozère region. It is composed from two infrastructure elements (Fig. VI.1): the Puylaurent water-dam placed at  $44^{\circ}31'47''N, 3^{\circ}53'13''E$  with the ridge height at about 943 m above sea level (ASL) and the Chastel landslide centered at  $44^{\circ}31'52''N, 3^{\circ}52'28''E$  with an ASL height between 940-1020 m.



(a)



(b)



(c)

Figure VI.1: Test site in the Lozère region: (a) Google Earth image, (b) Puylaurent water-dam, (c) Chastel landslide.

### VI.1.1 SAR data

In this study, two different sets of SAR images are chosen to investigate the feasibility of the refocusing and tomographic detection technique in order to extract displacements of the two areas. Each SAR image is acquired in high-resolution (300 MHz bandwidth) sliding spotlight mode by the TerraSAR-X or TanDEM-X satellites and consists of a single look slant-range projected complex (SSC) product. The data sets cover the period 2013-2014 and were provided through the TanDEM-X mission. The data set acquired from the descending orbit comprises 22 SAR images covering the period April 2013-December 2014, while the one from the ascending orbit is composed of 19 SAR images captured during May 2013-December 2014.

A particularity of the data sets is that the SAR images are obtained from experimental products acquired either by the TerraSAR-X or the TanDEM-X satellites in various acquisition modes (monostatic, pursuit monostatic and alternating bi-static). However, the actual SAR image used in processing is the monostatic image existing in each delivered product. In the case of pursuit monostatic mode, in the delivered product there are two mono-static co-registered images acquired independently by the two satellites. The image used in the proposed processing is the master image (denoted MON1). In the alternating bistatic case, there are four co-registered images acquired at a single pass (two monostatic and two bistatic), but the image used for processing is the monostatic active channel (denoted BTX1). Although the extra images available for some passes may slightly increase the tomographic elevation-velocity profile reconstruction performance, the refocusing method is not suited to already co-registered images or equivalent phase centers placed in-between orbits (like in the case of bistatic acquisitions). Moreover, from an operational point of view, infrastructure monitoring will be performed with sensors that provide one mono-static image at each pass. The acquisition dates and different particularities of the data sets are summarized in Table VI.1.

### VI.1.2 Point Clouds generation

This subsection presents the topography and lasergrammetry surveys performed by the Électricité de France (EDF) company on the Chastel landslide and on the Puylaurient dam in order to obtain a point cloud of each of these two zones in a global geodesic system compatible with the system in which the state vectors of the satellite data are provided.

The measurements were realised between 8-11 July 2013 using a LEICA TS30 total station, a RIEGL VZ-400 laser scanner, GPS receivers, prisms and a nadir lens. All fixed points were positioned using the nadir lens to ensure the centering on the physical ground points. The fixed points recordings were simultaneously performed for the two

## High-Resolution SAR Signal Processing for Infrastructure Monitoring

---

Table VI.1: 2013-2014 High-Resolution TerraSAR-X/TanDEM-X Sliding Spotlight SAR Images

| (a) Descending orbit, Spot 055 |            |            |           | (b) Ascending orbit, Spot 079 |            |            |           |
|--------------------------------|------------|------------|-----------|-------------------------------|------------|------------|-----------|
| No.                            | Date       | Image type | Satellite | No.                           | Date       | Image type | Satellite |
| 1                              | 11.04.2013 | SSC-BTX1   | TSX       | 1                             | 21.05.2013 | SSC-BTX1   | TDX       |
| 2                              | 25.05.2013 | SSC-BTX1   | TSX       | 2                             | 01.06.2013 | SSC-MON1   | TDX       |
| 3                              | 05.06.2013 | SSC-BTX1   | TSX       | 3                             | 12.06.2013 | SSC-MON1   | TDX       |
| 4                              | 16.06.2013 | SSC-BTX1   | TSX       | 4                             | 26.07.2013 | SSC-MON1   | TDX       |
| 5                              | 27.06.2013 | SSC-BTX1   | TSX       | 5                             | 17.08.2013 | SSC-BTX1   | TDX       |
| 6                              | 19.07.2013 | SSC-BTX1   | TSX       | 6                             | 28.08.2013 | SSC-BTX1   | TDX       |
| 7                              | 30.07.2013 | SSC-BTX1   | TSX       | 7                             | 11.10.2013 | SSC-BTX1   | TDX       |
| 8                              | 15.10.2013 | SSC-MON1   | TSX       | 8                             | 22.10.2013 | SSC-BTX1   | TDX       |
| 9                              | 02.02.2014 | SSC-MON1   | TSX       | 9                             | 27.12.2013 | SSC-BTX1   | TDX       |
| 10                             | 13.02.2014 | SSC-MON1   | TDX       | 10                            | 09.02.2014 | SSC-BTX1   | TDX       |
| 11                             | 18.03.2014 | SSC-MON1   | TDX       | 11                            | 28.09.2014 | SSC        | TDX       |
| 12                             | 30.08.2014 | SSC        | TSX       | 12                            | 09.10.2014 | SSC        | TSX       |
| 13                             | 10.09.2014 | SSC        | TSX       | 13                            | 20.10.2014 | SSC        | TSX       |
| 14                             | 02.10.2014 | SSC        | TSX       | 14                            | 31.10.2014 | SSC        | TSX       |
| 15                             | 13.10.2014 | SSC        | TDX       | 15                            | 11.11.2014 | SSC        | TSX       |
| 16                             | 24.10.2014 | SSC        | TSX       | 16                            | 22.11.2014 | SSC        | TSX       |
| 17                             | 04.11.2014 | SSC        | TDX       | 17                            | 03.12.2014 | SSC        | TSX       |
| 18                             | 15.11.2014 | SSC        | TSX       | 18                            | 14.12.2014 | SSC        | TSX       |
| 19                             | 26.11.2014 | SSC        | TDX       | 19                            | 25.12.2014 | SSC        | TSX       |
| 20                             | 07.12.2014 | SSC        | TSX       |                               |            |            |           |
| 21                             | 18.12.2014 | SSC        | TSX       |                               |            |            |           |
| 22                             | 29.12.2014 | SSC        | TSX       |                               |            |            |           |

zones during two GPS measurement sessions (of around 12 and 15 hours, respectively) in which a recording was made every 30 s. In total, 4 reference points on the landslide (denoted 2001, 2002, 2004, 2005) and 3 on the water-dam (denoted 1000, 1001, 1002) were precisely localized by GPS (these points are shown in Fig. VI.2). The coordinates of each point were adjusted using data provided by the French National Geographic Institute (IGN) from the nearest reference stations of the permanent GNSS network at the survey date.

## Chapter VI. Combining SAR data with 3D Point Clouds

---

Consequently, the geodetic system used is RGF93v2 corresponding to GRS80 ellipsoidal model, ETRS89 terrestrial reference system and ETRF2000 frame at epoch 2009.

Note that on the water-dam there was no existing topographic referential, since in-situ monitoring is made internally through various sensors (such as pendulums). Hence, the 3 GPS-measured points were specially created for the survey and consist of implanted bolts on a stable rock or on the water-dam itself. Contrariwise, the landslide is equipped with references for topographic survey monitoring (the auscultation devices used are described in detail in the next subsection). Specifically, points 2001 and 2002 are topographic pillars equipped with centering plates, whereas points 2004 and 2005 are massifs fitted with prisms.

The surveys for both zones (landslide and dam) were accomplished by topographic measurements followed by laser scanning. In the landslide case, the total station was placed on pillar 2002 to measure the points 2001, 2004, 2005 as well as an independent point of the auscultation device that allows verification of the laser scanner. Onwards, the laser scanner was positioned by means of forced centering on pillar 2002 and the scanning of the landslide was performed with an angular step representing about 5 cm at the farthest measured distance. The points previously obtained with the total station permitted the registration of the laser scanner data.

The measurements on the water-dam were made from several points (denoted ScanPos) shown in Fig.VI.3 superimposed on the resulting point cloud of the dam.



Figure VI.2: GPS-localized points overlaid by the Google Earth image.

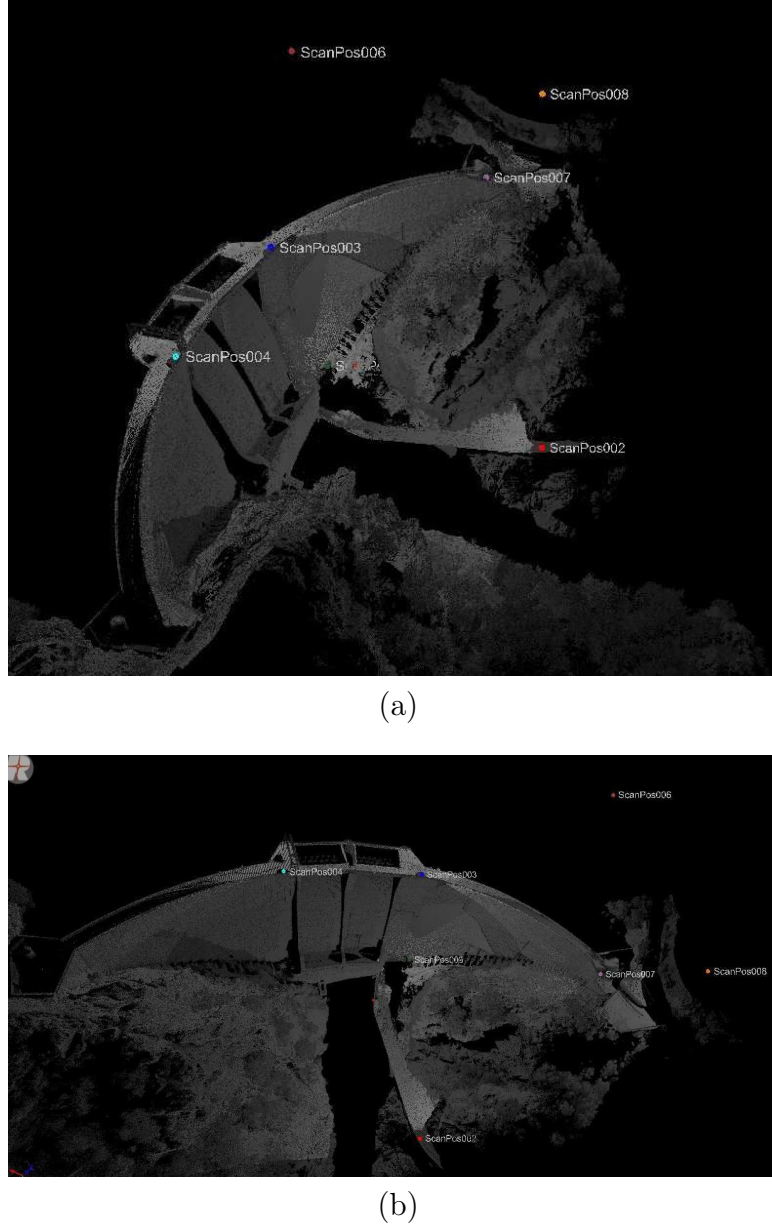


Figure VI.3: Laser scanners positions overlaid on the final point cloud of the Puylaurent dam: (a) lateral view and (b) downstream to upstream view.

First, for each point, a total station measurement was performed by noting the available tripod-prisms, as well as retro-reflective targets placed on mini-canis. The data was acquired taking into account temperature, pressure and hygrometric values. Afterwards, the laser scanner was placed in turn in upright position (by forced centering) on top of the following total stations: ScanPos002, ScanPos003, ScanPos004, ScanPos006 and ScanPos008. The envisaged laser scanner configuration is presented in Fig. VI.4a.

## Chapter VI. Combining SAR data with 3D Point Clouds

---

For the laser scanning, the prisms used for topographic survey were replaced by retro-reflective targets. The laser scans were performed with a density of one point at about every 5 cm. Station ScanPos007 was used in tilt mount configuration (Fig. VI.4b) to measure points situated close to the scanner in its nadir direction and was afterwards registered with a near-by total station. An additional station (ScanPos009) was mounted on the left bank, without a topographical point for registration (a free station), in order to complete the laser scan of the dam's base. This station's survey is registered only by using the retro-reflective targets and the plans shared with previous laser scans.

Each total station measurement, can provide an additional point for laser scan registration. To achieve this, the measured coordinates have to be modified in order to compensate the height differences: between the prism used with the total station and the target used with the laser scanner (determined with a measuring tape on the ground) and between the total station tilting axis and the laser scanner axis (the laser scanner was placed 60.7 mm above the total station).

The registration between different laser scans was performed in two steps. First, only the retro-reflective targets were used for a coarse registration. Then, the obtained coordinates were fine registered by taking into account the height of the scanner's trunnion and by adjusting the scanner's angles.



(a)



(b)

Figure VI.4: Laser scanner: (a) placed by forced centering in the position of the total station, (b) in "tilt mount" configuration.

The processed (resampled) data were grouped in two point clouds (one for the landslide and one for the water dam) having an average distance between adjacent points of 25 cm. A decimated version (for visualization purpose) of the two point clouds are shown superimposed on the corresponding Google Earth images in Fig. VI.5.

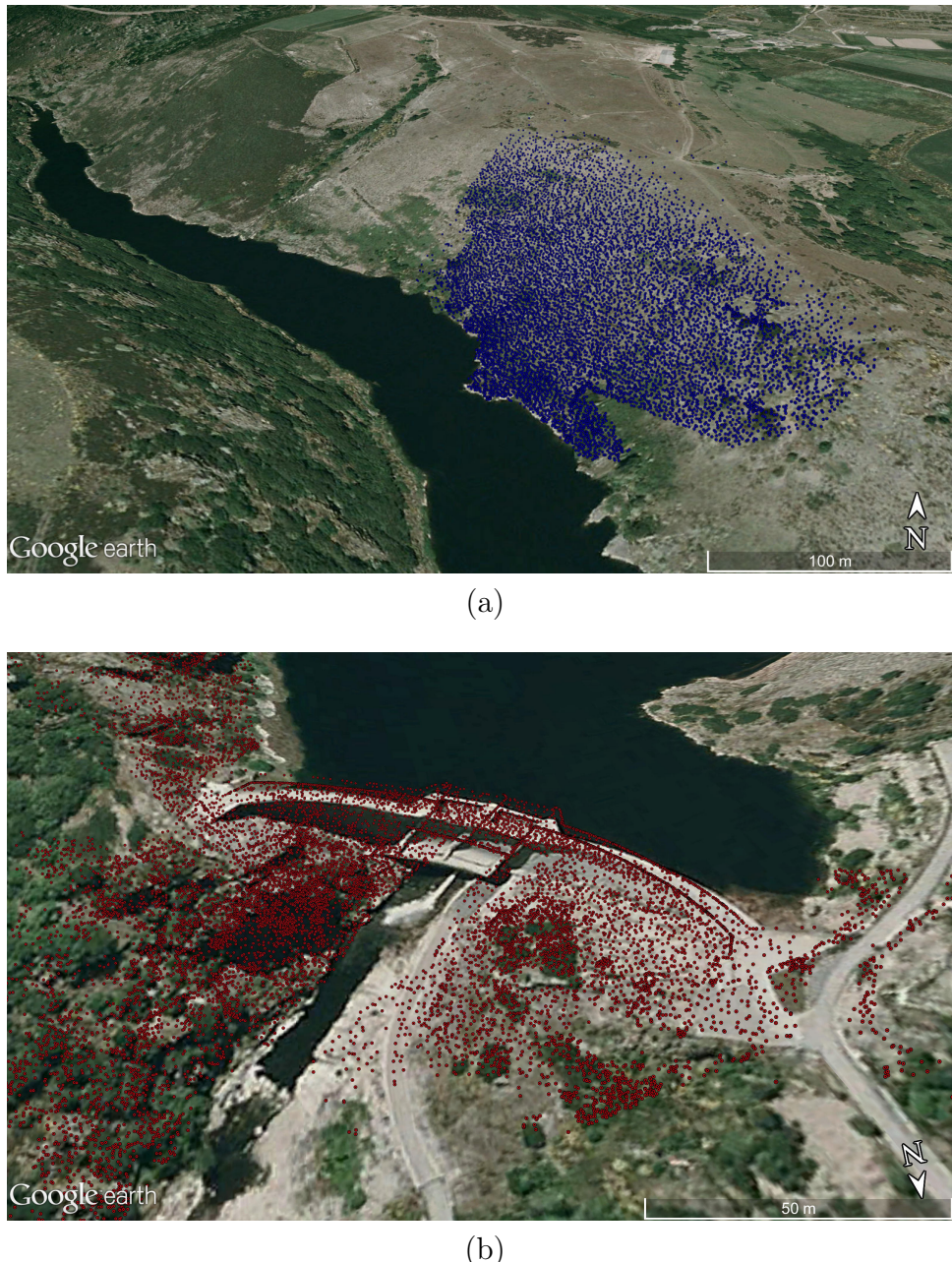


Figure VI.5: Point clouds overlaid on Google Earth images: (a) the Chastel landslide, (b) the Puylaurent dam.

### VI.1.3 In-situ measurements devices

In this subsection we describe the existing in-situ monitoring devices from the two areas.

The Chastel landslide area is equipped with 40 topographic points consisting of mini-prisms placed at about 1 m above the ground. Of these, on 20 points (denoted I1 to I20) from the higher zone of the landslide (due to access security reasons) were mounted corner reflector (CR) targets above the mini-prisms. The 3D coordinates of each target were measured at different dates in-between satellite acquisitions.

A measurement is performed using a motorized theodolite, the mini-prisms with CRs and 4 reference prisms. The theodolite is mounted on pillar 2002 and the references correspond to a massif (point 2003) and the GPS-localized points described in the previous subsection (pillar 2001 on the right bank, massifs 2004 and 2005 on the left bank). The configuration is displayed in Fig. VI.6. Because the measures are performed at different dates and the theodolite is replaced each time, the first step before each measurement, is to perform an overview of the 4 references to set up the orientation and determine the necessary atmospheric correction for accurate distance measurements. Next, the 3D coordinates of the 20 points with CRs are computed.

In case of the Puylaurent dam, the in-situ data is provided by a set of pendulums placed inside the water-dam. These pendulums measure the tangential and radial displacements between different points of the dam's ridge (shown in Fig. VI.7). The orientations of the tangential and radial axis are depicted in Fig. VI.7a. There is no in-situ device to measure the dam's vertical movements.

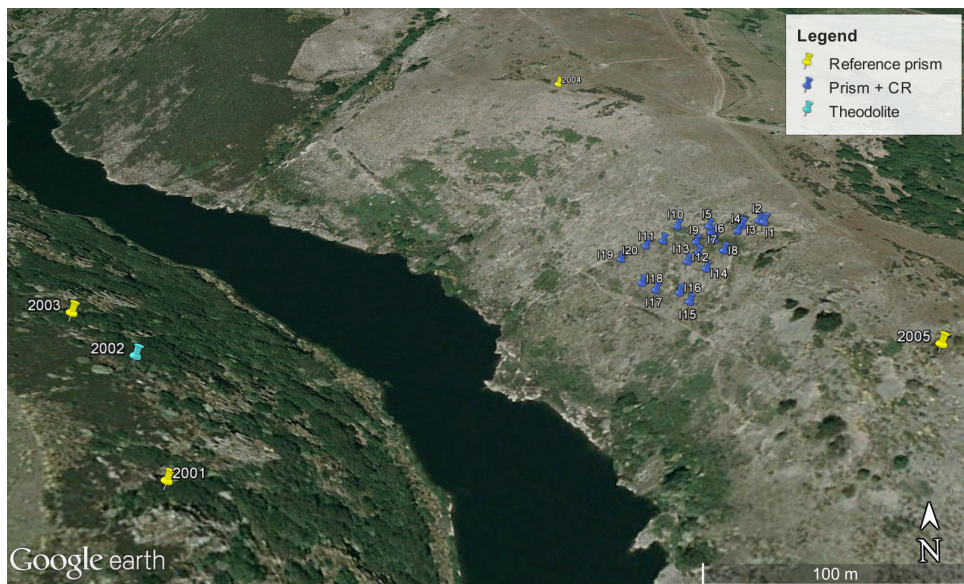
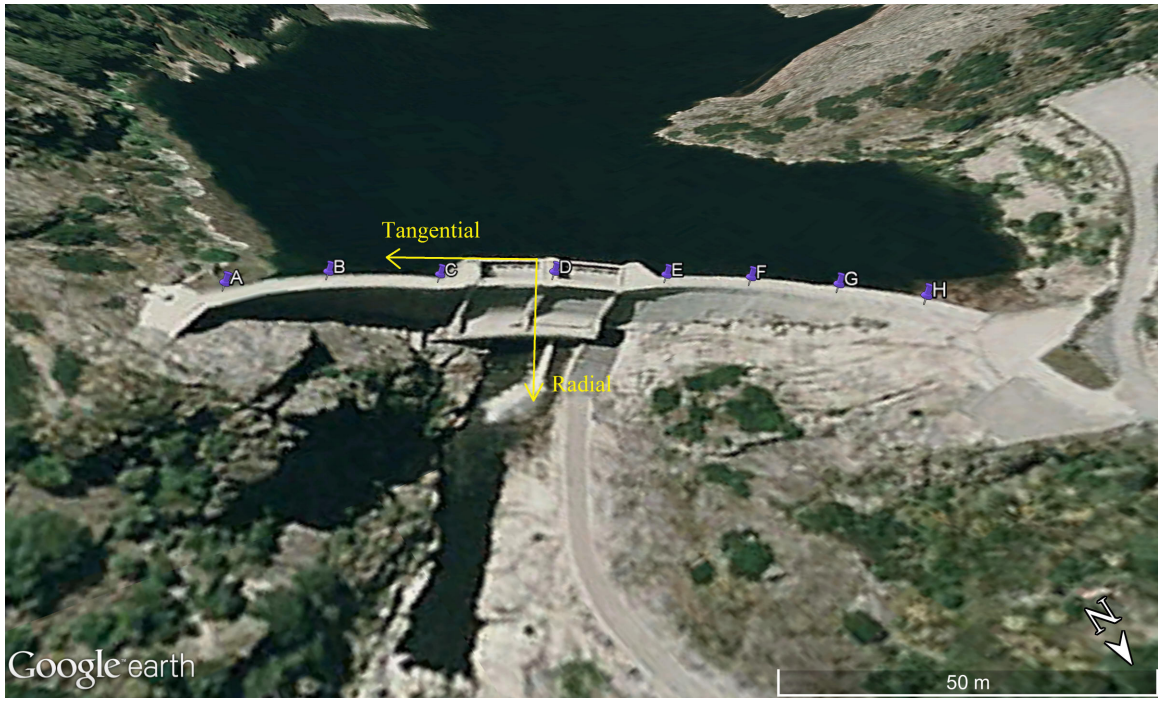
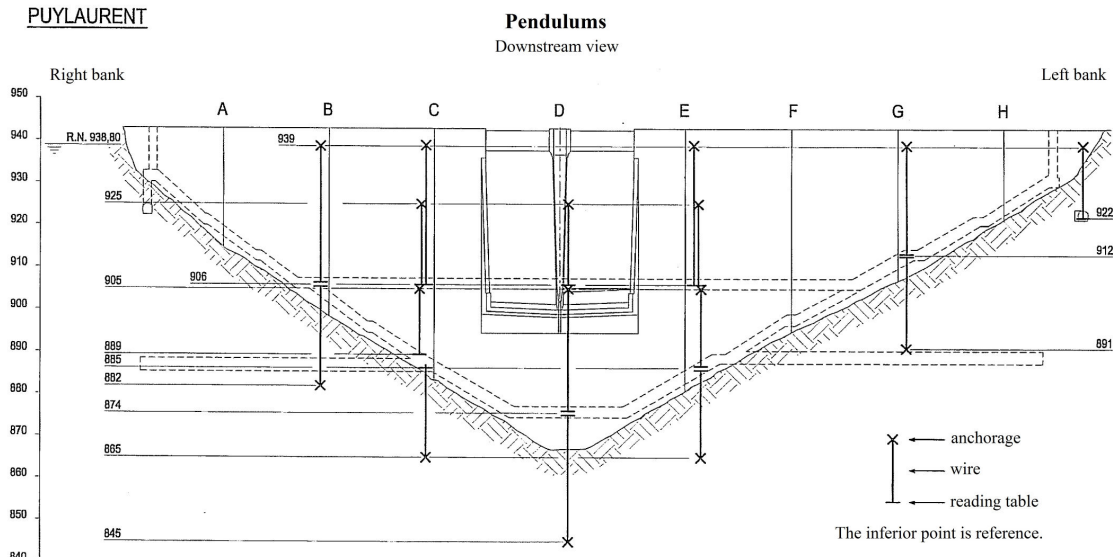


Figure VI.6: In-situ measurement configuration of the Chastel landslide.



(a)



(b)

Figure VI.7: In-situ measurement points on the Puylaurent dam: (a) overlaid on Google Earth image, (b) detailed diagram (the heights are in IGN 69 system).

## VI.2 SAR data and Point Cloud processing

In this section we present the main processing steps involved in the real data processing finishing with estimation of the mean deformation velocity and time series extraction. The required SAR data processing in order to refocus the complex images on the point cloud and to detect the reliable scattering centers was analytically developed in the first part of the thesis. Therefore, in the following we make a review of the key points involved in the processing with an emphasis on the particularities of real data.

The first step consists in a data pre-conditioning. The sliding spotlight SAR images acquired by the TerraSAR-X/TanDEM-X satellites may have slightly different bandwidths and pulse repetition frequencies for the same illuminated scene in similar conditions. This happens due to different estimated parameters (such Doppler centroid and beam sweep rate) by the SAR processor before the image is focused. Moreover, the spectrum of the focused image is sampled such that it locally avoids aliasing, but the linear frequency drift induces a wrap of the Doppler spectrum especially at the beginning and at the end of the azimuth acquisition period. In order to counteract these effects, a common band filtering similar to the one proposed in [2] is employed along with an increase of the sampling rate with a factor of two performed between the actual filtering and reramping (for phase preserving processing).

In the following, the azimuth defocus of the SAR image is performed in order to gain access to the phase history of each scatterer. By employing the previously discussed pre-conditioning, the spectrograms of the azimuth defocused lines do not have any wraps and the instantaneous frequency law describing each target is bijectively related to the zero-Doppler time. The spectrogram of an azimuth defocused line is given in Fig. VI.8.

After obtaining the azimuth defocused images, they all have to be projected (refocused) on the available point clouds. In order to focus the azimuth response of a given point by the modified back-projection (matched filtering-based technique), the expected phase history is reconstructed and matched to the acquired signal. The exactness of the reconstructed phase history depends on how accurate and precise are the coordinates of the orbit and the ground point known and how well are the atmospheric effects compensated. The orbit's trajectory is given by the state vectors with scientific precision ( $\pm 3$  cm in a best case scenario [106]), while the ground point's position is determined by topographic measurements with millimetric error. Each analytically computed phase history using the orbit and ground point coordinates has to be corrected for the atmospheric effects (which are annotated in the available products) and consist in ionospheric range delays and azimuth timing offsets [79]. After this correction the geo-location error is placed in the centimeter range [106]. Still, a possible offset between the real and estimated position of each scattering center may appear due to different reference frames between the satellite's state

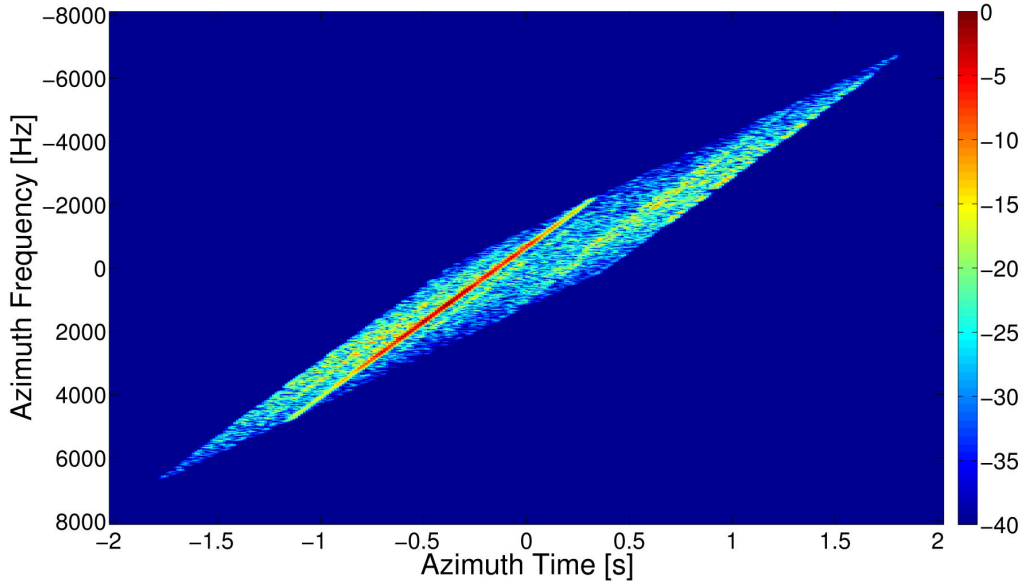


Figure VI.8: Spectrogram of an azimuth defocused line in sliding spotlight acquisition mode.

vectors and the differential GPS measurements [107]. Anyway, any residual atmospheric or topographic phase is mitigated by employing a phase difference between each refocused point and a very reflective reference scatterer placed in the vicinity of the test site.

For the first refocusing experiments, we have used a uniformly spaced rectangular 2D grid (a pixel has  $0.5m \times 0.5m$ ) aligned with the local latitude/longitude axis, centered on the Puylaurent water dam and situated at the height of the dam's ridge. Additionally, of a set of differential GPS measured points on the water dam's ridge was available (the points were converted from latitude/longitude to ECEF coordinates considering that they are all at the ridge's altitude). By overlapping the image focused on the 2D grid with the GPS measured position we can check the consistency between the location of the dam's ridge in the refocused image and the actual position given by the set of points. This fact can be observed in Fig. VI.9: Fig. VI.9a shows one of the images acquired by the TerraSAR-X satellite on 11 April 2013, while the corresponding refocused image on the rectangular grid is shown in Fig. VI.9b overlaid by the set of GPS measured points.

An example of initial and refocused images on the 3D point clouds are presented in Figs. VI.10-VI.11 and VI.12-VI.13 for both the Puylaurent water-dam and the Chastel landslide in descending/ascending orbits. The figures also show: in the case of the Puylaurent dam, the position of a few corner reflectors and reference points from the dam's ridge, while for the landslide the 20 points that have to be monitored are clearly highlighted. Note that in the 3D image of the water-dam the highly reflective regions from the initial image appear at different heights and only a part of them are actually provided by the dam's ridge.

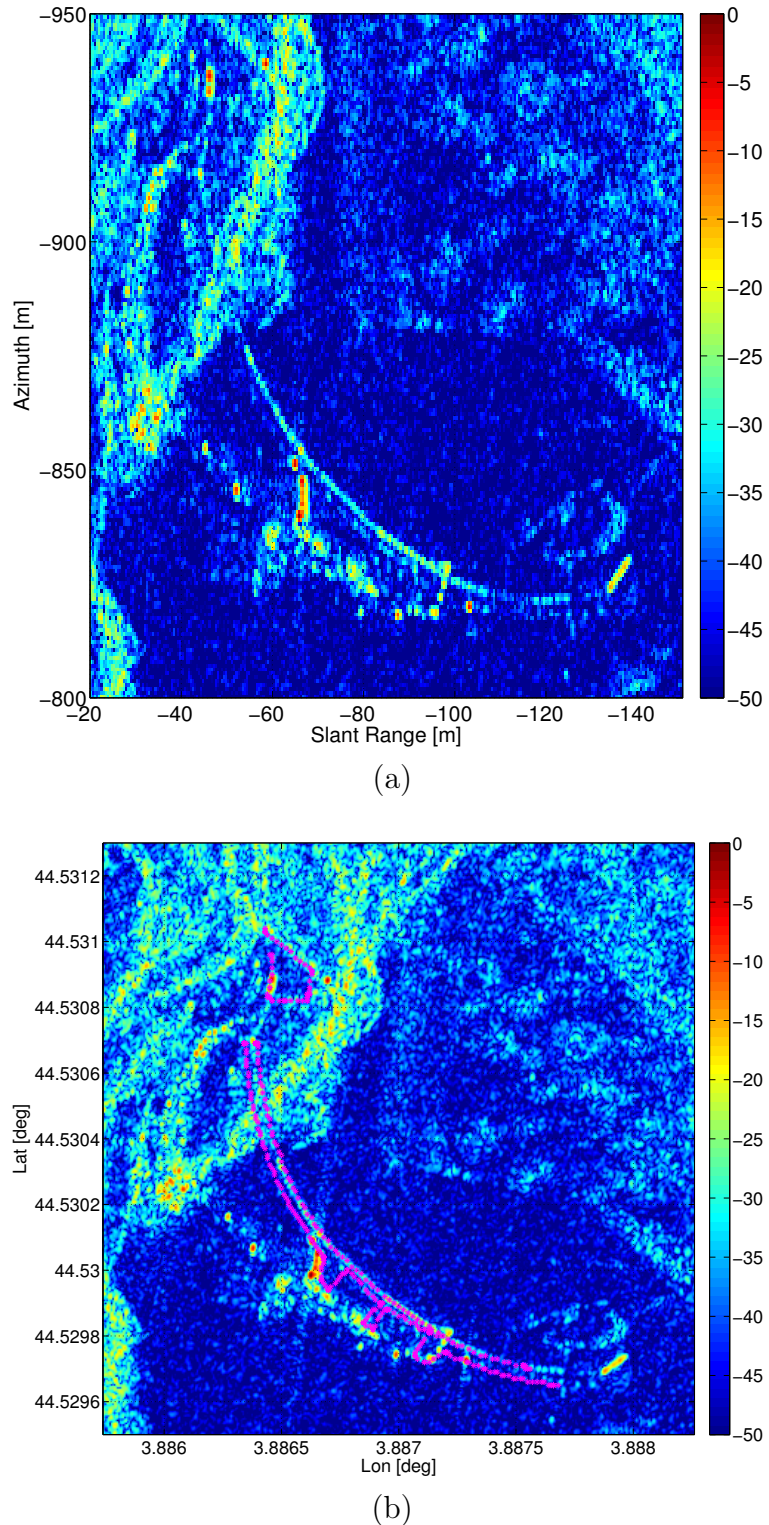


Figure VI.9: 2D Grid Refocusing. (a) High-Resolution Spotlight TerraSAR-X SAR image of the Puyaurent dam acquired on 11.04.2013. (b) Refocused TerraSAR-X image on the rectangular grid overlaid by the set of GPS measured points on the ridge of the dam.

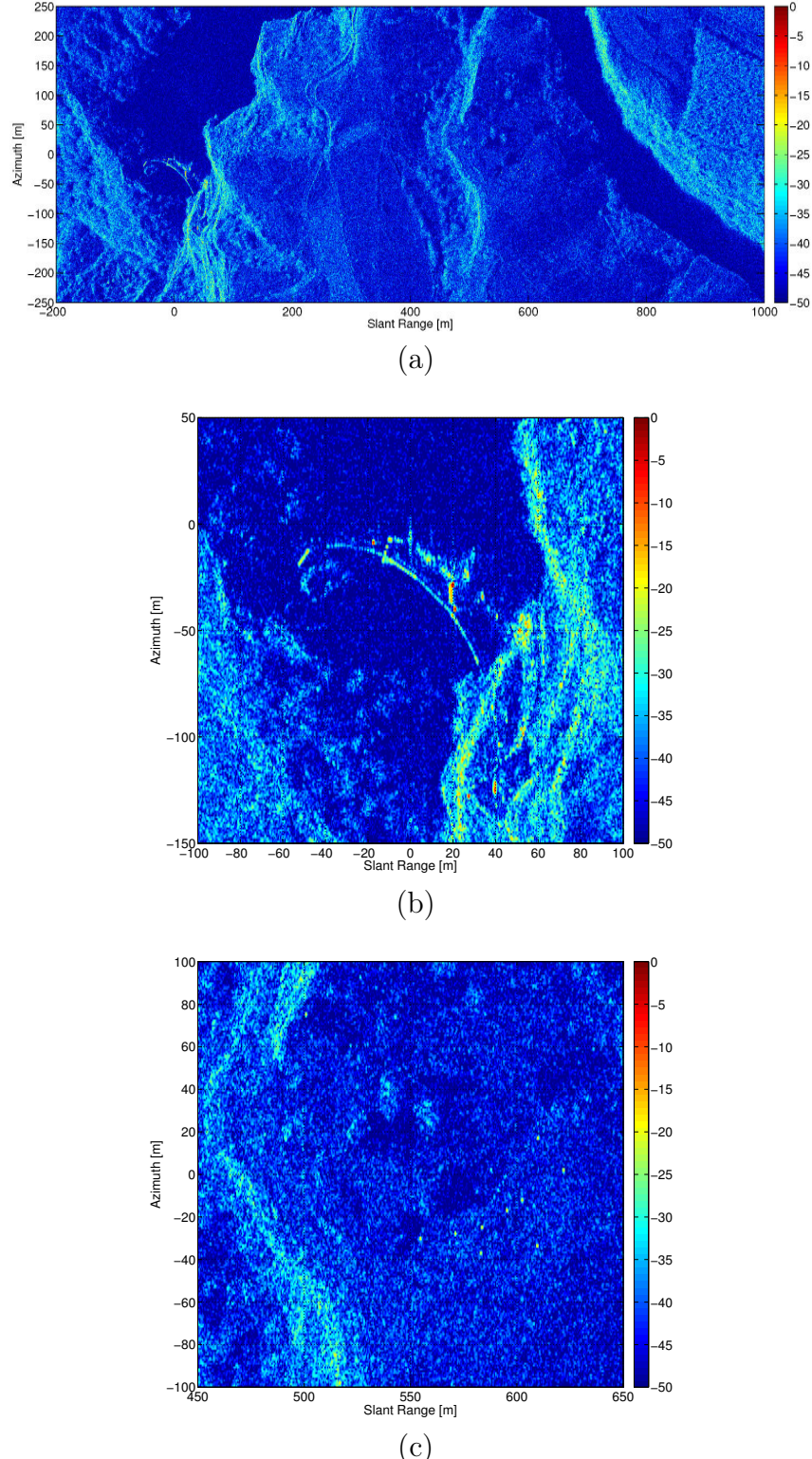


Figure VI.10: TerraSAR-X data, Descending orbit, 24.10.2014: Initial image in slant range-azimuth geometry (a), and zoom in on the Puylaurent water-dam (b) and the Chastel landslide (c).

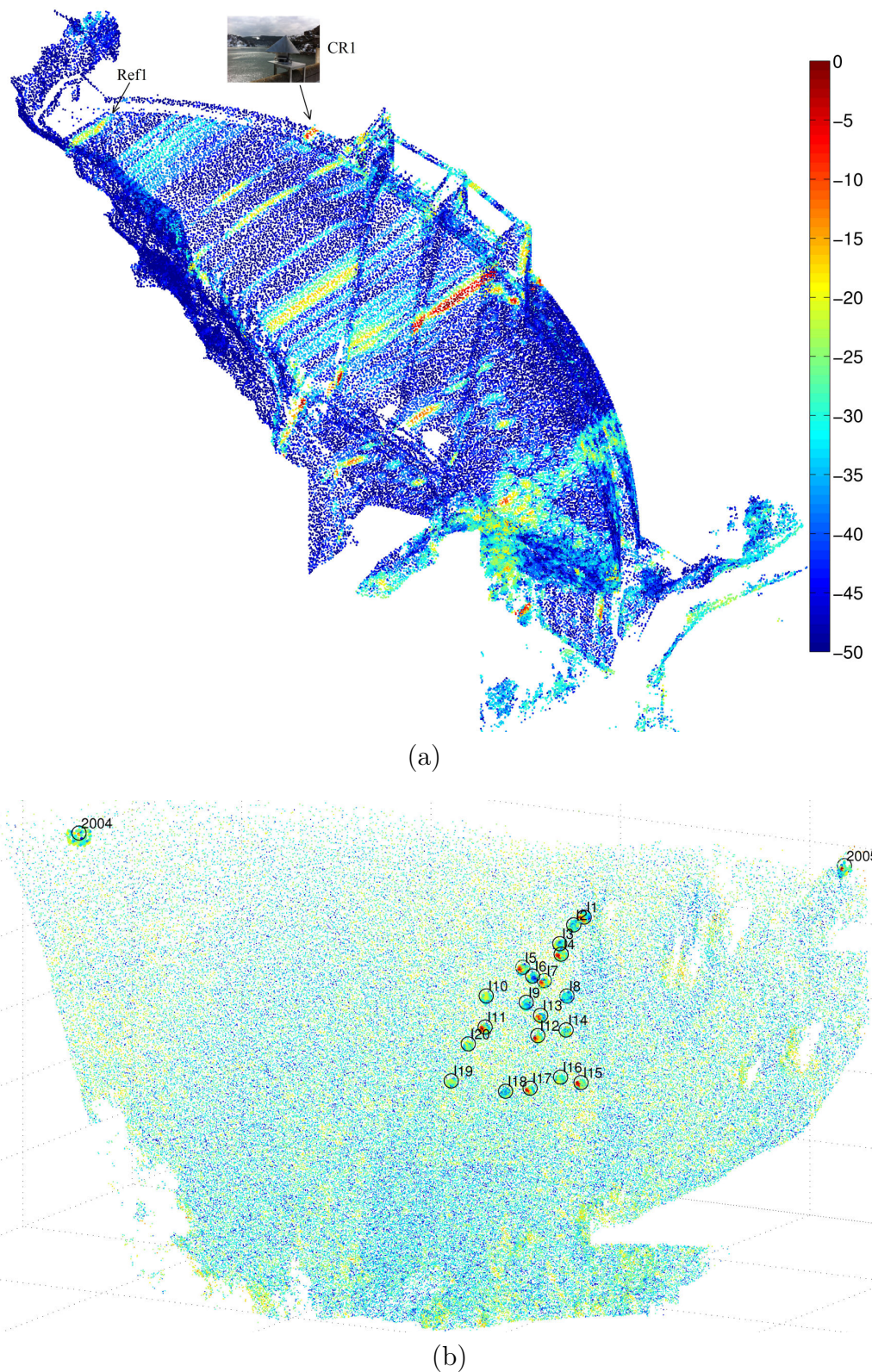


Figure VI.11: TerraSAR-X data, Descending orbit, 24.10.2014: Refocused image on the water-dam (a) and landslide (b) point clouds (same colorbar).

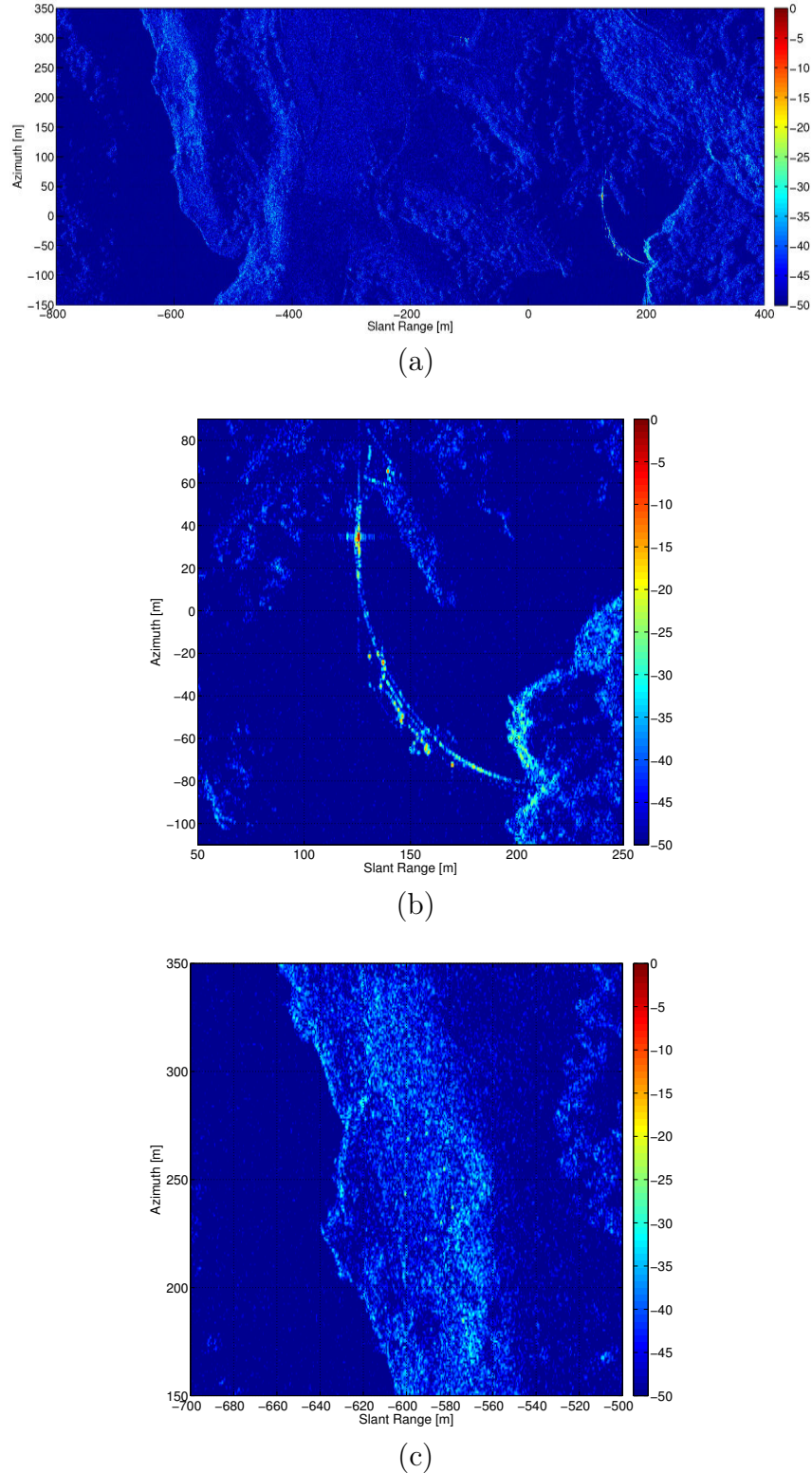


Figure VI.12: TerraSAR-X data, Ascending orbit, 31.10.2014: Initial image in slant range-azimuth geometry (a), and zoom in on the Puylaurent water-dam (b) and the Chastel landslide (c).

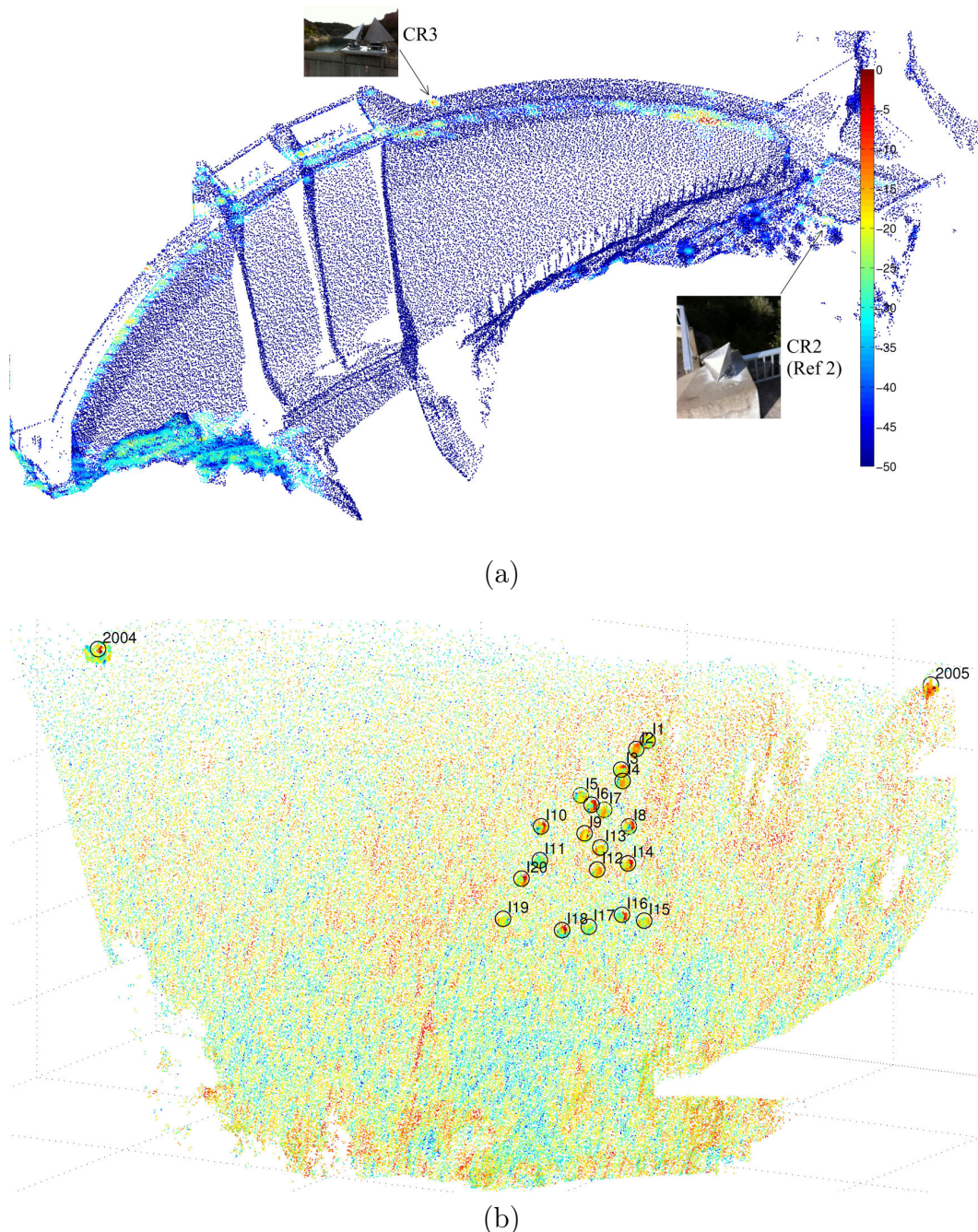


Figure VI.13: TerraSAR-X data, Ascending orbit, 31.10.2014: Refocused image on the water-dam (a) and landslide (b) point clouds (same colorbar).

When the refocusing of each image on the point cloud is complete, each point is tested if it is a reliable scattering center in all the images using the proposed position test in the EV plane. In order to use the 2D Capon beam-former in the reconstruction of the elevation-velocity plane, the first step is to estimate the covariance matrix on a few points neighboring the point under consideration. Hence, depending on the number of images, for each tested point, the nearest 10-25 points (from the point cloud) are used for the covariance matrix estimation. In this way, we actually identify the reliable scattering regions from the given point cloud (with the expense of a slight resolution loss). A typical normalized experimental EV plane for one given point in the presence of only one dominant scatterer is shown in Fig. VI.14. Notice that the main lobe is situated around zero elevation and is not dispersed on the velocity axis.

The last step in the processing is to compute the mean deformation velocities (MDV) and the displacements time series as explained in the methodological part. Depending on the deformation nature, the interpretation of the extracted displacements may not be straightforward when the actual deformation does not have the same linear trend during the whole analyzed period. In this case the MDV cannot be directly linked to a physical speed of deformation of the structure during a certain period, it is just an average of the displacements (which can be part of two or several different trends of deformation). This may also cause some additional phase wraps which have to be corrected in order to give a physical meaning to the displacements time series.

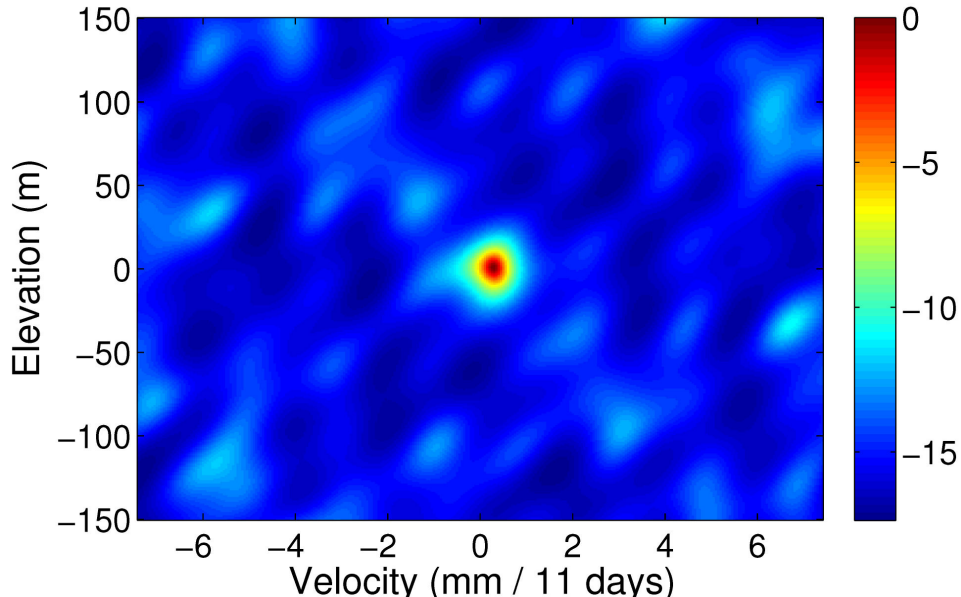


Figure VI.14: Normalized experimental PSD in the EV plane for a refocused point having one dominant scatterer. The chosen time unit is the satellite's revisit time of 11 days.

## VI.3 Deformation measurements

This section presents how deformation measurements are obtained starting from detected scattering centers in the point clouds. The results are compared with the available in-situ data for both the Puylaurent dam and the Chastel landslide.

### VI.3.1 Chastel landslide

In the landslide case, displacements monitoring is performed on the mounted corner reflectors on top of the topographic points. The landslide has essentially a uniform motion throughout the monitoring period and consequently the 4D tomography model with a mean displacement velocity is an appropriate choice for scatterers detection.

Using in-situ measured 3D coordinates at successive acquisitions during a longer period, we have determined the mean deformation vector (model) of each point with corner reflector. Consequently, the projection angle between the line of sight direction and the average deformation vector direction can be computed. Fig. VI.15 shows the projection angles intervals for the ascending/descending orbits overlaid on an image of the targets and the point cloud regions used for scattering centers identification. A positive projected displacement is in keeping with the direction of the vectors.

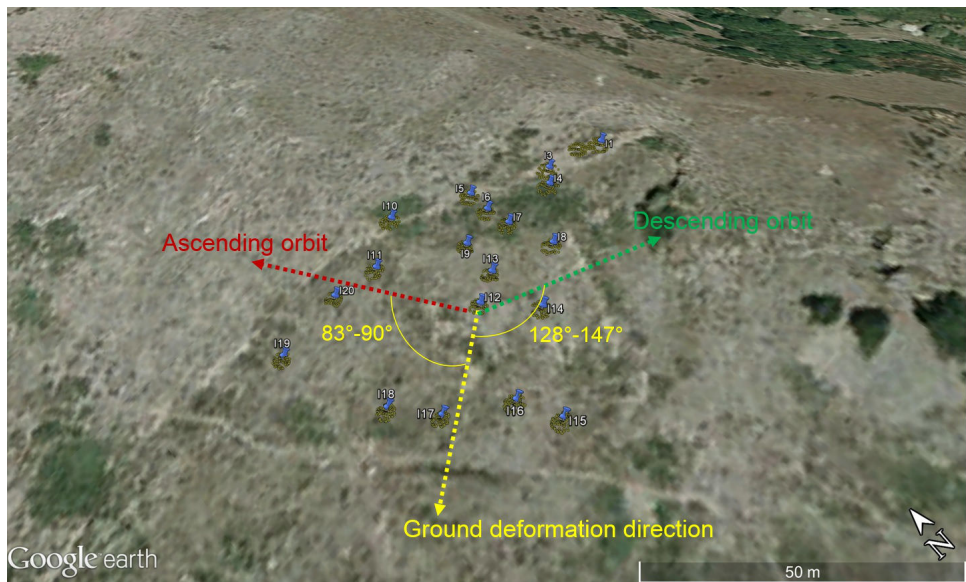


Figure VI.15: The projection angles intervals for the deformation model of each target.

In the descending orbit, from 9 visible points, 8 were detected as reliable scattering

centers and their displacements time series in line of sight are shown in Figs. VI.16-VI.19. The reference is point 2005. The error bars for the satellite measures are obtained through Monte Carlo simulations at the respective SNRs. Note that each error bar actually comes from four different independent noise sources: the target and the reference point in both the current image and the first (reference) one [108]. On the plots, there is also shown the linear trend corresponding to the estimated MDV and the evolution of the SNR for the envisaged target and the reference point.

The differences between the estimated and in-situ measurements can reach up to 10 mm and may come from different reasons described in the following. First, there is no simultaneous satellite-ground measurement and the data are aligned through an interpolated offset which may not be consistent for all the points of the plot. Second, the quite high fluctuations of the displacements around a rather constant level during the satellite measurements in 2013 may be linked to the instability of the reference point at the top of the landslide (which was actually confirmed by ground truth). This can cause errors to both satellite and ground measurements. Third, the topographic measurements which are taken as ground truth also have their own errors that can reach a few millimeters.

The ground mean displacement velocity (G-MDV) is estimated from the LOS MDV and the local projection angle. The MDV dispersion is obtained by simulations with the given SNRs considering as velocity estimator the reconstructed elevation-velocity plane. To compute the in-situ G-MDV we have projected each 3D displacement on the average displacement vector and applied a York linear fit [109] in order to determine the slope and its standard deviation. We computed the dispersion of the projected in-situ measured displacements using the movement of a theoretically fixed point (2004), yielding around 3.5 mm. The resulting slope dispersion after the linear fit is about 2.5 mm/yr for each point. The results are summarized in Table VI.2.

For the ascending orbit, although there are visible reflections from the mounted CRs, the average deformation vector of the landslide (computed with in-situ 3D coordinates measurements) is almost orthogonal to the line of sight and hence, the structure cannot be monitored from this orbit.

## Chapter VI. Combining SAR data with 3D Point Clouds

---

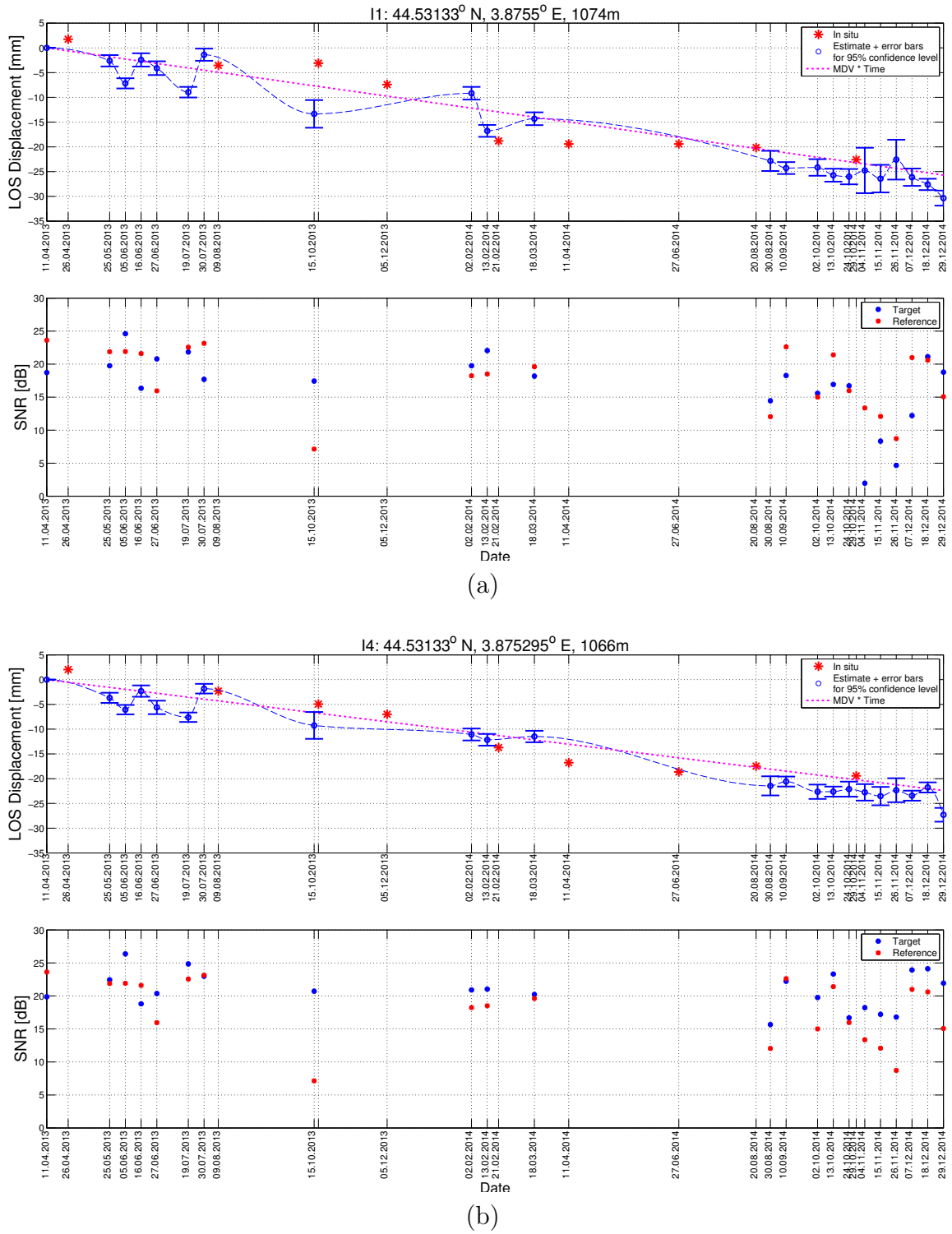


Figure VI.16: Estimated vs. in-situ LOS displacements for the detected scatterers on the Chastel landslide: (a) I1, (b) I4.

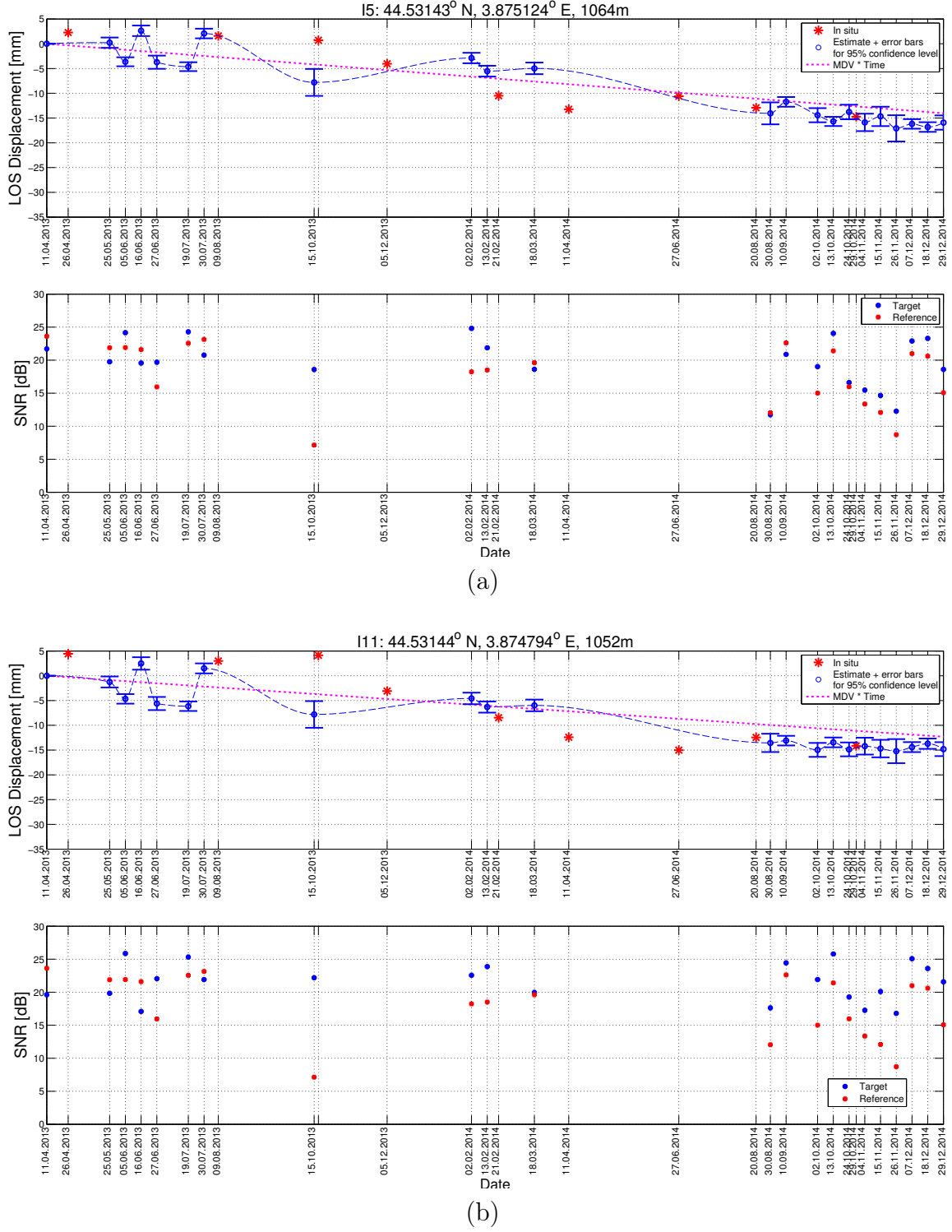


Figure VI.17: Estimated vs. in-situ LOS displacements for the detected scatterers on the Chastel landslide: (a) I5, (b) I11.

## Chapter VI. Combining SAR data with 3D Point Clouds

---

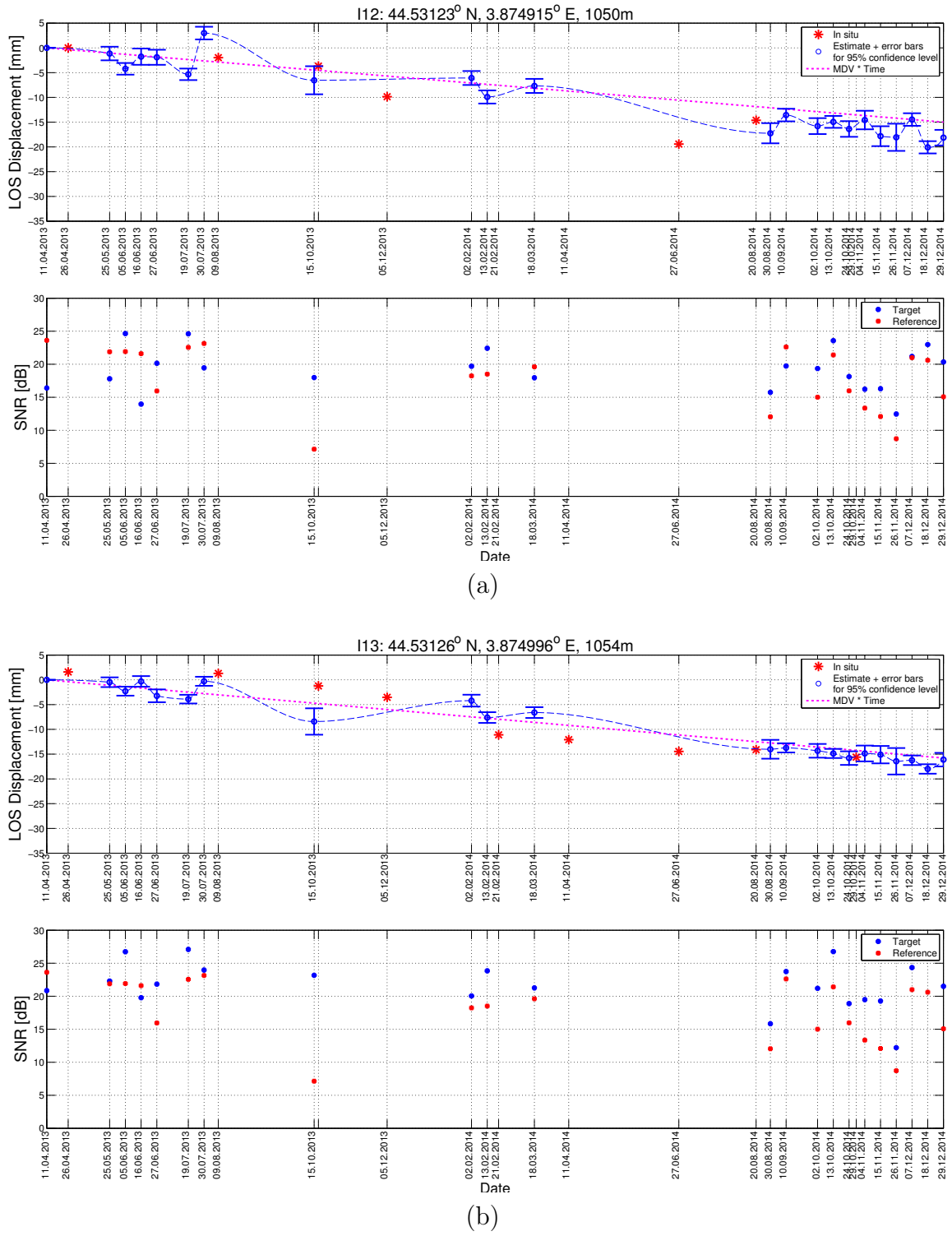


Figure VI.18: Estimated vs. in-situ LOS displacements for the detected scatterers on the Chastel landslide: (a) I12, (b) I13.

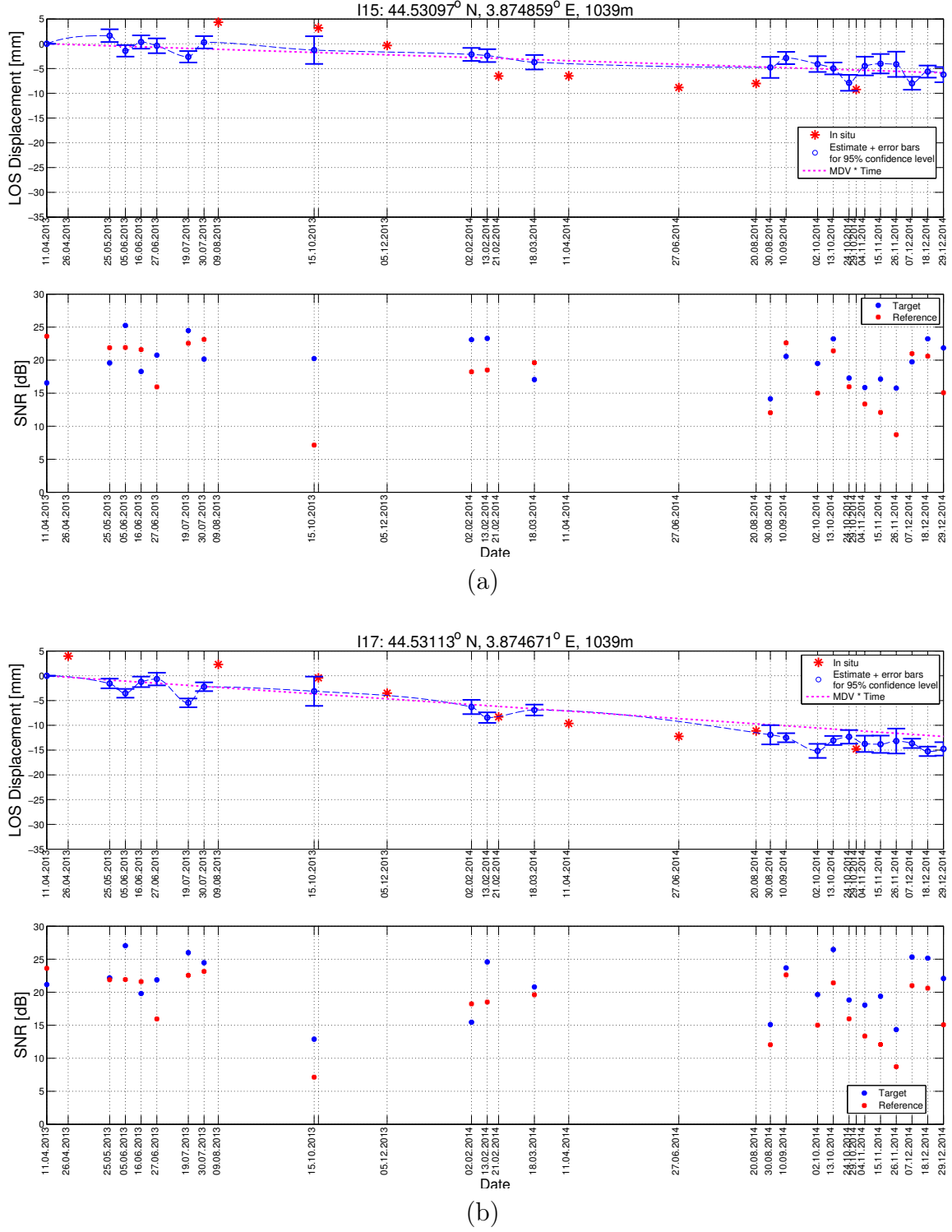


Figure VI.19: Estimated vs. in-situ LOS displacements for the detected scatterers on the Chastel landslide: (a) I15, (b) I17.

Table VI.2: Ground Mean Displacement Velocity of the Chastel landslide

| Point | LOS MDV $\pm 2\sigma$ [mm/yr] | Projection angle [ $^\circ$ ] | G-MDV $\pm 2\sigma$ [mm/yr] | In-situ G-MDV [mm/yr] $\pm 2\sigma$ |
|-------|-------------------------------|-------------------------------|-----------------------------|-------------------------------------|
| I1    | -14.9 $\pm$ 2.0               | 135.4                         | 21.0 $\pm$ 2.8              | 16.2 $\pm$ 5.0                      |
| I4    | -13.0 $\pm$ 1.5               | 129.5                         | 20.5 $\pm$ 2.3              | 15.1 $\pm$ 5.0                      |
| I5    | -8.2 $\pm$ 1.5                | 130.0                         | 12.7 $\pm$ 2.4              | 11.1 $\pm$ 5.0                      |
| I11   | -7.2 $\pm$ 1.4                | 140.7                         | 9.3 $\pm$ 1.8               | 10.9 $\pm$ 5.0                      |
| I12   | -8.7 $\pm$ 1.6                | 138.6                         | 11.6 $\pm$ 2.1              | 13.8 $\pm$ 5.0                      |
| I13   | -9.2 $\pm$ 1.4                | 137.6                         | 12.4 $\pm$ 1.9              | 10.4 $\pm$ 5.0                      |
| I15   | -3.4 $\pm$ 1.5                | 128.3                         | 5.5 $\pm$ 2.4               | 7.5 $\pm$ 5.0                       |
| I17   | -7.1 $\pm$ 1.4                | 147.4                         | 8.5 $\pm$ 1.7               | 9.1 $\pm$ 5.0                       |

### VI.3.2 Puylaurent dam

For the water-dam, the region tested for scattering centers is composed of points situated near the dam's ridge and the surrounding massifs. The dam typically has a seasonal movement and does not follow a single linear trend, so the MDV will have a physical meaning only if it is computed for relatively short periods. The reference in the descending orbits is the highly reflective region from the right bank side of the ridge (denoted Ref1 in Fig. VI.11a), whereas in the ascending orbit the reference is a corner reflector placed on the left blank plateau of the ridge (CR2/Ref2 in Fig. VI.13a).

In Fig. VI.20 and Fig. VI.21 are presented the MDVs of the detected scattering centers in two intervals for which we have relatively dense acquisitions: April-October 2013 and September-December 2014. In each of these intervals the movement is relatively linear with a single trend and the MDV has a clear meaning. The positive and negative values indicate the movement of the structure in LOS when is getting closer and respectively farther from the satellite (in keeping with the LOS unit vector). In the descending orbits, the satellite points the dam from a lateral-downstream direction (as results from Fig. VI.10b) and there are a lot of reflections coming from the ridge's vertical wall, while in the ascending one the pointing comes from an upstream direction (easily noticeable in Fig. VI.12b), which leads to very few scattering centers on the laser scanned part of the dam. Notice that the points with zero MDV appear on stable regions from the sides of the water-dam.

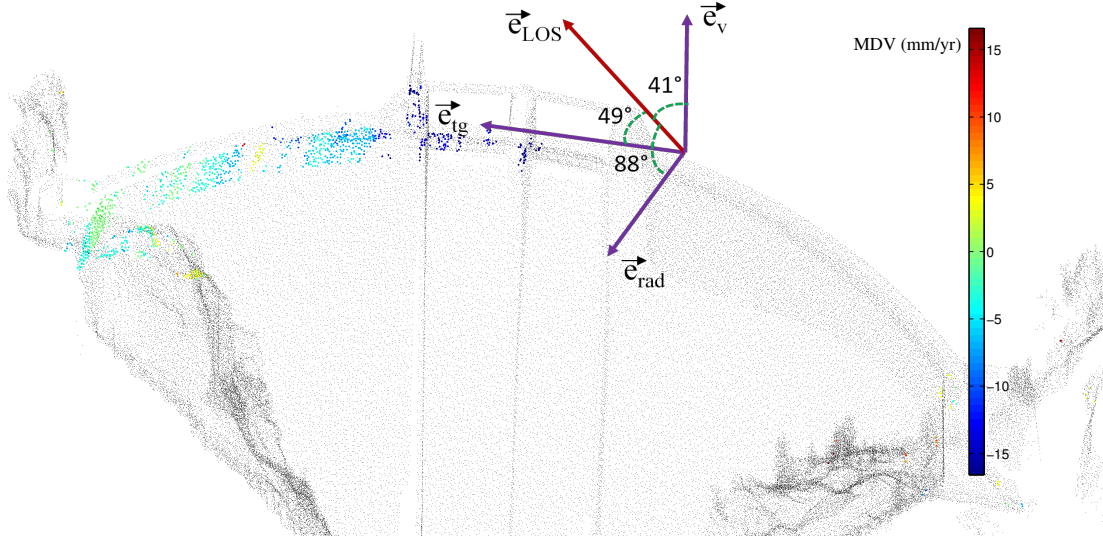


Figure VI.20: Puylaurent dam's scattering centers and their MDVs on the descending orbit between April-October 2013. On the figure we highlight the angles between the LOS direction and the local unit vectors (tangential, radial, vertical).

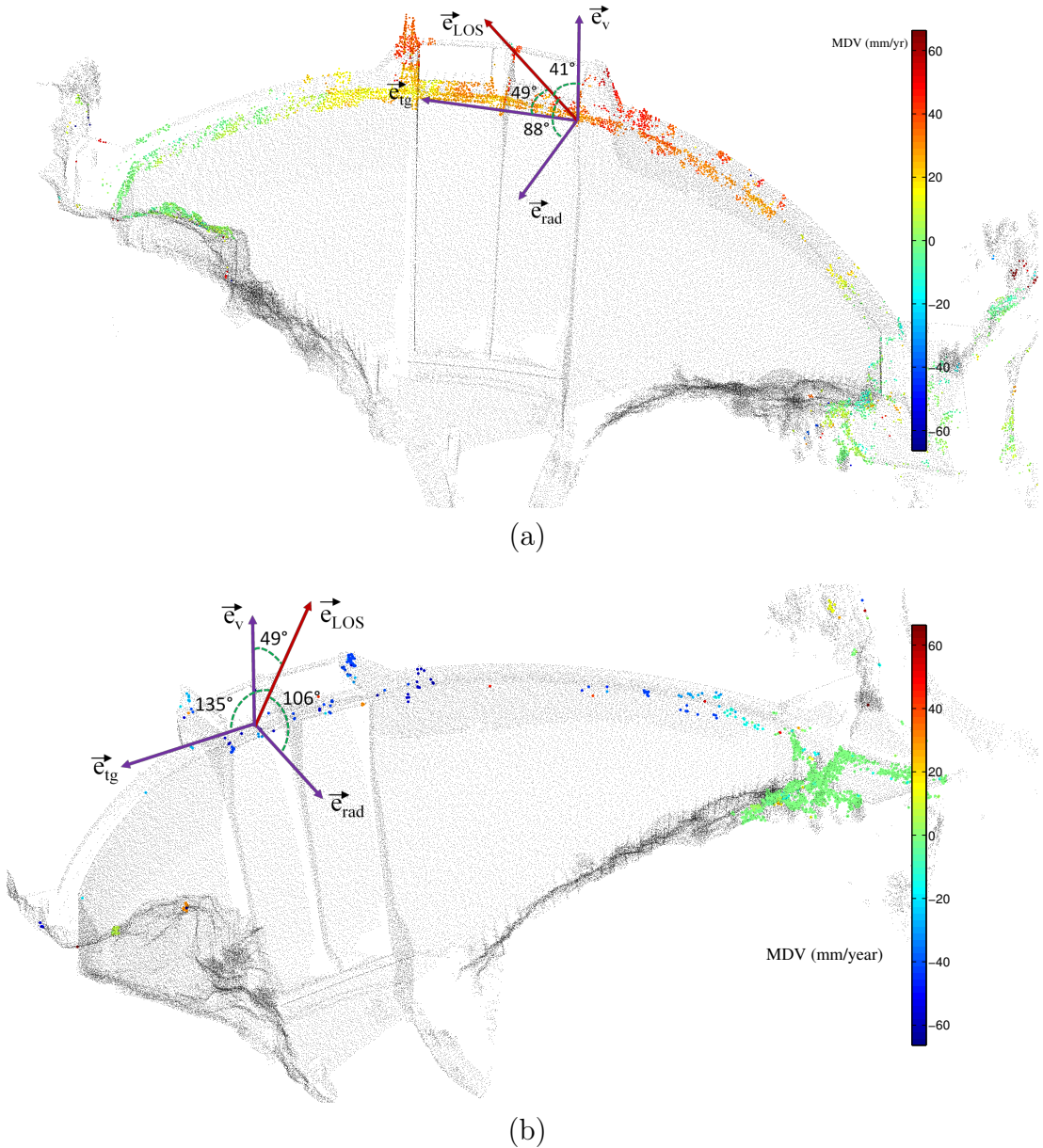


Figure VI.21: Puylaurent dam's scattering centers and their MDVs between September-December 2014: (a) Descending orbit, (b) Ascending orbit. On the figures we highlight the angles between the LOS direction and the local unit vectors (tangential, radial, vertical).

For the descending orbit, where the reference is a side of the ridge, stable points appear both near the reference and (for some data sets) on the other side of the dam (on massifs) which shows a good coherence along the whole ridge. However, the points near the opposite side of the reference (used in the descending orbit) tend to be rejected due to layover with the massif.

Table VI.3 shows a comparison between the estimated and in-situ LOS MDV for various points on the water-dam equipped with pendulums (shown in Fig. VI.7b). Note that the detection and MDV estimation works for a relatively low number of necessary tracks (between 8-11). The main cause for the difference between estimated and in-situ values is that there is no in-situ information about the vertical movement of the dam and only the tangential and radial displacements are projected in LOS.

In order to obtain accurate displacements time series, these are extracted from the phases of CRs placed on the dam (CR1 from VI.11a for the descending orbit and CR3 from Fig. VI.13a for the ascending orbit). Both CRs appear as pertinent scattering centers when the detection is performed on the whole data set. Fig. VI.22 shows the displacements evolution of the two CRs from the dam between 2013-2014 (in the data acquired from the ascending orbit the dam is visible only from 15 images) among with the water level in the reservoir and the temperature from a nearby meteorological station. The resulting dispersion (quantified by the error bars) for the descending orbit is higher because the reference is not a corner reflector. The in-situ data comes only from displacements in the horizontal plane (tangential and radial) and does not comprise the vertical movements. Obviously, the LOS remote sensed movement is a mixture from all three components, which explains the differences between the two plots. For visualisation, the remote sensed and in-situ displacements are aligned on the plot with an offset leading to the same mean value.

The in-situ measurements are displacements in the horizontal plane (tangential and radial) and don't comprise the vertical movements. Obviously, the LOS remote sensed movement is a mixture from all three components, which explains the differences between the two plots. For visualisation, the remote sensed and in-situ displacements are aligned on the plot with an offset leading to the same mean value. The differences between the satellite measured displacements and ground truth are situated around a few millimeters and mainly come from the lack of in-situ vertical movement data. Besides this, the satellite displacements rely on a reference point on the side of the water-dam which is not exactly the same as the reference of the pendulum systems. The anchorage point of each pendulum

Table VI.3: LOS MDV Measurements on the water-dam.

| Interval                | Orbit      | Number of tracks | Point | MDV $\pm 2\sigma$ [mm/yr] | In-situ MDV [mm/yr] |
|-------------------------|------------|------------------|-------|---------------------------|---------------------|
| April-October 2013      | Descending | 8                | C/CR1 | -6.7 $\pm$ 1.7            | -7.2                |
| September-December 2014 | Descending | 11               | C/CR1 | 9.9 $\pm$ 1.7             | 10.1                |
| September-December 2014 | Ascending  | 9                | E/CR3 | -46.5 $\pm$ 1.6           | -51.8               |

## **Chapter VI. Combining SAR data with 3D Point Clouds**

---

is not on the dam's exterior and the provided displacement may not be identical to the one the spaceborne sensor perceives.

The movement of the dam comes from the water level fluctuations and dilation/contraction due to temperature variations. This can be noted on the plots, from the correlation between water level/temperature and the dam's displacement, but is rather difficult to separate the effects of temperature variations and water level fluctuations. For example, the rapid decrease of the water level between February-March 2014 and the constant temperature decrease between August-December 2014 are noticed on both in-situ and remote sensed displacements time series.

Because the vertical movement of the dam (for which there is no in-situ sensor) is mainly provided by temperature variations, some quick temperature fluctuations at constant water level can be retrieved only on the remote sensed displacement. For instance, in June 2013 the temperature has a sudden variation that is clearly reflected in the time series for both ascending and descending orbits.

## High-Resolution SAR Signal Processing for Infrastructure Monitoring

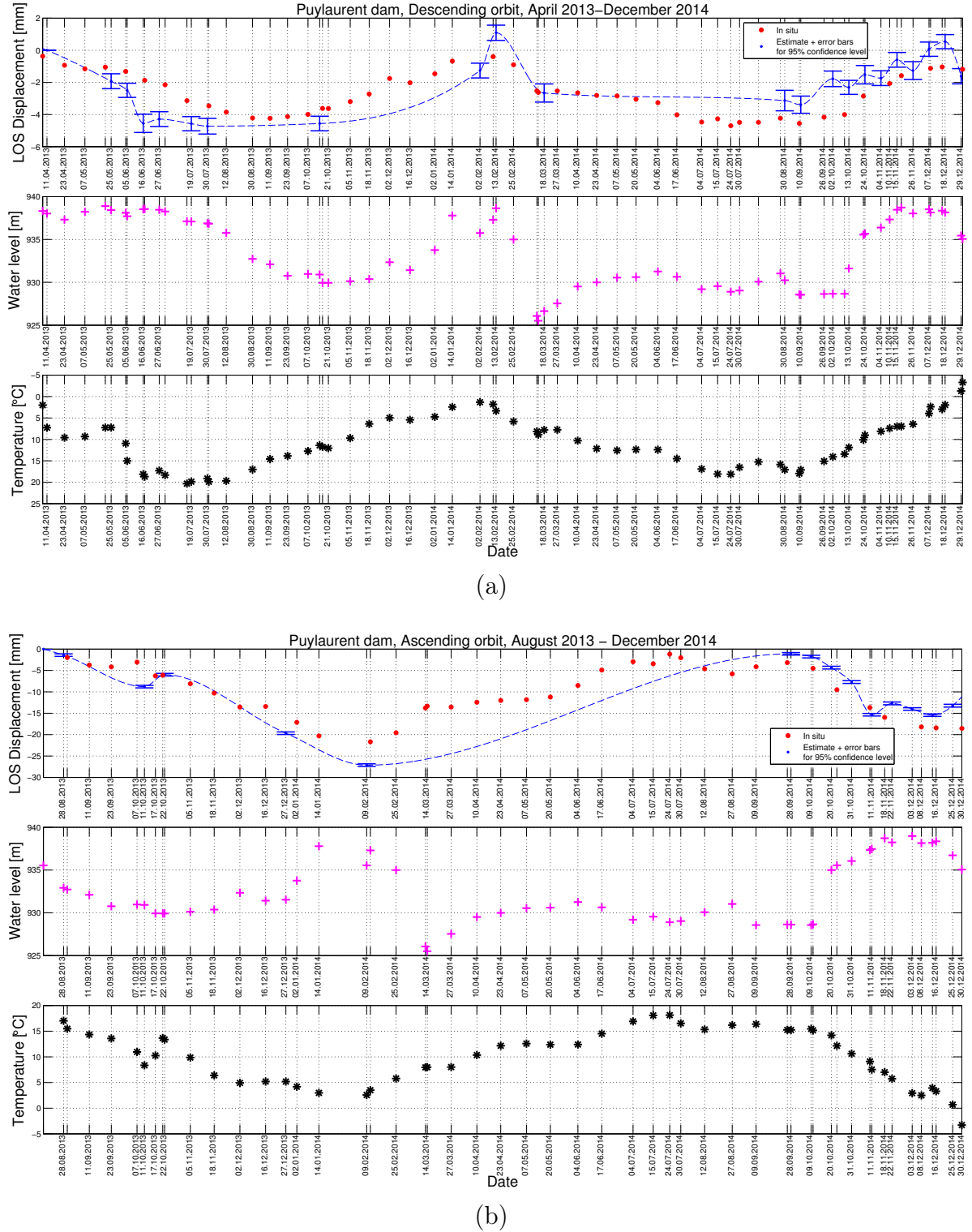


Figure VI.22: Puylaurent dam's displacements time series for corner reflector targets: (a) Descending orbit, between CR1-Ref1 (b) Ascending orbit, between CR3-Ref2.

## **VI.4 Conclusions**

In this chapter, the results presented on the Puylaurent water-dam and Chastel landslide highlight the assets of using both SAR remote sensing data and a 3D point cloud for infrastructure monitoring applications: reliable scattering centers identification performed directly on the structure, relatively small number of necessary images for scatterers detection, direct co-registration of the SAR data adapted to the specific imaging mode.

The SAR images used were acquired in sliding spotlight mode through the TerraSAR-X/TanDEM-X missions, while the point clouds were generated using GPS measurements, topographic surveys and laser scans. The actual combination between the SAR images and the point clouds was done by refocusing each image on the point cloud and detecting the scattering centers by means of four dimensional tomography. The issues and particularities of this specific way of SAR data processing have been analyzed.

The monitoring results were given through mean deformation velocities and displacements time series in the line of sight direction. Where available, the mean displacement was projected on the local deformation model. The measured displacements were in good agreement with in-situ data and in correlation with other physical factors like dilation and water level in the case of the dam.



# Overall remarks, contributions and perspectives

This thesis aimed to display in a consistent manner our contributions to the field of radar remote sensing. The idea was to formulate original answers to a theoretical question and a more applied one in the light of deformation monitoring. On one hand, provided our biased environment towards time-frequency processing of non-stationary signals, the answers to the former question manage to introduce suitable time-frequency interpretations to synthetic aperture radar signals among with the appropriate processing tools designed for both range and azimuth signals. On the other hand, the solution provided to the latter question, raised from the industrial context of the thesis, introduces a new processing methodology of spaceborne SAR images adapted to infrastructure monitoring applications.

Since the conclusions and detailed remarks were already provided at the end of each chapter of both methodological and applied parts, in the following we briefly review the major results and contributions of the thesis:

- We have developed two range nonlinearity correction methods for wideband FMCW radars based on the concept of time warping combined with the high-order ambiguity functions [110, 111, 112, 97] and respectively with a measure of spectral concentration [113]. The HAF-based method estimates the nonlinearities on the beat signal corresponding to a reference target, while the range autofocusing algorithm warps in turn the beat signal according to different modulation functions and selects as the best-matched function the one that delivers the highest spectral concentration of the warped signal. The algorithms were tested and compared using various simulation scenarios and real data acquired with an X-band FMCW radar platform designed for displacement measurements of short-range targets. Based on the nonlinearity corrected range profiles and SAR images we have measured displacements of highly reflective targets with sub-millimetric accuracy.
- A novel spaceborne SAR images processing methodology was designed. The method exploits an accurate digital surface model of the imaged scene and is based on azimuth refocusing followed by identification of scattering centers using the four dimensional tomography framework [114, 64, 65]. The simulations conducted to evaluate the algorithm's performances aimed several aspects. First, we emphasized that the refocusing approach provides better results than a few two-dimensional interpolation methods of conversion from slant range-azimuth coordinates to ground geometry, in terms of average coherence and phase dispersion. Afterwards, we studied the developed

method of scatterers detection and displacements estimation in different simulation scenarios in order to determine the impact of certain parameters (SNR, number of tracks, elevation accuracy, nonlinear movement and targets in layover) on the algorithm's performances. Finally, we compared the proposed zero elevation position test with classical scatterers detection techniques used in PSI and differential tomography. We highlighted that the position test can inherently reject targets affected by layover using the external information provided by the digital surface model.

- We outlined the main issues to be addressed in the context of deformation monitoring in order to combine high-resolution SAR images acquired in various imaging modes with the 3D point cloud of a certain infrastructure [115]. We applied the developed methodology on two sets of SAR images acquired in sliding spotlight mode through the TerraSAR-X/TanDEM-X missions for the monitoring of two test sites: the Puy-laurent water-dam and the Chastel landslide. The point clouds of the structures were generated using GPS measurements, topographic surveys and laser scans. The particularities of the proposed SAR data processing chain have been reviewed from the light of real data, considering issues like atmospheric effects, orbit precision, deviation from the assumed deformation model or Doppler spectrum wrapping. The monitoring results are shown as mean displacement velocities, displacements time series in LOS direction and ground deformation velocities (where local deformation models were available). The measured displacements were in good agreement with in-situ data and were correlated with physical factors like dilation and water level (in the case of the water-dam).

In the future, the presented work will be further developed and exploited in various contexts. The most plausible perspectives for the listed contributions are as follows:

- The nonlinearity correction methods can be extended to arbitrary tuning curves using the proposed estimation algorithms for local approximations of the nonlinear shape, followed by a reconstruction of the time-frequency trajectory. This upgrade is useful to compensate residual nonlinearities which may appear even in the case of mostly linear VCOs.
- The range autofocusing algorithm can be viewed as a general parameters estimation algorithm for signals having the same structure as the nonlinear FMCW beat signals. For instance, the method can be extended as kernel for time-frequency tracking of non-stationary signals with harmonics, such as acoustic signals. First results of this approach have been presented in [116] for signals from underwater mammals.
- For the matched signal transform (or time warping followed by a Fourier transform) employed in the developed algorithms to obtain a non-linearity corrected range profile, there is no discussion in the literature about the statistical detection of signals

## **Overall remarks, contributions and perspectives**

---

represented in this transformed domain. Therefore, an interesting perspective is to analyze the noise statistics in the matched signal transformed domain and propose an adequate detection scheme. The upgrade of this processing tool with a statistically characterized detector is essential for its applications in radar and communications. First results on this topic are presented in [117].

- The azimuth defocusing algorithm can be used for micro-Doppler time-frequency tracking. The defocusing method is a practical way to gain access to the micro-Doppler phase history starting from the delivered products. This is important because in the azimuth focusing steps, the micro-Doppler may be altered and just an inverse Fourier transform of the SAR image may not recover it correctly. First trials of this extension are presented in [118, 119] for vibration estimation.
- The proposed SAR images processing methodology can be completed by employing other elevation-velocity plane estimators (eventually newer developments [120, 121, 122]) combined with non-linear deformation models. Moreover, the detection based on the position test could be further developed by performing the detection before the azimuth focusing, using the azimuth position given by the 3D model. In this way we can combine the position test detection (based on multi-temporal/multi-baseline elevation focusing) with a detection based on azimuth sub-bands/sub-looks like the one recently proposed in [123] for coherent scatterers in a single SAR image. The availability of the azimuth phase history (obtained in the defocusing step) permits various combinations between azimuth time intervals, frequency bands and the elevation aperture in order to generate an (azimuth) time-(azimuth) frequency-(elevation) space detector which can simultaneously exploit a scatterer's characteristics in azimuth and elevation.



# Publications

## International journal papers:

- [110] A. Anghel, G. Vasile, R. Cacoveanu, C. Ioana, and S. Ciochina. “Short-Range Wideband FMCW Radar for Millimetric Displacement Measurements”. In: *IEEE Transactions on Geoscience and Remote Sensing* 52.9 (Sept. 2014), pp. 5633–5642 (cit. on p. 115).
- [114] A. Anghel, G. Vasile, R. Cacoveanu, C. Ioana, S. Ciochina, and J.-P. Ovarlez. “Scattering Centers Detection and Tracking in Refocused Spaceborne SAR Images for Infrastructure Monitoring”. In: *IEEE Transactions on Geoscience and Remote Sensing* 53.8 (Aug. 2015), pp. 4379–4393 (cit. on p. 115).
- [115] A. Anghel, G. Vasile, R. Boudon, G. d’Urso, A. Girard, and D. Boldo. “Combining Spaceborne SAR images with 3D Point Clouds for Infrastructure Monitoring Applications”. In: *submitted to ISPRS Journal of Photogrammetry and Remote Sensing* (2015) (cit. on p. 116).
- [119] A. Anghel, G. Vasile, C. Ioana, R. Cacoveanu, and S. Ciochina. “Micro-Doppler Reconstruction in Spaceborne SAR images using Azimuth Time-Frequency Tracking of the Phase History”. In: *submitted to IEEE Geoscience and Remote Sensing Letters* (2015) (cit. on p. 117).
- [126] N. Besic, G. Vasile, A. Anghel, T. Petrut, C. Ioana, S. Stankovic, A. Girard, and G. d’Urso. “Zernike Ultrasonic Tomography for Fluid Velocity Imaging based on Pipeline Intrusive Time-of-Flight Measurements”. In: *IEEE Transactions on Ultrasonics, Ferroelectrics, and Frequency Control* 61.11 (Nov. 2014).
- [128] A. Anghel and R. Cacoveanu. “Improved Composite Right/Left-Handed Cell for Leaky-Wave Antenna”. In: *Progress in Electromagnetics Research Letters* 22 (2011), pp. 59–69.

## National journal papers:

- [63] G. Vasile, A. Anghel, D. Boldo, R. Boudon, G. d’Urso, and R. Muja. “Potential of Multi-Pass High-Resolution SAR Interferometry for Dam Monitoring”. In: *MTA Review (ISSN 1843-3391), special issue of the COMM’12 conference, Romanian Military Technical Academy Publishing House* 22.4 (2012), pp. 235–246 (cit. on p. 37).

- [124] A. Anghel and R. Cacoveanu. “A new microstrip composite right/left-handed transmission line implementation”. In: *University Politehnica of Bucharest Scientific Bulletin, Series C* 73.4 (2011), pp. 235–246.

### Conference papers:

- [64] A. Anghel, G. Vasile, C. Ioana, R. Cacoveanu, S. Ciocchina, J.-P. Ovarlez, R. Boudon, and G. d’Urso. “SAR Images Refocusing and Scattering Center Detection for Infrastructure Monitoring”. In: *Proceedings of the IEEE Radar Conference (RadarCon)*. Cincinnati, Ohio, USA, May 2014, pp. 334–339 (cit. on pp. 38, 115).
- [65] A. Anghel, G. Vasile, C. Ioana, R. Cacoveanu, S. Ciocchina, J.-P. Ovarlez, R. Boudon, G. d’Urso, and I. Hajnsek. “Scattering centers monitoring in refocused SAR images on a high-resolution DEM”. In: *Proceedings of the IEEE International Geoscience and Remote Sensing Symposium (IGARSS)*. Quebec City, QC, Canada, 2014, pp. 1883–1886 (cit. on pp. 38, 115).
- [86] A. Anghel, G. Vasile, J.-P. Ovarlez, G. D’Urso, and D. Boldo. “Stable Scatterers detection and tracking in heterogeneous clutter by repeat-pass SAR interferometry”. In: *Proceedings of the European Conference on Synthetic Aperture Radar (EuSAR)*. Nuremberg, Germany, Apr. 2012, pp. 477–480 (cit. on pp. 64, 80).
- [97] A. Anghel, G. Vasile, R. Cacoveanu, C. Ioana, and S. Ciocchina. “Short-range FMCW X-band radar platform for millimetric displacements measurement”. In: *Proceedings of the IEEE International Geoscience and Remote Sensing Symposium*. Melbourne, Australia, July 2013, pp. 1111–1114 (cit. on pp. 67, 115).
- [111] A. Anghel, G. Vasile, R. Cacoveanu, C. Ioana, and S. Ciocchina. “FMCW Transceiver Wideband Sweep Nonlinearity Software Correction”. In: *Proceedings of the IEEE Radar Conference (RadarCon)*. Ottawa, ON, Canada, May 2013 (cit. on p. 115).
- [112] A. Anghel, G. Vasile, R. Cacoveanu, C. Ioana, and S. Ciocchina. “Nonlinearity correction algorithm for wideband FMCW radars”. In: *Proceedings of the European Signal Processing Conference (EUSIPCO)*. Marrakech, Morocco, Sept. 2013, pp. 1–5 (cit. on p. 115).
- [113] A. Anghel, G. Vasile, R. Cacoveanu, C. Ioana, and S. Ciocchina. “Range Autofocusing for FMCW Radars using Time Warping and a Spectral Concentration Measure”. In: *Proceedings of the 2015 IEEE International Radar Conference*. Arlington, VA, USA, May 2015, pp. 581–586 (cit. on p. 115).

## Publications

---

- [116] A. Anghel, G. Vasile, C. Ioana, R. Cacoveanu, and S. Ciochina. “Model-based Parameters Estimation of Non-stationary Signals using Time Warping and a Measure of Spectral Concentration”. In: *Proceedings of the IEEE International Conference on Acoustics, Speech, and Signal Processing (ICASSP)*. Brisbane, Australia, Apr. 2015, pp. 3706–3710 (cit. on p. 116).
- [117] A. Anghel, G. Vasile, C. Ioana, R. Cacoveanu, and S. Ciochina. “On the Detection of Non-stationary Signals in the Matched Signal Transform Domain”. In: *submitted to 2016 IEEE International Conference on Acoustics, Speech, and Signal Processing (ICASSP)* (2016) (cit. on p. 117).
- [118] A. Anghel, G. Vasile, C. Ioana, R. Cacoveanu, and S. Ciochina. “Vibration Estimation in SAR images using Azimuth Time-Frequency Tracking and a Matched Signal Transform”. In: *Proceedings of the IEEE International Geoscience and Remote Sensing Symposium (IGARSS)*. Milan, Italy, July 2015, pp. 2576–2579 (cit. on p. 117).
- [125] G. Vasile, N. Besic, A. Anghel, C. Ioana, and J. Chanussot. “Sphericity of complex stochastic models in multivariate SAR images”. In: *Proceedings of the IEEE International Geoscience and Remote Sensing Symposium (IGARSS)*. Melbourne, Australia, July 2013, pp. 2994–2997.
- [127] L. Pralon, G. Vasile, A. Anghel, and N. Besic. “On the Robustness of the ICA based ICTD with respect to the Spherical Symmetry of the POLSAR data”. In: *Proceedings of the IEEE International Geoscience and Remote Sensing Symposium (IGARSS)*. Milan, Italy, July 2015, pp. 1570–1573.



# Bibliography

- [1] A. Ferretti, C. Prati, and F. Rocca. “Nonlinear subsidence rate estimation using permanent scatterers in differential SAR interferometry”. In: *IEEE Transactions on Geoscience and Remote Sensing* 38.5 (Sept. 2000), pp. 2202–2212 (cit. on p. 3).
- [2] M. Eineder, N. Adam, R. Bamler, N. Yague-Martinez, and H. Breit. “Spaceborne Spotlight SAR Interferometry With TerraSAR-X”. In: *IEEE Transactions on Geoscience and Remote Sensing* 47.5 (2009), pp. 1524–1535 (cit. on pp. 3, 37, 39, 45, 93).
- [3] T. Fritz, C. Rossi, N. Yague-Martinez, F. Rodriguez-Gonzalez, M. Lachaise, and H. Breit. “Interferometric processing of TanDEM-X data”. In: *Proceedings of the IEEE International Geoscience and Remote Sensing Symposium (IGARSS)*. Vancouver, Canada, 2011, pp. 2428–2431 (cit. on pp. 3, 37).
- [4] M.T. Chiaradia, G. Fornaro, A. Freni, G. Franceschetti, P. Imperatore, F. Intini, A. Iodice, A. Mori, D.O. Nitti, R. Nutricato, D. Reale, D. Riccio, and P. Trivero. “COSMO/SkyMed AO projects - advanced 2D and 3D Focusing of COSMO/SkyMed SAR data”. In: *Proceedings of the IEEE International Geoscience and Remote Sensing Symposium (IGARSS)*. Munich, Germany, July 2012, pp. 6797–6800 (cit. on p. 3).
- [5] N. Acito, S. Resta, G. Corsini, and M. Diani. “Change detection in spotlight SAR Cosmo-SkyMed images for harbour infrastructures monitoring: A case study”. In: *Tyrrhenian Workshop on Advances in Radar and Remote Sensing (TyWRRS)*. Naples, Italy, Sept. 2012, pp. 193–197 (cit. on p. 3).
- [6] D. Massonnet. “Producing ground deformation maps automatically: the DIAPASON concept”. In: *Proceedings of the IEEE International Geoscience and Remote Sensing (IGARSS)*. Vol. 3. Singapore, Aug. 1997, 1338–1340 vol.3 (cit. on p. 3).
- [7] P.A. Rosen, S. Hensley, G. Peltzer, and M. Simons. “Updated repeat orbit interferometry package released”. In: *Eos Transactions American Geophysical Union* 85.5 (2004), pp. 47–47 (cit. on p. 3).
- [8] F. Lombardini. “Differential tomography: a new framework for SAR interferometry”. In: *IEEE Transactions on Geoscience and Remote Sensing* 43.1 (2005), pp. 37–44 (cit. on pp. 3, 38, 51).

- [9] G. Fornaro, D. Reale, and F. Serafino. “Four-Dimensional SAR Imaging for Height Estimation and Monitoring of Single and Double Scatterers”. In: *IEEE Transactions on Geoscience and Remote Sensing* 47.1 (2009), pp. 224–237 (cit. on pp. 3, 20, 21, 38, 39, 47, 64).
- [10] F. Lombardini and M. Pardini. “Superresolution Differential Tomography: Experiments on Identification of Multiple Scatterers in Spaceborne SAR Data”. In: *IEEE Transactions on Geoscience and Remote Sensing* 50.4 (2012), pp. 1117–1129 (cit. on pp. 3, 21, 38, 64).
- [11] S. Peleg and B. Porat. “Estimation and classification of signals with polynomial phase”. In: *IEEE Transactions on Information Theory* 37.2 (1991), pp. 422–430 (cit. on pp. 10, 13).
- [12] Y. Wang and G. Zhou. “On the use of high order ambiguity functions for multi-component polynomial phase signals”. In: *Signal Processing* 65 (1998), pp. 283–296 (cit. on pp. 10, 12).
- [13] S. Barbarossa, A. Scaglione, and G. B. Giannakis. “Product high-order ambiguity function for multicomponent polynomial-phase signal modeling”. In: *IEEE Transactions on Signal Processing* 46.3 (Mar. 1998), pp. 691–708 (cit. on pp. 10, 14, 29).
- [14] C. Ioana and A. Quinquis. “Time-Frequency Analysis using Warped-based High-Order Phase Modeling”. In: *EURASIP Journal on Applied Signal Processing* 17 (2005), pp. 2856–2873 (cit. on pp. 10, 13).
- [15] D.-S. Pham and A.M. Zoubir. “Analysis of Multicomponent Polynomial Phase Signals”. In: *IEEE Transactions on Signal Processing* 55.1 (Jan. 2007), pp. 56–65 (cit. on pp. 10, 28).
- [16] A. Papandreou-Suppappola. “Generalized time-shift covariant quadratic time-frequency representations with arbitrary group delays”. In: *Conference Record of the Twenty-Ninth Asilomar Conference on Signals, Systems and Computers*. Vol. 1. Pacific Grove, CA, USA, Oct. 1995, pp. 553–557 (cit. on p. 10).
- [17] H. Shen and A. Papandreou-Suppappola. “Wideband time-varying interference suppression using matched signal transforms”. In: *IEEE Transactions on Signal Processing* 53.7 (July 2005), pp. 2607–2612 (cit. on pp. 10, 16).
- [18] A. Papandreou-Suppappola, F. Hlawatsch, and G. F. Boudreux-Bartels. “Quadratic Time-Frequency Representations with Scale Covariance and Generalized Time-Shift Covariance: A Unified Framework for the Affine, Hyperbolic, and Power Classes”. In: *Digital Signal Processing* 8.1 (Jan. 1998), pp. 3 –48 (cit. on p. 10).

## Bibliography

---

- [19] A. Papandreou, F. Hlawatsch, and G.F. Boudreux-Bartels. “The hyperbolic class of quadratic time-frequency representations. I. Constant-Q warping, the hyperbolic paradigm, properties, and members”. In: *IEEE Transactions on Signal Processing* 41.12 (Dec. 1993), pp. 3425–3444 (cit. on p. 10).
- [20] J.-P. Ovarlez, J. Bertrand, and P. Bertrand. “Computation of affine time-frequency distributions using the fast Mellin transform”. In: *Proceedings of the IEEE International Conference on Acoustics, Speech, and Signal Processing*. Vol. 5. San Francisco, CA, USA, Mar. 1992, pp. 117–120 (cit. on p. 10).
- [21] A. Papandreou-Suppappola and G.F. Boudreux-Bartels. “The exponential class and generalized time-shift covariant quadratic time-frequency representations”. In: *Proceedings of the IEEE-SP International Symposium on Time-Frequency and Time-Scale Analysis*. Pittsburgh, PA, USA, June 1996, pp. 429–432 (cit. on p. 10).
- [22] L. Stankovic, M. Dakovic, and T. Thayaparan. *Time-Frequency Signal Analysis with Applications*. Boston: Artech House, 2013 (cit. on pp. 10, 12).
- [23] J.-P. Ovarlez. *Temps-Fréquence - Cours ENST*. Apr. 1998 (cit. on p. 10).
- [24] D.L. Jones and T.W. Parks. “A high resolution data-adaptive time-frequency representation”. In: *IEEE Transactions on Acoustics, Speech and Signal Processing* 38.12 (Dec. 1990), pp. 2127–2135 (cit. on p. 12).
- [25] P. Flandrin, R.G. Baraniuk, and O. Michel. “Time-frequency complexity and information”. In: *Proceedings of the IEEE International Conference on Acoustics, Speech, and Signal Processing*. Vol. 3. Adelaide, Australia, Apr. 1994, pp. 329–332 (cit. on p. 12).
- [26] T.-H. Sang and W.J. Williams. “Renyi information and signal-dependent optimal kernel design”. In: *Proceedings of the IEEE International Conference on Acoustics, Speech, and Signal Processing*. Vol. 2. Detroit, MI, USA, May 1995, pp. 997–1000 (cit. on p. 12).
- [27] L. Stankovic. “A measure of some time-frequency distributions concentration”. In: *Signal Processing* 81.3 (Mar. 2001), pp. 621–631 (cit. on pp. 12, 30).
- [28] R.G. Baraniuk and D.L. Jones. “Unitary equivalence: a new twist on signal processing”. In: *IEEE Transactions on Signal Processing* 43.10 (Oct. 1995), pp. 2269–2282 (cit. on p. 15).
- [29] M.D. Desai and W.K. Jenkins. “Convolution backprojection image reconstruction for spotlight mode synthetic aperture radar”. In: *IEEE Transactions on Image Processing* 1.4 (Oct. 1992), pp. 505–517 (cit. on pp. 18, 45).
- [30] Marcelo Albuquerque, Pau Prats, and Rolf Scheiber. “Applications of Time-Domain Back-Projection SAR Processing in the Airborne Case”. In: *Proceedings of the European Conference on Synthetic Aperture Radar (EuSAR)*. Friedrichshafen, Germany, June 2008, pp. 1–4 (cit. on pp. 18, 45).

- [31] A. Reigber and A. Moreira. “First demonstration of airborne SAR tomography using multibaseline L-band data”. In: *IEEE Transactions on Geoscience and Remote Sensing* 38.5 (Sept. 2000), pp. 2142–2152 (cit. on p. 21).
- [32] G. Fornaro, F. Serafino, and F. Soldovieri. “Three-dimensional focusing with multipass SAR data”. In: *IEEE Transactions on Geoscience and Remote Sensing* 41.3 (Mar. 2003), pp. 507–517 (cit. on p. 21).
- [33] J. Capon. “High-resolution frequency-wavenumber spectrum analysis”. In: *Proceedings of the IEEE* 57.8 (1969), pp. 1408–1418 (cit. on p. 21).
- [34] M. Capelli. “Radio Altimeter”. In: *Aeronautical and Navigational Electronics, Transactions of the IRE Professional Group on ANE-1.2* (June 1954), pp. 3–7 (cit. on p. 23).
- [35] P. Lowbridge. “A low cost mm-wave cruise control system for automotive applications”. In: *Microwave Journal* (Oct. 1993), pp. 24–36 (cit. on p. 23).
- [36] A.G. Stove. “Linear FMCW radar techniques”. In: *IEE Proceedings Part F Radar and Signal Processing* 139.5 (Oct. 1998), pp. 283–296 (cit. on p. 23).
- [37] F. Bao, L. Arend, S. Bertl, and J. Detlefsen. “Application of FMCW radar principle for fast inhomogeneity identification on transmission lines”. In: *Proceedings of the German Microwave Conference (GeMIC)*. Darmstadt, Germany, Mar. 2011, pp. 1–4 (cit. on p. 23).
- [38] A. Meta, P. Hoogeboom, and L. P. Ligthart. “Signal Processing for FMCW SAR”. In: *IEEE Transactions on Geoscience and Remote Sensing* 45.11 (Nov. 2007), pp. 3519–3532 (cit. on p. 24).
- [39] P.J. Burke. “Ultra-linear chirp generation via VCO tuning predistortion”. In: *IEEE MTT-S International Microwave Symposium Digest*. Vol. 2. San Diego, CA, USA, May 1994, pp. 957–960 (cit. on p. 24).
- [40] S. Scheiblhofer, S. Schuster, and A. Stelzer. “High-Speed FMCW Radar Frequency Synthesizer With DDS Based Linearization”. In: *IEEE Microwave and Wireless Components Letters* 17.5 (May 2007), pp. 397–399 (cit. on p. 24).
- [41] W.J. Caputi. “Stabilized Linear FM Generator”. In: *IEEE Transactions on Aerospace and Electronic Systems* 9.5 (Sept. 1973), pp. 670–678 (cit. on p. 24).
- [42] N. Pohl, T. Jacschke, and M. Vogt. “Ultra High Resolution SAR Imaging using an 80 GHz FMCW-Radar with 25 GHz Bandwidth”. In: *Proceedings of the European Synthetic Aperture Radar Conference (EuSAR)*. Nuremberg, Germany, Apr. 2012, pp. 189–192 (cit. on p. 24).
- [43] T. Mitomo, N. Ono, H. Hoshino, Y. Yoshihara, O. Watanabe, and I. Seto. “A 77 GHz 90 nm CMOS Transceiver for FMCW Radar Applications”. In: *IEEE Journal of Solid-State Circuits* 45.4 (Apr. 2010), pp. 928–937 (cit. on p. 24).

## Bibliography

---

- [44] C. Wagner, R. Feger, A. Haderer, A. Fischer, A. Stelzer, and H. Jager. “A 77-GHz FMCW radar using a digital phase-locked synthesizer”. In: *Microwave Symposium Digest, IEEE MTT-S International*. June 2008, pp. 351–354 (cit. on p. 24).
- [45] M. Vossiek, P. Heide, M. Nalezinski, and V. Magori. “Novel FMCW radar system concept with adaptive compensation of phase errors”. In: *Proceedings of the European Microwave Conference (EuMC)*. Vol. 1. Prague, Czech Republic, Sept. 1996, pp. 135–138 (cit. on pp. 24, 36, 73).
- [46] A. Meta, P. Hoogeboom, and L. Ligthart. “Range nonlinearities correction in FMCW SAR”. In: *Proceedings of the IEEE International Geoscience and Remote Sensing Symposium (IGARSS)*. Denver, CO, USA, July 2006, pp. 403–406 (cit. on pp. 24, 36, 73).
- [47] Jian Yang, Chang Liu, and Yanfei Wang. “Nonlinearity Correction of FMCW SAR Based on Homomorphic Deconvolution”. In: *IEEE Geoscience and Remote Sensing Letters* 10.5 (Sept. 2013), pp. 991–995 (cit. on p. 24).
- [48] R.J.C. Middleton, D.G. Macfarlane, and D.A. Robertson. “Range autofocus for linearly frequency-modulated continuous wave radar”. In: *IET Radar, Sonar Navigation* 5.3 (Mar. 2011), pp. 288–295 (cit. on p. 24).
- [49] E. Avignon-Meseldzija, W. Liu, H. Feng, S. Azarian, M. Lesturgie, and Y. Lu. “Compensation of Analog Imperfections in a Ka-band FMCW SAR”. In: *Proceedings of the European Synthetic Aperture Radar Conference (EuSAR)*. Nuremberg, Germany, Apr. 2012, pp. 60–63 (cit. on pp. 24, 73).
- [50] W. Ying, L. Qingshan, G. Deyun, and Z. Guangyong. “Research on Nonlinearity correction Imaging Algorithm of FMCW SAR”. In: *Proceedings of the International Conference on Signal Processing Systems (ICSPS)*. Vol. 1. Dalian, China, July 2010, pp. 425–429 (cit. on p. 24).
- [51] F. A. Marvasti. *Nonuniform Sampling: Theory and Practice*. New York: Kluwer Academic/Plenum Publishers, 2001 (cit. on p. 26).
- [52] S. M. Kay. *Fundamentals of Statistical Signal Processing: Estimation Theory*. Vol. 1. New Jersey: Prentice Hall PTR, 1993 (cit. on p. 28).
- [53] B. Porat and B. Friedlander. “Accuracy analysis of estimation algorithms for parameters of multiple polynomial-phase signals”. In: *Proceedings of the IEEE International Conference on Acoustics, Speech and Signal Processing*. Detroit, MI, USA, May 1995, pp. 1800–1803 (cit. on p. 29).
- [54] J. A. Nelder and R. Mead. “A Simplex Method for Function Minimization”. In: *The Computer Journal* 7.4 (1965), pp. 308–313. eprint: <http://comjnl.oxfordjournals.org/content/7/4/308.full.pdf+html> (cit. on p. 30).

- [55] J.C. Lagarias, J. A. Reeds, M. H. Wright, and P. E. Wright. “Convergence Properties of the Nelder-Mead Simplex Method in Low Dimensions”. In: *SIAM Journal on Optimization* 9.1 (1998), pp. 112–147 (cit. on p. 30).
- [56] J. D’Errico. *Bound constrained optimization using fminsearch*. MATLAB Central File Exchange. 2012 (cit. on p. 31).
- [57] L. Weruaga and M. Kepesi. “The fan-chirp transform for nonstationary harmonic signals”. In: *Signal Processing* 87.6 (June 2007), pp. 1504–1522 (cit. on p. 31).
- [58] Marián Képesi and Luis Weruaga. “Adaptive chirp-based time–frequency analysis of speech signals”. In: *Speech Communication* 48.5 (2006), pp. 474 –492 (cit. on p. 31).
- [59] F. Zhang, Y. Q. Chen, and G. Bi. “Adaptive harmonic fractional Fourier transform”. In: *IEEE Signal Processing Letters* 6.11 (Nov. 1999), pp. 281–283 (cit. on p. 31).
- [60] J.G. Vargas-Rubio and B. Santhanam. “An improved spectrogram using the multi-angle centered discrete fractional Fourier transform”. In: *Proceedings of the IEEE International Conference on Acoustics, Speech, and Signal Processing (ICASSP)*. Vol. 4. Philadelphia, PA, USA, Mar. 2005, pp. 505–508 (cit. on p. 31).
- [61] P.V. Brennan, Y. Huang, M. Ash, and K. Chetty. “Determination of Sweep Linearity requirements in FMCW Radar Systems Based on Simple Voltage-Controlled Oscillator Sources”. In: *IEEE Transactions on Aerospace and Electronic Systems* 47.3 (July 2011), pp. 1594–1604 (cit. on p. 32).
- [62] United States Department of Defense. “General specification for crystal controlled oscillator. Specification MIL-PRF-55310”. In: Columbus, OH, 2006 (cit. on p. 32).
- [66] S. Ugur, O. Arikan, and A.C. Gurbuz. “Off-grid sparse SAR image reconstruction by EMMP algorithm”. In: *Proceedings of the IEEE Radar Conference (RadarCon)*. Ottawa, ON, Canada, 2013, pp. 1–4 (cit. on p. 38).
- [67] Antonio De Maio, G. Fornaro, and A. Pauciullo. “Detection of Single Scatterers in Multidimensional SAR Imaging”. In: *IEEE Transactions on Geoscience and Remote Sensing* 47.7 (July 2009), pp. 2284–2297 (cit. on pp. 39, 61).
- [68] A. Pauciullo, D. Reale, Antonio De Maio, and G. Fornaro. “Detection of Double Scatterers in SAR Tomography”. In: *IEEE Transactions on Geoscience and Remote Sensing* 50.9 (2012), pp. 3567–3586 (cit. on p. 39).
- [69] D. Reale, G. Fornaro, and A. Pauciullo. “Extension of 4-D SAR Imaging to the Monitoring of Thermally Dilating Scatterers”. In: *IEEE Transactions on Geoscience and Remote Sensing* 51.12 (Dec. 2013), pp. 5296–5306 (cit. on p. 39).
- [70] A. Moreira, J. Mittermayer, and R. Scheiber. “Extended chirp scaling algorithm for air- and spaceborne SAR data processing in stripmap and ScanSAR imaging modes”. In: *IEEE Transactions on Geoscience and Remote Sensing* 34.5 (1996), pp. 1123–1136 (cit. on p. 42).

## Bibliography

---

- [71] J. Mittermayer, A. Moreira, and O. Loffeld. “Spotlight SAR data processing using the frequency scaling algorithm”. In: *IEEE Transactions on Geoscience and Remote Sensing* 37.5 (1999), pp. 2198–2214 (cit. on pp. 42, 44, 48).
- [72] A. Moreira. “Real-time synthetic aperture radar (SAR) processing with a new sub-aperture approach”. In: *IEEE Transactions on Geoscience and Remote Sensing* 30.4 (1992), pp. 714–722 (cit. on p. 42).
- [73] J. Mittermayer, R. Lord, and E. Borner. “Sliding spotlight SAR processing for TerraSAR-X using a new formulation of the extended chirp scaling algorithm”. In: *Proceedings of the IEEE International Geoscience and Remote Sensing Symposium (IGARSS)*. Vol. 3. Toulouse, France, July 2003, pp. 1462–1464 (cit. on p. 42).
- [74] P. Prats, R. Scheiber, J. Mittermayer, A. Meta, and A. Moreira. “Processing of Sliding Spotlight and TOPS SAR Data Using Baseband Azimuth Scaling”. In: *IEEE Transactions on Geoscience and Remote Sensing* 48.2 (Feb. 2010), pp. 770–780 (cit. on p. 42).
- [75] M. Sack, M.R. Ito, and I.G. Cumming. “Application of efficient linear FM matched filtering algorithms to synthetic aperture radar processing”. In: *IEE Proceedings F Communications, Radar and Signal Processing*, 132.1 (Feb. 1985), pp. 45–57 (cit. on p. 43).
- [76] W. G. Carrara, R. S. Goodman, and R. M. Majewski. *Spotlight Synthetic Aperture Radar: Signal Processing Algorithms*. Boston: Artech House, 1995 (cit. on pp. 43, 44, 69).
- [77] M Born and E Wolf. “Principles of Optics”. In: Cambridge University Press, 1999. Chap. Appendix 3 (cit. on p. 44).
- [78] R.K. Raney. “A New And Fundamental Fourier Transform Pair”. In: *Proceedings of the IEEE International Geoscience and Remote Sensing Symposium (IGARSS)*. Vol. 1. Houston, TX, USA, 1992, pp. 106–107 (cit. on p. 44).
- [79] T. Fritz, Mittermayer J., B. Schättler, Balzer W., S. Buckreuß, and R. Werninghaus. “TerraSAR-X Ground Segment Level 1b Product Format Specification”. In: DLR, 2007 (cit. on pp. 45, 93).
- [80] P. Prats-Iraola, R. Scheiber, M. Rodriguez-Cassola, S. Wollstadt, J. Mittermayer, B. Brautigam, M. Schwerdt, A. Reigber, and A. Moreira. “High precision SAR focusing of TerraSAR-X experimental staring spotlight data”. In: *Proceedings of the IEEE International Geoscience and Remote Sensing Symposium (IGARSS)*. 2012, pp. 3576–3579 (cit. on p. 45).
- [81] Jr. Munson D.C., J.D. O’Brien, and W. Jenkins. “A tomographic formulation of spotlight-mode synthetic aperture radar”. In: *Proceedings of the IEEE* 71.8 (Aug. 1983), pp. 917–925 (cit. on p. 45).

- [82] LeRoy A. Gorham and Linda J. Moore. “SAR image formation toolbox for MATLAB”. In: vol. 7699. 2010, pp. 769906–769906–13 (cit. on pp. 45, 64).
- [83] H.L. Van Trees. “Detection, Estimation, and Modulation Theory: Optimum Array Processing”. In: New York, Wiley-Interscience, 2002 (cit. on p. 51).
- [84] A. Ferretti, C. Prati, and F. Rocca. “Permanent scatterers in SAR interferometry”. In: *IEEE Transactions on Geoscience and Remote Sensing* 39.1 (Jan. 2001), pp. 8–20 (cit. on pp. 61, 64).
- [85] C. Colesanti, A. Ferretti, F. Novali, C. Prati, and F. Rocca. “SAR monitoring of progressive and seasonal ground deformation using the permanent scatterers technique”. In: *IEEE Transactions on Geoscience and Remote Sensing* 41.7 (July 2003), pp. 1685–1701 (cit. on pp. 61, 64).
- [87] G. Vasile, J. Ovarlez, F. Pascal, M. Gay, G. D’Urso, and D. Boldo. “Stable Scatterers detection and tracking in heterogeneous clutter by repeat-pass SAR interferometry”. In: *Conference Record of the Forty Fourth Asilomar Conference on Signals, Systems and Computers (ASILOMAR)*. Pacific Grove, CA, USA, Nov. 2010, pp. 1343–1347 (cit. on p. 64).
- [88] F. Serafino. “SAR image coregistration based on isolated point scatterers”. In: *IEEE Geoscience and Remote Sensing Letters* 3.3 (July 2006), pp. 354–358 (cit. on p. 64).
- [89] R. Scheiber and A. Moreira. “Coregistration of interferometric SAR images using spectral diversity”. In: *IEEE Transactions on Geoscience and Remote Sensing* 38.5 (Sept. 2000), pp. 2179–2191 (cit. on p. 64).
- [90] S. Sauer, L. Ferro-Famil, A. Reigber, and E. Pottier. “Three-Dimensional Imaging and Scattering Mechanism Estimation Over Urban Scenes Using Dual-Baseline Polarimetric InSAR Observations at L-Band”. In: *IEEE Transactions on Geoscience and Remote Sensing* 49.11 (Nov. 2011), pp. 4616–4629 (cit. on p. 64).
- [91] M. Nannini, R. Scheiber, and A. Moreira. “Estimation of the Minimum Number of Tracks for SAR Tomography”. In: *IEEE Transactions on Geoscience and Remote Sensing* 47.2 (Feb. 2009), pp. 531–543 (cit. on p. 64).
- [92] Xiao Xiang Zhu and R. Bamler. “Tomographic SAR Inversion by  $L_1$ -Norm Regularization-The Compressive Sensing Approach”. In: *IEEE Transactions on Geoscience and Remote Sensing* 48.10 (Oct. 2010), pp. 3839–3846 (cit. on p. 64).
- [93] Xiao Xiang Zhu and R. Bamler. “Let’s Do the Time Warp: Multicomponent Non-linear Motion Estimation in Differential SAR Tomography”. In: *IEEE Geoscience and Remote Sensing Letters* 8.4 (July 2011), pp. 735–739 (cit. on p. 64).
- [94] A. Meta, P. Hakkart, F.V. der Zwan, P. Hoogeboom, and L. Ligthart. “First demonstration of an X-band airborne FMCW SAR”. In: *Proceedings of the European Synthetic Aperture Radar Conference EuSAR*. Dresden, Germany, May 2006, pp. 1–4 (cit. on p. 67).

## Bibliography

---

- [95] G. L. Charvat. “Low-Cost, High Resolution X-Band Laboratory Radar System for Synthetic Aperture Radar Applications”. In: *Proceedings of the IEEE International Conference on Electro/information Technology*. East Lansing, MI, USA, May 2006, pp. 529–531 (cit. on p. 67).
- [96] L. Besser and R. Gilmore. *Practical RF Circuit Design for Modern Wireless Systems*. London: Artech House, 2003 (cit. on p. 67).
- [98] G. L. Charvat, L. C. Kempel, E. J. Rothwell, C. M. Coleman, and E. L. Mokole. “A Through-Dielectric Ultrawideband (UWB) Switched-Antenna-Array Radar Imaging System”. In: *IEEE Transactions on Antennas and Propagation* 60.11 (2012), pp. 5495–5500 (cit. on pp. 67, 68).
- [99] G.L. Charvat, Leo C. Kempel, E.J. Rothwell, C.M. Coleman, and E. Mokole. “A Through-Dielectric Radar Imaging System”. In: *IEEE Transactions on Antennas and Propagation* 58.8 (2010), pp. 2594–2603 (cit. on pp. 67, 68).
- [100] G.L. Charvat, L. Kempell, and C. Coleman. “A Low-Power High-Sensitivity X-Band Rail SAR Imaging System [Measurement’s Corner]”. In: *IEEE Antennas and Propagation Magazine* 50.3 (2008), pp. 108–115 (cit. on pp. 67, 68).
- [101] G.L. Charvat. “A Low-Power Radar Imaging System”. In: *Ph.D. dissertation, Department of Electrical and Computer Engineering, Michigan State University*. East Lansing, MI, 2007 (cit. on pp. 67, 70).
- [102] Jungang Yang, J. Thompson, Xiaotao Huang, Tian Jin, and Zhimin Zhou. “Random-Frequency SAR Imaging Based on Compressed Sensing”. In: *IEEE Transactions on Geoscience and Remote Sensing* 51.2 (2013), pp. 983–994 (cit. on p. 68).
- [103] Adriano Meta. “Signal processing of FMCW synthetic aperture radar data”. In: *Ph.D. dissertation, Delft Univ. Technol.* Delft, The Netherlands, 2006 (cit. on p. 68).
- [104] M. Soumekh. *Synthetic Aperture Radar Signal Processing: with MATLAB Algorithms*. New York: John Wiley & Sons, 1999 (cit. on p. 75).
- [105] R. Touzi, A. Lopes, J. Bruniquel, and P.W. Vachon. “Coherence estimation for SAR imagery”. In: *IEEE Transactions on Geoscience and Remote Sensing* 37.1 (1999), pp. 135–149 (cit. on p. 80).
- [106] T. Fritz, H. Breit, and M. Eineder. “TerraSAR-X Products – Tips and Tricks”. In: *TerraSAR-X Science Meeting 2008*. DLR, Oberpfaffenhofen, Germany, 2008 (cit. on p. 93).
- [107] A. Schubert, M. Jehle, D. Small, and E. Meier. “Influence of Atmospheric Path Delay on the Absolute Geolocation Accuracy of TerraSAR-X High-Resolution Products”. In: *Geoscience and Remote Sensing, IEEE Transactions on* 48.2 (Feb. 2010), pp. 751–758 (cit. on p. 94).

- [108] A. Ferretti, G. Savio, R. Barzaghi, A. Borghi, S. Musazzi, F. Novali, C. Prati, and F. Rocca. “Submillimeter Accuracy of InSAR Time Series: Experimental Validation”. In: *IEEE Transactions on Geoscience and Remote Sensing* 45.5 (May 2007), pp. 1142–1153 (cit. on p. 102).
- [109] D. York, N. Evensen, M. Martinez, and J. Delgado. “Unified equations for the slope, intercept, and standard errors of the best straight line”. In: *American Journal of Physics* 72.3 (Mar. 2004) (cit. on p. 102).
- [120] Lianhuan Wei, T. Balz, Lu Zhang, and Mingsheng Liao. “A Novel Fast Approach for SAR Tomography: Two-Step Iterative Shrinkage/Thresholding”. In: *Geoscience and Remote Sensing Letters, IEEE* 12.6 (June 2015), pp. 1377–1381 (cit. on p. 117).
- [121] G. Fornaro, A. Pauciullo, D. Reale, and S. Verde. “Multilook SAR tomography for sensing built structures with very high resolution spaceborne sensors”. In: *European Radar Conference (EuRAD), 2014 11th*. Oct. 2014, pp. 221–224 (cit. on p. 117).
- [122] F. Biondi. “SAR tomography optimization by Interior Point Methods via atomic decomposition - The Convex Optimization approach”. In: *Geoscience and Remote Sensing Symposium (IGARSS), 2014 IEEE International*. July 2014, pp. 1879–1882 (cit. on p. 117).
- [123] M.J. Sanjuan-Ferrer, I. Hajnsek, K.P. Papathanassiou, and A. Moreira. “A New Detection Algorithm for Coherent Scatterers in SAR Data”. In: *IEEE Transactions on Geoscience and Remote Sensing* 53.11 (Nov. 2015), pp. 6293–6307 (cit. on p. 117).

# *Abstract (en)*

## **High-Resolution Time-Frequency SAR Signal Processing for Large Infrastructure Monitoring**

**Key words:** Signal Processing, Time-Frequency, Radar, Interferometry, SAR Tomography.

---

The thesis is composed of two research axis. The first one consists in proposing time-frequency signal processing tools for frequency modulated continuous wave (FMCW) radars used for displacements measurements, while the second one consists in designing a spaceborne synthetic aperture radar (SAR) signal processing methodology for infrastructure monitoring when an external point cloud of the envisaged structure is available.

In the first part of the thesis, we propose our solutions to the nonlinearity problem of an X-band FMCW radar designed for millimetric displacement measurements of short-range targets. The nonlinear tuning curve of the voltage controlled oscillator from the transceiver can cause a dramatic resolution degradation for wideband sweeps. To mitigate this shortcoming, we have developed two time warping-based methods adapted to wideband nonlinearities: one estimates the nonlinear terms using the high order ambiguity function, while the other is an autofocus approach which exploits the spectral concentration of the beat signal.

Onwards, as the core of the thesis, we propose a novel method for scattering centers detection and tracking in spaceborne SAR images adapted to infrastructure monitoring applications. The method is based on refocusing each SAR image on a provided 3D point cloud of the envisaged infrastructure and identifying the reliable scatterers to be monitored by means of four dimensional (4D) tomography. The refocusing algorithm is compatible with stripmap, spotlight and sliding spotlight SAR images and consists of an azimuth defocusing followed by a modified back-projection algorithm on the given set of points which exploits the time-frequency structure of the defocused azimuth signal. The scattering centers of the refocused image are detected in the 4D tomography framework by testing if the main response is at zero elevation in the local elevation-velocity spectral distribution. The mean displacement velocity is estimated from the peak response on the zero elevation axis, while the displacements time series for detected single scatterers is computed as double phase difference of complex amplitudes.

Finally, we present the measurement campaigns carried out on the Puylaurent water-dam and the Chastel landslide using GPS measurements, topographic surveys and laser scans to generate the point clouds of the two structures. The comparison between in-situ data and the results obtained by combining TerraSAR-X data with the generated point clouds validate the developed SAR signal processing chain.

---



# Résumé (fr)

## Analyse temps-fréquence et traitement des signaux RSO à haute résolution spatiale pour la surveillance des grands ouvrages d'art

**Mots clés:** Traitement du signal, Temps-fréquence, Radar, Interférométrie, Tomographie RSO.

---

Cette thèse s'articule autour de deux axes de recherche. Le premier axe aborde les aspects méthodologiques liés au traitement temps-fréquence des signaux issus d'un radar FMCW (à onde continue modulée en fréquence) dans le contexte de la mesure des déplacements fins. Le second axe est dédié à la conception et à la validation d'une chaîne de traitement des images RSO (radar à synthèse d'ouverture) satellitaire. Lorsqu'un maillage 3D de la structure envisagée est disponible, les traitements proposés sont validés par l'intercomparaison avec les techniques conventionnelles d'auscultation des grands ouvrages d'art.

D'une part, nous étudions la correction de la non-linéarité d'un radar FMCW en bande X, à courte portée, conçu pour la mesure des déplacements millimétriques. La caractéristique de commande non linéaire de l'oscillateur à large bande, entraîne une perte de résolution à la réception. Afin de pallier cet inconvénient, nous avons développé deux méthodes basées sur le ré-échantillonnage temporel (time warping) dans le cas des signaux à large bande non-stationnaires. La première approche estime la loi de fréquence instantanée non linéaire à l'aide de la fonction d'ambiguïté d'ordre supérieur, tandis que la deuxième approche exploite la mesure de concentration spectrale du signal de battement dans un algorithme d'autofocus radial.

D'autre part, nous proposons un cadre méthodologique général pour la détection et le pistage des centres de diffusion dans les images RSO pour la surveillance des grands ouvrages d'art. La méthode est basée sur la réfocalisation de chaque image radar sur le maillage 3D de l'infrastructure étudiée afin d'identifier les diffuseurs pertinents par tomographie 4D (distance – azimut – élévation – vitesse de déformation). L'algorithme de réfocalisation est parfaitement compatible avec les images RSO acquises dans les différents modes (« stripmap », « spotlight » et « sliding spotlight ») : défocalisation en azimut suivie par rétroprojection modifiée (conditionnée par la structure temps-fréquence du signal) sur l'ensemble donné des points. Dans la pile d'images réfocalisées, les centres de diffusion sont détectés par tomographie 4D : test de conformité à l'hypothèse d'élévation zéro dans le plan élévation – vitesse de déformation. La vitesse moyenne correspond au maximum à l'élévation zéro, tandis que la série temporelle des déplacements est obtenue par double différence de phase des amplitudes complexes pour chaque diffuseur pertinent.

---

Nous présentons également les campagnes *in situ* effectuées au barrage de Puylaurent (et glissement de Chastel) : les relevés GPS, topographiques et LIDAR sol employés au calcul des maillages 3D. La comparaison entre les déplacements mesurés *in situ* et les résultats obtenus par l'exploitation conjointe de la télédétection RSO satellitaires et les maillages 3D valident la chaîne de traitement proposée.



# *Rezumat (ro)*

## **Analiza timp-frecvență și prelucrarea semnalelor SAR de înaltă rezoluție pentru monitorizarea infrastructurii critice**

**Cuvinte cheie:** Prelucrarea semnalelor, Timp-frecvență, Radar, Interferometrie, Tomografie SAR.

---

Teza cuprinde două axe principale de cercetare. Prima axă abordează aspecte metodologice de prelucrare timp-frecvență a semnalelor furnizate de radare cu emisie continuă și modulație de frecvență (FMCW) în contextul măsurării deplasărilor milimetrice. În cadrul celei de-a doua axe, este proiectată și validată o metodă de prelucrare a imaginilor satelitare SAR (radar cu apertură sintetică) ce este destinată monitorizării infrastructurii critice și care se bazează pe existența unui model 3D al structurii respective.

În prima parte a tezei, sunt investigate soluții de corecție a neliniarității unui radar FMCW în banda X destinat măsurării deplasărilor milimetrice. Caracteristica de comandă neliniară a oscilatorului de bandă largă determină o degradare a rezoluției în distanță. Pentru a rezolva acest inconvenient, au fost elaborate două metode de corecție a neliniarității, adaptate pentru semnale de bandă largă, ce se bazează pe conceptul de reeșantionare neuniformă sau deformare a axei temporare. Prima abordare estimează parametrii neliniarității utilizând funcții de ambiguitate de ordin superior, iar cea de-a doua exploatează o măsură de concentrație spectrală a semnalului de bătăi într-un algoritm de autofocalizare în distanță.

În a doua parte a lucrării, este propusă o metodologie generală de detecție și monitorizare a centrilor de împrăștiere în imagini SAR în scopul monitorizării elementelor de infrastructură critică. Metoda se bazează pe refocalizarea fiecărei imagini radar pe un model 3D al structurii investigate în scopul identificării centrilor de împrăștiere pertinenti (ținte fiabile ce pot fi monitorizate în timp) cu ajutorul tomografiei SAR 4D (distanță-azimut-elevație-viteză de deplasare). Algoritmul de refocalizare este compatibil cu imagini SAR achiziționate în moduri diferite (« stripmap », « spotlight » și « sliding spotlight ») și constă într-o defocalizare în azimut urmată de o retroproiecție modificată (condiționată de structura timp-frecvență a semnalului) pe modelul 3D al structurii. Țintele sunt identificate în stiva de imagini refocalizate cu ajutorul tomografiei 4D prin efectuarea unui test de conformitate cu ipoteza că centrii de împrăștiere pertinenti vor avea elevație zero în planul local elevație-viteză. Viteza medie de deformare corespunde maximului de pe axa de elevație nulă, iar seria temporară a deplasărilor se obține printr-o dublă diferență de fază a amplitudinilor complexe corespunzătoare țintelor identificate.

În final sunt prezentate campaniile de măsurători pe teren efectuate la un baraj și o alunecare de teren din regiunea Puylaurent (Franța) destinate obținerii modelului 3D al celor două elemente de infrastructură prin măsurători GPS, topografice și LIDAR. Comparația între deformările măsurate pe teren și rezultatele obținute prin combinarea imaginilor SAR cu modelele 3D au permis validarea metodologiei propuse.

---



# *Résumé étendu (fr)*

## **Analyse temps-fréquence et traitement des signaux RSO à haute résolution spatiale pour la surveillance des grands ouvrages d'art**

### **I Introduction**

La télédétection à micro-ondes est un type particulier de télédétection qui concerne principalement l'obtention d'informations sur les objets éloignés. Dans cette région du spectre la propagation des ondes électromagnétiques est largement indépendante des conditions climatiques. Le type le plus utilisé de télédétection à micro-ondes est la détection active (ou radar) dont les capteurs ont leur propre source d'éclairage qui les rend utiles à la fois le jour et la nuit.

Un senseur micro-ondes actif qui a été développé et largement utilisé les dernières 30 années est le radar à synthèse d'ouverture (RSO, synthetic aperture radar - SAR). Il dispose d'une large gamme d'applications dans la géoscience, la climatologie, la surveillance des ouvrages ou la cartographie. Une image RSO est essentiellement une carte bidimensionnelle de la réflectivité d'une région, obtenue en déplaçant le capteur sur la zone envisagée. La direction du mouvement est désignée azimut et la direction de la ligne de visée est considérée comme un axe de distances. La zone couverte par l'antenne du capteur en mouvement crée une antenne artificielle avec une résolution azimutale comparable à celle en distance. Un thème essentiel de recherche dans la communauté radar est l'interprétation et le traitement des informations fournies par les images RSO. Ce problème se produit car une image RSO ou une carte de réflectivité ne peuvent pas être considérées comme une image optique. Par conséquent, il y a plusieurs choses à analyser: l'interprétation physique différente pour les deux axes (azimut et distance) des images RSO, l'interaction entre la cible et l'onde électromagnétique ou la géométrie d'acquisition.

Cette thèse apporte des contributions à l'interprétation et le traitement des images RSO en utilisant l'approche temps-fréquence et vise à trouver des réponses à une question théorique et une autre plus appliquée:

- Que pouvons-nous gagner en exploitant les structures temps-fréquence non-stationnaires des signaux radar qui constituent les images RSO?

- Comment pouvons-nous mieux surveiller à l'aide d'un senseur RSO les grands ouvrages d'art pour lesquels nous avons un modèle tridimensionnel précis?

La surveillance de l'infrastructure critique à l'aide de la télédétection radar est récemment devenue de plus en plus nécessaire pour des raisons économiques et de sécurité. Un grand ouvrage d'art qui n'est pas équipé de senseurs de déformation est généralement surveillé par des relevés topographiques *in situ*. Cependant, ces relevés ne peuvent pas être effectués très souvent et des méthodes complémentaires sont souhaitables. L'utilisation des données radar terrestres ou spatiales est donc une manière faisable pour la surveillance des infrastructures.

Au cadre de cette thèse, la structure temps-fréquence et les procédés qui peuvent être utilisés sont étudiés séparément pour les radars au sol et satellitaires. Plus spécifiquement, pour le radar au sol le traitement se concentre sur les signaux en distance, tandis que les signaux du radar satellitaire sont analysés en azimut à partir d'un point de vue plus pratique.

Pour le radar au sol, nous proposons deux méthodes différentes conçues afin de palier la dégradation de la résolution en distance des radars à onde continue modulée en fréquence (frequency modulated continuous wave - FMCW) équipés des oscillateurs ayant une réponse tension/courant-fréquence non linéaire, dans le contexte de la mesure des déplacements fins. Cet inconvénient peut entraîner une forte dégradation de la résolution des images RSO au sol qui implique un rapport signal-bruit (RSB) faible et un éventuel mélange des cibles. Du point de vue des mesures de déformation, un rapport plus faible entre le niveau de crête et le niveau de bruit dans un profil de distance conduira à une forte dispersion de phase qui se traduit par une estimation de déplacement moins précis. Afin de rétablir la résolution de la plage la plus proche possible de la valeur théorique dictée par la bande du système, nous proposons une méthodologie basée sur le concept de la déformation du temps (*time warping*) ou ré-échantillonnage temporel. Dans la terminologie RSO, nous employons en fait une déformation du temps rapide (*fast time*) avec la réponse non linéaire afin d'atténuer le contenu non stationnaire en temps-fréquence induit par la non-linéarité de l'oscillateur.

Dans le cas des données satellitaires, les mesures de déformation sont obtenues par interférométrie RSO différentielle (D-InSAR) à l'aide des produits RSO comme ceux fournis par les missions TerraSAR-X, TanDEM-X ou COSMO-SkyMed. Le traitement D-InSAR nécessite généralement des étapes spécifiques utilisées pour soustraire la phase topographique de la phase interférométrique. Typiquement, la géométrie de la structure est donnée par un modèle numérique d'élévation (MNT), mais le processeur RSO n'a pas ce modèle comme entrée, et en conséquence si les structures imagées ont des variations significatives d'hauteur, les effets spécifiques de visée latérale (compression, repliement et ombrage) peuvent apparaître sur l'image RSO. Par conséquent, la position des cibles pertinentes (qui peuvent être

## Résumé étendu (fr)

---

pistées dans le temps) d'une structure ne peut pas être évidente à partir de la géométrie du radar, dans lequel les produits RSO sont livrés.

Afin d'intégrer pleinement la géométrie d'un élément de l'infrastructure, la méthodologie proposée dans cette thèse est basée sur le recentrage de chacune des images RSO de la géométrie initiale (distance, azimut) sur un ensemble de points qui décrivent la structure étudiée. Le recentrage exploite la forme temps-fréquence du signal défocalisé pour ainsi déterminer précisément la réponse impulsionale d'une cible en azimut dans différents modes d'acquisition. Ensuite, les cibles pertinentes identifiées en utilisant un détecteur à tomographie 4D qui teste si la réponse maximale se trouve sur l'axe d'élévation nulle dans le plan élévation-vitesse (de déformation).

Cette thèse est divisée en deux parties. La première présente les développements théoriques dans le traitement du signal radar qui comprennent deux axes de recherche: le traitement temps-fréquence des signaux issus d'un radar FMCW d'une part, et la conception et validation d'une chaîne de traitement des images RSO satellitaire, d'autre part. Dans la deuxième partie de la thèse, l'accent est mis sur l'application des méthodes développées sur les données RSO au sol et spatiales. En plus, nous présentons également les campagnes *in situ* effectuées au barrage de Puylaurent (et glissement de Chastel) : les relevés GPS, topographiques et LIDAR employées pour le calcul des maillages 3D nécessaires dans la chaîne de traitement développée.

## Partie A: Contexte méthodologique

### II Analyse temps-fréquence et traitement des images RSO

*Ce chapitre fait une revue des méthodes spécifiques utilisées dans l'analyse temps-fréquence et le traitement des signaux RSO. La combinaison de certaines de ces méthodes est à la base des contributions théoriques de la thèse.*

#### II.1 Traitement des signaux non-stationnaires basé sur les outils à temps-fréquences

Dans de nombreuses applications, les signaux analysés sont non-stationnaires (ce qui signifie ici que la fréquence est variable dans le temps) et sont composés de plusieurs éléments, chacun ayant sa propre loi de fréquence instantanée (LFI). Le plus souvent, la phase d'un

composant analytique non stationnaire peut être décrite par un modèle paramétrique. En l'absence d'une information a priori sur la nature du signal, un modèle souvent utilisé est le signal à phase polynômiale (PPS) qui est basé sur le théorème d'approximation de Weierstrass. Les méthodes d'estimation de paramètres généralement utilisés pour les PPS avec plusieurs composantes sont basées sur la fonction d'ambiguïté d'ordre supérieur (high order ambiguity function - HAF) ou la méthode des moindres carrés. Ces approches sont affectées par les problèmes spécifiques des signaux avec plusieurs composantes: l'interaction entre les composantes peut créer des termes croisés et les composantes individuelles ne peuvent pas être démodulées en présence des autres.

Lorsque la forme temps-fréquence des composantes du signal est connue, l'estimation des paramètres peut être faite en utilisant une transformée adapté au signal (matched signal transform - MST) ou une transformation de Fourier du signal avec l'axe des temps déformé. Cette transformation localise les signaux avec une certaine fonction caractéristique à leurs taux de modulation de la même façon que la transformée de Fourier localise les signaux sinusoïdaux à leurs fréquences. De plus, cette transformation évite le problème de termes croisés, car il comprend une modulation d'amplitude proportionnelle au module de la dérivée de la fonction caractéristique qui rend les composantes orthogonales.

Par la suite, nous présentons brièvement les principales méthodes utilisées au cours de la thèse pour le traitement des signaux non-stationnaires: la transformée de Fourier à court terme, les mesures de concentration utilisées pour les représentations temps-fréquence, la fonction d'ambiguïté d'ordre supérieur et le concept de déformation de l'axe de temps inclus dans la transformée adaptée au signal.

### II.1.1 La transformée de Fourier à court terme

Les signaux non-stationnaires réels sont généralement localisés dans le temps et la transformée de Fourier ne peut pas fournir des informations sur le contenu spectral à différents instants de temps, mais seulement dans tout le spectre du signal analysé. Cela arrive parce que la base sur laquelle le signal est décomposé par la transformée de Fourier est un support théorique infini qui n'est pas compatible avec les signaux localisés dans le temps. Une solution à ce problème est l'analyse spectrale sur de courtes périodes qui s'appelle la transformée de Fourier à court terme (short time Fourier transform - STFT). Pour un signal  $x(t)$ , la transformée de Fourier à court terme s'écrit:

$$F_x(t, f) = \int_{-\infty}^{\infty} x(\tau) h^*(\tau - t) \exp(-j2\pi f\tau) d\tau, \quad (\text{A1})$$

où  $h^*(\tau - t)$  est la fonction de fenêtrage centrée au temps  $t$ . Le module carré de  $F_x(t, f)$  correspond à la distribution d'énergie dans le plan temps-fréquence et généralement s'appelle spectrogramme.

### II.1.2 Les mesures de concentration de représentations temps-fréquence

Un critère pour évaluer la qualité d'une représentation temps-fréquence est la concentration. Une meilleure concentration dans le plan temps-fréquence veut dire que l'énergie du signal est concentrée dans une région étroite, et donc, nous attendons que la détection et l'estimation effectuée dans ce plan soit plus efficace. Dans la littérature sont proposées différentes mesures de concentration, et chacune de ces mesures peuvent être appliquées seulement en fréquence pour mesurer la concentration spectrale.

### II.1.3 La fonction d'ambiguïté d'ordre supérieur

Pour définir la fonction d'ambiguïté d'ordre supérieur, le point de départ est le moment instantané d'ordre supérieur (high-order instantaneous momentum – HIM) qui pour un signal  $s(t)$  s'écrit:

$$\text{HIM}_k[s(t); \tau] = \prod_{i=0}^{k-1} [s^{(*i)}(t - i\tau)]^{\binom{k-1}{i}}, \quad (\text{A2})$$

où  $k$  est l'ordre,  $\tau$  est le retard et la notation  $(*i)$  signifie le nombre d'applications de l'opérateur de conjugaison complexe. La fonction d'ambiguïté d'ordre supérieur (high-order ambiguity function - HAF) est définie comme la transformée de Fourier du moment instantané d'ordre supérieur. En supposant un signal analysé de type PPS, une propriété essentielle est le fait que le moment instantané d'ordre  $k$  est réduit à une sinusoïde si l'ordre de polynôme est également  $k$ .

### II.1.4 La déformation de l'axe des temps et la transformée adaptée au signal

Nous considérons un signal constitué par une somme de composantes non stationnaires. Toutes les composantes ont la même structure temps-fréquence décrite par une fonction bijective de temps  $\theta(t)$ . Un tel signal ayant  $K$  éléments peut être écrit comme:

$$s(t) = \sum_{k=1}^K a_k \exp \{j(\varphi_k + \alpha_k \theta(t))\}, \quad (\text{A3})$$

où  $a_k$ ,  $\varphi_k$  et  $\alpha_k$  sont respectivement l'amplitude, la phase et le taux de modulation de la composante  $k$ . Le contenu temps-fréquence de ce signal peut être linéarisé par la déformation de l'axe de temps et/ou fréquence. Ceci est réalisé par un opérateur de déformation qui est défini pour un signal d'énergie finie  $x(t)$  et une loi de déformation  $w(t)$  par:

$$\left\{ \mathbf{W} \left| \frac{dw(t)}{dt} > 0; x(t) \rightarrow \mathbf{W}x(t) = x(w(t)) \right. \right\}. \quad (\text{A4})$$

Dans ce qui suit, un signal  $x(t)$  déformé par un opérateur  $\mathbf{W}$  ayant la loi de déformation  $\theta^{-1}(t)$  est désigné par  $x_w(\theta)$ . La variable  $\theta$  est utilisée afin de mettre en évidence le fait que le signal est représenté dans un nouvel axe de temps. Lorsque  $x(t)$  est égal à  $s(t)$  définis ci-dessus, le signal  $s(t)$  dans l'axe de temps déformé (notée  $s_w(\theta)$ ) est constitué en fait d'une somme des composantes sinusoïdales et par conséquence la transformée de Fourier de ce signal a des pics aux fréquences  $\alpha_k$ . Cette transformation peut être calculée également dans l'axe des temps initial par un changement de variable. En fait cela signifie la définition de la transformée adaptée au signal.

## II.2 Traitement des signaux RSO

Dans cette section, nous présentons en bref: le modèle de signal RSO, la focalisation dans le temps et la tomographie RSO différentielle. L'analyse se concentre seulement sur les méthodes de traitement utilisées dans les chapitres suivants.

### II.2.1 Les signaux RSO

La géométrie considérée est représentée sur la Fig. A1. Le vecteur unitaire  $\vec{u}$  décrit la direction de vol du satellite. Après démodulation, la réponse d'un ensemble de  $N$  cibles situées aux positions  $\vec{r}_i$  est une fonction de deux variables ("temps lent" et "temps rapide"):

$$s(t, \tau) = \sum_{i=1}^N A_i p_0 \left( \tau - \frac{2\Delta r_i(t)}{c} \right) \exp \left\{ -j \frac{4\pi f_c}{c} \Delta r_i(t) \right\} \text{rect} \left[ \frac{t - t_i}{T_{ap}} \right], \quad (\text{A5})$$

où  $A_i$  est l'amplitude complexe de la cible  $i$ ,  $f_c$  est la fréquence centrale,  $c$  est la vitesse de la lumière dans le vide,  $T_{ap}$  est le temps de l'ouverture synthétique et  $p_0(\tau)$  est l'enveloppe complexe du signal transmis. La fonction  $\text{rect}(t/T_{ap})$  est une fenêtre de longueur  $T_{ap}$  centrée à l'origine.

### II.2.2 Focalisation des signaux RSO dans le domaine temporel

Une méthode directe pour la focalisation des images RSO est la convolution des données brutes avec un filtre à deux dimensions (la distance et l'azimut). Une première mise en œuvre de cette méthode est de réaliser une corrélation bidimensionnelle avec la signature RSO de chaque point. En utilisant les notations précédentes, l'équation de calcul de la réponse intégrée sur l'ouverture synthétique pour un point décrit par le vecteur de position  $\vec{r}_k$  est écrite comme:

$$g_{MF}(\vec{r}_k) = \int_t \int_\tau s(t, \tau) p_k^*(t, \tau) dt d\tau. \quad (\text{A6})$$

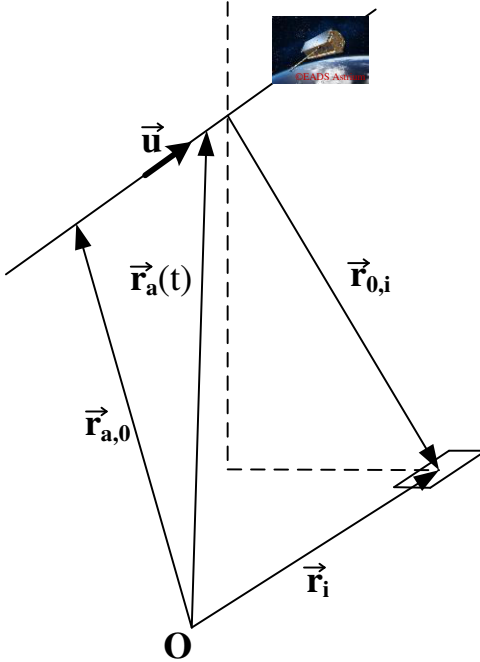


Figure A1: La géométrie d'acquisition considérée pour un point ayant le vecteur de position  $\vec{r}_i$

Une technique plus efficace de focalisation dans le domaine temporel est la rétroprojection. Cette méthode améliore le temps d'exécution en calculant séparément la réponse filtrée dans les deux domaines ("temps lent" et "temps rapide"), ce qui implique une séparation de l'intégrale double précédente.

### II.2.3 La tomographie RSO différentielle (en 4 dimensions)

Cette section est une courte présentation de la tomographie RSO différentielle (en 4 dimensions) adaptée aux images RSO focalisées sur un maillage particulier en utilisant les méthodes mentionnées ci-dessus. La géométrie envisagée est représentée sur la Fig. A2.

Nous considérons  $N$  passages de radar aux instants de temps  $t_n$ . Les distances (perpendiculaire à la direction de la ligne de visée) entre le passage  $n$  et le premier passage sont notées  $b_{\perp,n}$ . Les amplitudes complexes de la cible  $k$ , désignée par  $g_n(\vec{r}_k)$ , sont groupées dans un vecteur  $\mathbf{g}(\vec{r}_k)$  avec  $N$  composantes. Comme pour les méthodes de focalisation antérieure mentionnées, la phase correspondant à la géométrie d'acquisition est déjà sous-

traite, chaque élément de  $\mathbf{g}(\vec{r}_k)$  est décomposé comme:

$$g_n(\vec{r}_k) = \int_{\Delta s} \gamma_0(s) \exp \left[ -j \frac{4\pi f_c}{c} (r_{n,s} - r_{n,k}) \right] \exp \left[ j \frac{4\pi f_c}{c} d(s, t_n) \right] ds, \quad (\text{A7})$$

où  $\gamma_0(s)$  est le profil de réflectivité en élévation ayant le support  $\Delta s$  et  $d(s, t_n)$  est la déformation dans la ligne de visée d'une cible placée à l'élévation  $s$ . En considérant les distances entre les passages beaucoup plus petites que les distances orbite-cible et en appliquant une expansion de Fourier pour chaque terme de déplacement  $d(s, t_n)$ , le vecteur des données devient:

$$\mathbf{g}(\vec{r}_k) = \int_{\Delta s} \int_{\Delta v} p_\gamma(s, v) \mathbf{a}(s, v) ds dv, \quad (\text{A8})$$

où  $p_\gamma(s, v)$  est la distribution spectrale en élévation et vitesse (ayant le support  $\Delta v$ ) et  $\mathbf{a}(s, v)$  est un vecteur dont les éléments sont définis comme:

$$a_n(s, v) = \exp \left[ j \frac{4\pi f_c}{c} \left( s \frac{b_{\perp,n}}{r_{0,k}} + vt_n \right) \right]. \quad (\text{A9})$$

Parce que les paires  $(b_{\perp,n}, t_n)$  sont rares et non uniformes, une méthode habituellement utilisée pour reconstruire la fonction  $p_\gamma(s, v)$  est le filtre Capon.

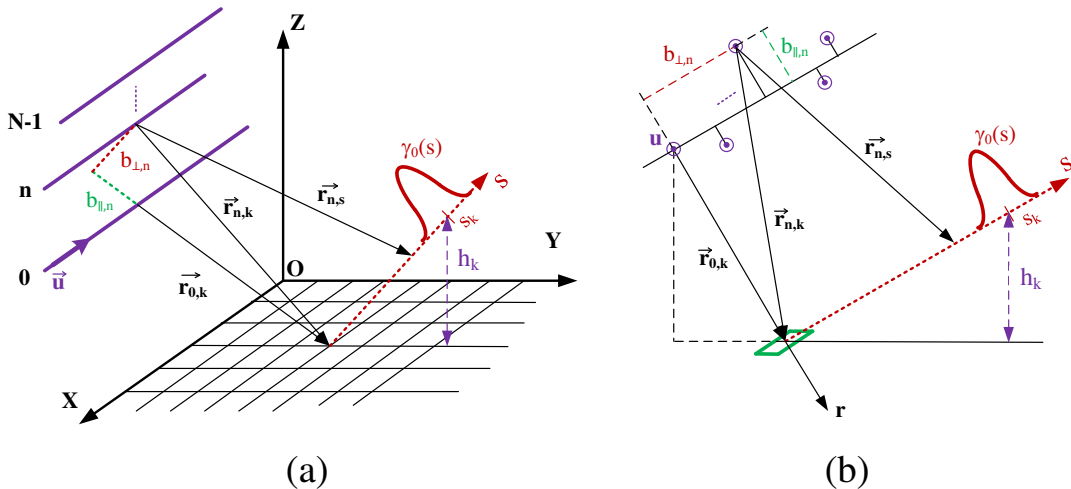


Figure A2: La géométrie de tomographie RSO différentielle: (a) vue 3D et (b) projection 2D parallèle à  $yOz$ .

## III Traitement des signaux radar FMCW en distance

*Ce chapitre présente les algorithmes de traitement du signal développés pour les radars FMCW. Les contributions sont axées sur la correction de la non-linéarité d'oscillateurs à large bande commandés en tension réalisés en exploitant la structure temps-fréquence du signal de battement du radar FMCW.*

### III.1 Le radar FMCW et le problème de la non-linéarité

Le radar à onde continue modulée en fréquence est une alternative au radar à impulsions et est généralement utilisé lorsque les distances envisagées sont relativement petites (dizaines ou centaines de mètres). Afin de mesurer ces distances avec un radar à impulsions le temps de commutation entre l'émission et la réception devrait être au maximum des dizaines de nanosecondes. Le principe du radar FMCW est actuellement utilisé dans des applications telles que les radioaltimètres, les systèmes d'anticollision ou les capteurs pour l'identification du défaut d'homogénéité sur les lignes de transmission.

L'information de distance à partir d'un radar FMCW est codée dans la fréquence de battement obtenue en mélangeant le signal reçu et le signal transmis. Un problème classique d'un radar FMCW est la non-linéarité en temps-fréquence de l'onde transmise induite par la caractéristique non-linéaire tension-fréquence de l'oscillateur commandé en tension (voltage controlled oscillator - VCO). Cela conduit à une perte de résolution en répartissant le signal de battement d'une cible dans une certaine bande des fréquences au cours d'un balayage de tension linéaire. Dans la littérature, il existe différentes approches pour résoudre ce problème.

Un procédé de correction simple consiste à utiliser une tension de commande prédéformée afin d'obtenir une modulation de fréquence linéaire. Cependant, cette solution a la difficulté que la pré-déformation est généralement faite avec la caractéristique fréquence-tension statique (mesurée par l'application de certaines tensions et la lecture des fréquences résultantes) qui peut différer de celui dynamique car elle ne prend pas en compte la réponse des circuits de commande ou tout changement dans les conditions externes (par exemple la vitesse de balayage, la température ou la tension d'alimentation). Une autre façon de résoudre le problème de la non-linéarité est avec des méthodes de post-traitement qui sont utilisées dans la plupart des cas pour les VCOs simples et pas cher. Ces méthodes évaluent la non-linéarité en utilisant soit un trajet de référence intégré entre émetteur et récepteur qui agit comme une cible ou une réponse fournie par un réflecteur réel de la scène.

### III.2 Le signal de battement non linéaire

Pour un balayage de tension d'accord linéaire, le signal analytique transmis d'un VCO dans l'intervalle  $[0, T]$  s'écrit comme:

$$s_T(t) = \exp \left[ j \left( 2\pi f_0 t + \beta_0 \int_0^t \theta_{\mathbf{p}_0}(x) dx \right) \right], \quad (\text{A10})$$

où  $f_0$  est la fréquence initiale,  $\beta_0$  est la pente de modulation dans l'origine et  $\theta_{\mathbf{p}_0}$  est une fonction monotone définie sur l'intervalle  $[0, T]$  décrivant la non-linéarité qui dépend de certains paramètres donnés par le vecteur  $\mathbf{p}_0 = [p_{0,1}, p_{0,2}, \dots, p_{0,L}]^T$ . Dans la suite, nous considérons que le signal réfléchi est issu de  $K$  cibles différentes. Le signal de battement résultant peut être exprimé sous la forme:

$$s(t) = \sum_{k=1}^K a_k \exp [j (\varphi_k + \alpha_k \theta_{\mathbf{p}_0}(t))], \quad (\text{A11})$$

où  $a_k$ ,  $\varphi_k$  et  $\alpha_k$  sont respectivement l'amplitude réelle, la phase et la pente de modulation de composante  $k$ . Dans ce contexte, les algorithmes de correction développés dans la thèse visent à estimer le vecteur de paramètres  $\mathbf{p}_0$  et simultanément de transformer toutes les composantes du signal de battement en sinusoïdes complexes en utilisant la déformation de temps.

### III.3 Correction de la non-linéarité basée sur la fonction d'ambiguïté d'ordre supérieur

Pour cette méthode, nous supposons une dépendance polynomiale entre fréquence et la tension de commande. L'estimation basée sur la fonction d'ambiguïté d'ordre supérieur est basée sur la présence d'une cible de référence dans le signal de battement. Ce composant particulier PPS peut être extrait par un filtrage passe-bande autour du signal de fréquence de battement correspondant au retard de référence. Après avoir appliqué l'algorithme d'estimation HAF sur le signal de référence, nous obtenons une estimation du vecteur  $\mathbf{p}_0$ , et le profil en distance corrigée est calculé par déformation de temps (ré-échantillonnage temporel) avec la fonction de non-linéarité estimée. L'algorithme de correction de non-linéarité basée sur HAF est résumé dans le schéma de la Fig. A3.

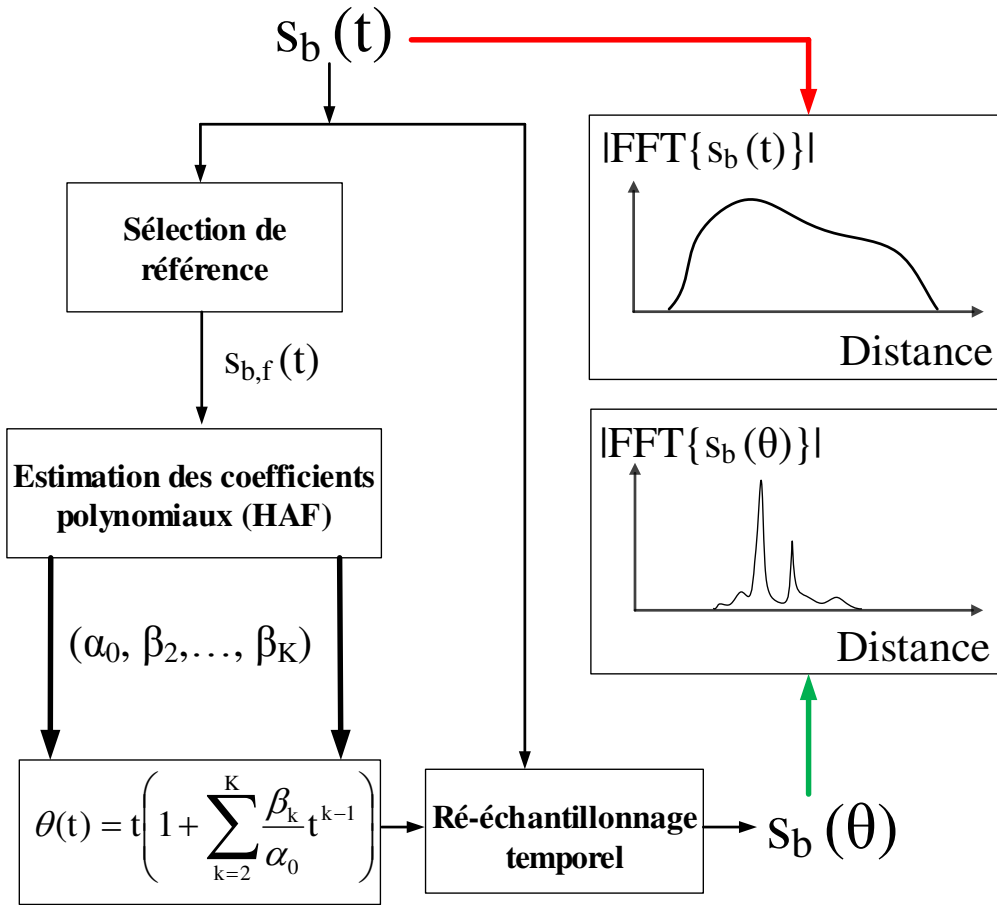


Figure A3: Algorithme de correction de non-linéarité basé sur les fonctions d'ambiguïté d'ordre supérieur et ré-échantillonnage temporel.

### III.4 L'autofocus radial (en distance) comme procédé de correction de non-linéarité

Habituellement, une mesure de concentration est utilisée pour déterminer un paramètre optimal dans une représentation temps-fréquence (par exemple la longueur de la fenêtre pour un spectrogramme). Toutefois, une telle mesure peut également être utilisée pour estimer les paramètres inconnus de la fonction non linéaire  $\theta_{p_0}(t)$ .

L'idée est de ré-échantillonner le signal de battement avec des fonctions de test obtenues pour différentes valeurs attribuées aux paramètres. Lorsque la fonction de test correspond à la fonction de base réelle, le signal ré-échantillonné sera essentiellement une somme de sinusoïdes complexes et son spectre aura le plus haut degré de concentration. Par con-

séquent, une mesure de la concentration appliquée au spectre du signal déformé atteindra sa valeur optimale lorsque la déformation se fait avec la fonction optimale. Donc, la mesure de la concentration peut être considérée comme une fonction de coût qui doit être réduit au minimum en ce qui concerne certains paramètres décrivant  $\theta_{p_0}(t)$ . Une fois que les paramètres optimaux sont déterminés, l'amplitude, la phase et la distance de chaque composant peuvent être extraits à partir du profil de distance obtenue à partir du signal de battement déformé par la fonction obtenue pour les paramètres déterminés. Notez que cette approche n'impose pas un certain modèle pour la non-linéarité, mais, pour des raisons de calcul, le nombre de paramètres doit être relativement faible. Le terme « autofocus » est utilisé afin de souligner que l'algorithme a besoin des cibles de la scène, sans tenir compte de leur nombre et ne nécessite pas des lignes supplémentaires entre émetteur et récepteur. Le diagramme de l'algorithme d'autofocus radial proposé dans le cas où le modèle a deux paramètres est représenté sur la Fig. A4.

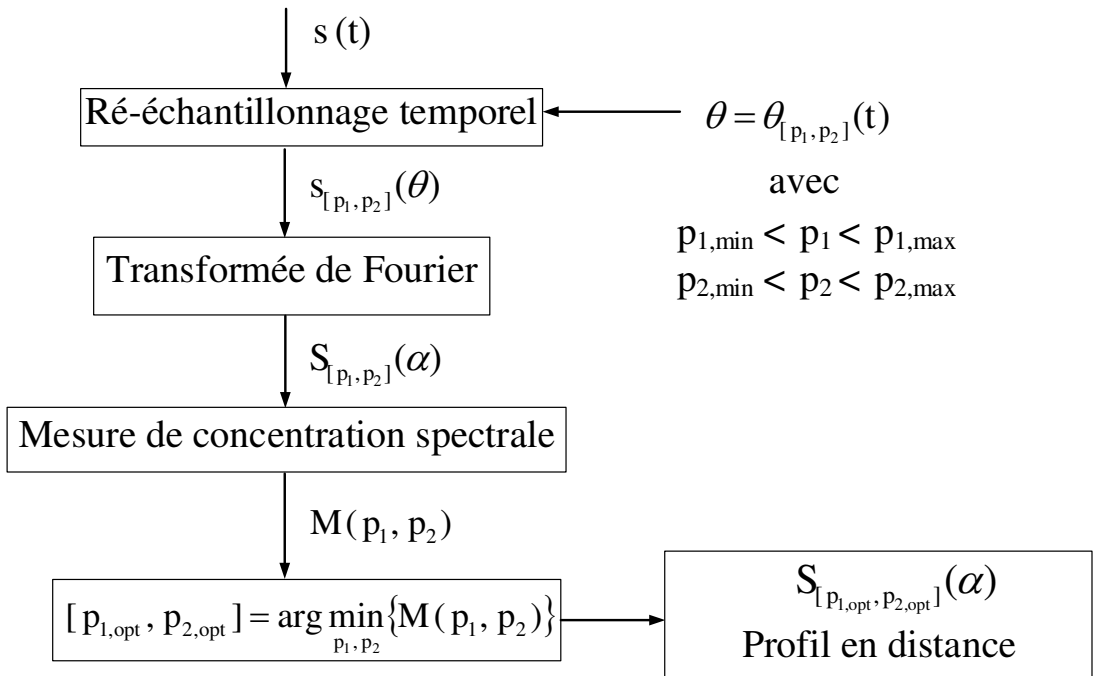


Figure A4: Algorithme d'autofocus radial (en distance) pour un modèle de non-linéarité avec deux paramètres.

## IV La surveillance des centres de diffusion dans les images RSO recentrées

*Ce chapitre présente une méthode pour surveiller les centres de diffusion basés sur le recentrage des images RSO sur un maillage (ou nuage de points) fournie d'une structure et d'identifier les régions de diffusion fiables au moyen de la tomographie RSO différentielle.*

### IV.1 Centres de diffusion dans les images RSO

Pour la surveillance de l'infrastructure, il est souvent nécessaire de suivre les mouvements lents de points sur les différents éléments de l'infrastructure (bâtiments, barrages, glissements de terrain, etc.). Cela peut être fait avec des capteurs aéroportés, tels que TerraSAR-X et TanDEM-X dû à leur courte longueur d'onde de 3,1 cm, le temps de revisite courte de 11 jours et en particulier la résolution en azimut dans l'ordre du mètre (pour les modes «spotlight»). Néanmoins, étant donné un certain élément d'infrastructure et une géométrie d'acquisition, nous pouvons observer la structure d'un seul côté. En tenant compte des effets typiques de la visée latérale (l'ambiguïté en élévation, les réflexions multiples ou l'ombrage), il n'est pas toujours clair quels points fournissent la réponse principale, lequel d'entre eux sont visibles depuis l'orbite considérée et, par conséquent, lequel d'entre eux peut être surveillé avec précision. Si les coordonnées d'un certain nombre de points de la structure sont connues avec au moins une précision centimétrique (mesurée avec des techniques de GPS ou LIDAR), leur réponse (s'il y en a une) pourrait être déterminée lorsque les données brutes sont focalisées sur un maillage 3D contenant précisément ces points. Cependant, dans la plupart des produits livrés, les images RSO sont déjà focalisées sur une grille distance-azimut qui n'est pas liée à un diffuseur spécifique.

Parce que les données brutes ne sont généralement pas disponibles, dans ce chapitre nous proposons une procédure pour surveiller les centres de diffusion basée sur le recentrage de données RSO sur un maillage de la structure observée. La méthode employée pour identifier les centres de diffusion réels du maillage (qui produisent la réponse principale et ne sont pas affectés par chevauchements en élévation) dans une pile d'images recentrées utilise la tomographie RSO différentielle (4D). Ceci est obtenu en exploitant le fait que chaque centre de diffusion recentré sera à zéro en élévation dans le plan local d'élévation-vitesse. Ainsi, la détection consiste en faisant un test de position par rapport au maillage donné.

Un avantage de l'approche de recentrage est qu'aucun déplacement ou rééchantillonnage (dans le cadre du processus de co-registration) ne sont pas nécessaires parce que les échantillons sont automatiquement alignés en recentrant chaque image sur

le même maillage. En outre, lors du calcul des réponses impulsionales en recentrant les données d'azimut défocalisé sur le modèle géographique 3D fourni, les décalages de phase correspondant à la géométrie d'acquisition et à la centroïde Doppler variable (spécifique pour le mode «sliding spotlight») sont naturellement pris en compte. Par conséquent, une co-registration implicite des images est obtenue et la phase interférométrique peut être calculée comme la différence de phase de points correspondants.

La méthode de détection basée sur le test de position en élévation pourrait également être utilisée en convertissant les points de la grille à partir de leurs coordonnées initiales (par exemple, «Earth Centered Earth Fixed» – ECEF ou latitude/longitude/altitude) aux coordonnées distance-azimut d'une image maître et interpoler l'amplitude complexe en utilisant les pixels voisins. Cependant, par rapport à l'approche de recentrage, cette méthode basée sur interpolation exige que toutes les images soient d'abord co-registrées. Ceci est encore plus important dans le cas des images acquises dans les modes «spotlight» où toute interpolation requise pour l'enregistrement doit être effectuée avec un noyau d'interpolation modulé afin de suivre la dérive Doppler en azimut. D'un point de vue différent, la procédure de recentrage peut également être considérée comme un noyau d'interpolation équivalent (en considérant que toutes les opérations concernées sont linéaires) dont les paramètres seront toujours adaptés au mode d'imagerie spécifique. En outre, parce que le recentrage est appliqué sur une petite zone de l'image RSO initiale, l'augmentation de la complexité n'est pas un inconvénient significatif.

Dans la procédure d'identification des centres de diffusion proposés, le problème de détection est posé d'une manière différente des approches typiques utilisées en tomographie RSO qui sont basées sur la théorie standard de la détection. Classiquement, la détection est effectuée en comparant le pic tomographique normalisé à un certain seuil. Dans ce cas, la dispersion d'élévation entre naturellement dans le schéma de détection en affectant la valeur de crête. Dans la méthode de détection proposée dans ce travail, l'élévation attendue est déjà connue (zéro pour cibles sur le maillage donné) et la détection consiste en fait dans un test de position du maximum global dans le plan élévation-vitesse. En conséquence, la dispersion d'élévation se traduit dans la précision tolérée du centre de diffusion par rapport au maillage fourni.

En avant, la procédure de surveillance des centres de diffusion est présentée en deux étapes: le recentrage des images RSO acquises sur le maillage fourni est décrite en premier, suivie par la détection des centres de diffusion et le calcul des déplacements. Un schéma général de la méthodologie proposée est affiché sur la Fig. A5.

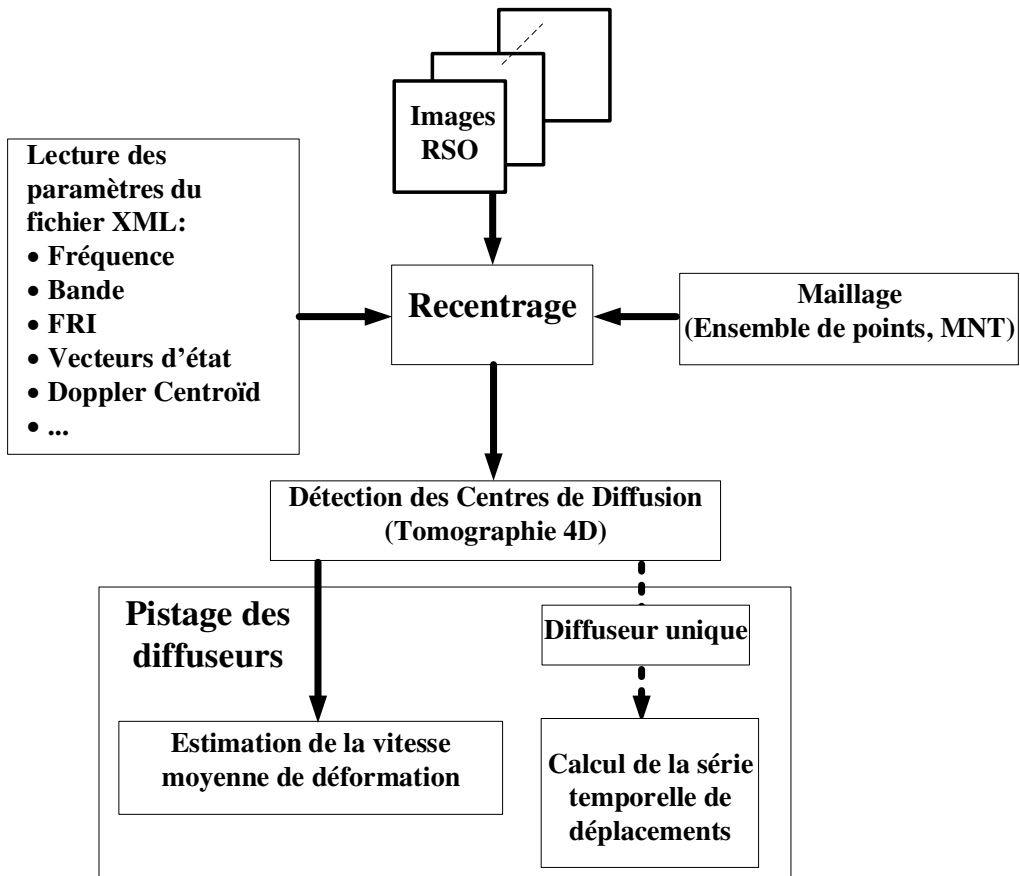


Figure A5: Détection et pistage des centres de diffusion par le recentrage des images RSO.

## IV.2 Recentrage des images RSO

Les principales étapes de l'algorithme de recentrage sont décrites ci-dessous et elles suivent le diagramme représenté sur la Fig. A6. Le recentrage est effectué en deux étapes –une défocalisation en azimut pour accéder à l'historique de phase de chaque diffuseur et une rétroposition sur le nuage de points.

La défocalisation en azimut est effectuée en utilisant une version inversée de l'algorithme SPECAN (analyse spectrale) généralement utilisé pour la focalisation en azimut après que le traitement en distance soit complété. Dans la perspective de l'implémentation, l'opération de défocalisation consiste en une série de transformations de Fourier (FT) et diverses multiplications complexes du signal en azimut. Afin de réduire les temps de calcul, la première opération consiste à découper dans les images RSO la région comprenant la scène d'intérêt (cette étape ne modifie pas le traitement parce que la compression en distance n'est pas modifiée au cours de la défocalisation en azimut).

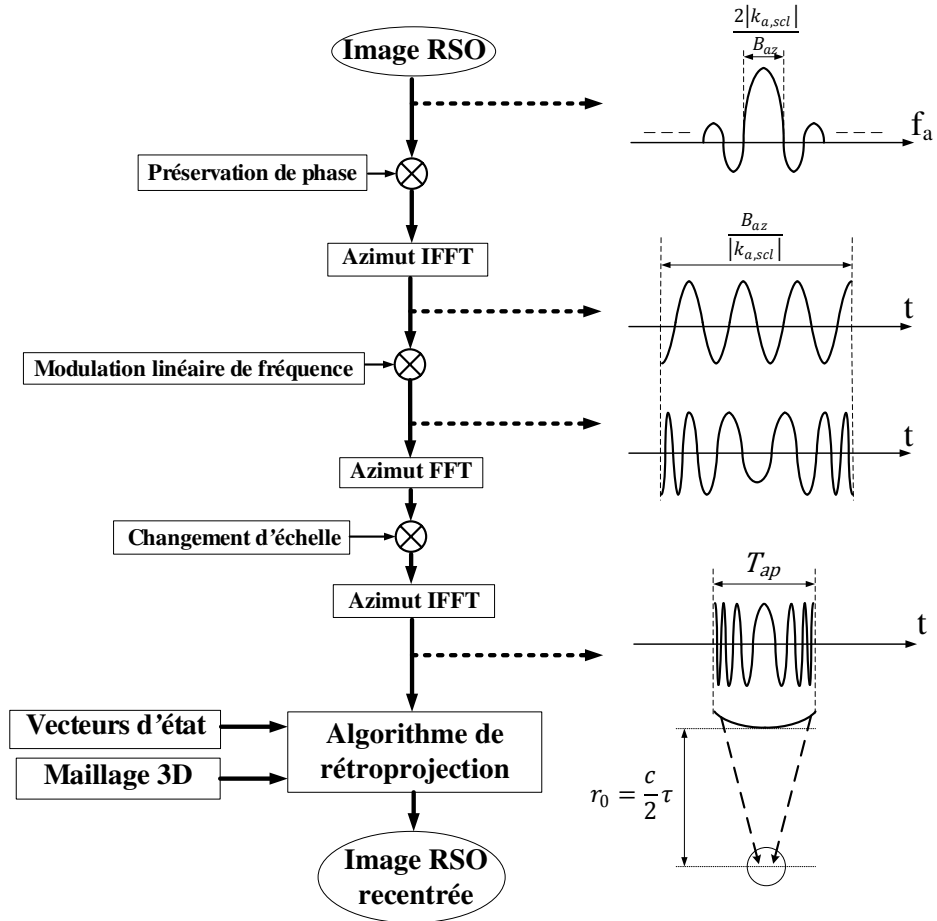


Figure A6: Le schéma de principe de l'algorithme de recentrage.

Dans le traitement SPECAN d'une ligne d'azimut, chaque lobe représente une cible qui provient d'un FT d'un signal sinusoïdal et la position en azimut de la cible est directement liée à la fréquence de la sinusoïde par un constant  $k_{a,scl}$  décrivant le changement d'échelle lors du traitement par SPECAN. Ainsi, après une multiplication complexe pour préserver la phase (une phase quadratique utilisée pour compenser les termes de phase qui apparaissent dans le traitement ultérieur), la première étape principale est une FT inverse qui conduit à un signal composé d'une somme de sinusoïdes à fenêtre (le support temporel de la fenêtre étant lié à la bande passante d'azimut  $B_{az}$ ). Ensuite, les sinusoïdes sont modulées en fréquence par multiplication avec un signal chirp qui détermine une histoire de phase quadratique à chaque cible. La forme définitive du signal defocalisé est obtenue par la succession FT-Changement d'échelle-FT inverse qui restitue à chaque cible l'histoire de phase hyperbolique qui apparaît naturellement au cours de l'acquisition. Le support temporel de la réponse de chaque cible est égal à la durée d'éclairage correspondant à l'ouverture synthétique  $T_{ap}$ .

## Résumé étendu (fr)

---

Après avoir obtenu les images defocalisées en azimut, elles doivent toutes être projetées (recentrées) sur les nuages de points disponibles. Le recentrage est employé par un domaine temporel de rétroposition, qui est essentiellement une version plus rapide du filtrage adapté. Afin de concentrer la réponse d'azimut par une technique à base de filtrage adapté, l'histoire de phase attendue doit être reconstruite et adaptée au signal acquis. L'exactitude de l'histoire de phase reconstruite dépend de la précision des coordonnées de l'orbite et du point sol et de la compensation des effets atmosphériques.

### IV.3 Détection et pistage des centres de diffusion par tomographie RSO différentielle

Pour deux images recentrées, les diffuseurs stables pourraient être détectés par l'évaluation de la cohérence sur le voisinage de chaque point recentré. Toutefois, afin de déterminer si le centre de diffusion est effectivement au point fourni, une approche basée sur une série d'acquisitions est nécessaire afin de créer une ouverture d'élévation. Par conséquent, le cadre de tomographie différentielle présentée plus tôt est utilisé. En changeant la configuration géométrique pour chaque point recentré, la position sur l'axe d'élévation est à zéro et tout autre diffuseur situé en chevauchement sera à une autre altitude. Par conséquent, les diffuseurs persistants provenant de l'ensemble des cibles qui ont le centre de diffusion réelle à la position donnée et ne sont pas affectés par chevauchement sont ceux qui ont une seule valeur maximale significative dans le plan d'élévation-vitesse à zéro élévation clairement séparée des autres éventuels pics locaux correspondant aux cibles en chevauchement. En outre, la dispersion de l'estimateur d'élévation peut être interprétée comme la précision du diffuseur détectée par rapport au maillage fourni.

La dernière étape dans le traitement des données consiste à calculer les vitesses moyennes de déformation (MDV) et la série temporelle de déplacements. Le MDV de chaque diffuseur est facilement identifié sur le profil élévation-vitesse, tandis que la série temporelle est calculée à partir de la différence de phase entre l'amplitude complexe à l'instant courant et l'une à l'instant initial. Les éventuels enroulements de phase qui apparaissent pour des déplacements plus grands que la demi-longueur d'onde peuvent être résolus en soustrayant la composante de phase linéaire générée par le MDV. Cependant, l'interprétation des déplacements ne peut pas être assez simple, lorsque la déformation actuelle n'a pas la même tendance linéaire pendant toute la période analysée. Dans ce cas, le MDV ne peut pas être directement lié à la vitesse physique de déformation de la structure pendant la période considérée, il est juste une moyenne des déplacements (qui peut être une partie de deux ou de plusieurs tendances différentes de déformation). Cela peut également provoquer certains enroulements de phase supplémentaires qui doivent être corrigés afin de donner un sens physique à la série des déplacements de temps.

## Partie B: Contexte appliqué

### V Plateforme radar FMCW

Dans ce chapitre nous décrivons la plateforme radar FMCW conçue pour les applications de surveillance de l'infrastructure (mesures des déplacements) et les tests effectués pour valider les méthodes de correction développées sur des cibles à courte portée. L'architecture du système démonstrateur ajoute quelques nouveaux éléments aux modèles existants dans la littérature.

#### L'architecture de radar FMCW à courte portée

La plateforme radar FMCW est basée sur une architecture hétérodyne représentée sur la Fig. A7. Le signal de balayage présente une variation linéaire (sur une période de 100 ms) et il est obtenu depuis un générateur de signaux numériques d'un oscilloscope USB. La longue période de temps de balayage combinée à la nature discrète du signal de commande (12 bits) conduit à une modulation de fréquence étagée avec une distance sans ambiguïté pour la bande passante maximale de 4 GHz d'environ 150 m (où le comportement est de type FMCW). Le bloc RF VCO est un VCO à bande X à faible coût qui fournit le signal de l'oscillateur local (LO). La non-linéarité élevée de ce VCO a été corrigée en utilisant les méthodes développées et nous n'avons pas besoin d'un VCO avec une caractéristique plus linéaire (comme un oscillateur YIG).

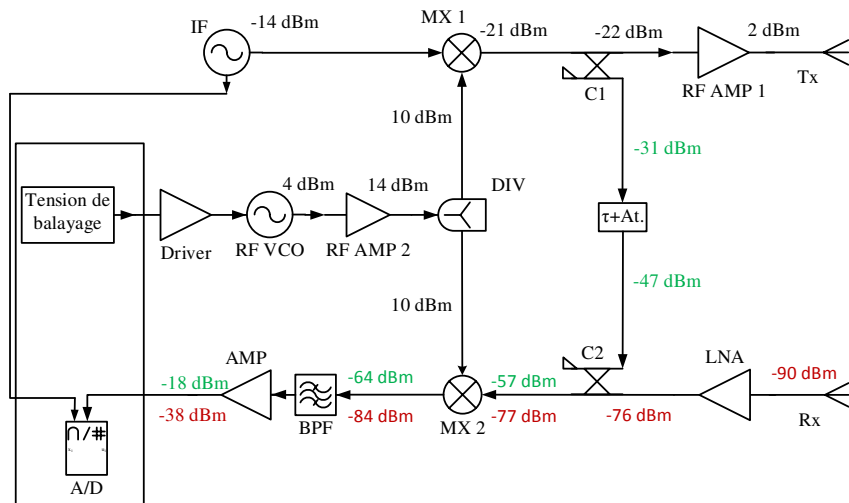


Figure A7: Le schéma du radar FMCW en bande X.

## V.1 Les résultats expérimentaux

Cette section comprend deux parties: la première valide les algorithmes de correction de non-linéarité à large bande sur les données réelles, tandis que la seconde partie est centrée sur les mesures de déplacement en utilisant la phase interférométrique dérivée des profils en distance et des images RSO.

Dans ce paragraphe, nous présentons les tests effectués avec les méthodes de correction de non-linéarité développées, pour une scène contenant deux disques métalliques (placés à 0,75 m et 3,5 m du radar). Les profils initiaux et celles corrigés sont présentés dans la Fig. A8. Initialement, les énergies des cibles sont réparties dans une certaine bande de fréquences, tandis qu'après la correction les cibles sont focalisées en pics clairs. La Fig. A9 présente les résultats obtenus pour une image RSO acquis en déplaçant le radar FMCW sur un rail de 30 cm. La scène contenait des barres métalliques et un disque hautement réfléchissant. La correction de non-linéarité a été employée en ré-échantillonnant chaque ligne de l'image initiale avant d'appliquer l'algorithme de rétroprojection pour obtenir l'image RSO. Notez que dans l'image de la Fig. A9a les cibles ne peuvent pas être distinguées, tandis que dans la version corrigée elles sont toutes beaucoup plus concentrées (Fig. A9b).

Les mesures de déplacement avec le radar FMCW ont été faites en utilisant les profils en distance et les images RSO pour la bande passante du signal transmis de 3 GHz. Différentes cibles telles que des barres métalliques et des coins réflecteurs ont été placés en face du radar à distances entre 1-6 m. Les mesures ont été effectuées comme suit. Une cible a été placée à une certaine distance du radar et le profil a été calculé après avoir cumulé le signal reçu sur 10 périodes de balayage.

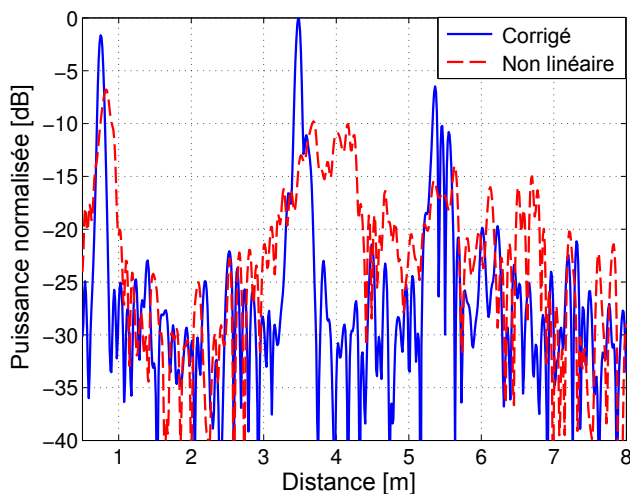


Figure A8: Profil en distance corrigé par rapport au profil initial (non linéaire).

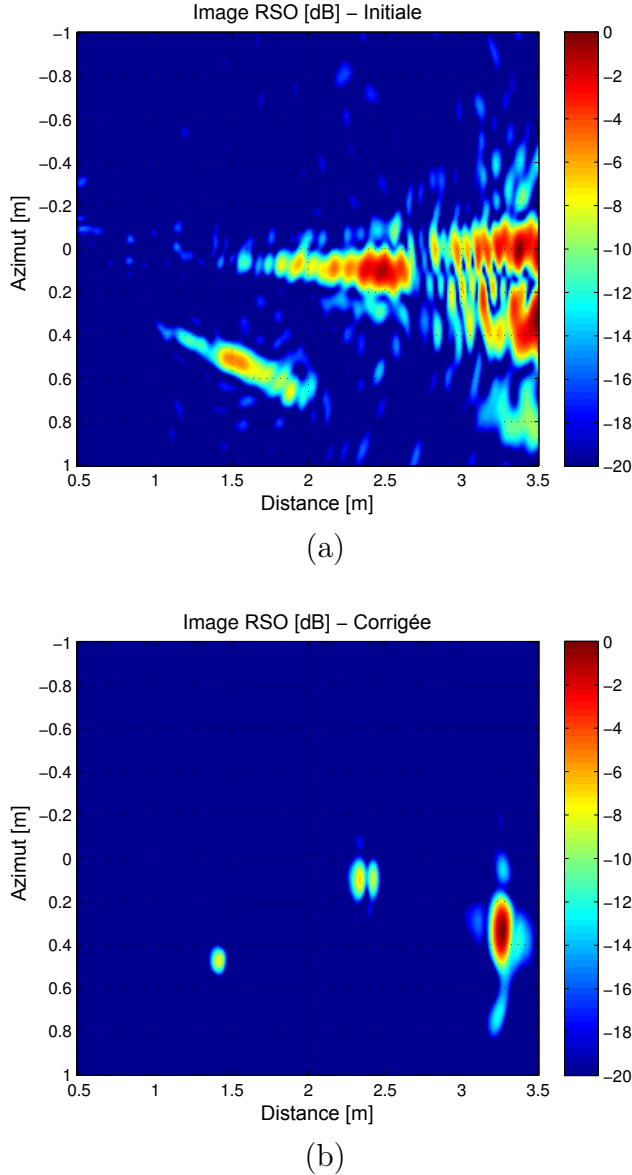


Figure A9: Les résultats de la correction de non-linéarité appliquée à une image RSO obtenue avec le radar FMCW. Dans l'image initiale (a) les cibles sont presque indiscernables, tandis que dans l'image corrigée (b) les cibles sont clairement séparées.

Par la suite, la cible a été déplacée de quelques millimètres à l'aide d'un vernier (avec une précision de 0,02 mm) lié à la cible et un autre profil de distance a été obtenu. Les déplacements mesurés et leurs erreurs absolues correspondantes dans quelques mesures sont résumés dans la Fig. A10. Dans la Fig. A10a sont représentés les déplacements obtenus à partir des profils en distance et sur la Fig. A10b sont présentés les déplacements en ligne de visée calculés à partir des images RSO.

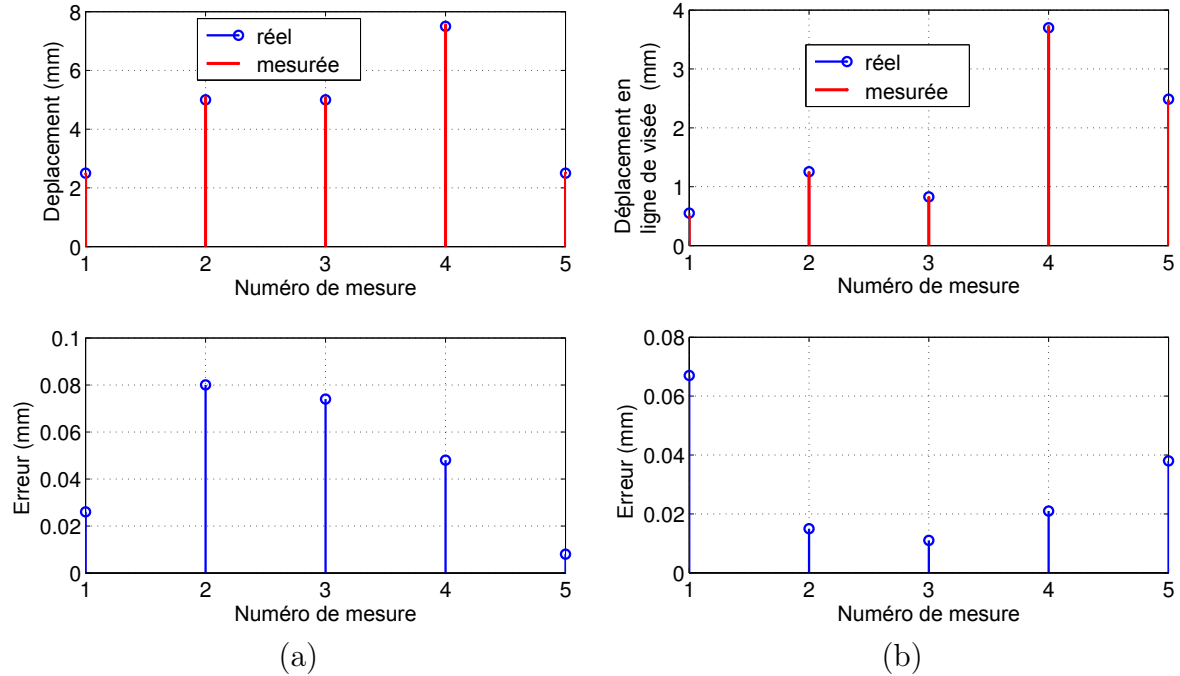


Figure A10: Mesures de déplacement calculées à partir de: (a) profils en distance et (b) images RSO.

## VI La combinaison entre les données RSO et le maillage 3D décrivant un grand ouvrage d'art

*Dans le présent chapitre, nous présentons les principaux résultats obtenus dans un ensemble de campagnes de mesures effectuées entre 2013 à 2014 dans deux sites d'essai en France: le barrage de Puylaurent et le glissement de terrain du Chastel. Le but de ces campagnes était de valider sur des données réelles la méthodologie de surveillance de l'infrastructure proposée, qui est basée sur la combinaison de données RSO avec des nuages de points 3D décrivant la structure envisagée.*

### VI.1 Le site d'essai et la description des données

Le site d'essai est situé en Lozère, France. Il est composé de deux éléments d'infrastructure: le barrage de Puylaurent situé à  $44^{\circ}31'47''N, 3^{\circ}53'13''E$  avec la hauteur de la crête à environ 943 m et le glissement de terrain du Chastel placée à  $44^{\circ}31'52''N, 3^{\circ}52'28''E$  avec une hauteur entre 940 à 1020 m (au-dessus du niveau de la mer).

Dans cette étude, deux piles d'images RSO sont choisis pour étudier la faisabilité du recentrage et la détection tomographique afin d'extraire les déplacements de ces deux zones. Chaque image RSO est acquise à haute résolution (bande passante de 300 MHz) dans le mode «sliding spotlight» par les satellites TerraSAR-X ou TanDEM-X. L'ensemble des données acquises à partir de l'orbite descendante comprend 22 images RSO couvrant la période Avril 2013 - Décembre 2014, tandis que celui de l'orbite ascendante est composé de 19 images RSO couvrant la période Mai 2013-Décembre 2014.

Dans ce qui suit, nous présentons les mesures GPS et topographiques et les relevés lasergrammétiques effectuées sur les deux sites afin d'obtenir un nuage de points de chaque zone dans un système géodésique compatible avec le système dans lequel les vecteurs d'état de données satellitaires sont fournis. Les relevés ont été réalisés entre 8-11 Juillet 2013 en utilisant une station totale, un scanner laser, récepteurs GPS et un ensemble de prismes.

Les premières mesures réalisées ont consisté à localiser précisément par GPS quelques points des deux zones. Au total, 4 points de référence sur le glissement de terrain (notés 2001, 2002, 2004, 2005) et 3 sur le barrage (notés 1000, 1001, 1002) ont été stationnés par GPS (ces points sont représentés sur la Fig. A11).



Figure A11: Les points stationnés par GPS superposés sur l'image de Google Earth.

Les coordonnées de chaque point ont été ajustées à l'aide des données fournies par les stations de référence (du réseau GNSS permanent) les plus proches du site. Le système géodésique utilisé est la deuxième version du "Réseau Géodésique Français 1993" (RGF93v2) correspondant à l'ETRS89 par réalisation ETRF2000 à l'époque 2009.0. Ce système assure une précision horizontale de 1-2 cm et une précision verticale de 2-5 cm par rapport au système global (dans lequel les vecteurs d'état du satellite sont fournis).

## Résumé étendu (fr)

---

Dans le cas de glissement de terrain, pour les mesures topographiques, la station totale a été placée sur le point de référence 2002 (un pilier) pour mesurer les points 2001, 2004, 2005 et un point indépendant du dispositif d'auscultation pour permettre la vérification du calage du scanner laser. Le scanner laser a ensuite été placé en centrage forcé sur le pilier 2002 et le relevé du glissement de terrain a été effectué au pas de 1 point tous les 5 cm.

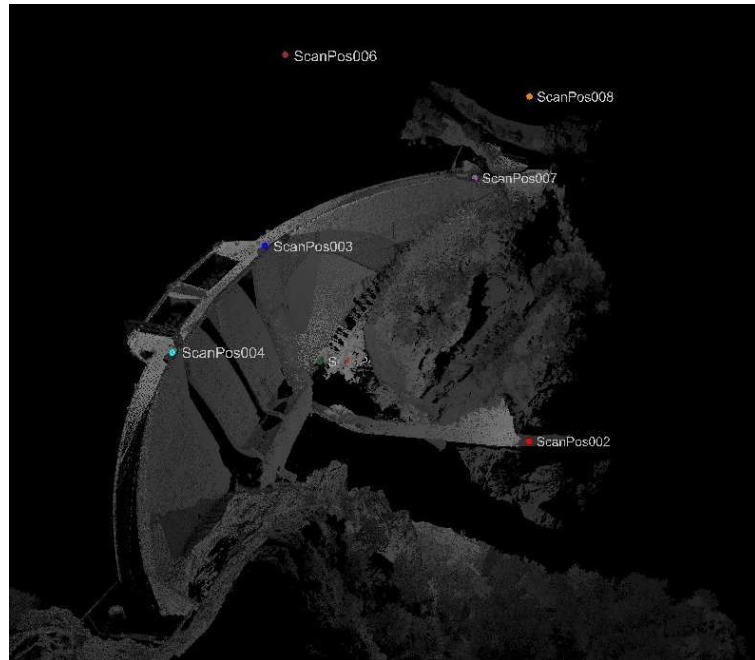


Figure A12: Positions de scanners laser superposées sur le nuage de points du barrage de Puylaurent.

Le barrage a été relevé depuis 7 stations dont les positions superposées sur le nuage de points résultant du barrage sont détaillées sur la Fig. A12. Pour chaque station, une mesure tachéométrique a été effectuée en relevant par mesure sur prisme les trépieds disponibles, ainsi que des cibles rétro-réfléchissantes placées sur des mini-cannes. Les relevés ont été effectués en tenant compte des valeurs de température, pression et hygrométrie. Après la mesure tachéométrique, le scanner laser a été placé en centrage forcé et en position verticale sur l'embase de la station totale pour les stations suivantes : ScanPos002, ScanPos003, ScanPos004, ScanPos006 et ScanPos008. Les prismes ont été remplacés par des cibles rétro-réfléchissantes. Le relevé par le scanner laser a été effectué avec une densité d'un point tous les 5 cm. Les données lasergrammétiques ont été ré-échantillonnées et formatées comme deux nuages de points (un pour le glissement et un pour le barrage) exprimées en coordonnées ECEF ayant la distance moyenne entre les points adjacents de 25 cm.

Ensuite, nous décrivons les dispositifs de mesures in situ existants dans les deux zones. Le glissement est équipé de 40 points topographiques, comprenant des mini-prismes placés

à environ 1 m au-dessus du sol. Parmi ceux-ci, sur les 20 points (notée I1 à I20) de la zone supérieure du glissement de terrain ont été montés des coins réflecteurs (CR) au-dessus des mini-prismes. Les coordonnées 3D de chaque cible ont été mesurées à différentes dates. Une mesure a été effectuée à l'aide d'un théodolite motorisé, des mini-prismes avec CR et des 4 prismes de référence. Dans le cas du barrage, les données in-situ ont été fournies par un ensemble de pendules placées à l'intérieur de la structure. Ces pendules mesurent les déplacements radiaux et tangentiels entre les différents points de la crête du barrage. Il n'y a aucun dispositif in situ pour mesurer les mouvements verticaux du barrage.

## VI.2 Mesure des déplacements

Cette section présente comment les mesures de déformation sont obtenues à partir des centres de diffusion détectés dans la pile d'images recentrées. Les résultats sont comparés avec les données in-situ.

### VI.2.1 Le glissement de terrain du Chastel

Dans le cas du glissement de terrain, la surveillance des déplacements est effectuée sur les coins réflecteurs montés au-dessus des points topographiques. Le glissement a essentiellement un mouvement uniforme tout au long de la période de surveillance et par conséquent le modèle de tomographie 4D avec une vitesse de déplacement moyenne est un choix approprié pour la détection des diffuseurs.

Dans l'orbite descendante, à partir des 9 points visibles, 8 ont été détectés comme centres de diffusion fiables. La série des déplacements de temps en ligne de visée (LOS) de l'un de ces diffuseurs est montré dans la Fig. A13. La référence est le point 2005. Les barres d'erreur pour les mesures satellitaires sont obtenues par des simulations de Monte Carlo. Notez que chaque barre d'erreur provient en réalité de quatre sources indépendantes de bruit: la cible et le point de référence à la fois dans l'image courante et dans la première image. Sur la figure, nous avons également représenté la tendance linéaire correspondant à la MDV estimée et l'évolution du rapport signal-bruit pour la cible envisagée et le point de référence.

Les différences entre les estimations et les mesures in situ peuvent atteindre jusqu'à 10 mm et peuvent provenir de différentes raisons décrites ci-après. Tout d'abord, il n'y a pas des mesures simultanées (satellitaires et in situ) et les données sont alignées par un décalage qui ne peut pas être compatible pour tous les points du graphique. Deuxièmement, les fluctuations relativement élevés des déplacements autour d'un niveau assez constant pendant les mesures satellitaires en 2013 peuvent être liées à l'instabilité du point de

## Résumé étendu (fr)

référence au sommet du glissement de terrain (qui a été effectivement confirmée par la réalité de terrain). Cela peut provoquer des erreurs à la fois pour les mesures satellitaires et topographiques. Troisièmement, les mesures in situ qui sont prises comme vérité ont aussi leurs propres erreurs qui peuvent atteindre quelques millimètres.

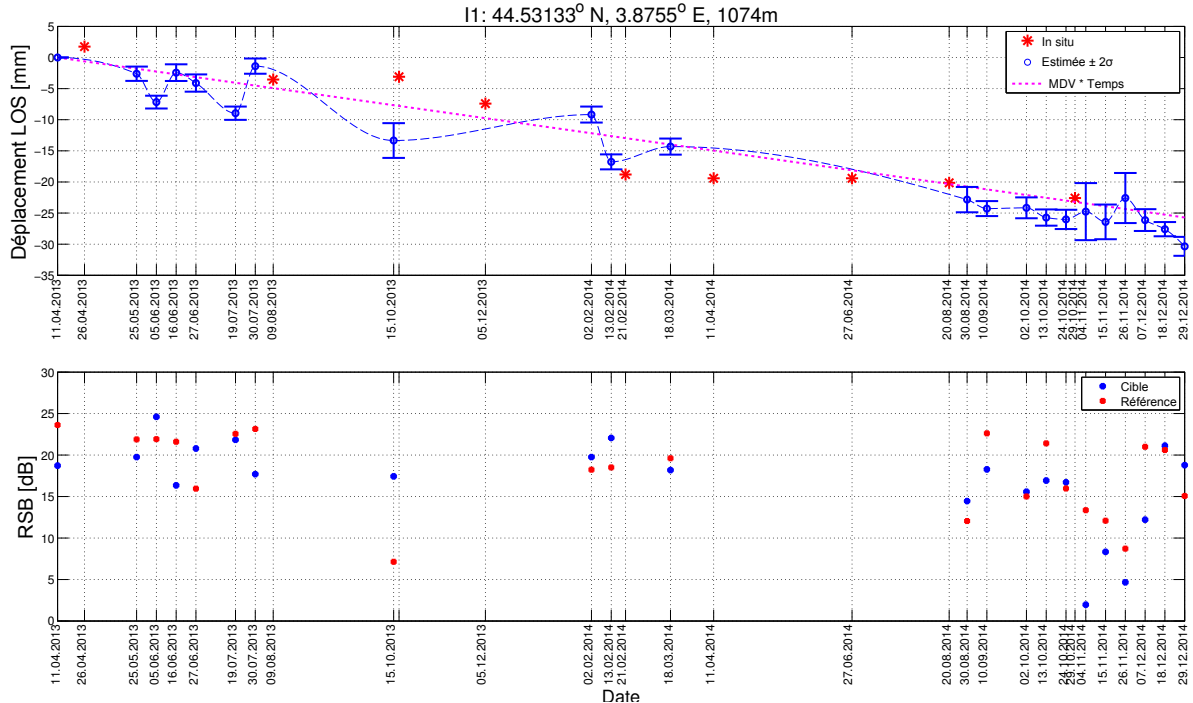


Figure A13: Déplacements LOS estimés versus in situ pour l'un des diffuseurs détectés sur le glissement de terrain du Chastel (I1).

### VI.2.2 Le barrage de Puylaurent

Pour le barrage, la région testée pour les centres de diffusion est composée de points situés près de la crête du barrage et les massifs environnants. Le barrage a généralement un mouvement saisonnier et ne suit pas une seule tendance linéaire, de sorte que le MDV n'aura une signification physique que s'il est calculé pour des périodes relativement courtes.

Dans la Fig. A14 sont présentés les centres de diffusion détectés et leurs MDVs pour l'orbite descendante dans l'intervalle Septembre-Décembre 2014 lorsque le mouvement est relativement linéaire avec une tendance unique. La référence choisie est une région hautement réfléchissante du côté de la rive droite de la crête (la région avec zéro MDV sur le côté gauche de la figure). Les valeurs positives et négatives indiquent le mouvement de la structure dans la ligne de visée quand il se rapproche, et respectivement, s'éloigne du satellite (en accord avec le vecteur unitaire LOS).

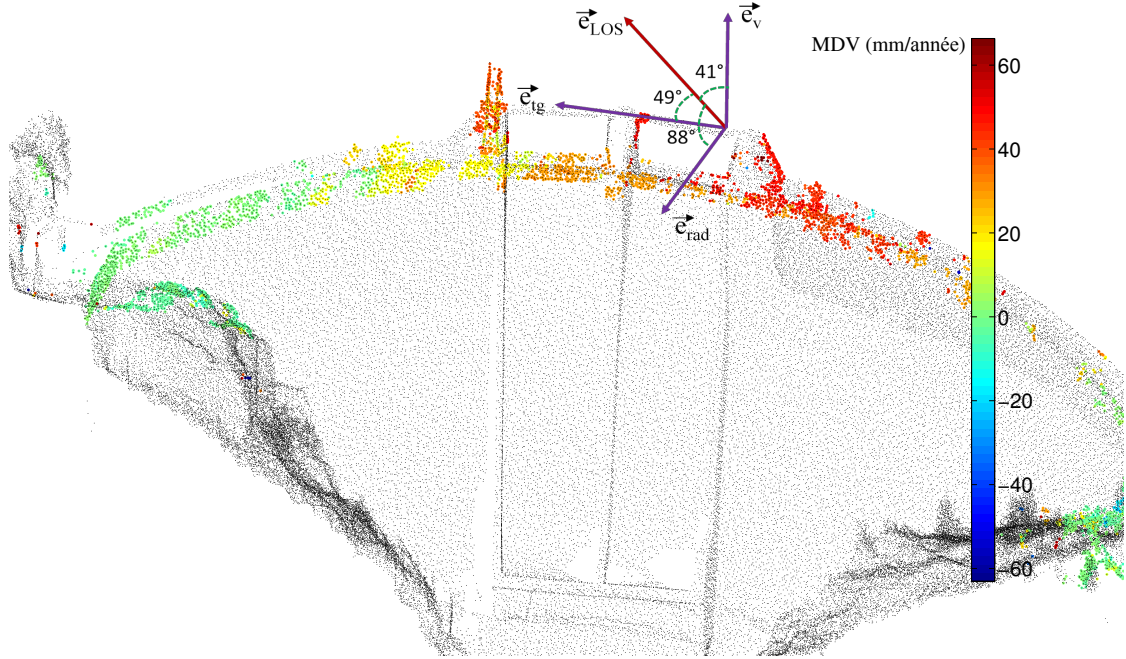


Figure A14: Les centres de diffusion du barrage Puylaurent et leurs MDV entre Septembre-Décembre 2014 de l'orbite descendante. Sur la figure, nous soulignons également les angles entre la direction LOS et les vecteurs locaux unitaires (tangential, radial, vertical).

Afin d'obtenir des séries temporelles de déplacements précis, les mesures des déplacements sont extraites des phases de coins réflecteurs placés sur le barrage. Fig. A15 montre l'évolution de déplacement d'un coin réflecteur entre 2013 à 2014, ainsi que les niveaux d'eau dans le réservoir et les températures obtenues à partir d'une station météorologique près du site.

Les données in-situ ne proviennent que de déplacements dans le plan horizontal (tangential et radial) et ne comprend pas les mouvements verticaux. Évidemment, le mouvement en lignée de visée obtenue par satellite est un mélange de tous les trois composantes, ce qui explique les différences entre les deux graphiques. Pour une bonne observation, les deux séries de temps (estimée et in situ) sont alignées de telle sorte que la valeur moyenne est la même. Les différences entre ces deux mesures sont situées à environ quelques millimètres et proviennent principalement de l'absence d'informations in situ sur les déplacements verticaux. Outre cela, les déplacements mesurées par satellite comptent sur un point de référence sur le côté de la crête qui n'est pas exactement le même que la référence du système de pendules. Le point d'ancrage de chaque pendule n'est pas à l'extérieur du barrage et par conséquence le déplacement n'est pas identique à celui perçu par le capteur spatial.

## Résumé étendu (fr)

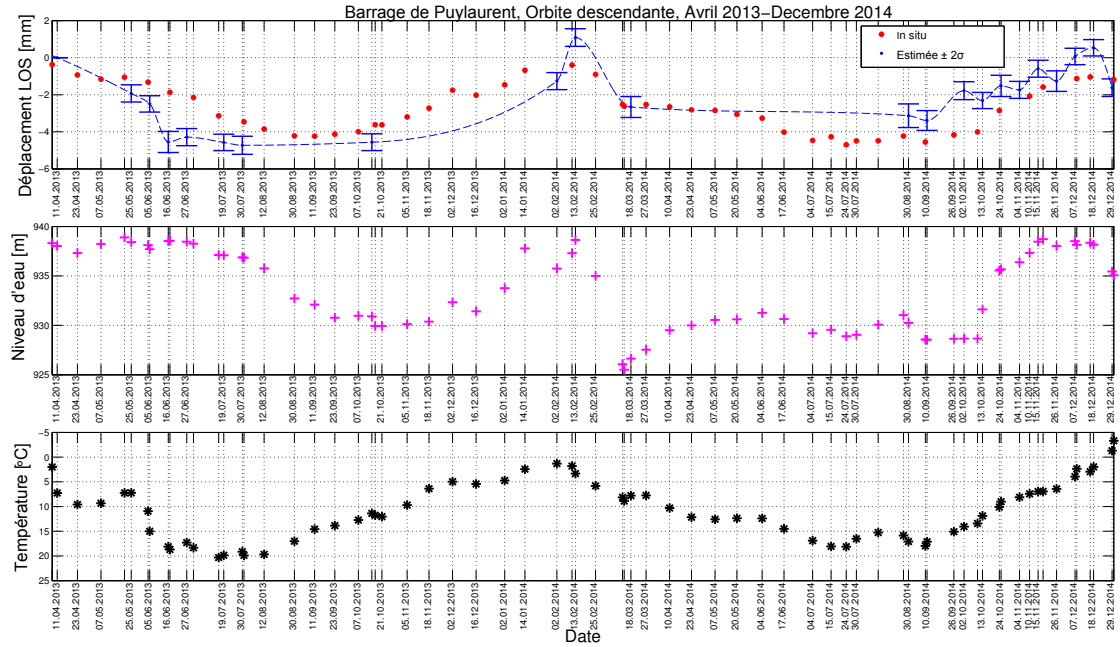


Figure A15: La série temporelle de déplacements d'un coin réflecteur placé sur la crête du barrage de Puylaurent pour l'orbite descendante dans l'intervalle 2013-2014.

Le mouvement du barrage provient des fluctuations des niveaux d'eau et de la dilatation/contraction dues aux variations de température. Cela peut être noté sur les graphiques par la corrélation entre le niveau d'eau/température et le déplacement des barrages, mais il est assez difficile de séparer les deux effets. Par exemple, la diminution rapide du niveau d'eau entre Février-Mars 2014 et la baisse de température relativement constante entre Août-Décembre 2014 sont remarquées à la fois par les mesures in situ et par télédétection.

Cependant, parce que le mouvement vertical du barrage (pour lesquels il n'y a pas de capteur in situ) est principalement assuré par les variations de température, des variations de température rapides au niveau d'eau constant peuvent être récupérées uniquement sur la série temporelle obtenue par télédétection. Par exemple, en Juin 2013, la température a une baisse soudaine qui est clairement reflétée dans la série temporelle estimée à partir des images RSO.

## Remarques générales, conclusions et perspectives

Cette thèse vise à montrer d'une manière cohérente nos contributions dans le domaine de la télédétection radar. L'idée était de formuler des réponses originales à une question théorique et une autre, plus appliquée concernant le suivi de déformation. D'une part, considérant notre environnement biaisé vers le traitement temps-fréquence des signaux non-stationnaires, les réponses à la première question parviennent à introduire des interprétations temps-fréquence adaptées aux signaux radar à synthèse d'ouverture avec les outils de traitement appropriés conçus à la fois pour les signaux RSO de distance et d'azimut. D'autre part, la solution apportée à la deuxième question, soulevée dans le contexte industriel de la thèse, introduit une nouvelle méthode de traitement des images RSO spatiales adaptée aux applications de surveillance de l'infrastructure.

Par la suite, nous revoyons les principaux résultats et contributions de la thèse:

- Nous avons développé deux méthodes de correction de non-linéarité en distance pour les radars FMCW à large bande basés sur la notion de ré-échantillonnage temporel combinée avec les fonctions d'ambiguïté d'ordre supérieur et, respectivement, avec une mesure de la concentration spectrale. La méthode basée sur HAF estime les non-linéarités sur le signal de battement correspondant à une cible de référence, tandis que l'algorithme d'autofocus radial (en distance) déforme, à la fois, le signal de battement selon les différentes fonctions de modulation et sélectionne comme la meilleure fonction celle qui offre la concentration spectrale la plus élevée du signal déformé. Les algorithmes ont été testés et comparés à l'aide de divers scénarios de simulation et de données réelles acquises avec une plateforme radar FMCW en bande X conçue pour les mesures de déplacement des cibles à courte portée. Sur la base des profils en distance et des images RSO corrigées de non-linéarité nous avons mesuré les déplacements de cibles très réfléchissantes avec une précision sous millimétrique.
- Une nouvelle méthodologie de traitement des images RSO a été conçue. La procédure exploite un modèle numérique de la scène imagée et elle est basée sur le recentrage en azimut des images RSO suivi par l'identification des centres de diffusion en utilisant le cadre de la tomographie RSO différentielle (à quatre dimensions). Les simulations réalisées pour évaluer les performances de l'algorithme visent plusieurs aspects. Tout d'abord, nous avons souligné que l'approche de recentrage fournit des meilleurs résultats que quelques méthodes d'interpolation à deux dimensions (utilisées pour la conversion à la géométrie du sol), en termes de cohérence moyenne et dispersion de phase. Ensuite, nous avons étudié la méthode de détection des diffuseurs et d'estimation des déplacements dans différents scénarios de simulation développés afin de déterminer l'impact sur les performances de certains paramètres: RSB, nombre de pistes, la précision en élévation, le mouvement non linéaire et les cibles

## Résumé étendu (fr)

---

en chevauchement. Enfin, nous avons comparé la méthode de détection développée (basée sur le test de position en élévation) à des approches classiques de détection des diffuseurs utilisées dans l'interférométrie des diffuseurs permanents (PSI) ou dans la tomographie différentielle. Nous avons souligné que le test de position peut intrinsèquement rejeter les cibles affectées par chevauchement en utilisant l'information externe fournie par le modèle numérique de terrain.

- Nous avons décrit les principaux problèmes à traiter dans le cadre de la surveillance de déformation afin de combiner des images RSO à haute résolution acquises dans différents modes d'imagerie avec le nuage de points 3D d'une certaine infrastructure. Nous avons appliqué la méthodologie développée sur deux ensembles d'images RSO acquises à travers les missions TerraSAR-X/TanDEM-X pour la surveillance des deux sites: le barrage de Puylaurent et le glissement de terrain du Chastel. Les nuages pour ces deux structures ont été générés à l'aide de mesures GPS, relevés topographiques et scanners laser. Les particularités de la chaîne de traitement de données proposée ont été examinées dans la perspective des données réelles, en tenant compte des problèmes spécifiques tels que –les effets atmosphériques, la précision de l'orbite, la déviation à partir du modèle de déformation ou le repliement du spectre Doppler. Les résultats de la surveillance consistent à vitesses de déformation moyennes et séries temporelles des déplacements LOS. Le cas échéant, les déplacements moyens ont été projetés sur le modèle de déformation locale. Les déplacements mesurés étaient en bon accord avec les données *in situ* et en corrélation avec d'autres facteurs physiques comme la dilatation et le niveau d'eau dans le cas du barrage.

Dans l'avenir, ces contributions seront développées et exploitées dans des contextes différents. Les perspectives les plus plausibles sont:

- Les procédés de correction de non-linéarité peuvent être étendus pour les VCO avec courbes de réglage arbitraires en utilisant les algorithmes proposés pour des approximations locales de la forme non linéaire, suivis d'une reconstruction de la trajectoire temps-fréquence. Cette mise à niveau est utile pour compenser les non-linéarités résiduelles qui peuvent apparaître même dans le cas des VCO essentiellement linéaires.
- L'algorithme d'autofocus peut être considéré comme une méthode générale d'estimation des paramètres des signaux ayant la même structure que les signaux de battement non linéaires. Par exemple, le procédé peut être étendu comme noyau pour suivre en temps-fréquence de signaux non stationnaires avec harmoniques, tels que les signaux acoustiques. Les premiers résultats de cette approche ont été testés pour les signaux provenant des mammifères marins.

- Pour la transformée adaptée au signal utilisé dans les algorithmes développés dans la thèse pour obtenir un profil en distance corrigé de non-linéarité, il n'y a pas de discussion dans la littérature à propos de la détection statistique des signaux représentés dans le domaine transformé. Par conséquent, une perspective intéressante est d'analyser les statistiques de bruit dans le domaine de la transformée adaptée au signal et proposer un schéma de détection adéquate. La mise à niveau de cet outil de traitement avec un détecteur statistiquement caractérisé est essentielle pour des applications dans le radar et les communications.
- La défocalisation en azimut peut être utilisée pour suivre en temps-fréquence le micro-Doppler de cibles mobiles. La méthode de défocalisation est un moyen pratique d'accéder à l'histoire de phase de micro-Doppler à partir des produits livrés. Ceci est important car dans le traitement en azimut, le micro-Doppler peut être modifié et juste une transformée de Fourier inverse en azimut de l'image RSO ne peut pas le récupérer correctement. Les premiers essais de cette extension ont été axés sur les problèmes d'estimation de vibration.
- La méthodologie de traitement des images RSO proposée peut être complétée en utilisant d'autres estimateurs pour le plan élévation-vitesse combinés avec des modèles de déformation non linéaires. En outre, la détection basée sur le test de position pourrait être renforcée en effectuant la détection avant la focalisation en azimut aidée par la position azimutale fournie par le modèle 3D. De cette façon, nous pouvons combiner le test de position (basé sur focalisation en élévation des données multi-temporelles/multi-distance) avec une détection des diffuseurs cohérents dans une seule image RSO basée sur la décomposition en sous-bandes d'azimut. La disponibilité de l'histoire de la phase d'azimut (obtenu à l'étape de défocalisation) permet différentes combinaisons entre les intervalles de temps d'azimut, les bandes de fréquences et l'ouverture d'élévation afin de générer un (azimut) temps - (azimut) fréquence - (élévation) espace détecteur qui peut simultanément exploiter les caractéristiques des diffuseurs en azimut et en élévation.